frontiers | Research Topics

Structural applications of concrete with recycled solid wastes and alternatives for cement

Edited by
Biao Hu, Jianping Lin and Nicola Nistico'

Coordinated by
Rui Hu

Published in
Frontiers in Materials

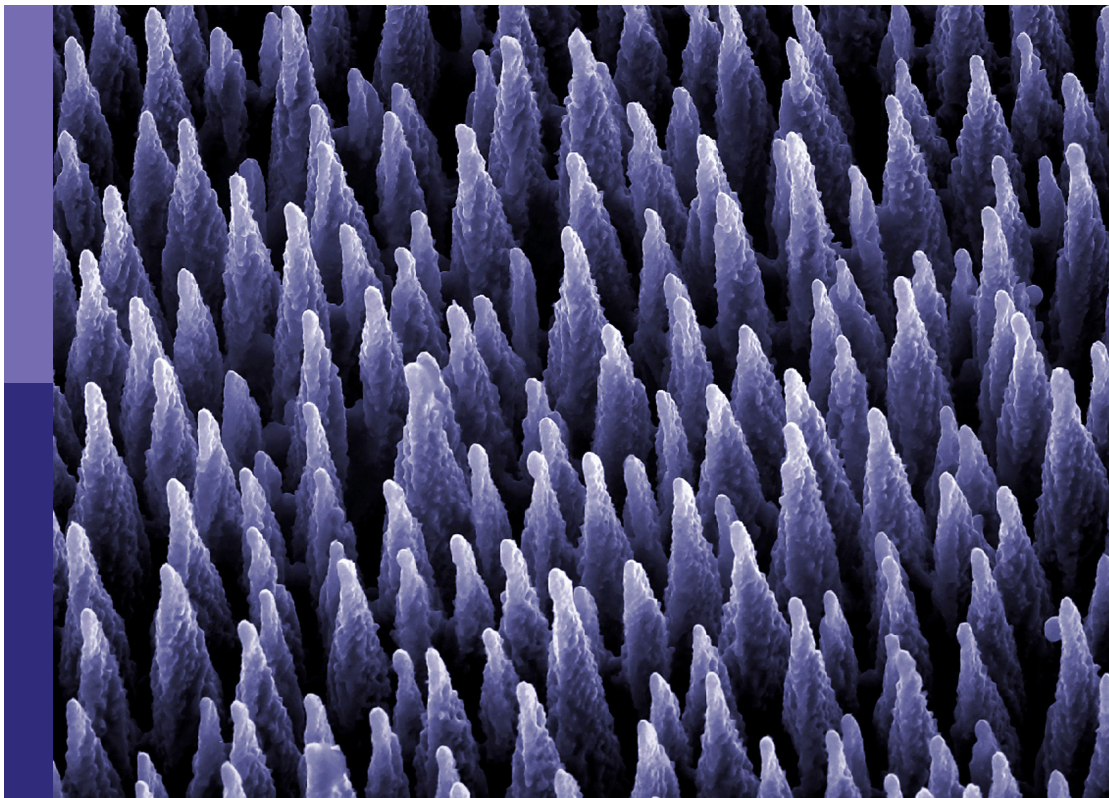

ISSN 1664-8714
ISBN 978-2-8325-6383-0
DOI 10.3389/978-2-8325-6383-0

About Frontiers

Frontiers is more than just an open access publisher of scholarly articles: it is a pioneering approach to the world of academia, radically improving the way scholarly research is managed. The grand vision of Frontiers is a world where all people have an equal opportunity to seek, share and generate knowledge. Frontiers provides immediate and permanent online open access to all its publications, but this alone is not enough to realize our grand goals.

Frontiers journal series

The Frontiers journal series is a multi-tier and interdisciplinary set of open-access, online journals, promising a paradigm shift from the current review, selection and dissemination processes in academic publishing. All Frontiers journals are driven by researchers for researchers; therefore, they constitute a service to the scholarly community. At the same time, the *Frontiers journal series* operates on a revolutionary invention, the tiered publishing system, initially addressing specific communities of scholars, and gradually climbing up to broader public understanding, thus serving the interests of the lay society, too.

Dedication to quality

Each Frontiers article is a landmark of the highest quality, thanks to genuinely collaborative interactions between authors and review editors, who include some of the world's best academicians. Research must be certified by peers before entering a stream of knowledge that may eventually reach the public - and shape society; therefore, Frontiers only applies the most rigorous and unbiased reviews. Frontiers revolutionizes research publishing by freely delivering the most outstanding research, evaluated with no bias from both the academic and social point of view. By applying the most advanced information technologies, Frontiers is catapulting scholarly publishing into a new generation.

What are Frontiers Research Topics?

Frontiers Research Topics are very popular trademarks of the *Frontiers journals series*: they are collections of at least ten articles, all centered on a particular subject. With their unique mix of varied contributions from Original Research to Review Articles, Frontiers Research Topics unify the most influential researchers, the latest key findings and historical advances in a hot research area.

Find out more on how to host your own Frontiers Research Topic or contribute to one as an author by contacting the Frontiers editorial office: frontiersin.org/about/contact

Structural applications of concrete with recycled solid wastes and alternatives for cement

Topic editors
Biao Hu — Shenzhen University, China
Jianping Lin — Huaqiao University, China
Nicola Nistico' — Sapienza University of Rome, Italy

Topic coordinator
Rui Hu — Shenzhen University, China

Citation
Hu, B., Lin, J., Nistico', N., Hu, R., eds. (2025). *Structural applications of concrete with recycled solid wastes and alternatives for cement*. Lausanne: Frontiers Media SA. doi: 10.3389/978-2-8325-6383-0

Table of contents

frontiers | Frontiers in Materials

TYPE Editorial
PUBLISHED 14 May 2025
DOI 10.3389/fmats.2025.1614419

OPEN ACCESS

EDITED AND REVIEWED BY
John L. Provis,
Paul Scherrer Institut (PSI), Switzerland

*CORRESPONDENCE
Rui Hu,
jiaruihu@szu.edu.cn
Muhammad Tahir,
engrmtahir09@szu.edu.cn

RECEIVED 18 April 2025
ACCEPTED 22 April 2025
PUBLISHED 14 May 2025

CITATION
Hu B, Lin J, Nistico' N, Hu R and Tahir M (2025) Editorial: Structural applications of concrete with recycled solid wastes and alternatives for cement.
Front. Mater. 12:1614419.
doi: 10.3389/fmats.2025.1614419

Editorial: Structural applications of concrete with recycled solid wastes and alternatives for cement

Biao Hu[1,2], Jianping Lin[3], Nicola Nistico'[4], Rui Hu[1,2]* and Muhammad Tahir[1,2]*

[1]Guangdong Provincial Key Lab of Durability for Marine Civil Engineering, Shenzhen University, Shenzhen, China, [2]National Key Laboratory of Green and Long-Life Road Engineering in Extreme Environment (Shenzhen), Shenzhen, China, [3]College of Civil Engineering, Huaqiao University, Xiamen, Fujian, China, [4]Department of Structural and Geotechnical Engineering, Sapienza University of Rome, Rome, Italy

KEYWORDS

green concrete, carbon emisions, solid waste, waste managemen, cement alternative

Editorial on the Research Topic
Editorial: Structural applications of concrete with recycled solid wastes and alternatives for cement

Concrete, as the most widely utilized construction material, has long been central to discussions on sustainability due to its intensive consumption of natural resources and significant carbon footprint. In light of increasing environmental and economic challenges, there is a growing interest among researchers and engineers in developing sustainable alternatives by integrating recycled solid waste and alternative binders into concrete. This paradigm shift not only addresses issues of waste management and resource depletion but also supports the advancement of innovative, high-performance materials suitable for structural applications. This special issue compiles a diverse range of original research and review articles focused on recent advances in sustainable concrete. The contributions span material development, durability assessment, and emerging computational and experimental strategies for optimizing mix design and structural behavior. These works collectively highlight the transition toward environmentally responsible, high-performance construction solutions.

Chen et al. proposed a systemic approach for the reuse of construction waste from abandoned buildings by establishing a material flow analysis and an evaluation index system. Their study identifies critical opportunities and challenges in the recycling process and offers a valuable framework for advancing circular economy practices within the built environment.

As far as material development is concerned, Umar et al. investigated the incorporation of bentonite clay and quarry dust as supplementary cementitious materials. Their findings indicate enhancements in compressive strength and resistance to both hydrochloric and sulfuric acids, underscoring the potential of these materials as sustainable and cost-effective alternatives to traditional cement. He et al. employed machine learning, specifically support vector regression, to predict the mechanical behavior of cement-based materials filled with

PVA-modified waste rubber. Their results affirm the utility of AI-driven tools in optimizing mix design and forecasting performance with high accuracy.

Bond behavior between concrete and steel reinforcement remains critical in structural applications. Shusen et al. explored the effect of a sludge-modified magnesium phosphate coating on bond performance. While bond strength improved for plain bars, a slight reduction was observed in ribbed bars, suggesting the need for differentiated strategies depending on reinforcement type.

Zhou et al. addressed long-term performance through enhanced creep modeling of green concrete. Utilizing the Weeks method of inverse Laplace transform, they obtained continuous retardation spectra with improved accuracy and computational efficiency. This advancement supports more reliable long-term structural analysis and deformation prediction.

Structural innovations were explored through advanced composite systems. Liu et al. introduced a novel multi-chamber concrete-filled steel tube (CFST) column with round-ended sections to enhance seismic performance. Static load testing confirmed increased ductility and energy dissipation. Jun et al. investigated CFST circular arches, analyzing the effects of geometric and material parameters. Their experimental and numerical studies revealed that arch foot slip and local buckling notably influence load-bearing capacity, offering practical insights for the design of underground support structures.

The reduction of CO_2 emissions is another central theme. Wang et al. examined the role of dispersants in nanocarbon black-modified cement paste. Their findings show that improved dispersion enhances mechanical and electrical properties, accelerates snow-melting performance, and lowers energy use and carbon emissions based on life-cycle assessment (LCA). Similarly, Ning et al. developed permeable concrete using alkali-activated sintered sludge and slag. Their work demonstrates that increasing sludge content significantly decreases CO_2 emissions while preserving adequate permeability, providing a viable solution for sustainable urban infrastructure.

Altogether, these contributions illustrate the breadth and depth of contemporary research on sustainable structural concrete. By integrating recycled materials and alternative binders and adopting advanced modeling and design techniques, researchers are paving the way toward environmentally responsible and economically feasible construction practices. The studies highlighted here demonstrate the value of interdisciplinary collaboration and innovation in achieving high-performance, sustainable infrastructure.

We extend our sincere appreciation to all authors for their contributions and to the editorial staff of *Frontiers in Materials* for facilitating this Research Topic.

Author contributions

BH: Supervision, Conceptualization, Writing – review and editing, Writing – original draft. JL: Writing – review and editing, Writing – original draft. NN: Writing – review and editing, Writing – original draft. RH: Writing – review and editing, Writing – original draft. MT: Writing – review and editing, Writing – original draft.

Funding

The author(s) declare that no financial support was received for the research and/or publication of this article.

Conflict of interest

The authors declare that the research was conducted in the absence of any commercial or financial relationships that could be construed as a potential conflict of interest.

The author(s) declared that they were an editorial board member of Frontiers, at the time of submission. This had no impact on the peer review process and the final decision.

Generative AI statement

The authors declare that Gen AI was used in the creation of this manuscript. Generative AI was used to improve the manuscript's English writing.

Publisher's note

frontiers | Frontiers in Materials

TYPE Original Research
PUBLISHED 05 December 2023
DOI 10.3389/fmats.2023.1285551

OPEN ACCESS

EDITED BY
Pengjiao Jia,
Soochow University, China

REVIEWED BY
Qian Bai,
Northeastern University, China
Cheng Cheng,
Soochow University, China

*CORRESPONDENCE
Zhu Chuangen,
574947149@qq.com

RECEIVED 30 August 2023
ACCEPTED 20 November 2023
PUBLISHED 05 December 2023

CITATION
Jun W, Chuangen Z, Fuli B, Guangming X, Yan L, Bo W, Guifeng D and Zhaolong T (2023), Experimental research and engineering application on bearing capacity of concrete-filled steel tube circular arch.
Front. Mater. 10:1285551.
doi: 10.3389/fmats.2023.1285551

Experimental research and engineering application on bearing capacity of concrete-filled steel tube circular arch

Wang Jun[1,2], Zhu Chuangen[1]*, Bo Fuli[3], Xin Guangming[3], Liu Yan[3], Wang Bo[4], Dong Guifeng[3] and Tian Zhaolong[3]

[1]School of Civil Engineering, Shandong Jianzhu University, Jinan, China, [2]Laboratory of Building Structural Retrofitting and Underground Space Engineering (Shandong Jianzhu University), Ministry of Education, Jinan, China, [3]Shandong Jikuang Luneng Coal Power Co., Ltd., Yangcheng Coal Mine, Jining, China, [4]School of Emergency Technology and Management, North China Institute of Science and Technology, Beijing, China

The bearing property and deformation failure law of the CFST circular arch were investigated in order to provide direction for the optimization of the concrete-filled steel tube (CFST) support. The flexural bearing capacity test of the 194 mm × 10 mm CFST was performed initially in this study. It was primarily explored how bearing capacity and deformation of circular arches were affected by the slip of the arch foot and anti-bending strengthening, and the neutral layer migration rule and anti-bending strengthening mechanism of circular arches were examined. The bearing performance of the circular arch under the condition of the concentrated load of the vault and the usual uniform load of the entire span is then simulated in an orthogonal test by numerical simulation in order to extend the experimental investigation. The effect of variables including the steel tube's outer diameter, thickness, slip of the arch foot, and the ratio of the arch rise to span on the bearing capacity of the circular arch is examined. The study demonstrates that under focused stress on the arch top or full-span normal uniform loading, the arch foot slip is the most important element impacting the CFST support's bearing capacity. In steel tubes with the same outer diameter and wall thickness, the vector span ratio has a bigger influence than anti-bending strengthening. When the span ratio is the same, the influence of the outer diameter and wall thickness are equal and outweigh the influence of bending strengthening. The circular arch with an outside diameter of 168 mm, a wall thickness of 10 mm, and a rise-span ratio of 0.207 has the best performance characteristics under the influence of concentrated load, and the ultimate failure mechanism is local waist drum deformation failure. Based on the aforementioned study findings, the circular CFST support's buckling deformation and drum deformation are examined, and a composite support consisting of "anchor net spray + CFST support" is directed for the north three deep track downhill of Yangcheng Coal Mine. Two failure types

expose the failure mechanism and provide a technique for optimization. The support had contributed to the circular CFST arc arch's best bearing performance in the event of waist drum deformation and failure.

KEYWORDS

concrete filled steel tube circular arch, arch foot slip, anti-bending strengthening, waist drum deformation, backwall filling

1 Introduction

The concrete-filled steel tube's (CFST) circular arch may convert an external load into an axial force acting on the arch, maximizing the benefits of the material's high axial bearing capacity and enabling CFST support with a circular arch. High carrying capacity is a benefit of the support (Gao et al., 2010; Li et al., 2017). It is being used frequently in deep roadway support and has produced positive supportive results (Li et al., 2013; He et al., 2015; Liu et al., 2018; Wang et al., 2020). However, there are still some issues with drum deformation failure or buckling deformation failure of steel tube supports that are filled with concrete in real-world engineering applications. Studying the causes of failure can help to direct and improve the support design of steel tube supports that are filled with concrete.

Relevant academics both domestically and internationally have conducted in-depth research on concrete filled steel tubular circular arches. Mark Andrew Bradfor and Yonglin Pi et al. (Bradford et al., 2011; Pi et al., 2011) studied the in-plane time-varying performance, buckling behavior, and various factors caused by shrinkage and creep of core concrete under radial uniform load through theoretical analysis and numerical simulation. Wang et al. (2011a,b) investigated the in-plane nonlinear stability carrying capacity of CFST circular arch under uniform load and the impact of core concrete shrinkage and creep, rise-span ratio, and arch stability outside of plane. The mechanical characteristics and stability of the CFST circular arch structure under concentrated load were examined and assessed by Luo et al. (2015). Through numerical simulation, Han et al. (2020) investigated the bearing behavior of the CFST circular arch's structural performance during an in-plane instability failure. They also looked at the effects of concrete strength, rise-span ratio, and other variables. Through theoretical research, laboratory testing, and numerical simulation, Lu and Sun. (2020) established the stress model of CFST circular arch, which offers a theoretical foundation for the design of subterranean engineering support. Shan et al. (2018) studied the effects of the arc arch under six-point equivalent loading, such as the vector span ratio and steel fiber content, on the mechanical properties of the specimen and discovered the reasons for the local instability failure of the component through laboratory tests, numerical simulation, and theoretical analysis. Through laboratory testing and theoretical research, Zhang et al. (2017) identified the circular arch's failure mode and came to the essential requirement for the circular arch's overall instability. Through laboratory testing and numerical simulations, Liu et al. (2018) investigated the impact of rise-span ratio on the failure characteristics and ultimate bearing capacity of CFST circular arches and revealed the compression failure mechanism of steel tubes and core concrete. Yan et al. (2018) examined the creep and bearing capacity of a circular fly ash-filled CFST arch and the mechanism by which internal structural forces affect the height of the neutral layer. Through laboratory tests, Hu et al. (2020) investigated the in-plane stability of circular CFST arches with various rise-span ratios under a concentrated five-point symmetric load.

The bearing capabilities and stability of the circular arch of CFST were primarily examined in the aforementioned literature. However, there are few studies on the deformation and failure analysis of the circular arch waist, and the study on the compression-bending performance of the CFST circular arch under the circumstances of anti-bending strengthening or sliding of the arch foot is not sufficiently thorough. Based on the experimental study on the bearing capacity of circular arches, the experimental study is enlarged by numerical simulation with the goal of addressing the yield failure problem of CFST circular arches. Different loading forms, steel tube wall thickness, rise-span ratio, anti-bending strengthening of the arch, and slip of the arch foot were evaluated as effect variables. The bending failure mechanism of the CFST circular arch was discovered, and this information was used to direct the structural optimization of the CFST circular support in the deep highway support.

2 Bearing performance test of CFST circular arch

The CFST tube support, which is often split into four circular arch sections, is a frequent supporting structure in deep roadways (Figure 1). In order to conduct experimental study, the 1/4 circular arch was removed. The bearing performance of the structure under centralized loading and full-span uniform loading of the arch was then examined.

2.1 Test group design

Made of seamless steel tubing of grade 20# measuring 194 mm by 10 mm, the circular arch is constructed. The two ends are flattened and treated perpendicular to the arch's axis. Concrete that hardens quickly, type C40, is poured within the steel tube. According to the diameter of the anti-bending round steel, six specimens were created. Steel rounds with diameters between 40 and 60 were used to weld the circular arch. The dimensions are depicted in Figure 2, and the parameters are presented in Supplementary Table S1. As indicated in Figure 3, the arch foot slip is initially 0 mm at the start of the test and is adjusted to 30 mm as the test progresses. The slip of arch foot is divided according to the distance between supporting structure and surrounding rock in actual field.

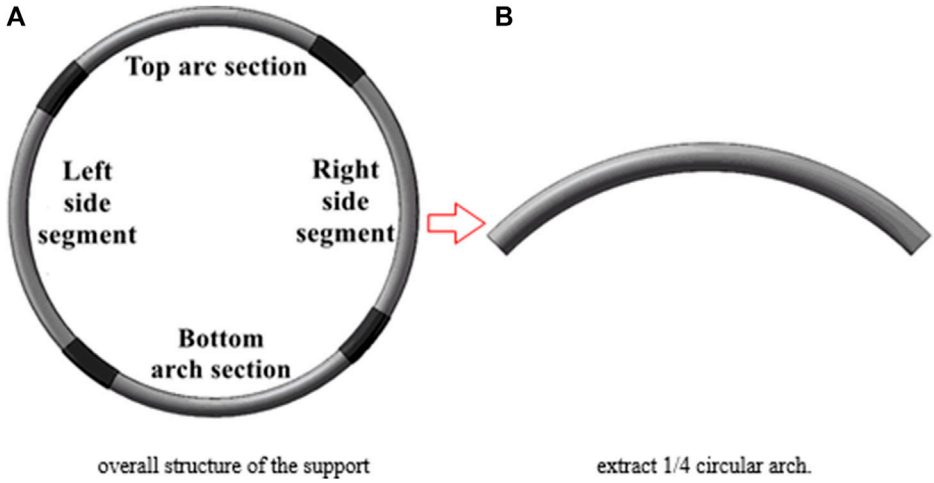

FIGURE 1
Extraction diagram of circular concrete-filled steel tube support test members.

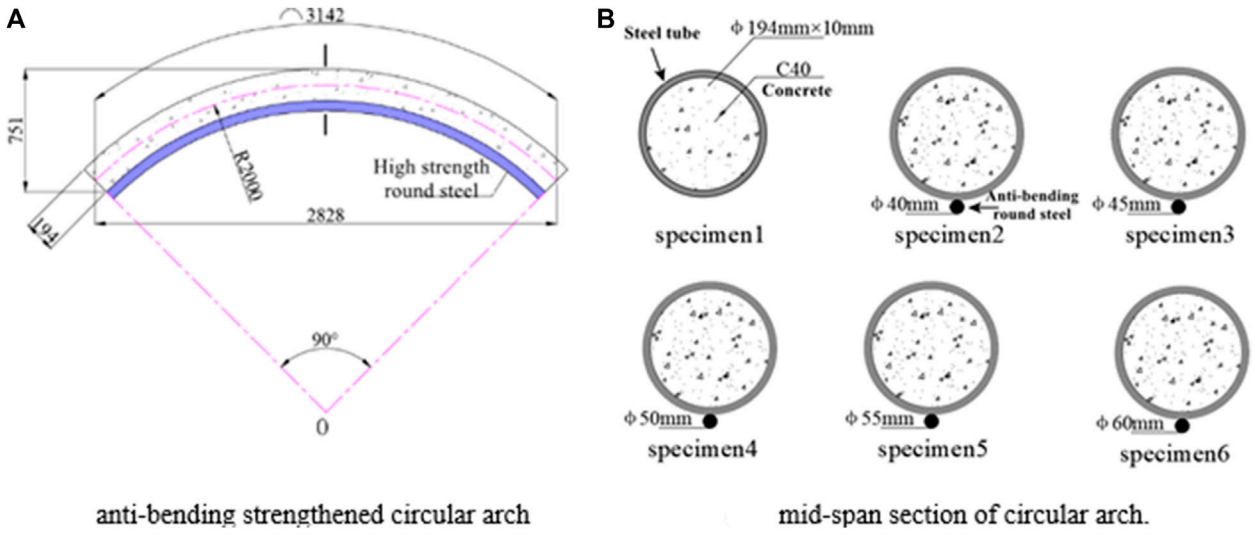

FIGURE 2
Size diagram and section feature diagram of circular arch structure strengthened by anti-bending.

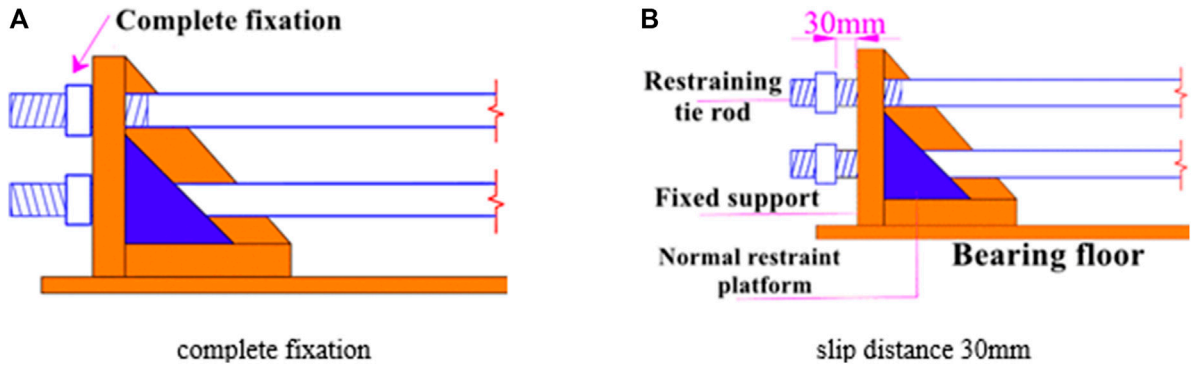

FIGURE 3
Design of slip quantity of support.

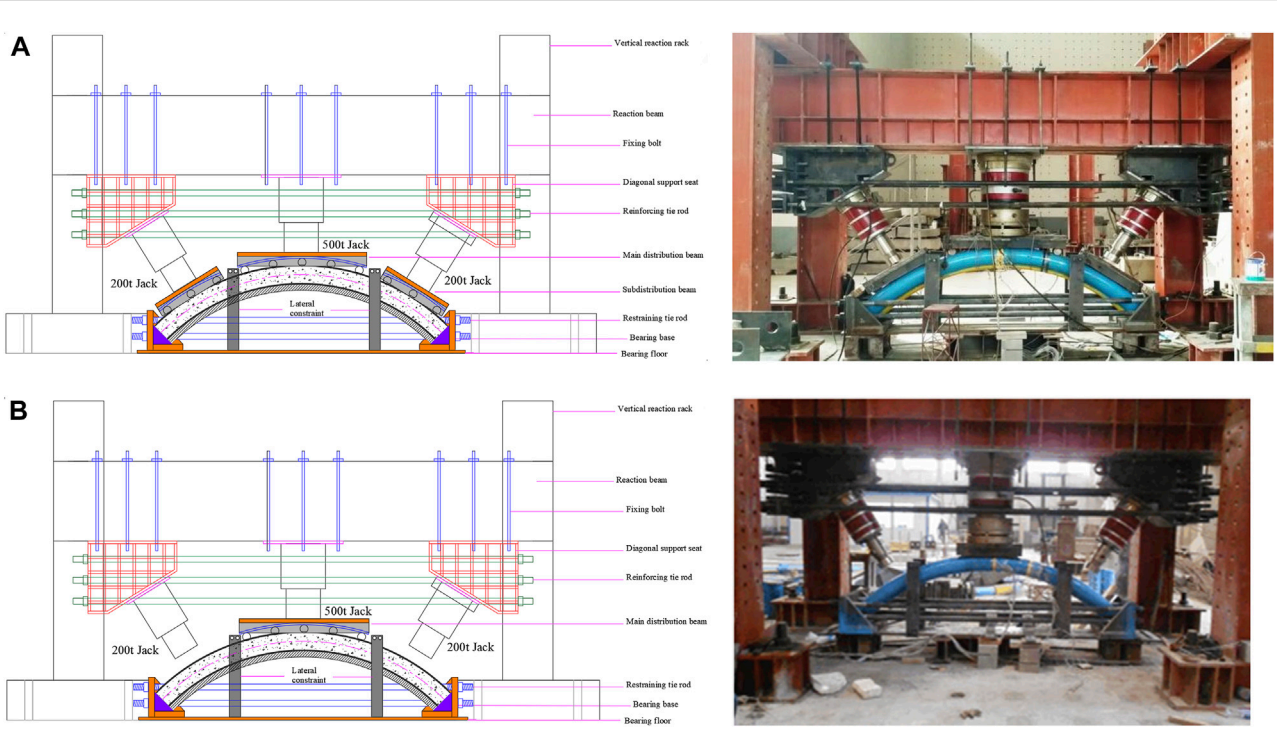

FIGURE 4
Design structure and picture of test bench.

2.2 Loading method

The structural laboratory of the School of Civil Engineering at Shandong Jianzhu University is where the test was conducted using a big reaction frame test bench. As seen in Figure 4A, B, the 200t hydraulic jack (both sides) and 500t hydraulic jack (vault) were employed. The three jacks are operated by the same hydraulic control system to produce synchronous equal pressure output for the loading form, which then allows for the realization of top centralized loading (vault 3 point loading) and full span uniform loading (full span 11 point loading) via the primary and secondary distribution beams. At the same time, the paired support plates are employed to create lateral restraints to prevent the circular arch from becoming out-of-plane.

3 Analysis of test results of CFST circular arch

The effect of support slip and anti-bending strengthening on the bearing performance of a circular arc arch was investigated, and the compression-bending deformation mechanism of a circular arc arch, which mostly contains neutral layer migration and anti-bending strengthening law, was developed.

3.1 Analysis of influence of support slip

(1) Test results under the constraint of full-span uniform distribution point loading + fixation

The CFST circular arch was tested, with the arch web welded with 45 mm bending round steel. There was no slide in the arch foot, and the full-span typical uniform point load was applied. When the jack load is 2000 kN, the vertical displacement of the specimen is approximately 10 mm; when the load is 3,000 kN, the vertical displacement of the specimen is approximately 18 mm. Continue to load until the hydraulic system's pressure reaches the limit, at which point the test is terminated. The vertical residual distortion in the middle span after unloading is 8 mm, and the deformation is nearly imperceptible.

(2) Test results under concentrated loading + fixed constraints on vault

There is no slide at the arch foot and concentrated loading at the arch top in the case of the circular CFST arch that was welded with 45 mm bending round steel on the soffit. Test methodology: When the vault jack force reaches 2000 kN, the specimen's mid-span displacement is 15 mm; when the jack load is increased to 3000 kN, the specimen's mid-span displacement is 30 mm, but the structural deformation is still not immediately apparent. The hydraulic system is now overrun once more, and the test is terminated. The specimen is somewhat distorted after unloading with a 20 mm vertical residual distortion.

(3) Test results of arch crown concentrated loading + arch foot sliding

As shown in Figure 5A, the CFST circular arch with 45 mm bending round steel is chosen to carry out concentrated loading on the vault because the results of the previous two tests are not

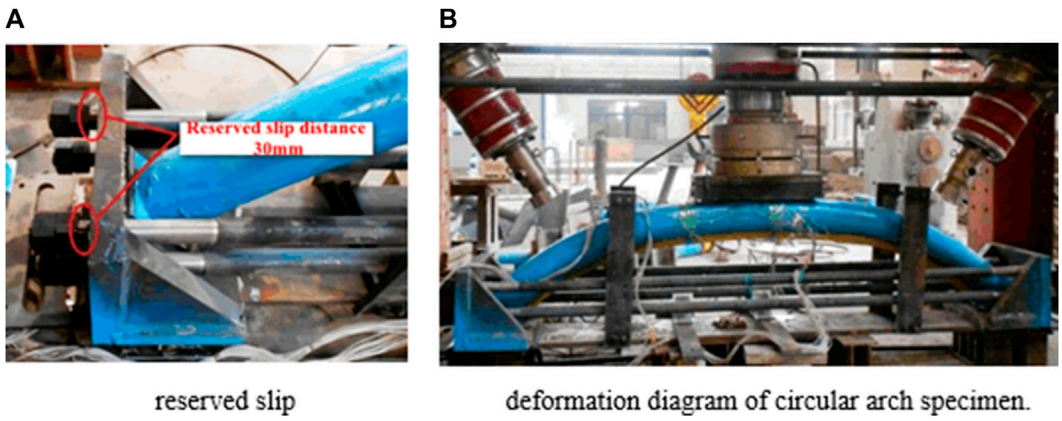

FIGURE 5
Test results of circular arch under top concentrated loading + arch foot slide.

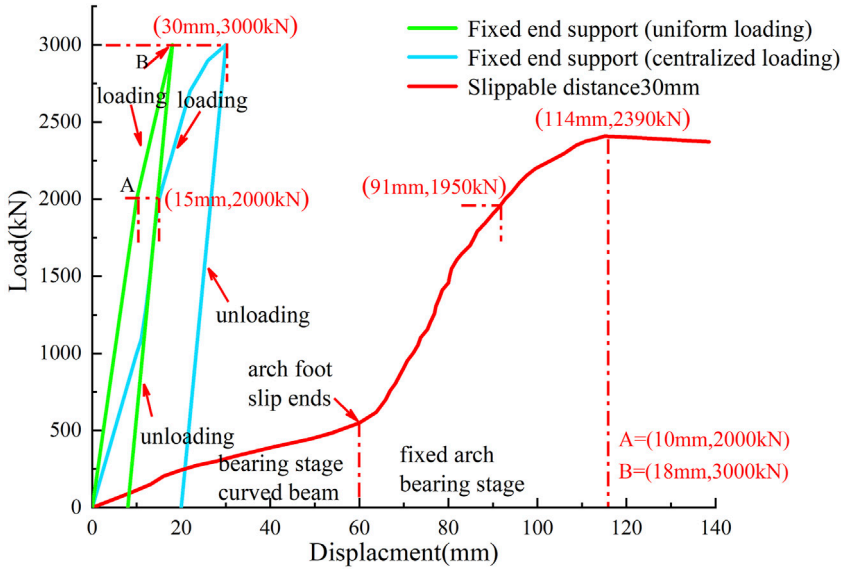

FIGURE 6
Relation curve between top load and mid-span displacement of circular arch.

statistically significant. Additionally, the slip of the arch foot is reserved on both sides of the support for 30 mm.

The supports at both ends progressively slide during the first loading stage, and the displacement in the middle of the span steadily grows. When the support's slip is complete, the strain on the arch jack is 600 kN, and the specimen's mid-span displacement is around 60 mm—almost equal to the total of the slip amounts of the two arch feet. The top of the arc arch plainly lowers and tends to be straight when the jack is loaded to 1950 kN. The specimen deforms visibly and displays waist drum deformation features on both sides of the mid-span when the jack is loaded to 2,390 kN (114 mm of mid-span displacement). In Figure 5B, the specimen's total deformation is depicted. Other arc arch research made use of the same experimental setup. As shown in Figure 6, relationship curves between the top load and the circular arch's mid-span displacement are created based on three testing conditions. When the support is fixed, the circular arch works well regardless of whether the load is uniformly distributed throughout the whole span or concentrated in the vault. When the support has arch foot slip, the carrying capacity of a circular arch increases gradually and linearly, which is compatible with the characteristics of a curved beam (Wang, 2014). After the support slips, the circular arch receives a horizontal push from the fixed end support, the curved beam effect is diminished, the circular arch's axial compression effect is intensified, and the circular arch's bearing capacity grows quickly until the component is destroyed.

3.2 Analysis of the influence law of anti-bending strengthening

As illustrated in Figure 7, the relationship curve between vault load and mid-span displacement is drawn after the test results of the

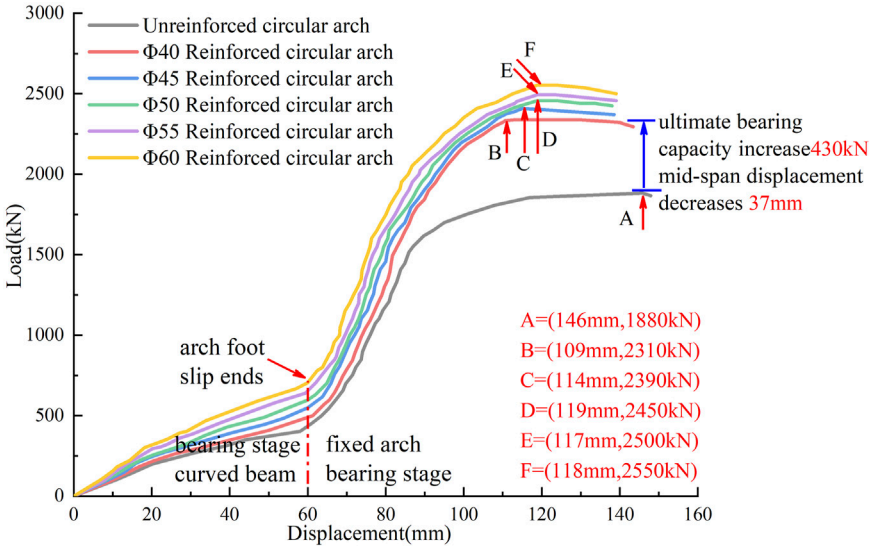

FIGURE 7
Load-displacement curves of circular arch strengthened by anti-bending.

FIGURE 8
Concrete filled steel tubular circular arch compression and bending deformation diagram.

bending-reinforced circular arch are combined. The diagram shows that by welding the anti-bending round steel to the arch belly, the circular arch's ultimate bearing capacity is significantly increased due to the increased tensile strength of the arch belly. Early on in the arch force, the difference gradually becomes noticeable, and by the time the arch foot slip has ended, it is extremely clear. Last but not least, the CFST circular arch with anti-bending round steel outperforms the circular arch without anti-bending round steel significantly in terms of bearing capacity, improving the ultimate bearing capacity by 430 kN and lowering the mid-span displacement by 37 mm. The diameter of the anti-bending round steel is closely associated with the bearing capacity of the circular arch. The ultimate bearing capacity of a circular arch increases with the diameter of the round steel under the same load, while the mid-span displacement decreases as the anti-bending strengthening increases. However, the anti-bending strengthening power rapidly declines as the diameter of the round steel grows.

3.3 Analysis of bending deformation characteristics of circular arch

It is discovered that the deformation of the six circular arch specimens is essentially the same under concentrated load: the vault flattens and the entire structure becomes a "flat bow," as seen in Figure 8. When the steel tube in the mid-span straight section of the arc arch without anti-bending reinforcement was opened, it was discovered that the concrete in the soffit section was clearly cracked, with the cracks primarily concentrated in the straight section of the arch and developing from the tension side to the compression side. After cutting the steel tube of the anti-bending reinforced circular arch, it was discovered that the concrete's cracking mechanism is comparable. However, when the diameter of the anti-bending round steel increases, the fracture range and depth steadily diminish, demonstrating that the anti-bending round steel successfully resists concrete cracking by bearing a significant amount of

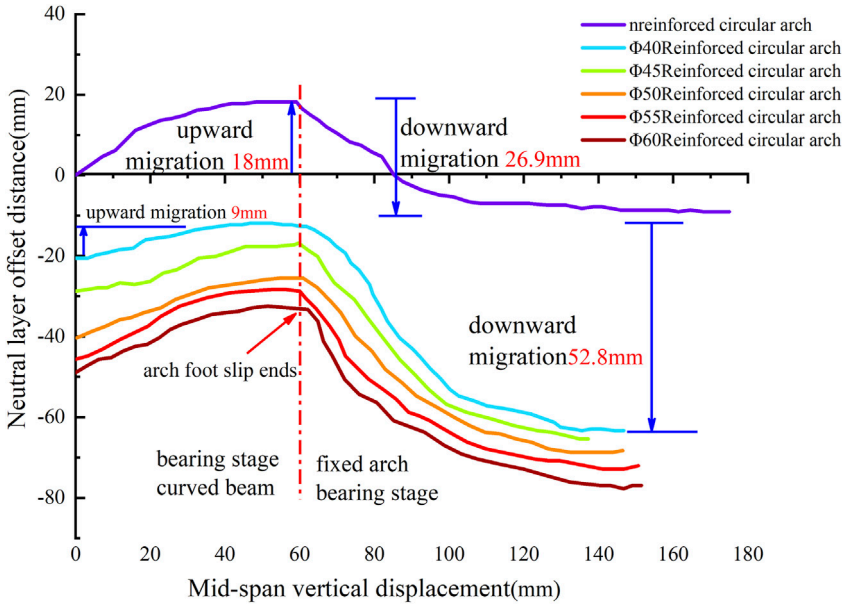

FIGURE 9
Mid-span displacement-neutral layer offset distance curves of circular arch.

tensile force and reducing the load applied to the concrete. The concrete at the waist drum of the unreinforced circular arch is crushed without developing cracks, which is compressive failure. Additionally, there is a wavy waist drum deformation from the arch shoulder to the inner arc side of the arch foot.

3.4 Analysis of neutral layer migration law of circular arch

On the circular arch's mid-span portion, strain gauges have been glued. To track the variations in strain in the mid-span portion, a total of 28–30 strain gauges are glued at equal angles. The neutral layer was the surface on which the zero line of strain value was found. The mid-span displacement and the neutral layer offset relationship curve are produced using the horizontal plane, where the center of the steel tube is positioned as the zero point. According to Figure 9, the neutral layer of the circular arch rises higher during the arch foot slip stage, suggesting that the area of the tension zone of the section expands and the compression zone contracts. The circular arch creates the appearance of a curved beam, and the arch's bending moment is large. When the arch foot no longer slipped, the neutral layer of the circular arch migrated lower, the area of the section compression zone expanded, the tension zone dropped, and the arc arch progressively manifested an axial compression effect while also strengthening its axial force effect.

The neutral layer of the unbendingly strengthened circular arch is first positioned in the middle of the steel tube section, whereas the neutral layer of the antibendingly strengthened circular arch is initially positioned lower. The starting location of the neutral layer is lower the greater the diameter of the anti-bending round steel is on the ventral side of the circular arch. The tension zone of the circular arch is always smaller than the compression zone, which significantly increases the circular arch's anti-bending resistance. All of the anti-bending, strengthened circular arch neutral layers are always located below the center of the steel tube section. The offset value of the neutral layer decreases by 52.8 mm at the ultimate bearing point of the circular arch and by 26.9 mm at the end of the arch foot slip as the diameter of the bending round steel increases from 0 to 40 mm, which is similar to the proportional antisymmetry of the increase in ultimate bearing capacity.

In order to find an appropriate method of CFST support optimization, other factors affecting the bearing capacity of circular arches should also be thoroughly studied during the test. Numerical simulation is used to supplement the analysis. The test primarily examines the influence of arch foot slip and anti-bending strengthening.

4 Numerical simulation analysis of CFST circular arch

Based on the test results, ABAQUS finite element software was used to model and analyze, and the orthogonal test analysis was carried out through numerical simulation to further study the compression-bending load-bearing characteristics of the CFST circular arch under the influence of other factors. The influence of various factors on the load-bearing performance of the circular arch was determined.

4.1 Modeling analysis

4.1.1 Modeling and boundary constraints

The effect parameters of the circular arch were preliminary optimized based on references (Wang. 2014) and typical support types in deep highway support, and a multi-factor orthogonal test table was created. As indicated in Supplementary Table S2, certain

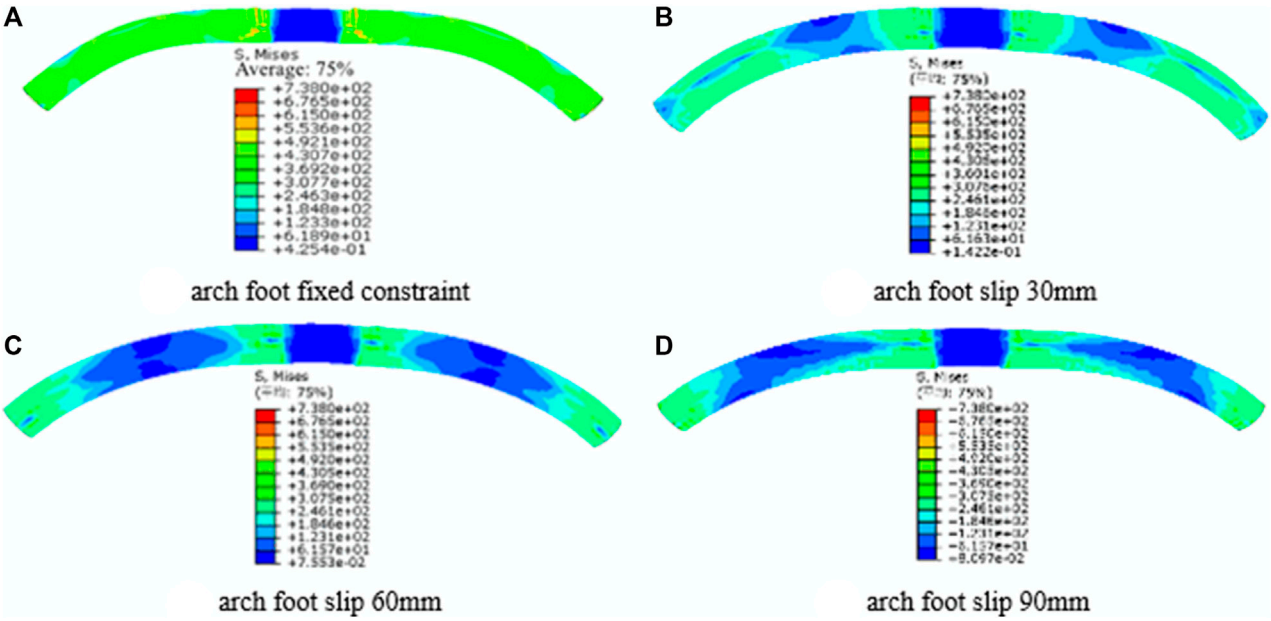

FIGURE 10
Stress nephogram of concrete-filled steel tube circular arch with different arch foot slip (concentrated load on vault).

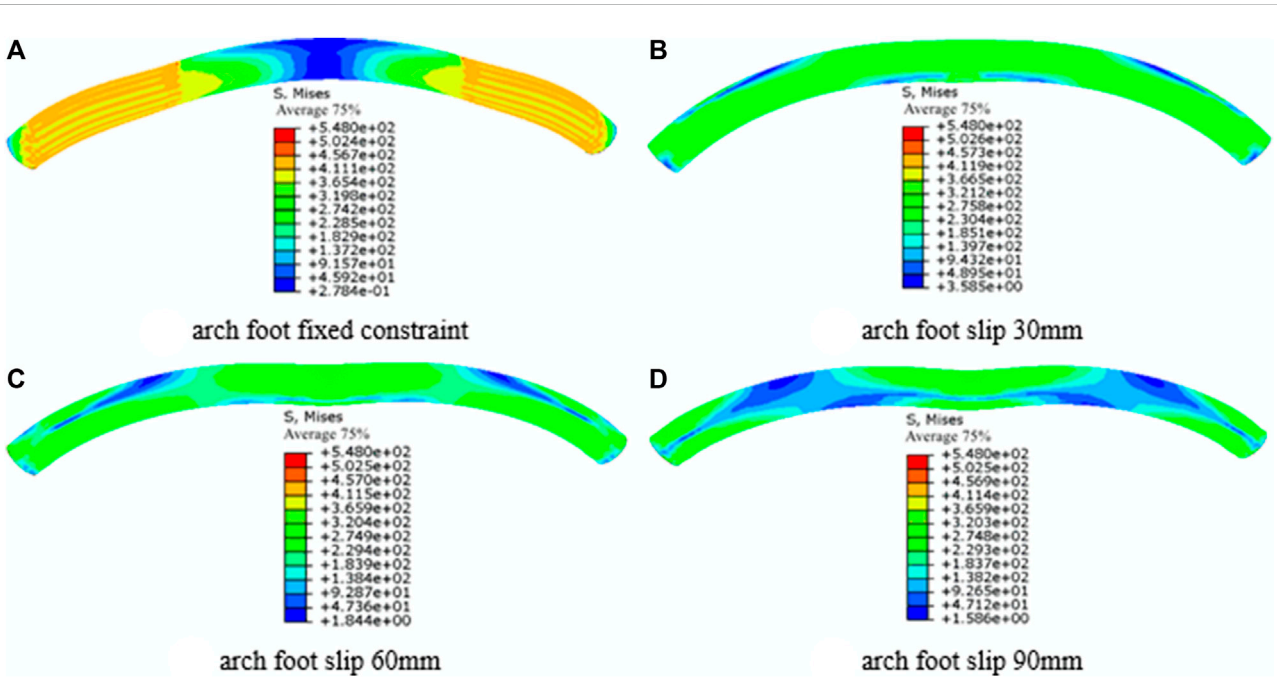

FIGURE 11
Stress nephogram of concrete filled steel tube circular arch with different arch foot slip (full span normal uniform load).

sample sites from the comprehensive test are chosen in accordance with the orthogonality to conduct the test, and the full-span normal uniform load and the vault focused load are applied accordingly. According to the actual stress area of the concrete-filled steel tube support in the surrounding rock, the actual stress state of the surrounding rock is realized through the pressure in the Load module of ABAQUS. In order to prevent out-of-plane instability, the arch foot adopts fixed limitations, and the entire construction cannot be offset. By specifying tangential friction and radial compression contact-adhesive sliding friction, the interaction between the steel tube and the core concrete contact surface is simulated.

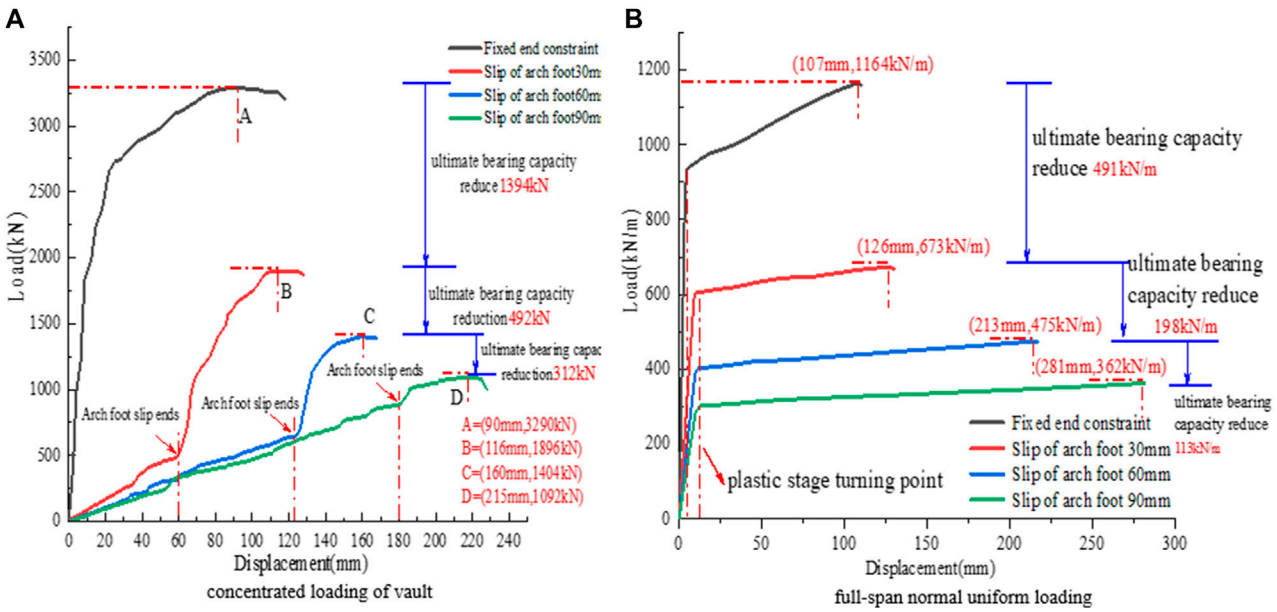

FIGURE 12
Mid-span load-displacement curves of concrete filled steel tube circular arch with different arch foot slip.

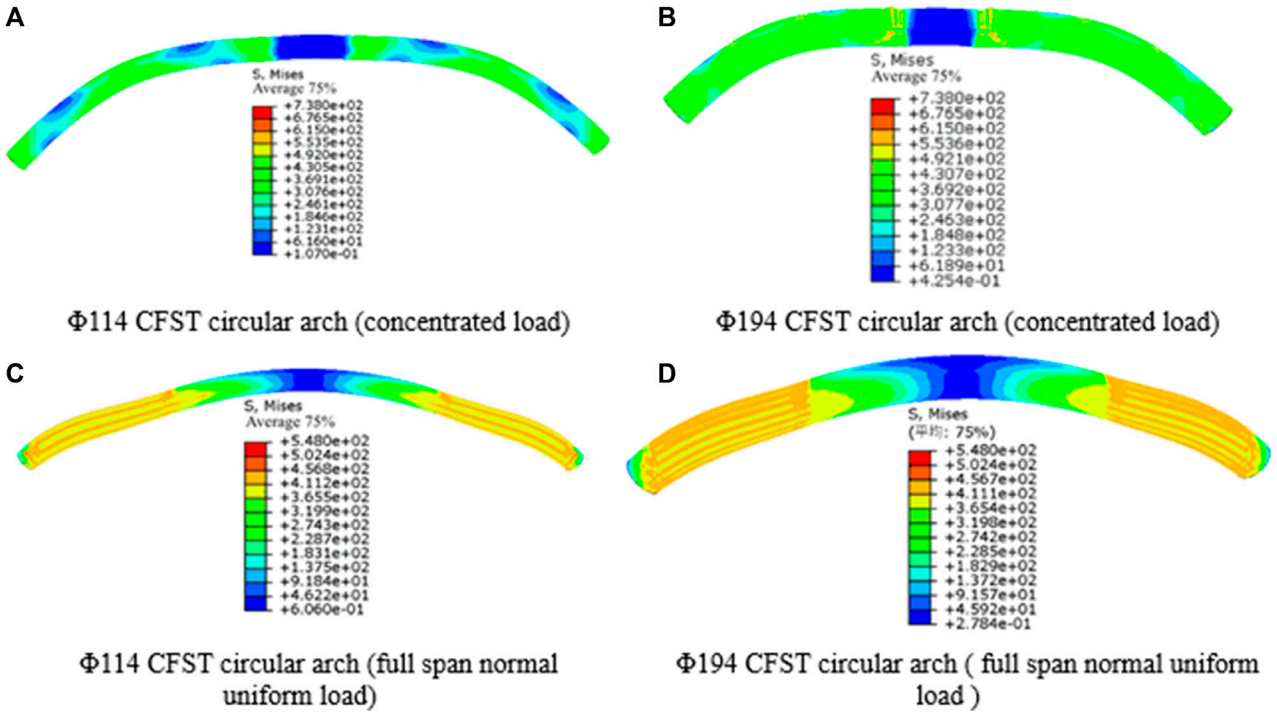

FIGURE 13
Stress nephogram of concrete filled steel tube circular arch with different outer diameters.

4.1.2 Selection of constitutive parameters

For the steel tube, the isotropic elastic-plastic model (Xie et al., 2015) is used, which complies with the relevant flow criteria and the Von Mises yield criterion. The concrete constitutive parameters are displayed in Supplementary Table S3 for the C40 core concrete, which is constructed using a Concrete Damaged Plasticity model that is subject to the non-correlated flow criteria.

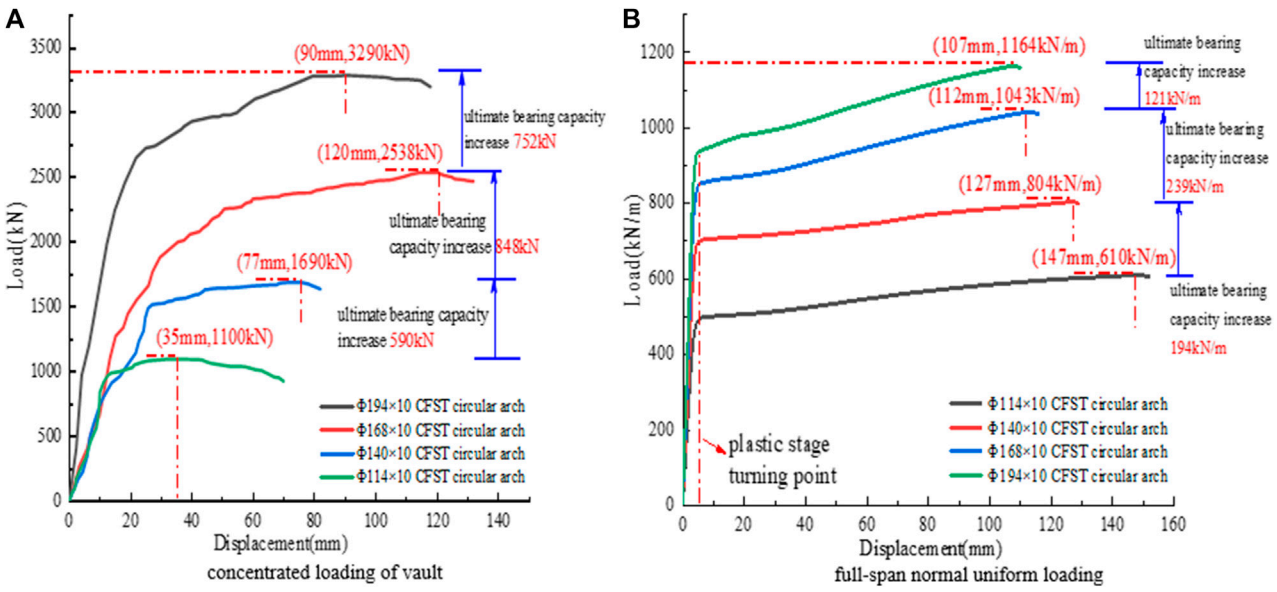

FIGURE 14
Mid-span load - displacement curves of concrete filled steel tube circular arch with different outer diameters.

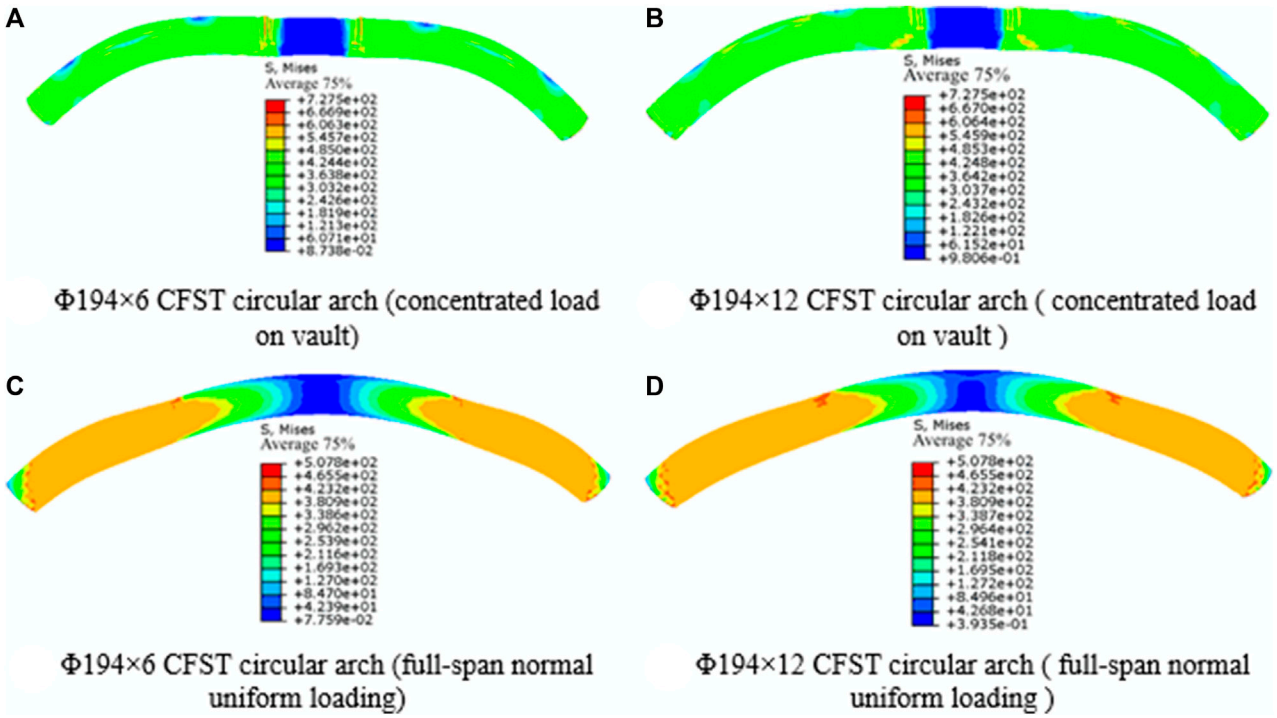

FIGURE 15
Stress nephogram of concrete filled steel tube circular arch with different wall thickness.

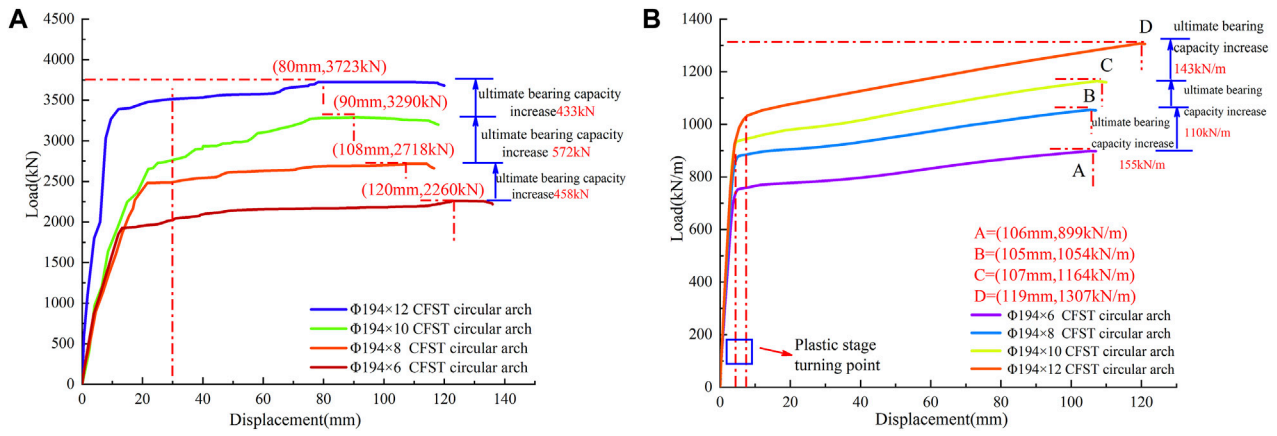

FIGURE 16
Mid-span load-displacement curves of concrete filled steel tube circular arch with different wall thicknesses.

4.2 Analysis of influence law of CFST circular arch compression-bending of CFST circular arch

4.2.1 Analysis of the influence law of arch foot slip

The Analyzed is the circular arch model made of CFST measuring 194 mm by 10 mm without anti-bending strengthening. The circular arch fails in flat bow failure mode when there is concentrated weight on the vault and no arch foot slip, and waist drum failure mode manifests on both sides of the vault. The 'waist drum' characteristic on both sides of the vault eventually disappears as the arch foot slips more, and as illustrated in Figure 10, the stress concentration and 'waist drum' phenomena occur there instead. Under the condition of full-span normal uniform loading, with the increase of slip, the failure mode of circular arch gradually evolves from vault protrusion to 'M' shape, and the arch foot also appears stress concentration and ' waist drum ' phenomenon, as shown in Figure 11.

The mid-span load and mid-span displacement correlation curves are depicted. As shown in Figure 12A, the ultimate bearing capacity of the CFST circular arch is lowered by 40.8% cliff-like under the situation of concentrated stress on the vault when the fixed constraint of the arch foot is changed to the arch foot slip of 30 mm. The final bearing capacity is decreased by 25.9% and 48.1%, respectively, as the arch foot slip rises from 30 mm to 60 mm and 90 mm. The carrying capacity of the circular arch with a slip of 90 mm is reduced by 88.9% when compared to the circular arch with fixed limitations at the arch foot.

As can be observed from Figure 12B, when the arch foot slips, there is no correlation between the vertical displacement of the mid-span and the arch foot slip under the condition of full-span normal uniform loading. The ultimate carrying capacity of the CFST circular arch is lowered by 35% in a cliff-like manner when the fixed restriction of the arch foot is adjusted to 30 mm. The ultimate bearing capacity decreases by 29.4%, 53.2%, and 88.2%, respectively, when the arch foot slip is raised from 30 mm to 60 mm and 90 mm, respectively. The bearing capacity of the circular arch with 90 mm of slip decreases by 88.2%. The circular arch's stability and safety are thus greatly endangered by the arch's foot slip.

The research mentioned above demonstrates that when the slip of the arch foot increases, the bearing capacity of the circular arch quickly diminishes. When the arch foot slip reaches 90 mm under focused loads, the circular arch even loses its noticeable arch effect after the slip has ended, degrading immediately into a curved beam, and the structural benefits of CFST all but vanish. As the arch foot slip grows under the full-span normal uniform load, the plastic deformation section progressively rotates clockwise, suggesting that the plastic strengthening capacity gradually declines as a result of the arch foot slip.

4.2.2 Analysis of influence law of outer diameter of circular arch steel tube

The stress nephograph of the circular arch is extracted after simulating the arch with various outer diameters, a wall thickness of 10 mm, and no slide at the arch foot. This is depicted in Figure 13: Stress concentration occurs on both sides of the vault and arch foot under concentrated loading on the vault, and the more apparent the waist drum phenomenon on both sides of the vault, the more likely the "flat bow" failure mode of the specimen as a whole. The specimen was convex overall under the full-span uniform normal load, and the "waist drum" characteristic appeared close to the arch foot. The more pronounced the "waist drum" feature, the larger the outside diameter.

It is concluded that there is a correlation between mid-span load and mid-span displacement. According to Figure 14A, when the outer diameter of the steel tube filled with concrete is increased from 114 mm to 140, 168, and 194 mm progressively under concentrated loading of the vault, the cross-sectional area increases by 50.8%, 44.0%, and 33.3%. The CFST circular arch now has an enhanced ultimate bearing capacity of 53.6%, 50.2%, and 29.6%, respectively. The contribution degree of the new section is measured as the ratio between the growth rates of bearing capacity and CFST cross-sectional area, and the values are 1.05, 1.14, and 0.887, respectively. This ratio illustrates a trend of initially increasing and then dropping.

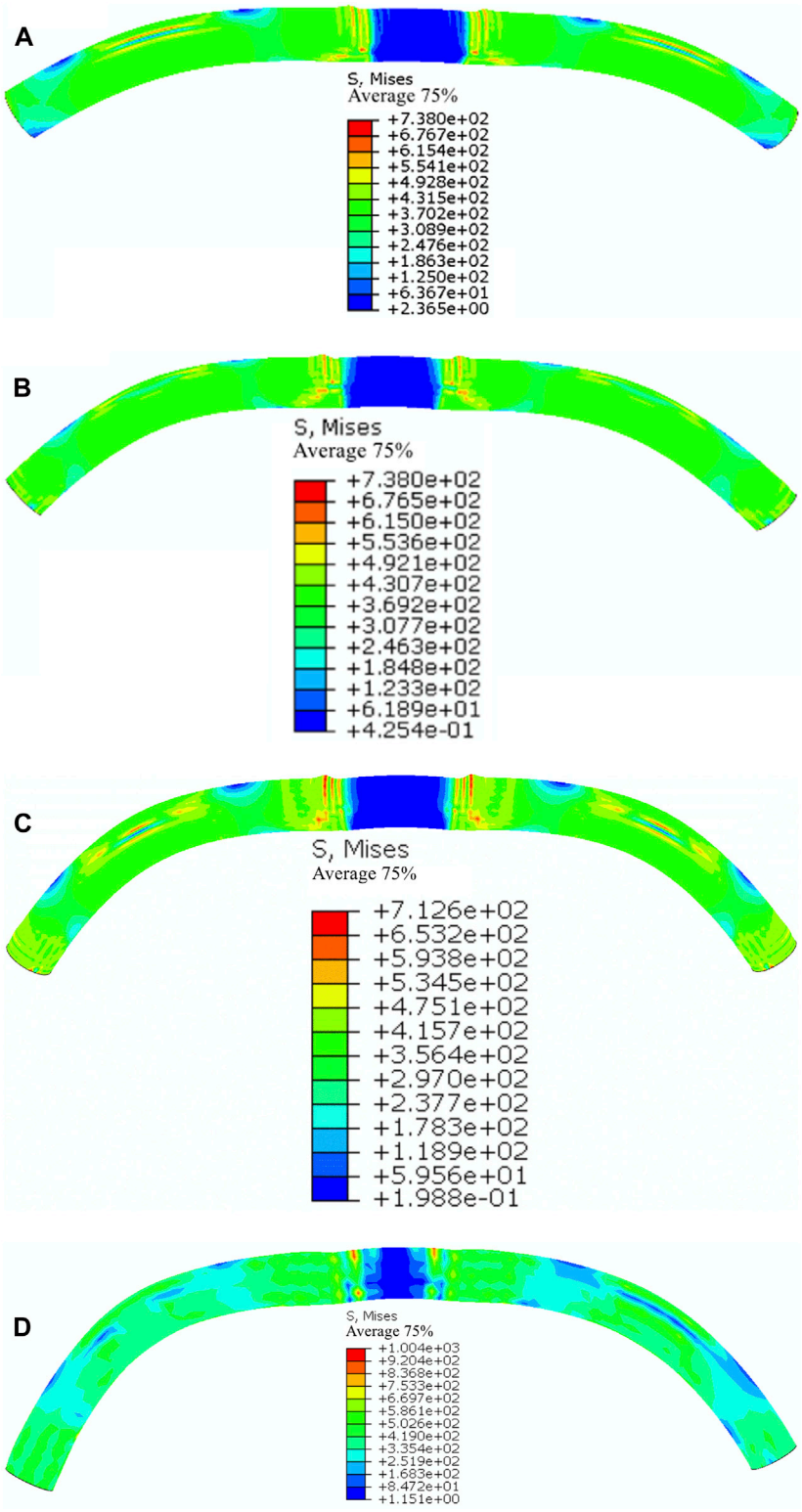

FIGURE 17
Different rise-span ratio of concrete filled steel tube circular arch stress nephogram (concentrated load on vault).

The ultimate bearing capacity of CFST circular arches increases by 31.8%, 29.7%, and 11.6%, respectively, as the outer diameter is gradually raised from 114 mm to 194 mm under full-span normal uniform loads, as shown in Figure 14B. The contributions of the new section are 0.626, 0.675, and 0.348, respectively, which also exhibit a tendency of increase followed by decline, but the increase is modest and the decline is substantial.

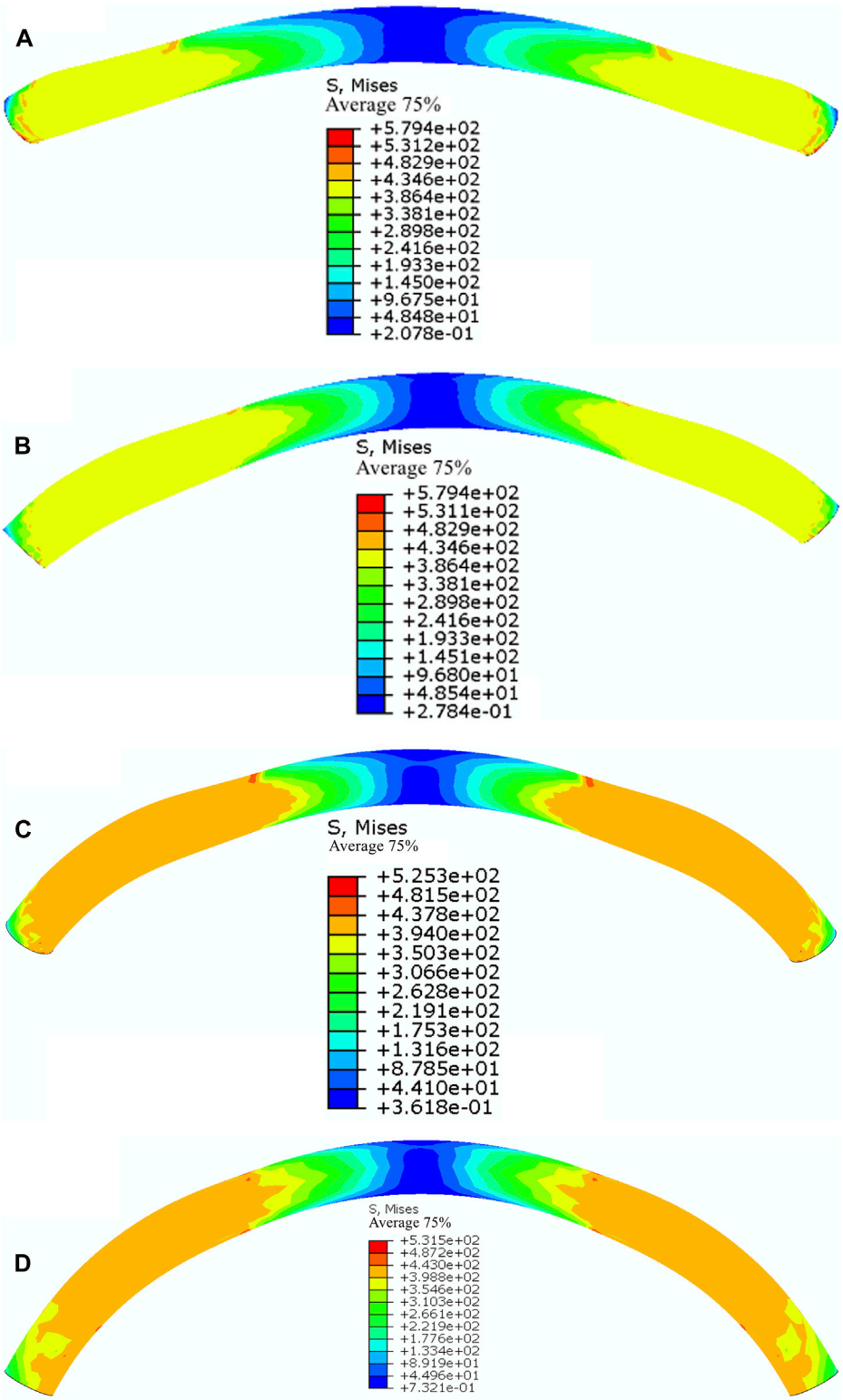

FIGURE 18
Different rise-span ratios of concrete filled steel tube circular arch stress nephogram (full span normal uniform load).

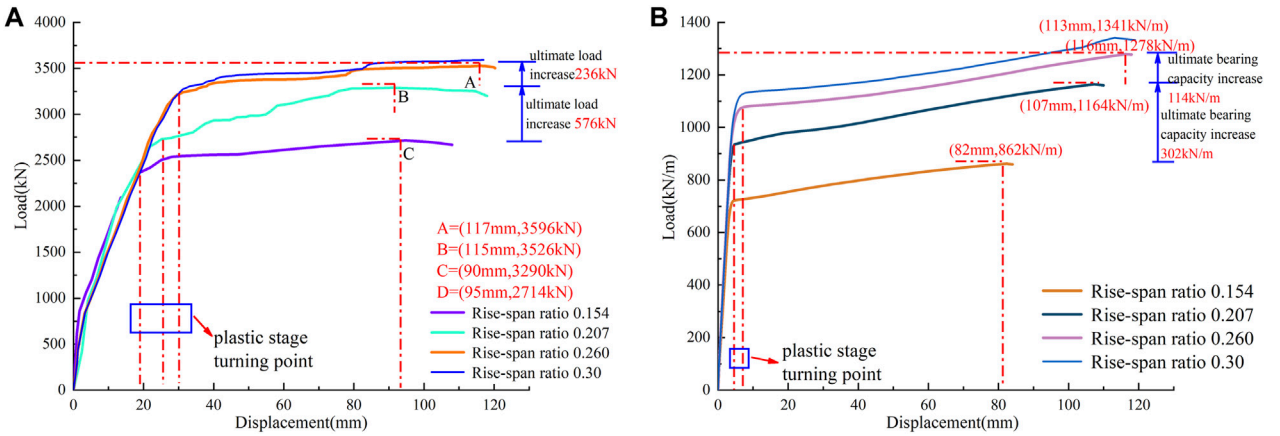

FIGURE 19
Mid-span load -displacement curves of circular concrete filled steel tube circular arch with different rise-span ratios.

4.2.3 Analysis of influence law of wall thickness of circular arch steel tube

The stress nephograph of circular arches is retrieved by performing numerical simulations on circular arches with various wall thicknesses, an outer diameter of 194 mm, and a non-slip arch foot. The circular arch's failure mode and stress concentration phenomenon are consistent with the explanation in Section 4.2.2, which is no longer repeated, as illustrated in Figure 15.

According to Figure 16A, when the wall thickness of the steel tube is gradually increased from 6 to 12 mm, the cross-sectional area of the pure steel tube increases by 31.9%, 23.6%, and 18.7%, respectively, and the ultimate bearing capacity of the CFST circular arch increases by 20.3%, 21%, and 13.2%, respectively. This is because the correlation curve is drawn using the mid-span load and the mid-span displacement. The contribution of new steel tubes is measured as the ratio of the growth rate of bearing capacity to the growth rate of steel tube area. The contribution rates, which show a tendency to grow initially and then fall, are 0.636, 0.887, and 0.706, respectively.

Figure 16B illustrates how, under the influence of full-span normal uniform loads, the ultimate bearing capacity of a CFST circular arch improves by 17.2%, 10.4%, and 12.3%, respectively, as the wall thickness of steel tube increases from 6mm to 12 mm. The relative contribution rates were 0.539, 0.440, and 0.658, with a pattern of first falling and then increasing.

In conjunction with the study in Section 4.2.2, the growth rate of the CFST circular arch's bearing capacity gradually slows down as the outer diameter and wall thickness of the steel tube rise. In addition, there should be an ideal contribution for the concentrated loading condition of the vault, meaning that the outer diameter should be between 114 and 194 mm, or roughly 168 mm, and the wall thickness should be between 6 and 12 mm, or roughly 10 mm. However, the ideal combination of wall thickness and outer diameter has not been discovered under the full-span normal uniform stress situation.

4.2.4 Analysis of influence law of rise-span ratio of circular arch

With no slip at the arch foot and no anti-bending strengthening, a simulation study of various rise-span ratios of 194 mm 10 mm CFST circular arches is conducted. As seen in Figure 17, the stress nephogram is extracted. The overall failure mechanism of the vault under concentrated loading conditions is "flat bow," and there is a clear "waist drum" occurrence on both sides of the vault. According to Figure 18, when full-span normal uniform loading is applied, the specimen's vault is slightly convex, the arch foot is positioned in a way that resembles a "waist drum" and the stress concentration occurs on the arch foot's bottom side.

By adding the mid-span load and the mid-span displacement, the correlation curve is created. As observed in Figure 19A, the rise-span ratio increasing from 0.154 to 0.30 enhances the ultimate bearing capacity of CFST circular arches by 21.2%, 7%, and 2%, respectively, under the situation of concentrated load on the vault. As observed in Figure 19B, the ultimate bearing capacity of the CFST circular arch improves by 35%, 9.9%, and 4.99%, respectively, when the rise-span ratio rises from 0.154 to 0.260 under the condition of a full-span uniform load. The contribution of the new rise-span ratio is measured as the ratio of the growth rate of ultimate bearing capacity to the growth rate of the rise-span ratio. The contributions are 0.616, 0.273, and 0.11 in the scenario of focused loading on the vault, respectively. The contributions under the full-span normal uniform load are 1.017, 0.387, and 0.201, respectively. As the rise-span ratio rises, it is evident that the contribution falls.

The orthogonal test is designed, computed, and sorted out by Design-Expert software as indicated in Supplementary Table S4 and the aforementioned simulation results are sorted out. It is evident that as tube diameter, wall thickness, and rise-span ratio increase, so does the circular arch's bearing capability. The circular arch's bearing capacity declines as arch foot slip increases, and the arch effect progressively disappears.

According to statistical analysis, the slip of the arch foot is the most important component impacting the bearing performance of the circular arch of CFST under centralized arch loading or full-span normal uniform loading. The carrying capacity of a circular arch gradually declines and weakens into a curved beam as arch foot slip increases. The bearing capacity of a circular arch improves as steel tube diameter, wall thickness, rise-span ratio, and anti-bending strengthening increase. However, the rise-span ratio has a bigger

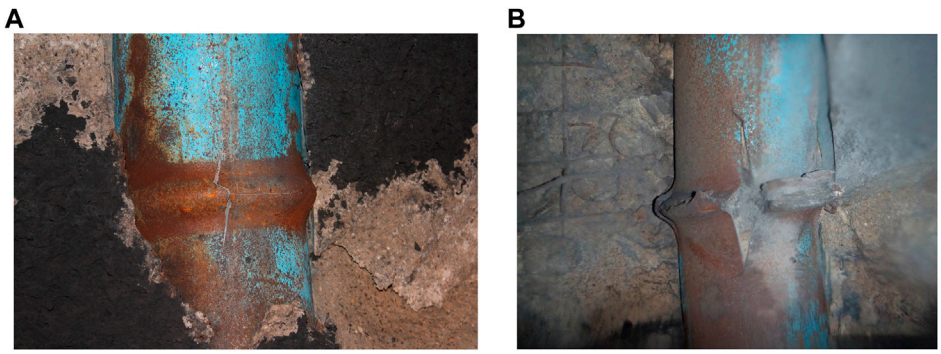

FIGURE 20
Circular concrete-filled steel tube support.

impact than anti-bending strengthening when the outer diameter and wall thickness of a steel tube are the same. Under the same rise-span ratio, the influence of the steel tube's outside diameter is marginally stronger than its wall thickness and stronger than its anti-bending strengthening. The outside diameter of the steel tube is 168 mm, the wall thickness is 10 mm, the rise-span ratio is 0.207, and the ultimate failure mechanism is local waist drum deformation failure. These specifications provide the circular arch's bearing capacity under concentrated loads.

When there is no arch foot slip, the mid-span load and mid-span displacement curves of circular arches in supine are essentially the same. The circular arch failure is essentially the deformation and failure of the arch foot or spandle brought on by axial compression exceeding the limit, meaning that the CFST structure locally experiences the ultimate compression failure. The compression-bending failure mode of the circular arch and the load shape have weak correlations when there is an arch foot slide. It is mostly impacted by the arch of the foot sliding, and noticeable buckling deformation features gradually arise. As a result, the CFST's bending moment exceeds the limit, which is consistent with the results of the orthogonal test.

When the arch foot slip reaches a particular point, the circular arch loses its arch effect forever. Therefore, it is impossible to avoid using the planned deformation space or construction gap between the support and the surrounding rock in the actual support. The displacement of the support from the filling space caused by an uncompacted filling is analogous to the circular arch experiment's arch foot slip. The void behind the support wall or the excessive pressure space, as well as the construction gap, must be avoided in order to guarantee that the arch axial compression effect of the circular CFST support is considerable.

5 Engineering application and optimization analysis

The integrated support of the roadway is created once many circular supports have been built, as shown in Supplementary Figure S1. The circular CFST support is made up of four circular arches. Studying the use of circular CFST supports in the Yangcheng Coal Mine's North Third Deep Track, operated by Jining Mining Group.

5.1 CFST support design

The Yangcheng Coal Mine of the Jining Mining Group has several rock faults, a deep mining depth, and complex geological circumstances. The average downhill buried depth of the third deep track is close to 1000 m. Medium sandstone, siltstone, and mudstone make up the roadway's excavation layer. Because of the surrounding rock's high vertical stress, poor strength, and severely inadequate self-bearing capability, the side wall of the road may flex significantly, and there may be significant floor heave. The surrounding rock is in a high ground stress state before the opening of the roadway, and the tectonic stress field is complex. These are the features of the stress field of the roadway in the ultra-deep well. After the opening of the roadway, high concentrated stress and deviatoric stress appear in the surrounding rock, which results in a significant change in the surrounding rock's deformation characteristics: the deformation of the surrounding rock shifts from brittleness to plasticity, and the rheology and dilatancy of the surrounding rock are prominent. The mine repeatedly tried to stabilize the roadway by using support techniques like "full-section hollow grouting anchor cable + bolt + floor pouring C40 concrete" and "anchor net spray + U29 steel," but these efforts were unsuccessful. With the analysis of the deep support mechanics principle combined (Kong et al., 2015; Xie et al., 2015), the deep track downhill support adopts the composite support scheme of "anchor net spray + circular CFST support," the roadway section is optimized to be circular, and the reserved space between the support and surrounding rock is filled with gangue bags. Supplementary Figure S2 displays the support layout.

The modeling and analysis were done using ABAQUS finite element software to confirm the viability of circular CFST support. The references (Shan et al., 2015; Xie et al., 2015) and the surrounding rock geology of the track downhill confirm the preliminary estimate of 1.15–1.45 MPa for the surrounding rock load acting on the support. A 3.0 MPa uniform load is applied to the support model in order to intuitively examine the support's performance. In Supplementary Figure S3, the simulation results are displayed. The support has a strong overall bearing performance. The track downhill highway at Yangcheng Coal Mine can be made safe and stable by having a maximum side displacement of about 7 mm and a maximum vault displacement of about 4 mm.

The downward slope of the Beisan deep track has maintained long-term stability since the support plan was established in 2020. Real-scene images of the on-site support obtained at the end of 2022 show that the roof, floor, and two sides are all well regulated, with just 1%–2% of the support deforming (Supplementary Figure S4A). Under this support scheme, the roof and the upper part get a good control effect, and they are basically stable after 25d. The displacement change curve is shown in Figure 13. The roof displacement is 109 mm, the roof subsidence is small, the maximum subsidence is 50 mm, and the maximum floor heave is about 70 mm. As shown in Supplementary Figure S4B.

5.2 Deformation and optimization analysis of CFST support

The two primary kinds of CFST support deformation are the support's overall buckling deformation failure and the failure of the support's waist drum.

1. The overall buckling deformation failure and optimization analysis of the support

The top arc section or side section of the CFST support typically exhibits this type of damage, and as can be seen in Supplementary Figure S5, there is a clear distinction between the upper and bottom portions of the joint casing. These are the primary causes: 1) Installation clearance room (about 10 mm) is often reserved in the joint casing (e.g., Φ223 mm × 10 mm) to guarantee the primary steel tube of the support (e.g., Φ194 mm × 10 mm) is installed without difficulty. As a result, after applying restricting pressure at the joints of each segment (i.e., the arch foot), the support will slide and the CFST at the joints will progressively split, as illustrated in Supplementary Figure S6. 2) It is difficult to place gangue bags above the shoulder joint sleeve in engineering, and the filling behind the wall is frequently not dense. Gangue bags are filled behind the support wall below the shoulder joint sleeve. The joint casing will be shifted or deflected as the support is squeezed, which is analogous to "arch foot slip" and reduces the arch effect while improving the curved beam effect. The circular arch is vulnerable to yielding under bending moments.

Therefore, the arch effect of the support should be increased and the anti-flexural bearing capacity should be improved in order to assure the stability of the concrete-filled steel tube support. You can utilize the three optimization techniques listed below: 1) To stop the end face of the main steel tube from separating, reduce the slip in the joint casing, raise the limit steel bar in the casing, and create reinforced concrete at the junction after pouring concrete; 2) Develop filling equipment, lower labor intensity, and ensure filling quality; 3) Weld the anti-bending round steel on the inside and outside of the circular arch to increase the support's bearing capacity for resistance to bending. This is done by optimizing the backfill of the support wall and filling the backfill of the full broken face with tightness.

2. Deformation failure and deformation analysis of support waist drum

The distortion of the CFST waist drum, as seen in Supplementary Figure S7, is the primary manifestation of this type of deformation and failure, which mostly manifests in the upper and lower regions of the joint casing or the side section. The general form of the support is currently steady and does not alter appreciably. The steel tube at the waist drum will crack and further break as the pressure from the surrounding rock increases, as shown in Figure 20, but it can still transmit axial pressure at this point, though the anti-bending resistance is almost completely lost. The primary cause is that the side wall portion of the support, which carries the weight of the roof and floor and has a tendency to bend when subjected to the surrounding rock, cannot be deformed by passive restraint from the rock, and there is high axial pressure in the arc arch. The axial compression effect gradually gets stronger, and the waist drum deforms under the impact of adjacent mining disturbances or the buildup of surrounding rock pressure. Steel tube breaking will result from increased waist drum deformation, which is brought on by the circular arch's axial compression's insufficient bearing capacity.

As a result, the absence of axial compression bearing capacity is the primary cause of waist drum deformation. However, at this point, the concrete-filled steel tube support has achieved its maximum bearing capacity, which makes it an optimal mode of failure. On the basis of addressing the filling behind the support wall, the support's ability to withstand axial compression should be increased. There are three types of optimization: 1) raise the steel tube's outer diameter, wall thickness, or concrete's strength and enhance the circular arch's axial compression bearing capacity, particularly the side portion of the support; 2) Under mining disturbance conditions, pressure relief behind the support wall should be performed on time to properly buffer the surrounding rock load of the circular arch of the side section; 3) Adopt high-strength active support technology or surrounding rock grouting modification technology to differentiate the surrounding rock load acting on the CFST support and achieve composite support stability.

6 Conclusion and prospect

The following results are established from the bearing test, numerical simulation, and engineering application study of the CFST circular arch:

1. In spite of centralized loading or full-span normal uniform loading, the circular arch of the CFST demonstrates greater bearing capacity when constrained by fixed arch feet. Under the situation of a full-span normal uniform load, the bearing capacity of a circular arc arch is superior to that of a concentrated load. The impact of the CFST's circular arch curved beam is improved, the neutral layer is transmitted to the compression zone, and the arch's bearing capacity gradually rises throughout the arch foot slip process. After the arch foot slips, the circular arch effect is reestablished, and the bearing capacity quickly increases. However, the circular arch immediately degrades into a curved beam without an arch effect when the slip of the arch foot exceeds 90 mm. When there is a concentrated load, the circular arch span's vertical displacement is approximately equal to the total slip of the two arch feet.

2. The numerical simulation research demonstrates that, for steel tubes with the same outer diameter and wall thickness, the impact of the rise-span ratio is larger than that of anti-bending strengthening. The impact of the steel tube's outer diameter is slightly greater than that of its wall thickness under the same rise-span ratio. The circular arch is defined by the distortion of the arch side or the vault's "waist drum" when there is no or only a slight slip at the arch foot. The circular arch exhibits general buckling deformation failure characteristics when the arch foot has a significant slip or the rise-span ratio is too short; The optimal bearing performance parameters for a circular arch with an outside diameter of 168 mm, a wall thickness of 10, and a rise-span ratio of 0.207 are found under concentrated load, and local waist drum deformation is the failure mode.
3. The composite support scheme of "anchor net spraying + CFST support" is suggested for the real project, and it essentially resolves the support issue. Analysis was done on the support's waist drum deformation and buckling deformation. It should be fair to minimize the installation clearance space of the joint casing or to reinforce the support wall since the buckling deformation of the support was brought on by insufficient anti-flexural capability. The CFST support's inadequate axial compressive capability is shown by the waist drum's deformation. The ultimate bearing condition of the material is reached at this point in the deformation. Improvements should be made to the steel tube's outer diameter, wall thickness, or concrete strength, and the side pressure relief should be completed promptly.

The investigation for this project is ongoing and does not just focus on the mechanical characteristics of the passive support system. Further optimization of the control strategy and rock factors surrounding the road is required. It is vital to thoroughly examine the influencing variables of surrounding rock deformation and identify the deeper control mechanism in order to address the issue of surrounding rock deformation and failure in soft rock, high-stress roadways, or junctions in a kilometer-deep well. The next stage is to research the CFST support (passive support + active support + grouting modification + backfill pressure relief) combined support technique for surrounding rock control in order to achieve space-time synergy.

Data availability statement

The original contributions presented in the study are included in the article/Supplementary Material, further inquiries can be directed to the corresponding author.

Author contributions

WJ: Funding acquisition, Investigation, Supervision, Writing–original draft, Writing–review and editing. ZC: Formal Analysis, Software, Writing–original draft, Writing–review and editing. BF: Investigation, Project administration, Writing–original draft. XG: Investigation, Writing–original draft. LY: Investigation, Writing–original draft. WB: Funding acquisition, Writing–original draft. DG: Investigation, Writing–original draft. TZ: Investigation, Writing–original draft.

Funding

The author(s) declare financial support was received for the research, authorship, and/or publication of this article. This work is Supported by the National Natural Science Foundation of China (Grant No. (52274121), the National Natural Science Foundation of Shandong Province (Grant No. (ZR2022ME162), the National Natural Science Foundation of Hebei Province (Grant No. (E2022508023) and Research leader Studio of "20 New Universities" funded project in Jinan City (Grant No. (202228106).

Conflict of interest

Authors BF, XG, LY, DG, and TZ were employed by Shandong Jikuang Luneng Coal Power Co Ltd.Yangcheng Coal Mine.

The remaining authors declare that the research was conducted in the absence of any commercial or financial relationships that could be construed as a potential conflict of interest.

Publisher's note

Supplementary material

The Supplementary Material for this article can be found online at: https://www.frontiersin.org/articles/10.3389/fmats.2023.1285551/full#supplementary-material

References

Bradford, M. A., Pi, Y.-L., and Qu, W. (2011). Time-dependent in-plane behaviour and buckling of concrete-filled steel tubular arches. *Eng. Struct.* 33 (5), 1781–1795. doi:10.1016/j.engstruct.2011.02.018

Gao, Z., and Yan, F. (2020). *Probability theory and mathematical statistics*. Nanjing, China: Nanjing University Pres.

Gao, Y., Wang, Bo, Wang, J., et al.(2010). Test on structural property and application of concrete - filled steel tube support of deep mine and soft rock roadway. *Chin. J. Rock Mech. Eng.* 29 (S1), 2604–2609. (in Chinese).

Han, Xu, Fernando, D., and Han, B. (2020). Numerical modelling of the in-plane behaviour of concrete-filled circular steel tubular arches. *Constr. Build. Mater.*, 264. doi:10.1016/j.conbuildmat.2020.120693

He, X., Liu, K., Zhang, L., et al.(2015). Structuraldesign and application of concrete-filled steel tube support at extremely soft rock roadway intersection. *J. China Coal Soc.* 40 (9), 2040–2048. (in Chinese). doi:10.13225/j.cnki.jccs.2014.1704

Hu, Q., Chang, Y., Yuan, C., Wang, Y., and Zhang, S. (2018). Experimental investigation into in-plane stability of concrete-filled steel tubular parabolic arches

under five-point concentrated loads. *Int. J. Steel Struct.* 20, 2038–2050. doi:10.1007/s13296-020-00429-y

Kang, H., Fan, M., Gao, F., et al. (2015). Deformation and support of rock roadway at depth more than 1000 meters. *Chin. J. Rock Mech. Eng.* 34 (11), 2227–2241. (in Chinese). doi:10.13722/j.cnki.jrme.2015.0859

Li, S., Wang, Qi, Jiang, B., He, M., Sun, H., Shao, X., et al. (2017). Modeling and Experimental study of mechanical properties of confined concrete arch in complicated deep underground engineering. *Int. J. Geomechanics* 17 (6), 1–14. doi:10.1061/(asce)gm.1943-5622.0000827

Li, X., Yang, R., Gao, Y., et al.(2013). High-strength steel tubular confined concrete supports support technology for large section soft rock inclinedshaft. *J. China Coal Soc.* 38 (10), 1742–1748. (in Chinese). doi:10.13225/j.cnki.jccs.2013.10.018

Liu, D., Zuo, J., Guo, S., et al.(2018). Research on load-bearing ability of steel tube confined concrete sup-ports for deep roadway: state of the art. *J. China Univ. Min. Technol.* 47 (6), 1193–1211. doi:10.13247/j.cnki.jcumt.000942

Lu, W., and Sun, H. (2020). Study on support characteristic curve of concrete-filled steel tubular arch in underground support. *Structures* 27, 1809–1819. doi:10.1016/j.istruc.2020.07.066

Luo, K., Pi, Y.-L., Gao, W., Bradford, M. A., and Hui, D. (2015). Investigation into long-term behaviour and stability of concrete-filled steel tubular arches. *J. Constr. Steel Res.* 104, 127–136. doi:10.1016/j.jcsr.2014.10.014

Pi, Y.-L., Bradford, M. A., and Qu, W. (2011). Long-term non-linear behaviour and buckling of shallow concrete-filled steel tubular arches. *Int. J. Non-Linear Mech.* 46 (9), 1155–1166. doi:10.1016/j.ijnonlinmec.2011.05.003

Shan, R., Xiao, Y., Liu, K., et al. (2018). Failure mechanism of the arch of concrete filled steel tube supports component. *J. China Coal Soc.* 43 (07), 1918–1929. (in Chinese). doi:10.13225/j.cnki.jccs.2018.0004

Wang, J. (2014). *Research on mechanical properties of anti-bending for Concrete filled Steel circular arch and its application*. Ph.D. Thesis. Beijing, China: China University of Mining and Technology Beijing. (in Chinese).

Wang, Qi, Xu, S., Jiang, B., et al.(2020). Research progress of confined concrete support theory and technology for underground engineering. *J. China Coal Soc.* 45 (8), 2760–2776. doi:10.1016/j.enpol.2013.02.011

Wang, Y., Liu, C., Yonglin, P. I., et al. (2011a). In-plane nonlinearity stability strength of circular concrete-filled steel tubular arches. *J. Huazhong Univ. Sci. Technol. Sci. Ed.* 39 (05), 34–38. (in Chinese). doi:10.13245/j.hust.2011.05.027

Wang, Y., Wu, X., Geng, Y., et al. (2011b). Analysis on creep stability of concrete-filled steel tubular arches under uniform load. *Prog. Steel Build. Struct.* 13 (06), 31–35+43. (in Chinese)). doi:10.13225/j.cnki.jccs.2019.0920

Xie, H., Gao, F., Yang, J. U., et al. (2015). Quantitative definition and investigation of deep mining. *J. China Coal Soc.* 40 (1), 1–10. (in Chinese). doi:10.13225/j.cnki.jccs.2014.1690

Yan, W., Han, B., Zhang, J., et al. (2018). Experimental study on creep behavior of fly ash concrete filled steel tube circular arches. *Steel Compos. Struct.* 27, 185–192. doi:10.12989/scs.2018.27.2.185

Zhang, W., Li, W., Yang, N., Wang, Q., Li, T., and Wang, G. (2017). Determination of the bearing capacity of a Concrete-filled Steel Tubular arch support for tunnel engineering: experimental and theoretical studies. *KSCE J. Civ. Eng.* 21, 2932–2945. doi:10.1007/s12205-017-1418-8

frontiers | Frontiers in Materials

TYPE Original Research
PUBLISHED 07 February 2024
DOI 10.3389/fmats.2024.1340883

OPEN ACCESS

EDITED BY
Jian-Guo Dai,
Hong Kong Polytechnic University, Hong Kong SAR, China

REVIEWED BY
Roberto Fedele,
Polytechnic University of Milan, Italy
Xiaohua Li,
Chongqing University, China

*CORRESPONDENCE
Xinglang Fan,
fanxinglang@cribc.com

RECEIVED 19 November 2023
ACCEPTED 02 January 2024
PUBLISHED 07 February 2024

CITATION
Zhou X, Bai L, Rong H, Fan X, Zheng J and Geng Y (2024), An improved approach for the continuous retardation spectra of concrete creep and applications.
Front. Mater. 11:1340883.
doi: 10.3389/fmats.2024.1340883

An improved approach for the continuous retardation spectra of concrete creep and applications

Xinzhu Zhou[1], Linhong Bai[1], Hua Rong[2], Xinglang Fan[2]*, Jianjun Zheng[1] and Yan Geng[2]

[1]College of Civil Engineering, Zhejiang University of Technology, Hangzhou, China, [2]Central Research Institute of Building and Construction, Metallurgical Group Corporation of China, Beijing, China

Creep is an important physical property of concrete and can lead to additional displacement, stress redistribution, and even cracking in concrete structures, inducing prestress loss of large-scale prestressed concrete structures. When an exponential algorithm is used to calculate the long-term creep of concrete, it is usually necessary to apply the continuous retardation spectra of the material. In the improved approach proposed here, the continuous retardation spectra can be obtained by the Weeks inverse Laplace transform. The CEB MC90 creep model is taken as an example to analyze the computational process, efficiency, and error of the approach. The improved approach is further applied to the ACI 209R-92, JSCE, and GL2000 concrete creep models. Through comparison with other methods, the advantages of the improved approach are illustrated, and some useful conclusions are drawn.

KEYWORDS

improved approach, concrete creep, continuous retardation spectra, Weeks inverse Laplace transform, Dirichlet series

1 Introduction

Concrete creep is defined as the time-dependent deformation of a concrete specimen under sustained load. Its magnitude is closely related to the stress applied, time, cement type, mix proportion of concrete, and environmental conditions (ACI Committee 209, 2005). In practice, concrete creep can lead to additional displacements, stress redistribution, and even cracking in concrete structures during their service life (Hubert Rüsch and Hilsdorf, 1983; Bažant et al., 1997). As a result, a prestress loss is often observed in many large-scale prestressed concrete structures, such as long-span bridges and nuclear containments, which could significantly affect their safety and durability.

Under low stress, concrete can be considered an aging viscoelastic material, with concrete creep following the Boltzmann superposition principle. Thus, its strain rate can be expressed as (Bažant and Jirásek, 2018)

$$\dot{\varepsilon}(t) = \frac{\dot{\sigma}(t)}{E(t)} + \int_0^t \dot{J}(t,t_0)\mathrm{d}\sigma(t_0), \tag{1}$$

where t is the age of concrete, t_0 is the time when the load is applied, $\dot{J}(t,t_0)$ is the first derivative of the compliance function $J(t,t_0)$ with respect to t, $E(t)$ is the instantaneous elastic modulus, and $\dot{\varepsilon}(t)$ and $\dot{\sigma}(t)$ are the strain and stress rates, respectively. Equation (1) can be

solved by the finite difference method. However, this method has some limitations. First, the entire stress history is required to obtain the strain increment at the current time step. As a result, in the process of solving creep by the finite element method, the entire stress history needs to be stored for the integration points of each element. For a large-scale problem with many time steps, the evaluation of these history variables is quite time-consuming. Second, the effects of some variable factors, such as temperature, humidity, and concrete cracks, cannot be considered.

It should be noted that the calculation method of $J(t,t_0)$ comes from different creep models, reflecting the ratio of strain value to stress of the material at time t (loaded at t_0), which is usually related to conditions such as material mix ratio, specimen shape, and environmental factors.

To overcome the difficulties of the finite difference method, Eq. (1) can be transformed into a differential rate-type equation, and an efficient exponential algorithm can be employed to calculate the concrete creep which exhibits a quadratic convergence rate and is unconditionally stable. Zienkiewicz et al. (1968) first applied this method to nonaging viscoelastic materials, and Bažant extended it to aging viscoelastic materials. This method can effectively improve computational efficiency with fixed internal variables. When using the efficient exponential algorithm, it is crucial to select a proper rheological model, such as the Kelvin chain model, to describe the viscoelastic behavior of the material. From a mathematical point of view, the creep compliance function of such a viscoelastic material can be approximated by the Dirichlet series. This can be achieved by curve fitting—the so-called retardation spectrum method.

The curve fitting method is usually based on the least squares method to obtain the coefficients of the Dirichlet series from test data. However, this method lacks actual physical meanings and does not follow the second law of thermodynamics, which sometimes leads to negative coefficients when the test data is not statistically ideal (Schapery, 1962). Many efforts have been made to solve the issue (Baumgaertel and Winter 1989; Elster and Honerkamp, 1991; Kaschta and Schwarzl, 1994; Mead, 1994; Emri and Tschoegl, 1995; Ramkumar et al., 1997; Park and Kim, 2001). Furthermore, for aging viscoelastic materials such as concrete, the coefficients of the Dirichlet series are time-dependent, and the curve fitting method becomes inefficient as the computational process needs additional optimization techniques.

With the continuous retardation spectrum method, the coefficients of the Dirichlet series can be determined by discretizing the continuous retardation spectrum, avoiding the issues encountered in the curve fitting method. Bažant and Xi (1995) studied the continuous retardation spectrum for concrete solidification theory and used the Post–Widder method to approximate the spectrum. In practice, however, a high-order Post–Widder formula is often needed to meet the precision requirement, which significantly increases the analytical complexity. Fortunately, Jirásek and Havlásek (2014) solved this issue using a low-order Post–Widder formula with time adjustment factors of retardation times. A high convergence speed and good accuracy are demonstrated for various concrete creep models. However, the method is heuristically based on empirical analyses, and the determination of time adjustment factors is highly dependent on personal experience and numerical experiments for different creep models.

The purpose of this paper is to develop an improved approach for efficiently approximating the continuous retardation spectra of various concrete creep models. The continuous retardation spectrum is first introduced, then the process of calculating the continuous retardation spectrum by the Post–Widder method and its corresponding shortcomings are analyzed, and an improved approach for solving the continuous retardation spectra based on the Weeks inverse Laplace transform method is proposed. By taking the CEB MC90 creep model as an example, the numerical solution of the continuous retardation spectra solved by the improved approach is analyzed. The proposed approach is then applied to the ACI 209R-92, JSCE, and GL2000 concrete creep models. Finally, the numerical results are compared with the other methods and some conclusions are drawn.

2 General solution for the continuous retardation spectrum

To describe viscoelastic materials, their constitutive properties can be represented by the Kelvin chain model. In the Kelvin chain model, the deformation of a material can be characterized by a number of Kelvin units and an additional spring unit assembled in series (Figure 1). Each Kelvin unit is composed of a spring and a dashpot assembled in parallel. All these units bear the same stress, and the total strain ε is equal to the sum of the deformations of each Kelvin unit and the spring unit.

$$\boldsymbol{\varepsilon} = \boldsymbol{\varepsilon_0} + \boldsymbol{\varepsilon_1} + \boldsymbol{\varepsilon_2} + \ldots + \boldsymbol{\varepsilon_M}. \tag{2}$$

For the nonaging Kelvin unit μ shown in Figure 2, the total stress is equal to the sum of the elastic stress and the viscous stress.

$$\boldsymbol{\sigma}(t) = \boldsymbol{E_\mu}\boldsymbol{\varepsilon_\mu}(t) + \boldsymbol{\eta_\mu}\dot{\boldsymbol{\varepsilon}}_\mu(t), \tag{3}$$

where both the spring elastic modulus E_μ and the dashpot viscosity η_μ do not change with age.

For aging viscoelastic materials such as concrete, the aging Kelvin chain model is needed. For the aging Kelvin unit μ, the stress–strain relationship can be expressed in rate form as

$$\dot{\boldsymbol{\sigma}}(t) = \boldsymbol{D_\mu}(t)\dot{\boldsymbol{\varepsilon}}_\mu(t) + \boldsymbol{\eta_\mu}\ddot{\boldsymbol{\varepsilon}}_\mu(t), \tag{4}$$

where the modified age-dependent modulus $D_\mu(t)$ is equal to

$$\boldsymbol{D_\mu}(t) = \boldsymbol{E_\mu}(t) + \dot{\boldsymbol{\eta}}_\mu(t). \tag{5}$$

Since $\dot{\sigma}(t)$ is equal to zero for creep tests, the boundary condition of $\varepsilon_\mu(t_0) = 0$ is satisfied and the strain of the aging Kelvin unit μ can be obtained as

$$\boldsymbol{\varepsilon_\mu}(t) = \frac{\boldsymbol{\sigma}}{\boldsymbol{D_\mu}(\boldsymbol{t_0})}\left\{\mathbf{1} - \mathbf{exp}\left[-(\boldsymbol{t}-\boldsymbol{t_0})/\boldsymbol{\tau_\mu}\right]\right\}, \tag{6}$$

where $\tau_\mu = \eta_\mu(t)/D_\mu(t)$ is the retardation time of the Kelvin unit μ and t_0 is the time when the load is applied.

When the aging Kelvin chain model is subjected to a unit stress, the strains of all the Kelvin units ($\mu = 0, 1, 2, \ldots, M$) and the spring unit are superimposed; the compliance function is given by (Bažant, 1988)

$$\boldsymbol{J}(\boldsymbol{t},\boldsymbol{t_0}) = \frac{\mathbf{1}}{\boldsymbol{E_0}(\boldsymbol{t_0})} + \sum_{\mu=1}^{M}\frac{\mathbf{1}}{\boldsymbol{D_\mu}(\boldsymbol{t_0})}\left\{\mathbf{1} - \mathbf{exp}\left[-(\boldsymbol{t}-\boldsymbol{t_0})/\boldsymbol{\tau_\mu}\right]\right\}, \tag{7}$$

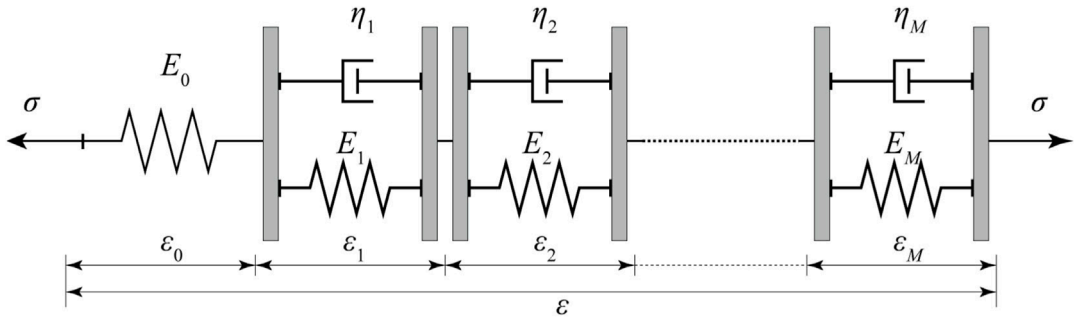

FIGURE 1
Nonaging Kelvin chain model.

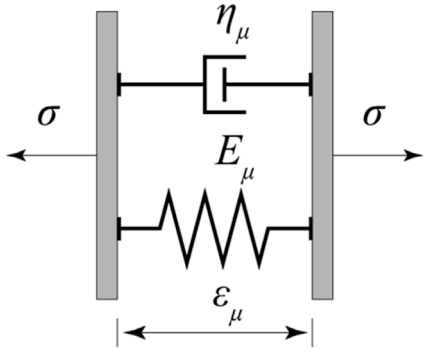

FIGURE 2
Nonaging Kelvin unit.

which can be considered a finite Dirichlet series. In the practical application process, once the compliance function is constructed in the form of Eq. (7), the long-term creep value of materials can be numerically calculated by exponential algorithm. For a given time t_0, when there are infinite number of Kelvin units in the chain and the retardation time distributes continuously, Eq. (7) can be converted into an integral form (Bažant and Xi, 1995):

$$J(t,t_0) = \frac{1}{E_0(t_0)} + \int_0^\infty \frac{1}{\tau} L(\tau)\{1 - \exp[-(t-t_0)/\tau]\}\mathrm{d}\tau, \quad (8)$$

where $L(\tau)$ is the continuous retardation spectrum. For a specific creep model, once the continuous retardation spectrum is given, the direct discrete method can be used to construct the compliance function in the form of finite Dirichlet series. For convenience sake, the compliance function $J(t,t_0)$ is rewritten as

$$J(t,t_0) = \frac{1}{E_0(t_0)} + \varphi(\xi), \quad (9)$$

where $\xi = t - t_0$ is the loading duration, and $\varphi(\xi)$ is defined as

$$\varphi(\xi) = \int_0^\infty \frac{1}{\tau} L(\tau)[1 - \exp(-\xi/\tau)]\mathrm{d}\tau. \quad (10)$$

By using the inverse Laplace transform method, Tschoegl (Nicholas, 1989) approximated $L(\tau)$ from the Post–Widder method as

$$L_k(\tau) = -\frac{(-k\tau)^k}{(k-1)!}\varphi^{(k)}(k\tau), \quad k = 1,2,\ldots, \quad (11)$$

where $\varphi^{(k)}(k\tau)$ is the kth order derivative of $\varphi(k\tau)$. When $k \to \infty$, $L_k(\tau)$ converges to the exact solution:

$$L(\tau) = \lim_{k\to\infty} L_k(\tau). \quad (12)$$

In this method, a sufficiently smooth function $\varphi(\xi)$ and a higher order k are required for an acceptable approximation of the continuous retardation spectrum. This method is straightforward and efficient for some problems with simple compliance functions. In practice, however, the computation of the high-order derivatives is usually quite complicated, and the process of solving them will become complicated. To improve this method, Jirásek and Havlásek (2014) analyzed the difference between the low-order Post–Widder method and the exact solution and proposed an approach for adjusting the retardation time by multiplying correction factor α_τ to improve the accuracy of calculating continuous retardation spectrum. Thus, the continuous retardation spectrum is defined as

$$L(\alpha_\tau \tau) = L_k(\tau). \quad (13)$$

When the correction factor α_τ is applied, the accuracy of the numerical solution of the compliance function is effectively improved, and the approximation order is well controlled within low ranges. In this method, however, the value of the correction factor is determined empirically and is different for different creep models.

In Section 3, in view of the shortcomings of the Post–Widder method, an improved method for solving continuous retardation spectra based on the Weeks inverse Laplace transform is proposed. Here, Eq. (10) is processed in advance.

The differentiation of Eq. (10) with respect to ξ yields

$$\varphi'(\xi) = \int_0^\infty \frac{1}{\tau^2} L(\tau)\exp(-\xi/\tau)\mathrm{d}\tau. \quad (14)$$

By setting $\delta = 1/\tau$, we have

$$\varphi'(\xi) = \int_0^\infty L(1/\delta)\exp(-\xi\delta)\mathrm{d}\delta. \quad (15)$$

It can be seen from Eq. (15) that $\varphi'(\xi)$ is the Laplace transform of $L(1/\delta)$. Therefore, once the inverse Laplace transform of $\varphi'(\xi)$ is determined, $L(1/\delta)$ can be obtained.

3 Weeks method for the continuous retardation spectrum

In the method by Weeks (1966), the Laguerre polynomials are used to numerically calculate the inverse Laplace transform. The main advantage is that an explicit solution can be obtained. In applying this method, the following two conditions should be fulfilled: the Laplace space function is a smooth function with bounded exponential growth, and it can be expressed as a Laguerre series. The above two conditions are fulfilled for commonly used creep models, including the CEB MC90, ACI 209R-92, JSCE, and GL2000 models.

For Laplace space function $F(x)$, the analytical expression of the time-domain function $f(t)$ can be obtained by the Weeks method as

$$f(t) = \exp(\sigma t)\sum_{n=0}^{\infty} a_n \exp(-bt)\mathrm{Lg}_n(2bt). \tag{16}$$

In Eq. (16), σ and b are two parameters that fulfill the conditions of $b > 0$ and $\sigma > \sigma_0$, where σ_0 is the Laplace convergence abscissa. a_n contains the information of the Laplace space function. It could be a scalar, vector, or matrix but does not change with time. With the Maclaurin series, the analytical expression of a_n is given by

$$\frac{2b}{1-\omega} F\left(\sigma + \frac{2b}{1-\omega} - b\right) = \sum_{n=0}^{\infty} a_n \omega^n, \quad |\omega| < R, \tag{17}$$

where R is the radius of convergence of the Maclaurin series.

$\mathrm{Lg}_n(x)$ in Eq. (16) is the Laguerre polynomial of degree n defined as

$$\mathrm{Lg}_n(x) = \frac{\exp(x)}{n!}\frac{d^n}{dx^n}[\exp(-x)x^n]. \tag{18}$$

For practical numerical calculation, Eq. (16) can approximately be expressed as

$$f_N(t) = \exp(\sigma t)\sum_{n=0}^{N-1} a_n \exp(-bt)\mathrm{Lg}_n(2bt), \tag{19}$$

where N is an integer. The exact solution of $f(t)$ can be obtained as N approaches infinity

$$f(t) = \lim_{N\to\infty} f_N(t). \tag{20}$$

By using the Bromwich integral and the fast Fourier transform, an approximate expression of a_n in Eq. (17) can be obtained as

$$a_n \approx \frac{\exp\left(-\frac{in\pi}{2N}\right)}{2N}\sum_{m=-N}^{N-1}\frac{2b\exp(-in\theta_m)}{1-\exp\left(i\theta_{m+1/2}\right)} F\left(\sigma - b\frac{\exp\left(i\theta_{m+1/2}\right)+1}{\exp\left(i\theta_{m+1/2}\right)-1}\right), \tag{21}$$

where $\theta_m = m\pi/N$.

In the Laplace transform formula of Eq. (15), the Laplace space function is $\varphi'(\xi)$, the complex variable is ξ, the time-domain function is $L(1/\delta)$, and the time-domain variable is δ. From Eq. (19), $L(1/\delta)$ can be obtained through the inverse Laplace transform as

$$L_N(1/\delta) = \exp(\sigma\delta)\sum_{n=0}^{N-1} a_n \exp(-b\delta)\mathrm{Lg}_n(2b\delta). \tag{22}$$

Substitution of $\tau = 1/\delta$ into Eq. (22) leads to

$$L_N(\tau) = \exp(\sigma/\tau)\sum_{n=0}^{N-1} a_n \exp(-b/\tau)\mathrm{Lg}_n(2b/\tau), \tag{23}$$

$$a_n \approx \frac{\exp\left(-\frac{in\pi}{2N}\right)}{2N}\sum_{m=-N}^{N-1}\frac{2b\exp(-in\theta_m)}{1-\exp\left(i\theta_{m+1/2}\right)}\varphi'\left(\sigma - b\frac{\exp\left(i\theta_{m+1/2}\right)+1}{\exp\left(i\theta_{m+1/2}\right)-1}\right). \tag{24}$$

In applying the Weeks method, it is obvious that the truncation error can be reduced by using a larger value of N. In addition, a proper choice of σ and b can lead to a higher convergence speed. Therefore, it is very important to choose the values of σ and b reasonably. For Eq. (19), according to the method provided by Weeks (1966), when solving $f_N(t)$ in the range of $0 < t < t_{max}$, the value can be simply determined as

$$\begin{cases} \sigma = \left(\sigma_0 + \frac{1}{t_{max}}\right)u\left(\sigma_0 + \frac{1}{t_{max}}\right), \\ b = \frac{N}{2t_{max}}, \end{cases} \tag{25}$$

$$u(x) = \begin{cases} 0 \text{ if } x < 0, \\ 1 \text{ if } x \geq 0. \end{cases} \tag{26}$$

For Eq. (23), let $t_{max} = 1/\tau$, and, considering that for all creep models $\sigma_0 = 0$, then σ and b can be taken as

$$\begin{cases} \sigma = \tau, \\ b = \frac{N\tau}{2}. \end{cases} \tag{27}$$

Equation (27) is simple and suitable for all creep models and can directly improve the computational accuracy by increasing N, which is recommended to take a value between 10 and 50. In order to fully improve the computational efficiency, N is taken as 10 in this paper, and, to further determine the values of σ and b for different models, the analysis process is shown as follows.

To determine the parameters σ and b, Weideman (1999) proposed a method by minimizing the theoretical error E

$$E = \exp(\sigma t)\left(\sum_{n=N}^{2N-1}|a_n| + \epsilon\sum_{n=0}^{N-1}|a_n|\right), \tag{28}$$

where ϵ is the machine round-off error.

Further analysis according to the method of Weideman (Weeks, 1966), taking the CEB MC90 creep model (CEB-FIP, 1993) as an example, the compliance function is

$$J(t,t_0) = \frac{\rho(t_0) + \phi_0\beta_c(t-t_0)}{E_{cm28}}, \tag{29}$$

where E_{cm28} is the average elastic modulus of concrete at 28 days, $\rho(t_0)$ is the correction factor related to the loading time t_0, ϕ_0 is the nominal creep coefficient related to the material strength, loading time, and the relative humidity of the environment, and the creep development coefficient $\beta_c(t-t_0)$ is equal to

$$\beta_c(t-t_0) = \left[\frac{(t-t_0)}{\beta_h + (t-t_0)}\right]^{0.3}, \tag{30}$$

with β_h being a coefficient related to the volume/surface ratio, the relative humidity, and the material strength, generally ranging from 250 to 1,500. By setting $\varphi(\xi) = \beta_c(t-t_0)$, the first-order derivative of $\varphi(\xi)$ is given by

$$\varphi'(\xi) = \frac{0.3\beta_h}{\xi^{0.7}(\beta_h + \xi)^{1.3}}. \tag{31}$$

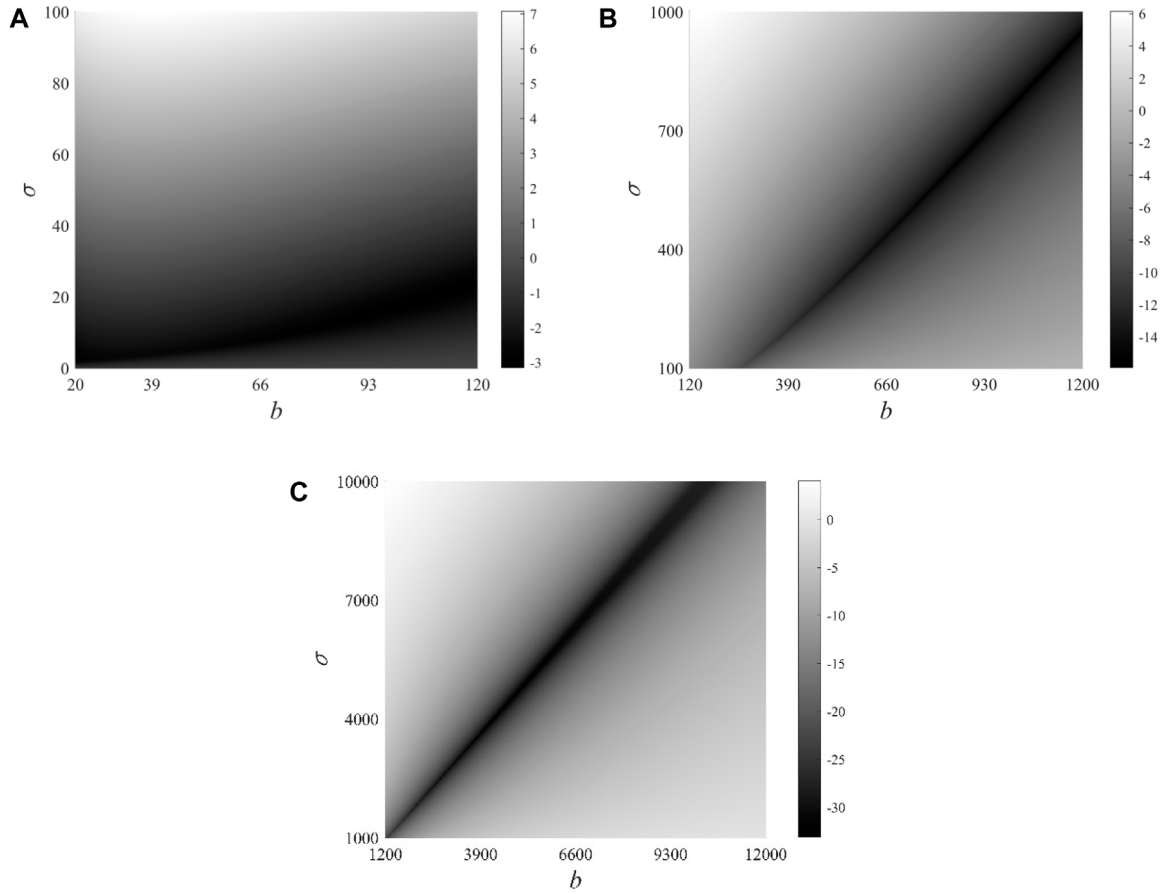

FIGURE 3
Distributions of log (*E*) (CEB MC90 model) for **(A)** τ = 10; **(B)** τ = 100; **(C)** τ = 1000.

When β_h, N, and τ are given, the error E as a function of σ and b can be obtained by substituting Eqs (24) and (31) into Eq. (28). N should be selected by considering computational accuracy and efficiency. When a larger N is used, the choice of σ and b is more flexible.

By setting $\beta_h = 500$ and $N = 10$, log (E) is obtained as a function of σ and b for different retardation times τ (Figure 3). The figure shows that the error E can be significantly reduced by a proper choice of the two parameters. In some zones where σ and b follow a certain relationship, the error E is kept within relatively low levels as the dark part shown in Figure 3.

Combine the three graphs in Figure 3 and represent the horizontal and vertical coordinates in exponential growth. Select several points with the smallest error E within different parameter ranges and use a few crosses to represent them, forming Figure 4.

If the relationship between σ and b can be determined under the condition of minimum error E, the method of parameter selection can be further determined. It was found that the relationship is related to the poles and branch points of the Laplace function (Weideman, 1999). If $s_1 = \alpha_1 + \beta_1 i$ and $s_2 = \alpha_2 + \beta_2 i$ are two farthest points to the origin of the Laplace function on the complex plane, we have

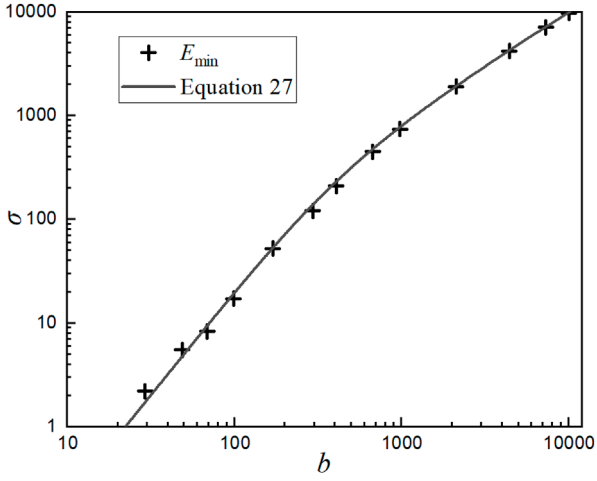

FIGURE 4
Relationship between σ and *b* (CEB MC90 model).

$$b^2 - \sigma^2 + \frac{|s_2|^2 - |s_1|^2}{\alpha_2 - \alpha_1}\sigma + \frac{\alpha_2|s_1|^2 - \alpha_1|s_2|^2}{\alpha_2 - \alpha_1} = 0. \quad (32)$$

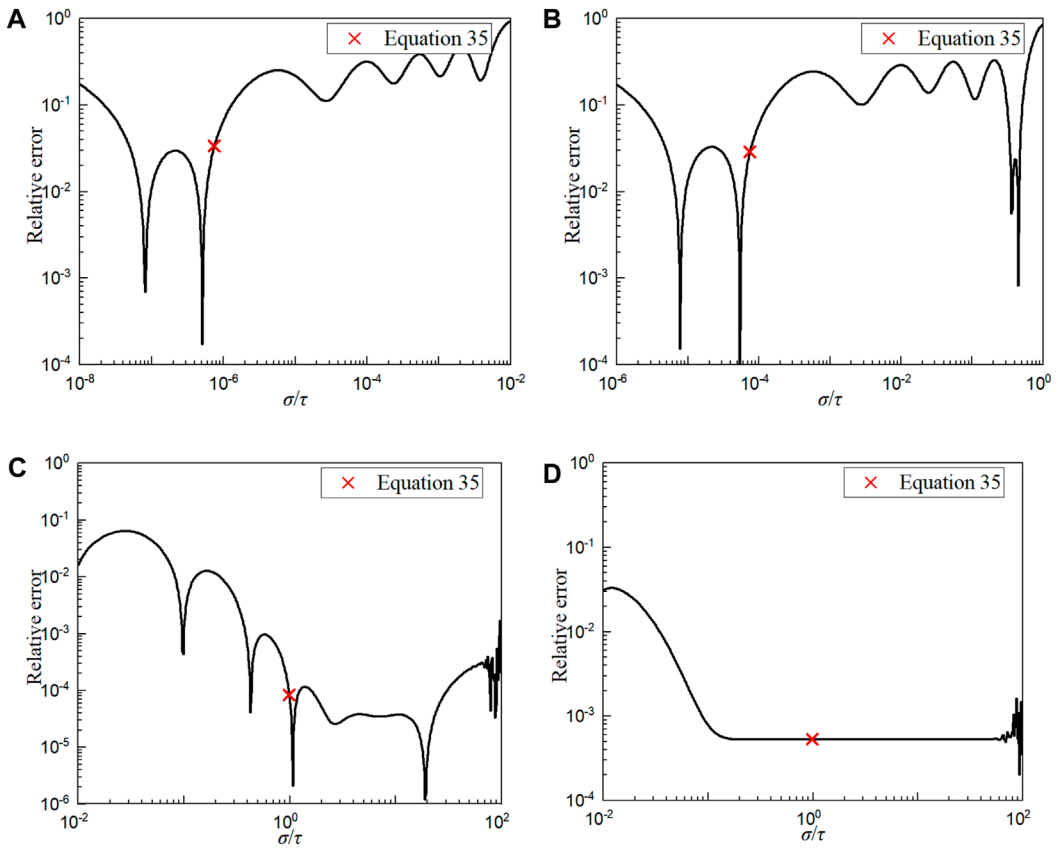

FIGURE 5
Relative errors of the Weeks method (CEB MC90 model) for **(A)** τ = 0.01; **(B)** τ = 1; **(C)** τ = 100; **(D)** τ = 1000.

Equation (31) has two branch points: $\xi = -\beta_h$ and $\xi = 0$. By using Eq. (32), the relationship between σ and b for the CEB MC90 model can be obtained as

$$\boldsymbol{b} = \sqrt{\boldsymbol{\beta_h}\boldsymbol{\sigma} + \boldsymbol{\sigma^2}}. \tag{33}$$

By taking $\beta_h = 500$, Eq. (33) is plotted as the solid line shown in Figure 4. It is apparent from Figure 4 that the numerical results from error minimization are very close to Eq. (33) for the CEB MC90 model. Therefore, for the CEB MC90 creep model, Eq. (33) can be determined as the relationship between σ and b.

As seen from Eq. (23), the relationship between σ (or b) and τ is also required to perform the inverse Laplace transform and will be determined empirically through error analysis. Thus, a reference solution $L_d(\tau)$ is obtained by a combination of the Durbin inverse Laplace transformation (Durbin, 1974) and an adaptive numerical integration. It should be pointed out that, although the reference solution $L_d(\tau)$ has higher accuracy, it is very time-consuming and needs to be calculated by long-term iterative calculation and is thus not suitable for practical applications. The relative error Er is defined as

$$\boldsymbol{Er} = \frac{|\boldsymbol{L_d}(\boldsymbol{\tau}) - \boldsymbol{L_N}(\boldsymbol{\tau})|}{\boldsymbol{L_d}(\boldsymbol{\tau})}. \tag{34}$$

When $\beta_h = 500$, $N = 10$, under the premise of using Eq. (33) for parameter values, the relative errors of the Weeks inverse Laplace transform for $\tau = 0.01, 1, 100, 1000$ are shown in Figure 5.

Figure 5 shows that, when τ is smaller than 1, the relative error exhibits larger changes from 10^{-4} to 1 (Figures 5A,B). When τ is larger than 100, the relative error is smaller than 10^{-1} and has a downward tendency as σ/τ increases (Figures 5C,D).

Based on the numerical results in Figure 5, an empirical value of σ for the CEB MC90 model is suggested as follows:

$$\begin{cases} \boldsymbol{\sigma} = \left(\dfrac{\mathbf{0.038}}{\boldsymbol{\beta_h}}\right)\boldsymbol{\tau^2}, \text{ for } \boldsymbol{\tau} < \mathbf{0.02}\boldsymbol{\beta_h}, \\ \boldsymbol{\sigma} = \mathbf{0.038}\boldsymbol{\tau^2}, \text{ for } \mathbf{0.02}\boldsymbol{\beta_h} \le \boldsymbol{\tau} < \mathbf{100}, \\ \boldsymbol{\sigma} = \boldsymbol{\tau}, \text{ for } \boldsymbol{\tau} \ge \mathbf{100}. \end{cases} \tag{35}$$

For different values of τ, the relative error calculated from Eq. (35) is also obtained as the red cross shown in Figure 5. It is seen from Figure 5 that, when using Eq. (35), the relative error is smaller than 10^{-1}. Particularly when τ is equal to 100 or 1,000, the relative error is smaller than 10^{-3}. Therefore, computational accuracy is guaranteed.

For $N = 10$ and different values of β_h, the continuous retardation spectra obtained from different methods are compared in Table 1, where $L_a(\tau)$ is calculated from Eqs (33) and (35) while $L_b(\tau)$ is calculated from Eq. (27), Er_a and Er_b are the relative errors between the calculated results obtained by the two calculation methods and the reference solution $L_d(\tau)$, respectively. It is seen from Table 1 that, compared with the Weeks parameter value method—Eq. (27)—the relative errors of the continuous retardation spectra given by

TABLE 1 Comparison of $L(\tau)$ calculated from two different methods (CEB MC90 model).

β_h	τ [day]	$L_d(\tau)$	$L_a(\tau)$	Er_a	$L_b(\tau)$	Er_b
500	1.0E-02	0.00903	0.00871	3.58E-02	0.00863	4.41E-02
	1.0E-01	0.01784	0.01739	2.54E-02	0.01725	3.33E-02
	1.0E+00	0.03586	0.03475	3.09E-02	0.03488	2.74E-02
	1.0E+01	0.07205	0.07388	2.54E-02	0.07437	3.23E-02
	1.0E+02	0.15782	0.15783	8.34E-05	0.15689	5.89E-03
	1.0E+03	0.10949	0.10944	5.30E-04	0.10753	1.79E-02
800	1.00E-02	0.007822	0.007572	3.20E-02	0.007498	4.14E-02
	1.00E-01	0.01571	0.015102	3.87E-02	0.014972	4.70E-02
	1.00E+00	0.031088	0.030159	2.99E-02	0.030117	3.12E-02
	1.00E+01	0.062401	0.061064	2.14E-02	0.06423	2.93E-02
	1.00E+02	0.13156	0.131,432	9.72E-04	0.130,819	5.63E-03
	1.00E+03	0.146,365	0.146,318	3.19E-04	0.144,544	1.24E-02
1,200	1.00E-02	0.006926	0.006698	3.29E-02	0.006639	4.14E-02
	1.00E-01	0.013834	0.013372	3.34E-02	0.013253	4.20E-02
	1.00E+00	0.027578	0.026719	3.11E-02	0.026585	3.60E-02
	1.00E+01	0.055185	0.053813	2.49E-02	0.055983	1.45E-02
	1.00E+02	0.113,781	0.113,619	1.43E-03	0.113,169	5.38E-03

Eqs (33) and (35) are smaller in most cases, and the computational accuracy is obviously improved. For the Weeks method, however, the computational accuracy can also be improved by increasing the value of N.

4 Application of the Weeks method to different creep models

In this section, the Weeks method is applied to the CEB MC90, ACI 209R-92, JSCE, and GL2000 creep models. $\varphi(\xi)$ is calculated and analyzed based on the aging Kelvin chain and different methods for the continuous retardation spectrum. $N = 10$ is used in all cases. The results obtained by a combination of the Durbin inverse Laplace transformation (Durbin, 1974) and an adaptive numerical integration are used as a reference solution.

4.1 CEB MC90 model

As discussed in the previous section, the continuous retardation spectrum of the CEB MC90 model can be obtained by the Weeks method. When $\beta_h = 500$, the continuous retardation spectra calculated by the Weeks method, the Post–Widder method with different orders, and the reference solution are shown in Figure 6.

Once $L(\tau)$ is known, $\varphi(\xi)$ can be obtained from Eq. (10). However, the integral involved should be approximated by the Dirichlet series for an aging material. Therefore, the discrete retardation times τ_μ are selected based on accuracy and efficiency. If τ_m is assumed to be a geometric series with an initial value of $\tau_0 = 10^{-4}$ and a base of 10, that is,

$$\boldsymbol{\tau_m = 10^{-4}, 10^{-3}, \ldots, 10^{6} \quad m = 0, 1, 2, \ldots, 10,} \tag{36}$$

then Eq. (10) is changed to

$$\begin{aligned}\boldsymbol{\varphi(\xi)} = &\int_{\tau=0}^{\tau=\sqrt{10}\tau_0} \frac{\mathbf{1}}{\boldsymbol{\tau}} \boldsymbol{L(\tau)}[\mathbf{1} - \mathbf{exp}(-\boldsymbol{\xi}/\boldsymbol{\tau})]\mathbf{d}\boldsymbol{\tau} \\ &+\sum_{m=1}^{10} \int_{\tau=\sqrt{10}\tau_{m-1}}^{\tau=\sqrt{10}\tau_m} \frac{\mathbf{1}}{\boldsymbol{\tau}} \boldsymbol{L(\tau)}[\mathbf{1} - \mathbf{exp}(-\boldsymbol{\xi}/\boldsymbol{\tau})]\mathbf{d}\boldsymbol{\tau} \\ &+\int_{\tau=\sqrt{10}\tau_{10}}^{\tau=+\infty} \frac{\mathbf{1}}{\boldsymbol{\tau}} \boldsymbol{L(\tau)}[\mathbf{1} - \mathbf{exp}(-\boldsymbol{\xi}/\boldsymbol{\tau})]\mathbf{d}\boldsymbol{\tau}.\end{aligned} \tag{37}$$

When $\tau < \sqrt{10}\tau_0$, $[1 - \exp(-\xi/\tau)]$ is close to unity, and the first term in Eq. (37) can be assumed to be $1/E_0$, which is not affected by the duration ξ. When $\tau > \sqrt{10}\tau_{10}$, $L(\tau)$ is close to zero, and the third term in Eq. (37) tends to be zero. Thus, Eq. (37) reduces to

$$\boldsymbol{\varphi(\xi)} = \frac{\mathbf{1}}{\boldsymbol{E_0}} + \sum_{m=1}^{10} \int_{\tau=\sqrt{10}\tau_{m-1}}^{\tau=\sqrt{10}\tau_m} \frac{\mathbf{1}}{\boldsymbol{\tau}} \boldsymbol{L(\tau)}[\mathbf{1} - \mathbf{exp}(-\boldsymbol{\xi}/\boldsymbol{\tau})]\mathbf{d}\boldsymbol{\tau}. \tag{38}$$

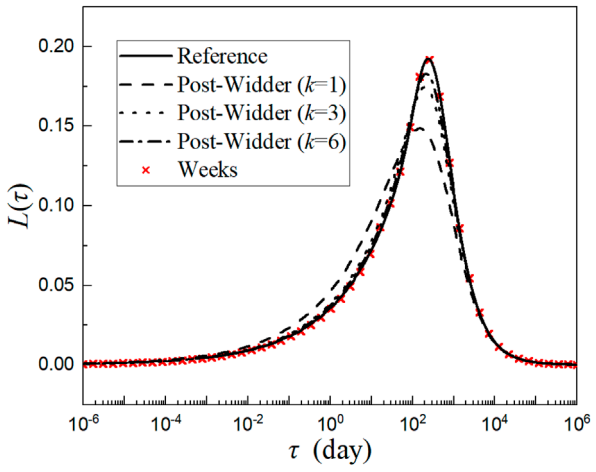

FIGURE 6
Continuous retardation spectra calculated by different methods (CEB MC90 model).

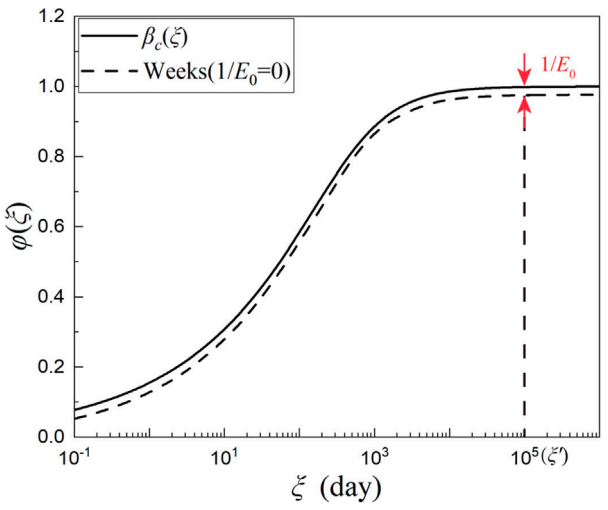

FIGURE 7
Analysis process of $1/E_0$.

The integral in Eq. (38) can be approximated by the two-point Gaussian quadrature rule:

$$\varphi(\xi) \approx \frac{1}{E_0} + \frac{\ln 10}{2}\sum_{m=1}^{10}\left\{\begin{array}{l} L\left(10^{-\sqrt{3}/6}\tau_m\right)\left[1-\exp\left(-\dfrac{\xi}{10^{-\sqrt{3}/6}\tau_m}\right)\right] \\ +L\left(10^{\sqrt{3}/6}\tau_m\right)\left[1-\exp\left(-\dfrac{\xi}{10^{\sqrt{3}/6}\tau_m}\right)\right] \end{array}\right\}. \tag{39}$$

The following definitions are used:

$$\left\{\begin{array}{l} \tau_\mu = 10^{-\sqrt{3}/6}\tau_{(\mu+1)/2}, \text{for } \mu \text{ is odd}, \\ \tau_\mu = 10^{\sqrt{3}/6}\tau_{\mu/2}, \text{for } \mu \text{ is even}. \end{array}\right. \tag{40}$$

Equation (39) then becomes

$$\varphi(\xi) \approx \frac{1}{E_0} + \sum_{\mu=1}^{20}\frac{\ln 10}{2}L(\tau_\mu)\left[1-\exp\left(-\xi/\tau_\mu\right)\right]. \tag{41}$$

If $1/D(\tau_\mu)$ is set to be $\ln 10 L(\tau_\mu)/2$, $\varphi(\xi)$ of the aging Kelvin chain model is changed to

$$\varphi(\xi) = \frac{1}{E_0} + \sum_{\mu=1}^{20}\frac{1}{D(\tau_\mu)}\left[1-\exp\left(-\xi/\tau_\mu\right)\right]. \tag{42}$$

Equation (42) is consistent with the form of Eq. (7), where the number of Kelvin units is set to $M = 20$. $1/E_0$ can be obtained by numerical integration algorithms (Jirásek and Havlásek, 2014), but this will cause some errors. In this paper, in order to reduce the effect of numerical integration at low retardation times, $1/E_0$ is solved by subtracting the difference between the numerical solution and the exact solution of $\varphi(\xi)$, which is $\beta_c(t-t_0)$ in Eq. (30) for the CEB MC90 model:

$$\frac{1}{E_0} = \beta_c(\xi') - \sum_{\mu=1}^{20}\frac{1}{D(\tau_\mu)}\left[1-\exp\left(-\xi'/\tau_\mu\right)\right], \tag{43}$$

where ξ' is the loading duration when $\beta_c(\xi')$ reaches the maximum value ($\xi' = 10^5$ for the CEB MC90 model). The analysis process is shown in Figure 7.

By taking β_h as 500, 800, and 1,200, the values of $\varphi(\xi)$ are obtained by the Weeks and Post–Widder methods with different orders (Figure 8).

The error is defined as $[\varphi(\xi) - \beta_c(\xi)]$ for the CEB MC90 model. Thus, the errors of different methods are shown in Figure 9. At the same time, the errors obtained from the method of Jirásek and Havlásek (2014) are also compared in Figure 9.

Equation (42) shows that $\varphi(\xi)$ is related to τ_μ. For the two-point Gaussian quadrature rule, $L(\tau_\mu)$ corresponding to different τ_μ is able to describe the retardation spectrum curve as accurately as possible. If $L(\tau_\mu)$ at two adjacent points τ_μ are connected by line segments, the approximation of $L(\tau_\mu)$ to the retardation spectrum curve can be observed more intuitively. As shown in Figure 10, the retardation spectrum curve can be described well when τ_μ takes values from Eq. (40).

In Eq. (42), the number of Kelvin units is taken as 20. If higher computational accuracy is required, the number of Kelvin units can be increased: $M = 20k, (k = 1, 2, 3, \ldots)$. Thus, Eq. (42) becomes

$$\varphi(\xi) = \frac{1}{E_0} + \sum_{\mu=1}^{M}\frac{1}{D(\tau_\mu)}\left[1-\exp\left(-\xi/\tau_\mu\right)\right], \tag{44}$$

where

$$\tau_{m,k} = 10^{-4}, 10^{-4+1/k}, 10^{-4+2/k}, \ldots, 10^{6} \quad m = 0, 1, 2, \ldots, 10k, \tag{45}$$

$$\left\{\begin{array}{l} \tau_\mu = 10^{-\sqrt{3}/(6k)}\tau_{(\mu+1)/2,k}, \text{ for } \mu \text{ is odd}, \\ \tau_\mu = 10^{\sqrt{3}/(6k)}\tau_{\mu/2,k}, \text{ for } \mu \text{ is even}, \end{array}\right. \tag{46}$$

$$\frac{1}{E_0} = \beta_c(\xi') - \sum_{\mu=1}^{M}\frac{1}{D(\tau_\mu)}\left[1-\exp\left(-\xi'/\tau_\mu\right)\right], \tag{47}$$

$$\frac{1}{D(\tau)} = \frac{\ln\left(10^{\frac{1}{k}}\right)L(\tau)}{2}. \tag{48}$$

It should be noted that, for most concrete creep models (CEB MC90, ACI 209R-92, and GL2000), the retardation spectra are relatively smooth, and taking $k = 1$ in Eq. (45) usually satisfies the precision requirement. However, if the retardation spectrum changes sharply in terms of retardation time, it is necessary to increase the value of k, which will be discussed in Section 4.3.

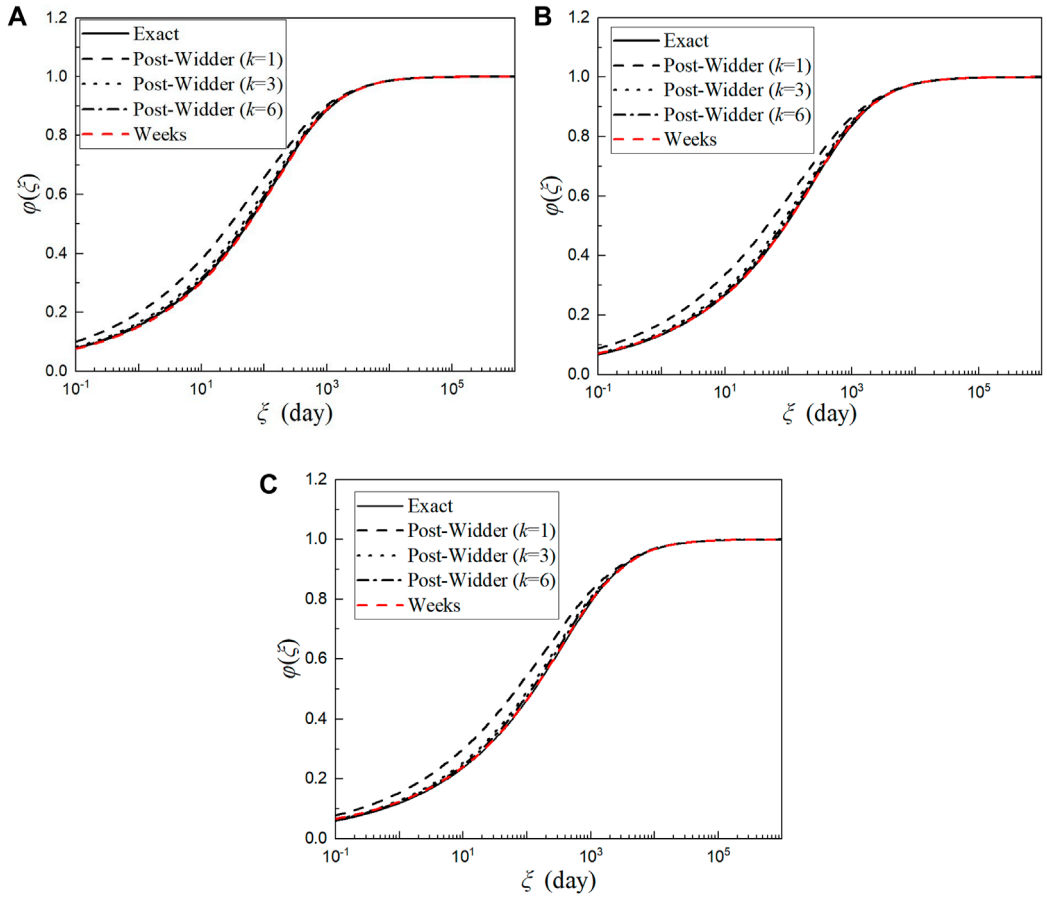

FIGURE 8
φ(ξ) calculated by different methods (CEB MC90 model) for **(A)** $\beta_h = 500$; **(B)** $\beta_h = 800$; **(C)** $\beta_h = 1{,}200$.

4.2 ACI 209R-92 model

The creep compliance function of the ACI 209R-92 model (ACI committee 209, 2008) is

$$J(t,t_0) = \frac{1+\phi(t,t_0)}{E(t_0)}, \tag{49}$$

where $\phi(t,t_0)$ is defined as

$$\phi(t,t_0) = \frac{(t-t_0)^{\psi}}{d+(t-t_0)^{\psi}}\phi_{\mu}. \tag{50}$$

In Eq. (50), ϕ_{μ} is the ultimate creep coefficient related to the curing conditions, slump, and ambient humidity of concrete structures and ψ and d are two parameters—usually taken as 0.6 and 10 according to the recommendations in ACI 209R-92, respectively.

To simplify the analysis process, $\varphi(\xi)$ is defined as

$$\varphi(\xi) = \frac{\xi^{\psi}}{d+\xi^{\psi}}. \tag{51}$$

Derivation of Eq. (51) with respect to ξ gives

$$\varphi'(\xi) = \frac{d\psi\xi^{\psi-1}}{(d+\xi^{\psi})^2}. \tag{52}$$

Since Eq. (52) has a branch point of $\xi = 0$, Eq. (32) cannot be directly used. For the ACI 209R-92 model, when $N = 10$, the computational accuracy of the creep compliance function obtained from Eq. (27) is not very satisfactory (Figure 13). With reference to the analysis of the CEB MC90 model, Eq. (28) is used to calculate E and analyze the relationship between σ and b. Thus b is given by

$$b = \sqrt{46\sigma+\sigma^2}. \tag{53}$$

When $N = 10$, the empirical expression of σ is expressed as

$$\begin{cases} \sigma = 0.05\tau^2, \text{ for } \tau < 20, \\ \sigma = \tau, \text{ for } \tau \geq 20. \end{cases} \tag{54}$$

The continuous retardation spectra calculated by the Weeks method and the Post–Widder method with different orders are shown in Figure 11.

From Eq. (42), the values of $\varphi(\xi)$ of the ACI 209R-92 model for different durations ξ are obtained as shown in Figure 12; the errors are shown in Figure 13. For comparison, the errors of $\varphi(\xi)$ calculated from Eq. (27) are also shown in Figure 13 for $N = 10$ and $N = 50$. Figure 13 shows that, when Eq. (53) and (54) are adopted, the computational accuracy is obviously improved under the same N value.

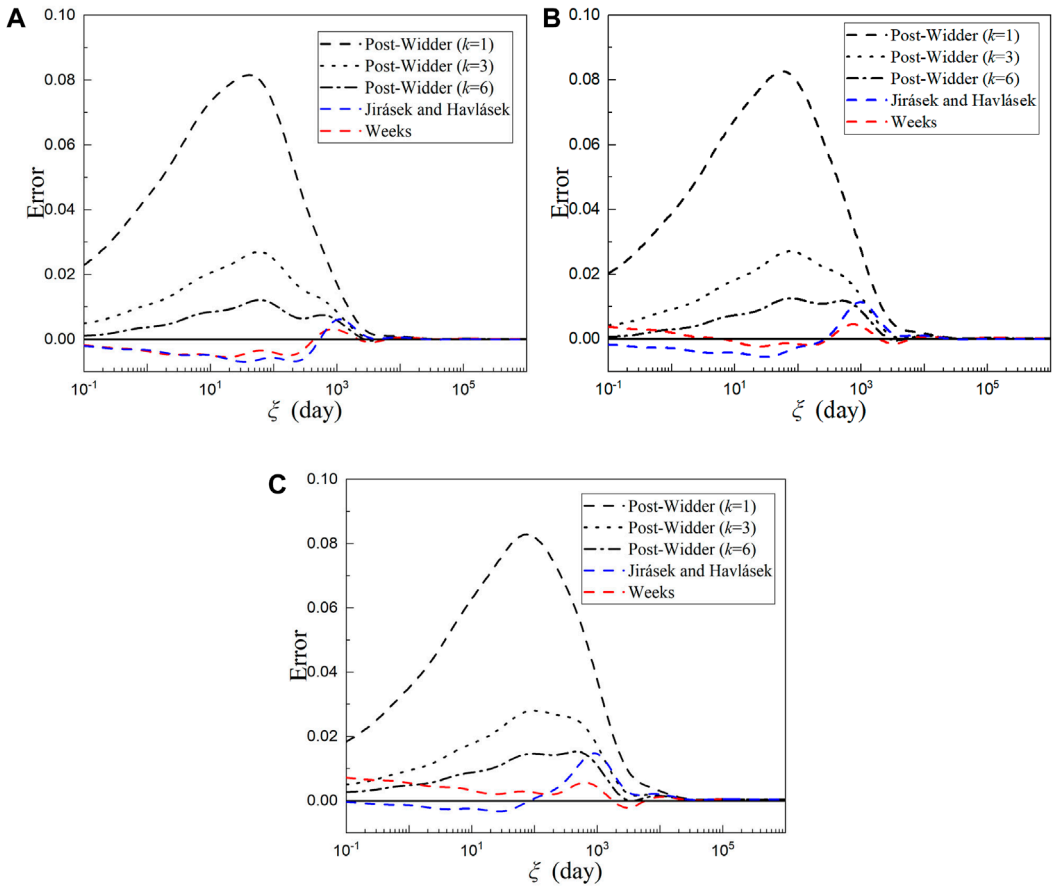

FIGURE 9
Errors of φ(ξ) calculated by different methods (CEB MC90 model) for **(A)** $\beta_h = 500$; **(B)** $\beta_h = 800$; **(C)** $\beta_h = 1{,}200$.

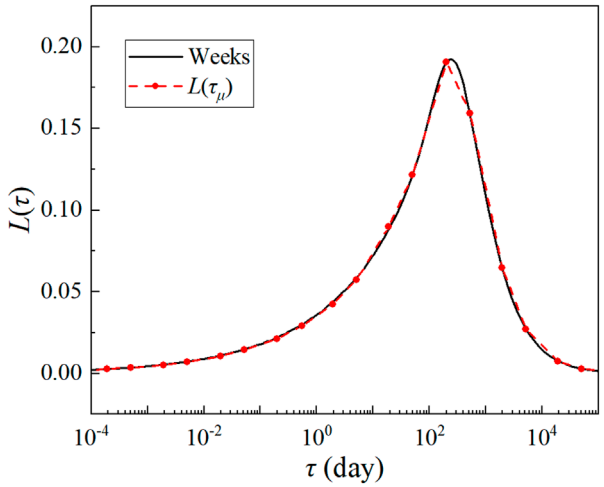

FIGURE 10
Approximation of $L(\tau_\mu)$ to the retardation spectrum (CEB MC90 model and $\beta_h = 500$).

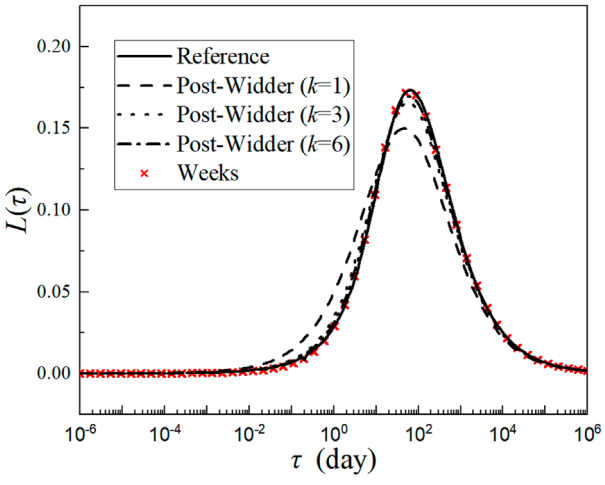

FIGURE 11
Continuous retardation spectra calculated by different methods (ACI 209R-92 model).

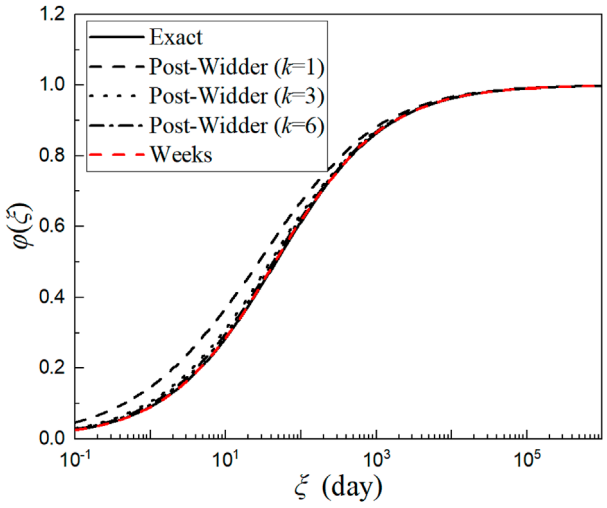

FIGURE 12
φ(ξ) calculated by different methods (ACI 209R-92 model).

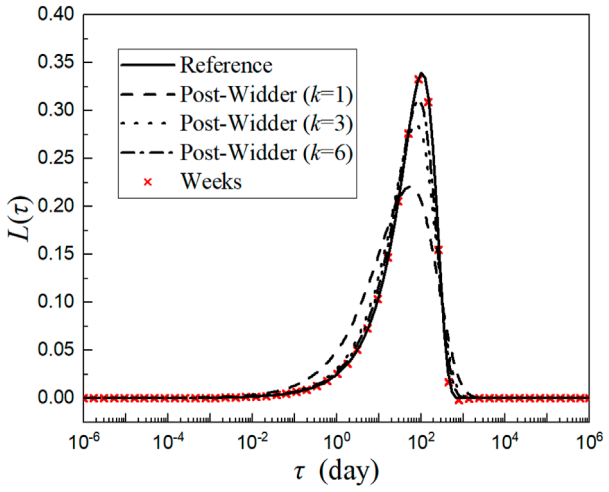

FIGURE 14
Continuous retardation spectra calculated by different methods (JSCE model).

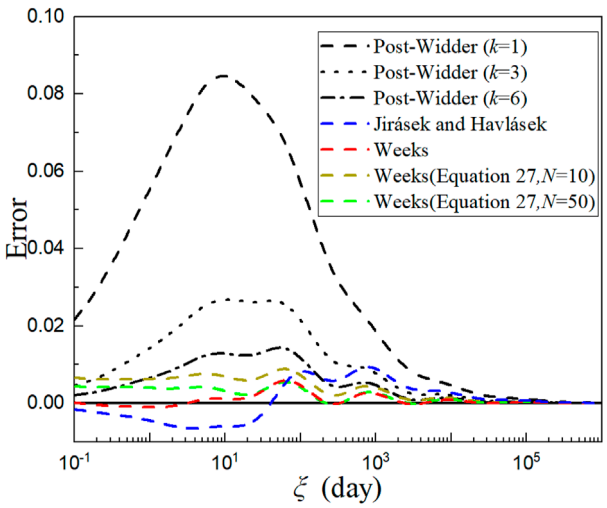

FIGURE 13
Errors of φ(ξ) calculated by different methods (ACI 209R-92 model).

4.3 JSCE model

The creep compliance function of the JSCE model (Uomoto et al., 2008) is defined as

$$J(t,t_0) = \left\{1 - \exp\left[-0.09(t-t_0)^{0.6}\right]\right\}\varepsilon'_{cr}, \tag{55}$$

where ε'_{cr} is the ultimate creep strain under unit stress and related to the ambient relative humidity, temperature, and the volume/surface ratio. $\varphi(\xi)$ is defined as

$$\varphi(\xi) = 1 - \exp\left(-0.09\xi^{0.6}\right). \tag{56}$$

Derivation of $\varphi(\xi)$ with respect to ξ gives

$$\varphi'(\xi) = 0.054\xi^{-0.4}\exp\left(-0.09\xi^{0.6}\right). \tag{57}$$

Since Eq. (57) has only a branch point $\xi = 0$, Eq. (32) cannot be directly used to evaluate the values of σ and b. Instead, Eq. (27) is adopted to determine the values of the two parameters. For $N = 10$, the continuous spectra calculated by the Weeks and Post–Widder methods with different orders are shown in Figure 14.

It is seen from Figure 14 that, compared with the CEB MC90 and ACI 209R-92 models, the continuous retardation spectra calculated by the Weeks method are steeper at the peak. The continuous retardation spectra of the CEB and ACI models show significant changes in the range from $\tau = 10^{-2}$ to $\tau = 10^{5}$, while that of the JSCE model mainly shows changes in the range from $\tau = 10^{-1}$ to $\tau = 10^{3}$. If $k = 1$ is set in Eq. (45), $L(\tau_\mu)$ cannot effectively describe the retardation spectrum curve. As shown in Figure 15A, the curve around $\tau = 10^{2}$ is not well reproduced. Therefore, it is necessary to increase the value of k. By setting the number of Kelvin units to $M = 40$— $k = 2$ in Eq. (45)—it is seen from Figure 15B that the computational accuracy is greatly improved. Therefore, for the JSCE model, it is necessary to adopt this retardation time value method. The numerical results and the errors for different methods are shown in Figures 16, 17, respectively.

4.4 GL2000 model

The creep compliance function of the GL2000 model (Gardner and Lockman, 2002) is defined as

$$J(t,t_0) = \frac{1}{E_{cmt0}} + \frac{\phi_{28}(t,t_0)}{E_{cm28}}, \tag{58}$$

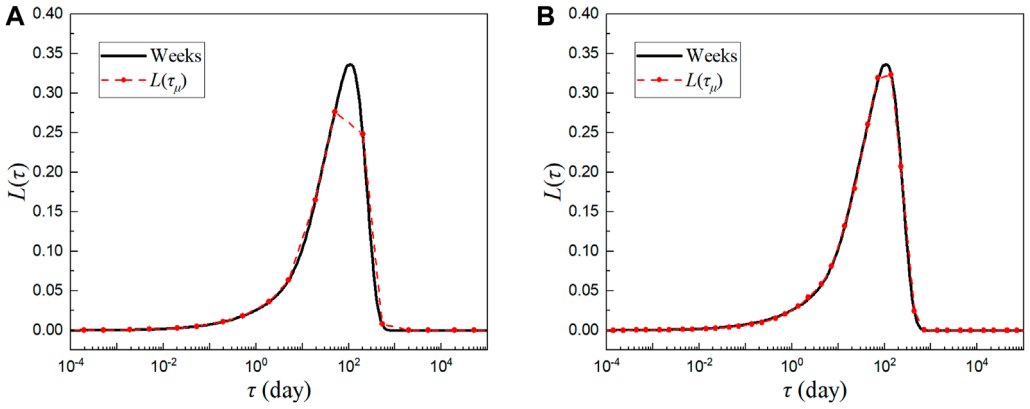

FIGURE 15
Approximation of $L(\tau_\mu)$ to the retardation spectrum (JSCE model) for **(A)** $k = 1$; **(B)** $k = 2$.

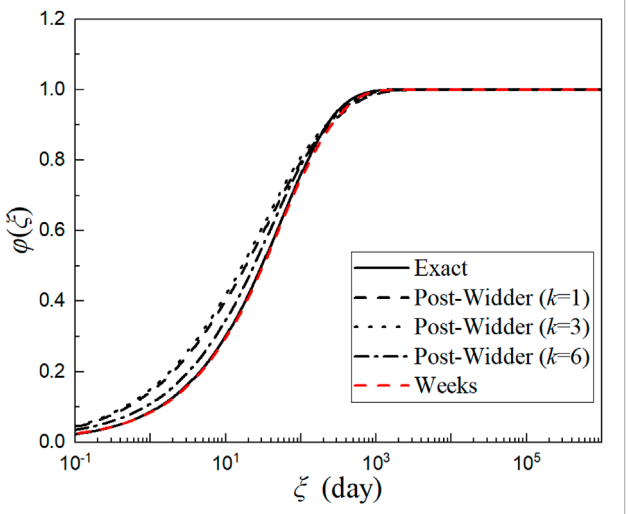

FIGURE 16
φ(ξ) calculated by different methods (JSCE model).

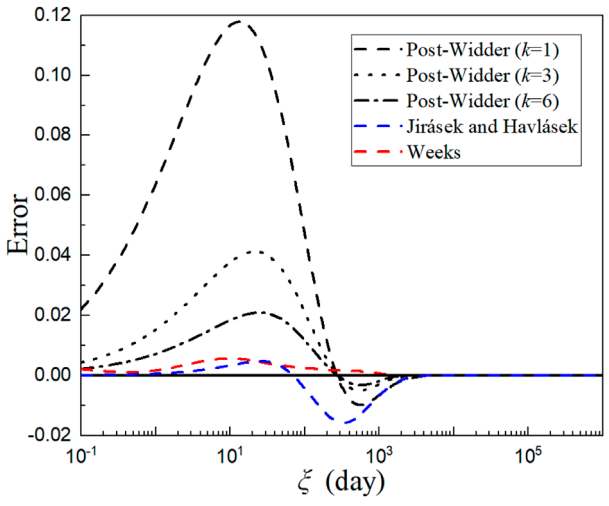

FIGURE 17
Errors of φ(ξ) calculated by different methods (JSCE model).

where E_{cmt0} is the elastic modulus at loading time and $\phi_{28}(t,t_0)$ is the creep coefficient at 28 days. The expression of $\phi_{28}(t,t_0)$ is

$$\phi_{28}(t,t_0) = \phi_c \left\{ \begin{array}{l} \dfrac{2(t-t_0)^{0.3}}{(t-t_0)^{0.3}+14} + \left(\dfrac{7}{t_0}\right)^{0.5}\left[\dfrac{(t-t_0)}{(t-t_0)+7}\right]^{0.5} \\ +2.5(1-1.086h^2)\left[\dfrac{(t-t_0)}{(t-t_0)+0.12(V/S)^2}\right]^{0.5} \end{array} \right\}. \tag{59}$$

In Eq. (59), ϕ_c is the correction term for the drying effect before loading, h is the relative humidity, and V/S is the volume/surface ratio of specimens. To simplify the calculation, $\varphi(\xi)$ is expressed as

$$\varphi(\xi) = 2\frac{\xi^{0.3}}{\xi^{0.3}+14} + \left(\frac{7}{t_0}\right)^{0.5}\left(\frac{\xi}{\xi+7}\right)^{0.5} + 2.5(1-1.086h^2)\left[\frac{\xi}{\xi+0.12(V/S)^2}\right]^{0.5}. \tag{60}$$

TABLE 2 Parameters for the two cases.

Case	t_0 [day]	h	V/S [mm]
1	14	70%	50
2	30	40%	100

If $\varphi_1(\xi)$ and $\varphi_2(\xi,\gamma)$ are defined as

$$\varphi_1(\xi) = \frac{\xi^{0.3}}{\xi^{0.3}+14}, \quad \varphi_2(\xi,\gamma) = \left(\frac{\xi}{\xi+\gamma}\right)^{0.5}, \tag{61}$$

the derivation of $\varphi(\xi)$ with respect to ξ yields

$$\varphi'(\xi) = 2\varphi_1'(\xi) + \left(\frac{7}{t_0}\right)^{0.5}\varphi_2'(\xi,7) + 2.5(1-1.086h^2)\varphi_2'(\xi,0.12(V/S)^2). \tag{62}$$

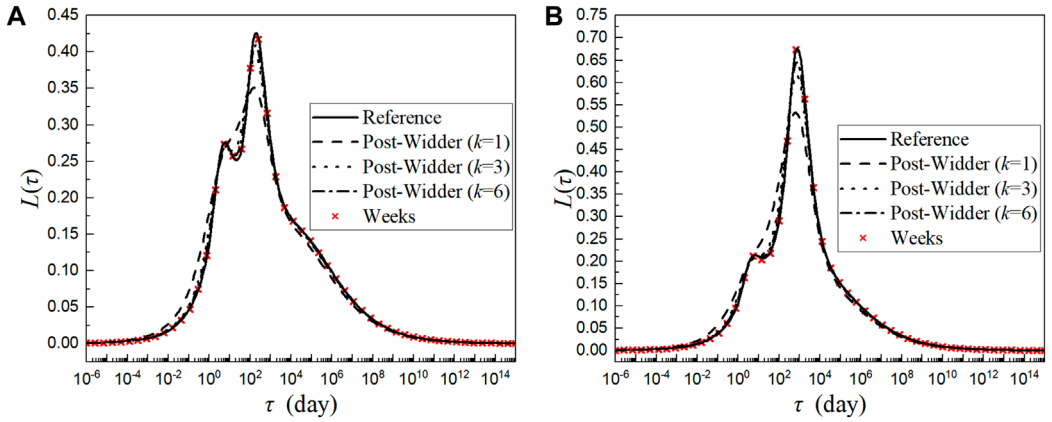

FIGURE 18
Continuous retardation spectra calculated by different methods (GL2000 model) for **(A)** case 1; **(B)** case 2.

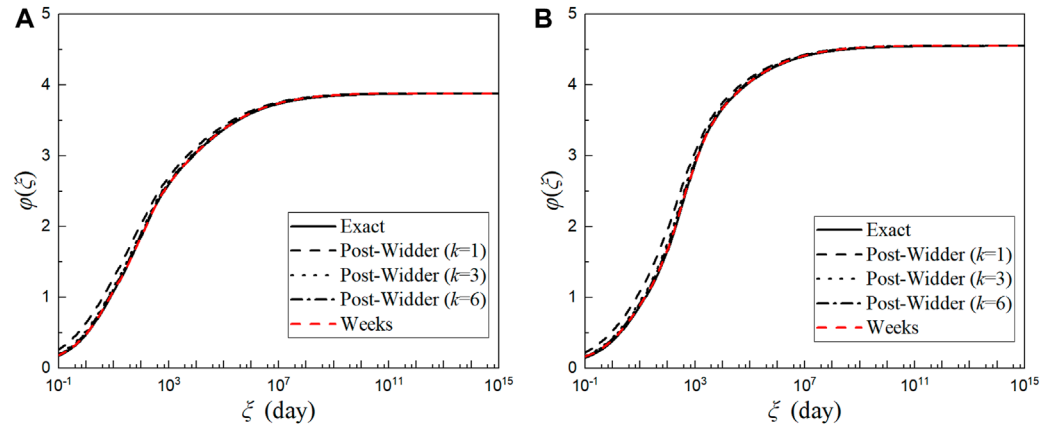

FIGURE 19
φ(ξ) calculated by different methods (GL2000 model) for **(A)** case 1; **(B)** case 2.

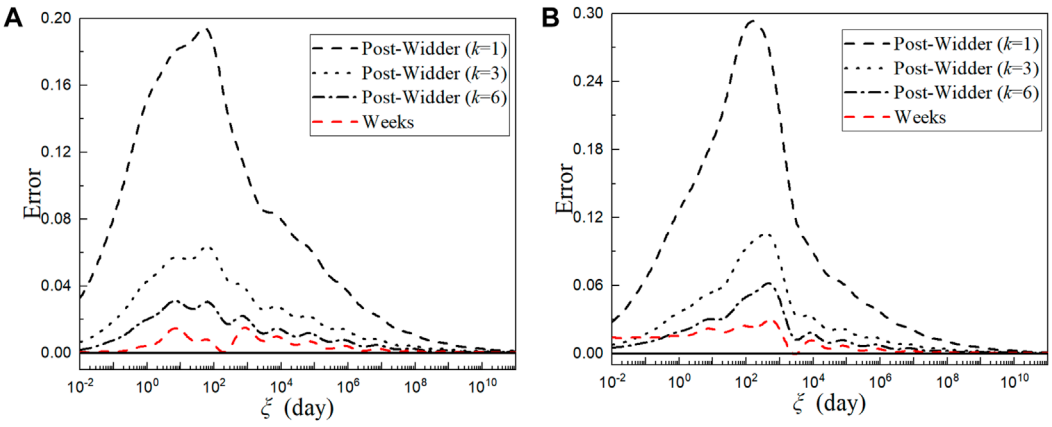

FIGURE 20
Errors of φ(ξ) calculated by different methods (GL2000 model) for **(A)** case 1; **(B)** case 2.

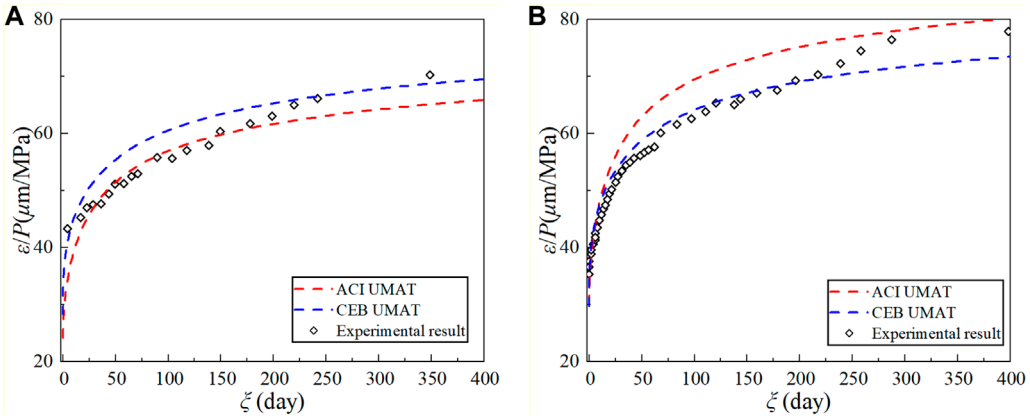

FIGURE 21
Comparison between experimental results and numerical results for **(A)** OPC; **(B)** SF10.

Because the function form of φ_2 is similar to Eq. (30), and the function form of φ_1 is similar to Eq. (51), the parameter value forms of the CEB MC90 and ACI 209R-92 models can be referred to respectively. For $N = 10$, the values of σ and b recommended for $\varphi_1'(\xi)$ and $\varphi_2'(\xi, \gamma)$ are

$$\boldsymbol{b_1 = \sigma_1, \sigma_1 = 0.6\tau}, \tag{63}$$

$$\boldsymbol{b_2} = \sqrt{\boldsymbol{\sigma_2^2 + \gamma\sigma_2}}, \begin{cases} \boldsymbol{\sigma_2 = (15/\gamma)\tau^2}, \text{ for } \boldsymbol{\tau < 0.04\gamma}, \\ \boldsymbol{\sigma_2 = 0.6\tau}, \text{ for } \boldsymbol{0.04\gamma \le \tau < 100}, \\ \boldsymbol{\sigma_2 = \tau}, \text{ for } \boldsymbol{\tau \ge 100}. \end{cases} \tag{64}$$

Two cases are considered, and the parameters are listed in Table 2. The continuous retardation spectra calculated by the Weeks and Post–Widder methods for different orders are shown in Figure 18.

It is apparent from Figure 18 that the continuous retardation spectra begin to grow significantly from $\tau = 10^{-4}$ and decrease gradually at a long retardation time. Therefore, more Kelvin units are needed to cover the range of the continuous retardation spectra. Consequently, τ_0 is set to 10^{-5}, the maximum value of m in Eq. (36) is taken as 18, $\tau_{18} = 10^{13}$ for this model, and the number of Kelvin units in Eq. (42) changes from 20 to 36. The values of $\varphi(\xi)$ of the GL2000 model for different duration ξ are obtained as per Figure 19, and the errors are shown in Figure 20. Since the GL2000 model was not discussed by Jirásek and Havlásek (2014), the error obtained from their method is not compared in Figure 20.

4.5 Discussion

For all the concrete creep models discussed in this section, the proposed approach based on the Weeks method improves the computational accuracy and efficiency of the continuous retardation spectra and the creep compliance. It should be noted that, for the case of long duration, the errors of $\varphi(\xi)$ decrease with the increase of ξ and approach zero. There are two main reasons for this phenomenon. First, the creep compliances used have negligible variation for a long duration and have a clear upper limit. Thus, the approximation through the Dirichlet series will maintain the same characteristics as long as the retardation time range selected is wide enough. Second, by calculating $1/E_0$ based on the most accurate compliance value—Eq. (43)—the effect of numerical integration for a short duration on the final results is reduced.

For the creep models considered, when $\xi \ge 1$, the absolute error of $\varphi(\xi)$ given by the improved approach (using the Weeks method) is smallest and maintains a lower level (usually smaller than 0.01). For the ACI 209R-92 and JSCE models, the results from the proposed approach achieve higher accuracy than the Post–Widder method. When calculated by the improved approach, $\varphi(\xi)$ of the ACI 209R-92 model is closest to the reference solution, while $\varphi(\xi)$ of the JSCE model exhibits the most significant improvement on the Post–Widder method.

The errors of $\varphi(\xi)$ obtained from the improved approach and the Jirásek–Havlásek method are both controlled at a relatively low level. For the CEB MC90 model, the results obtained from Jirásek–Havlásek are more accurate for low retardation times, while those obtained from Weeks are more accurate for high retardation times. As shown in Figure 9, the errors corresponding to the Weeks method are smaller compared to the Jirásek–Havlásek method when $\xi > 10$. For the ACI 209R-9 and JSCE models, the results obtained from Weeks are more accurate and the errors of $\varphi(\xi)$ are smaller.

For the other creep models which are not discussed in this paper, the proposed approach is still applicable when they fulfill the requirement of the Weeks inverse transform. In general, a large value of N can be used to achieve the required computational accuracy and a proper choice of σ and b can significantly improve computational efficiency. In general, Eq. (27) can be used to determine the parameters, and $10 \le N \le 50$ is recommended. The larger the value of N, the more accurate the calculation results, but computational efficiency will be reduced. If $\varphi'(\xi)$ has two or more poles and branch points, Eq. (32) can also be used to determine the parameters, and precision requirements are usually satisfied when $N = 10$.

5 Comparison with experimental results

To further verify the validity of the improved approach, the finite element method is used to compute the long-term creep of concrete by combining the retardation spectrum obtained by the Weeks method with the second-order exponential algorithm (Bažant and Jirásek, 2018). For this purpose, two sets of experimental data, OPC and SF10, were selected from Mazloom et al. (2004). They had different mix proportions, and a pressure of 10 MPa was applied on the OPC and SF10 cylinders on the 28th and 7th days, respectively. Two UMAT user subroutines for material behavior—ACI UMAT and CEB UMAT—of the commercial finite element software ABAQUS were coded. The concrete strain was calculated using the CEB MC90 and ACI 209R-92 creep models. The results are shown in Figure 21, which shows that the finite element results are in good agreement with the experimental results. For the OPC group, the ACI 209R-92 model has higher accuracy, while, for the SF10 group, the CEB MC90 has higher accuracy.

It is noted that one of the purposes of this paper is to ensure that the numerical results agree well with the corresponding expressions of $J(t,t_0)$. As a result, the accuracy of the final numerical results is mainly dependent on whether the analytical expression of $J(t,t_0)$ given by design codes is close to the practical situation. Therefore, before the concrete creep is calculated, it is necessary to select a reasonable model according to the practical situation, including the mix proportion, the component shape, loading, and environmental conditions, to ensure the computational accuracy of the numerical results. It should also be noted that, since this paper is mainly concerned with improving on the continuous retardation method, finding a viable, stable strategy to identify the optimal dimension of the approximation in the presence of an error (uncertainty) on data is not addressed. This limitation is expected to be removed in our future work.

6 Conclusion

Based on the Weeks method, an efficient approximation approach has been developed for the continuous retardation spectra of aging viscoelastic materials. Compared with the existing methods, the approach has several advantages.

(1) It can calculate the continuous retardation spectrum more accurately by only using the first-order derivative of the creep compliance function. The difficulty of calculating the high-order derivatives in the Post–Widder method is avoided.
(2) Unlike the method proposed by Jirásek and Havlásek (2014), in which the correction factor is empirically determined for each concrete creep model at a given derivative order, the proposed approach is based on a solid theoretical foundation and can be conveniently applied to various concrete creep models.
(3) Better computational accuracy can be achieved for a long loading duration. As illustrated by different concrete creep models, the error of the creep compliance function obtained by the proposed approach is controlled within 0.02 for a loading duration of $10^{-1} < \xi < 10^{6}$. Therefore, the approach is applicable to long-term creep analyses of aging viscoelastic materials, such as concrete.

It should be noted that the proposed approach is only applicable to concrete creep models when the first-order derivative of the compliance function fulfills the requirement of the Weeks method. For concrete creep models with logarithmic compliance functions, such as the fib model (CEB-FIP, 2010), the inversion formula of the Laplace transform has an analytical solution and does not require the Weeks method for the continuous retardation spectrum. In this research, to achieve high computational efficiency and accuracy, the values of σ and b for the CEB MC90, ACI 209R-92, and GL2000 models are determined empirically for $N = 10$. As for the JSCE model, a good precision requirement can be achieved when the parameters are taken directly through Eq. (27) for $N = 10$. If the proposed approach is applied to other creep models, the parameters can be determined by referring to the analytical process of this paper or directly by increasing the value of N to meet the precision requirements.

Data availability statement

The raw data supporting the conclusion of this article will be made available by the authors, without undue reservation.

Author contributions

XZ: Conceptualization, Methodology, Writing–review and editing. LB: Formal Analysis, Validation, Writing–original draft. HR: Data curation, Software, Writing–original draft. XF: Funding acquisition, Project administration, Supervision, Writing–original draft. JZ: Funding acquisition, Resources, Writing–review and editing. YG: Investigation, Visualization, Writing–original draft.

Funding

The author(s) declare financial support was received for the research, authorship, and/or publication of this article. This research was funded by the National Science Foundation for Excellent Young Scholars (Grant No. 52222808), the Zhejiang Provincial Natural Science Foundation (Grant No. LY20E080027), and the National Natural Science Foundation of the People's Republic of China (Grant Nos 52008413, 52078509, 52178255, and 52278279).

Conflict of interest

Authors HR, XF, and YG were employed by Metallurgical Group Corporation of China.

The remaining authors declare that the research was conducted in the absence of any commercial or financial relationships that could be construed as a potential conflict of interest.

The handling editor J-GD declared a past co-authorship with the author JZ.

Publisher's note

Supplementary material

The Supplementary Material for this article can be found online at: https://www.frontiersin.org/articles/10.3389/fmats.2024.1340883/full#supplementary-material

References

ACI Committee 209 (2005). *Report on factors affecting shrinkage and creep of hardened concrete*. Farmington Hills: American Concrete Institute.

ACI Committee 209 (2008). *Guide for modeling and calculating shrinkage and creep in hardened concrete*. Farmington Hills: American Concrete Institute.

Baumgaertel, M., and Winter, H. H. (1989). Determination of discrete relaxation and retardation time spectra from dynamic mechanical data. *Rheol. Acta* 28, 511–519. doi:10.1007/BF01332922

Bažant, Z. P. (1988). *Mathematical modeling of creep and shrinkage of concrete*. New York: John Wiley and Sons.

Bažant, Z. P., Hauggaard, A. B., Baweja, S., and Ulm, F. J. (1997). Microprestress-solidification theory for concrete creep. I: aging and drying effects. *J. Eng. Mech.* 123, 1188–1194. doi:10.1061/(asce)0733-9399(1997)123:11(1188)(1997)123:11(1188)

Bažant, Z. P., and Jirásek, M. (2018). *Creep and hygrothermal effects in concrete structures*. Netherland: Springer Dordrecht.

Bažant, Z. P., and Xi, Y. (1995). Continuous retardation spectrum for solidification theory of concrete creep. *J. Eng. Mech.* 121, 281–288. doi:10.1061/(asce)0733-9399(1995)121:2(281)(1995)121:2(281)

CEB-FIP (1993). *Design of concrete structures, CEB-FIP model-code 1990*. London: British Standard Institution.

CEB-FIP (2010). *Fib Model Code for concrete structures 2010*. London: British Standard Institution.

Durbin, F. (1974). Numerical inversion of laplace transforms: an efficient improvement to dubner and abate's method. *Comput. J.* 17, 371–376. doi:10.1093/comjnl/17.4.371

Elster, C., and Honerkamp, J. (1991). Modified maximum entropy method and its application to creep data. *Macromolecules* 24, 310–314. doi:10.1021/ma00001a047

Emri, I., and Tschoegl, N. W. (1995). Determination of mechanical spectra from experimental responses. *Int. J. Solids Struct.* 32, 817–826. doi:10.1016/0020-7683(94)00162-P

Gardner, N. J., and Lockman, M. J. (2002). Design provisions for drying shrinkage and creep of normal-strength concrete. *ACI Mater. J.* 98, 159–167. doi:10.14359/10199

Hubert Rüsch, D. J., and Hilsdorf, H. K. (1983). *Creep and shrinkage*. New York: Springer.

Jirásek, M., and Havlásek, P. (2014). Accurate approximations of concrete creep compliance functions based on continuous retardation spectra. *Comput. Struct.* 135, 155–168. doi:10.1016/j.compstruc.2014.01.024

Kaschta, J., and Schwarzl, R. R. (1994). Calculation of discrete retardation spectra from creep data-I. Method. *Rheol. Acta* 33, 517–529. doi:10.1007/BF00366336

Mazloom, M., Ramezanianpour, A. A., and Brooks, J. J. (2004). Effect of silica fume on mechanical properties of high-strength concrete. *Cem. Concr. Compos.* 26, 347–357. doi:10.1016/s0958-9465(03)00017-9

Mead, D. W. (1994). Numerical interconversion of linear viscoelastic material functions. *J. Rheology* 38, 1769–1795. doi:10.1122/1.550526

Nicholas, W. T. (1989). *The phenomenological theory of linear viscoelastic behavior*. Heidelberg: Springer.

Park, S. W., and Kim, Y. R. (2001). Fitting prony-series viscoelastic models with power-law presmoothing. *J. Mater. Civ. Eng.* 13, 26–32. doi:10.1061/(asce)0899-1561(2001)13:1(26)(2001)13:1(26)

Ramkumar, D. H. S., Caruthers, J. M., Mavridis, H., and Shroff, R. (1997). Computation of the linear viscoelastic relaxation spectrum from experimental data. *J. Appl. Polym. Sci.* 64, 2177–2189. doi:10.1002/(SICI)1097-4628(19970613)64:11<2177::AID-APP14>3.0.CO;2-1

Schapery, R. (1962). "*A simple collocation method for fitting viscoelastic models to experimental data*", in: Graduate Aeronautical Laboratory. (California: California Institute of Technology).

Uomoto, T., Ishibashi, T., Nobuta, Y., Satoh, T., Kawano, H., Takewaka, K., et al. (2008). Standard specifications for concrete structures-2007 by Japan society of Civil engineers. *Concr. J.* 46, 3–14. doi:10.3151/coj1975.46.7_3

Weeks, W. T. (1966). Numerical inversion of laplace transforms using Laguerre functions. *J. ACM* 13, 419–429. doi:10.1145/321341.321351

Weideman, J. a.C. (1999). Algorithms for parameter selection in the weeks method for inverting the laplace transform. *Siam J. Sci. Comput.* 21, 111–128. doi:10.1137/s1064827596312432

Zienkiewicz, O. C., Watson, M., and King, I. P. (1968). A numerical method of visco-elastic stress analysis. *Int. J. Mech. Sci.* 10, 807–827. doi:10.1016/0020-7403(68)90022-2

frontiers | Frontiers in Materials

TYPE Original Research
PUBLISHED 22 February 2024
DOI 10.3389/fmats.2024.1363206

OPEN ACCESS

EDITED BY
Biao Hu,
Shenzhen University, China

REVIEWED BY
Bing Tu,
Guangxi University, China
Aiming Song,
Yancheng Institute of Technology, China

*CORRESPONDENCE
Yawei Fang,
fangyawei@hnu.edu.cn

RECEIVED 30 December 2023
ACCEPTED 31 January 2024
PUBLISHED 22 February 2024

CITATION
Liu J, Yu W, Fang Y and Pan Z (2024), Experimental study on the seismic performance of concrete-filled steel tube columns with a multiple-chamber round-ended cross-section.
Front. Mater. 11:1363206.
doi: 10.3389/fmats.2024.1363206

Experimental study on the seismic performance of concrete-filled steel tube columns with a multiple-chamber round-ended cross-section

Jing Liu[1,2], Wenzuo Yu[1], Yawei Fang[3,4]* and Zimao Pan[1]

[1]Hunan Engineering Research Center of Development and Application of Ceramsite Concrete Technology, Hunan City University, Yiyang, China, [2]Key Laboratory of Green Building and Intelligent Construction in Higher Educational Institutions of Hunan Province, Hunan City University, Yiyang, China, [3]College of Civil Engineering, Hunan University, Changsha, Hunan, China, [4]Department of Civil and Environmental Engineering, Hong Kong Polytechnic University, Kowloon, Hong Kong, China

Reinforced concrete bridge piers with round-ended sections are susceptible to bending, bending–shear, and shear failure after earthquakes in high-intensity areas, thus necessitating improved seismic performance. This study introduced a novel design for a concrete-filled steel tube (CFST) column, featuring a multi-chambered, round-ended cross-section. The use of longitudinal and transverse stiffeners divided the column section into distinct chambers, thereby enhancing the seismic performance of the columns. A total of 12 groups of static tests were performed to examine the effect of chamber layout, axial compression ratio, and aspect ratio on columns' hysteresis behavior, and the hysteresis curves, skeleton curves, failure modes, stiffness degradation, ductility, and energy dissipation capacity were obtained. Results demonstrated the favorable seismic performance of composite columns. Additionally, an increase in chambers led to a full hysteresis curve, enhancing bearing and energy dissipation capacities. The displacement ductility coefficient (μ) ranged between 3.88 and 7.45, and the design parameters have minimal influence on the stiffness degradation of the composite beam. Based on the results, the long and short sides of the CFST columns with a large length–width ratio should be arranged to be relatively close in length.

KEYWORDS

concrete-filled steel tubular column, round-ended section, hysteretic behavior, multichamber restraint, ductility, stiffness degradation

1 Introduction

Reinforced concrete (RC) bridge piers with round-ended sections are widely used as substructures in heavy-haul railway and long-span bridges. Over time, RC bridge piers in high-intensity areas generally experience post-earthquake bending, flexural shear, or shear failure; consequently, the seismic performance of these piers must be improved (Wang, 2015). Utilizing a concrete-filled steel tube (CFST) structure is an ideal choice to improve the seismic performance of RC bridge piers (Fei et al., 2020). During loading, the

TABLE 1 The test parameters of composite columns.

No.	specimen	$B \times D \times t \times H$/mm	Chamber arrangement	n	Strong or weak axis	f_s MPa	f_{cu} MPa	ρ_s
1	CFST-C1	228 × 114 × 3 × 1,150	Single cavity	0.1	strong	359	45.2	7.58
2	CFST-C2	228 × 114 × 3 × 1,150	Two cavity	0.1	strong	359	45.2	9.05
3	CFST-C3	228 × 114 × 3 × 1,150	Three cavity	0.1	strong	359	45.2	10.53
4	CFST-C4	228 × 114 × 3 × 1,150	Four cavity	0.1	strong	359	45.2	12.00
5	CFST-C5	228 × 114 × 3 × 1,150	Single cavity	0.3	strong	359	45.2	7.58
6	CFST-C6	228 × 114 × 3 × 1,150	Two cavity	0.3	strong	359	45.2	9.05
7	CFST-C7	228 × 114 × 3 × 1,150	Three cavity	0.3	strong	359	45.2	10.53
8	CFST-C8	228 × 114 × 3 × 1,150	Four cavity	0.3	strong	359	45.2	12.00
9	CFST-C9	342 × 114 × 3 × 1,650	Single cavity	0.1	strong	359	45.2	6.75
10	CFST-C10	342 × 114 × 3 × 1,650	Two cavity	0.1	strong	359	45.2	7.69
11	CFST-C11	342 × 114 × 3 × 1,650	Three cavity	0.1	strong	359	45.2	8.64
12	CFST-C12	342 × 114 × 3 × 1,650	Four cavity	0.1	strong	359	45.2	10.53

steel tube can provide effective restraints to the core concrete and retard the longitudinal cracking of the concrete under pressure; meanwhile, the internal concrete delays the local buckling of the steel tube. This synergy between those materials maximizes their benefits of mechanical properties, thereby leading to an increased static bearing capacity, ductility, and seismic performance of the bridge piers while promoting construction efficiency and cost effectiveness (Zhou et al., 2019; Hu et al., 2022a; Hu et al., 2022b; Zhou et al., 2022; Zhou et al., 2023).

Many bridges in earthquake-prone areas, such as the Houhu Bridge and Xinglin Bridge, have implemented CFST piers (Shen et al., 2020; Wang and Shen, 2023). A previous research conducted by the authors (Ding et al., 2016) demonstrated that when the section aspect ratio of a round-ended CFST column was greater than 5.0, the constraints to the core concrete by a single-cavity steel tube became negligible. Therefore, given the distinctive features of the large section length–width ratio of columns with circular sections in practical engineering, proposing a CFST column with a multichamber round-ended section in the current study is logical. The round-ended section is partitioned into multiple chambers by employing vertical and horizontal stiffening ribs. This design amplifies the restraining effect of the steel tubes on the core concrete through multicavity constraints, thereby bolstering the seismic performance of the column.

In recent years, some researchers have conducted experimental and numerical studies on the restraint mechanism of CFST columns with round-ended sections. Shen et al. (Shen et al., 2020) conducted an experimental study on axially loaded welded tubular joints with round-ended oval hollow sections (ROHS). They introduced a method for predicting the axial compression resistance of the ROHS tubular joint. Hassanein and Patel (Hassanein and Patel, 2018) completed a finite element analysis (FEA) on round-ended rectangular CFST short columns under axial compression, and on the basis of the results of FEA, a design model was established to estimate the reasonable strength of the columns under different loadings. Zhang et al. (Zhang and FuXu, 2020) established a fiber beam–column model to analyze the nonlinear behavior of round-ended CFSTs, and their model accurately described the nonlinear behavior of these round-ended CFSTs. Ren et al. (Ren et al., 2022) proposed a "central angle" concept to extend the cross-section design of round-ended rectangular CFST columns, and a reliable analytical model for predicting the axial ultimate bearing capacity of CFST was developed and validated. Shen et al. (Shen et al., 2022) investigated the performance of cold-formed round-ended CFST columns under cyclic loading using experimental and numerical approaches. Their research provided insightful revelations about the failure modes, hysteretic curves, ductility ratio, energy dissipation, stiffness, and strength degradation of these columns.

As for CFST columns with multiple cavities, Wu et al. (Wu et al., 2017) conducted tests on six columns under cyclic uniaxial compressive load, scrutinizing the effects of cavity construction, reinforcement arrangement, and concrete strength on failure characteristics, load-bearing capacity, stiffness, and residual deformation; moreover, a reasonable calculation method by dividing concrete into active and inactive confined regions was proposed. Qiao et al. (Qiao et al., 2018) executed a quasistatic test on four 1/30-scale uniquely shaped concrete-filled tube (CFT) columns with multiple cavities and investigated the seismic behavior of the CFT columns with multiple cavities under axial tension or axial compression. Wu et al. (Wu et al., 2016) studied the uniaxial compressive constitutive relationship

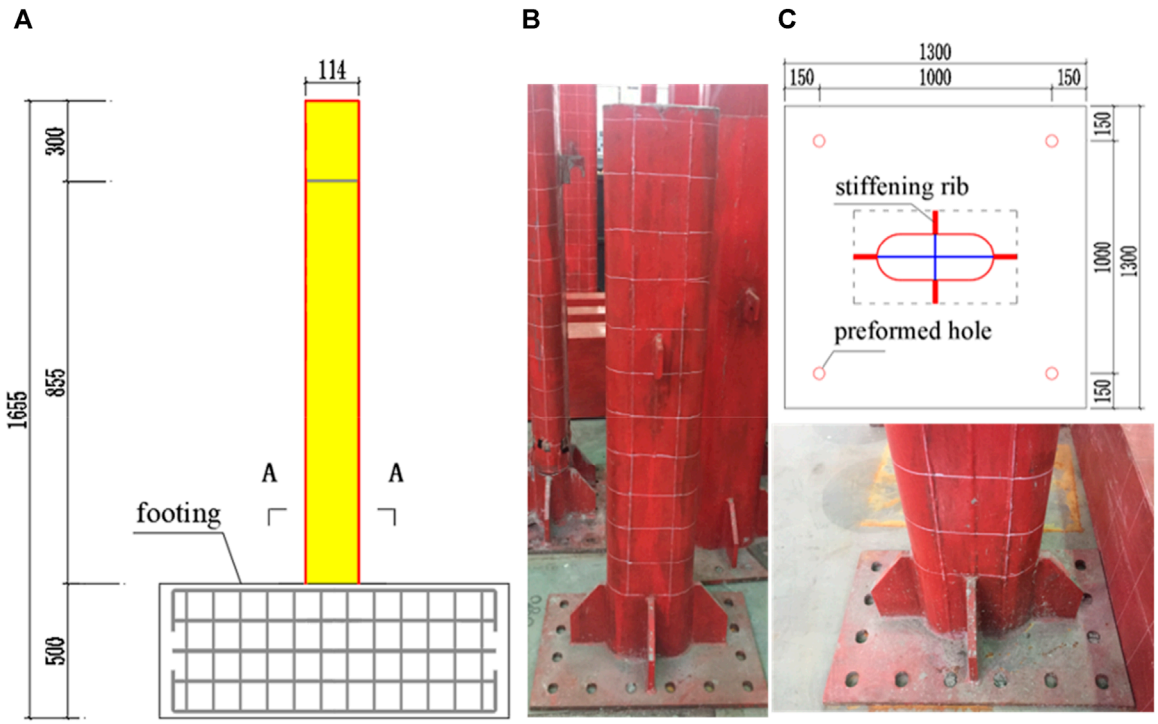

FIGURE 1
Layouts of the specimens. **(A)** Vertical view. **(B)** Actual photo. **(C)** Specimen base.

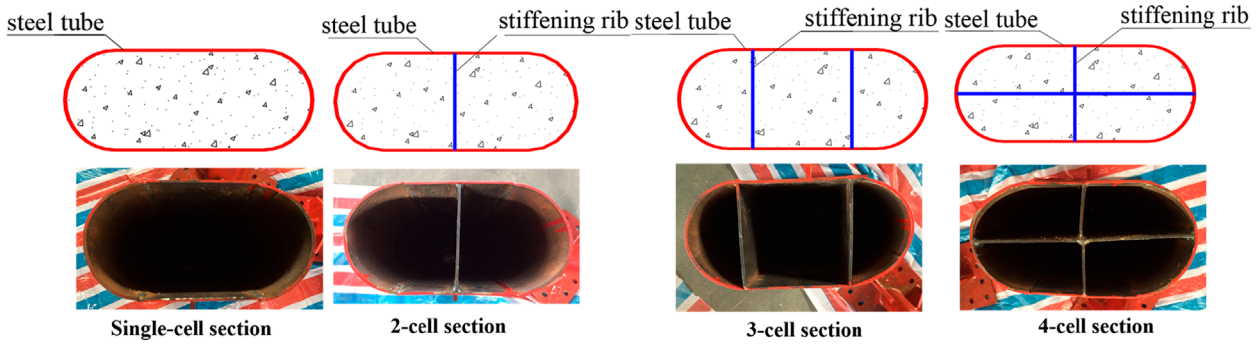

FIGURE 2
Cross-section of specimens.

of concrete confined by a special-shaped steel tube coupled with multiple cavities and proposed a method that predicts the associated complete stress–strain curves. Chen et al. (Chen et al., 2021) completed a comprehensive experimental study on the seismic behavior of prefabricated L-shaped CFST columns with rectangular multichamber columns under different lateral loading directions. The results indicated that multichamber, special-shaped steel tubes had a considerable restraining effect on the core concrete. Yin et al. (Yin et al., 2020) conducted experimental and analytical studies on the seismic behavior of special-shaped multichamber composite CFST columns. They proposed a theoretical method to predict the seismic behavior of the columns, and the calculation results showed good consistency with the test ones. Alatshan et al. (Alatshan et al., 2020) conducted a comprehensive study on the compressive performance of CFST columns with various reinforcement, partition, and tie rods. On the basis of the test results, the effects of these parameters on the mechanical properties of the composite columns were uncovered.

The foregoing literature review reveals that substantial research has been conducted on CFST columns with multiple chambers, but studies on CFST columns with multichamber round-ended cross-sections are few (Wu et al., 2016; Wu et al., 2017; Qiao et al., 2018; Alatshan et al., 2020; Yin et al., 2020; Chen et al., 2021). However,

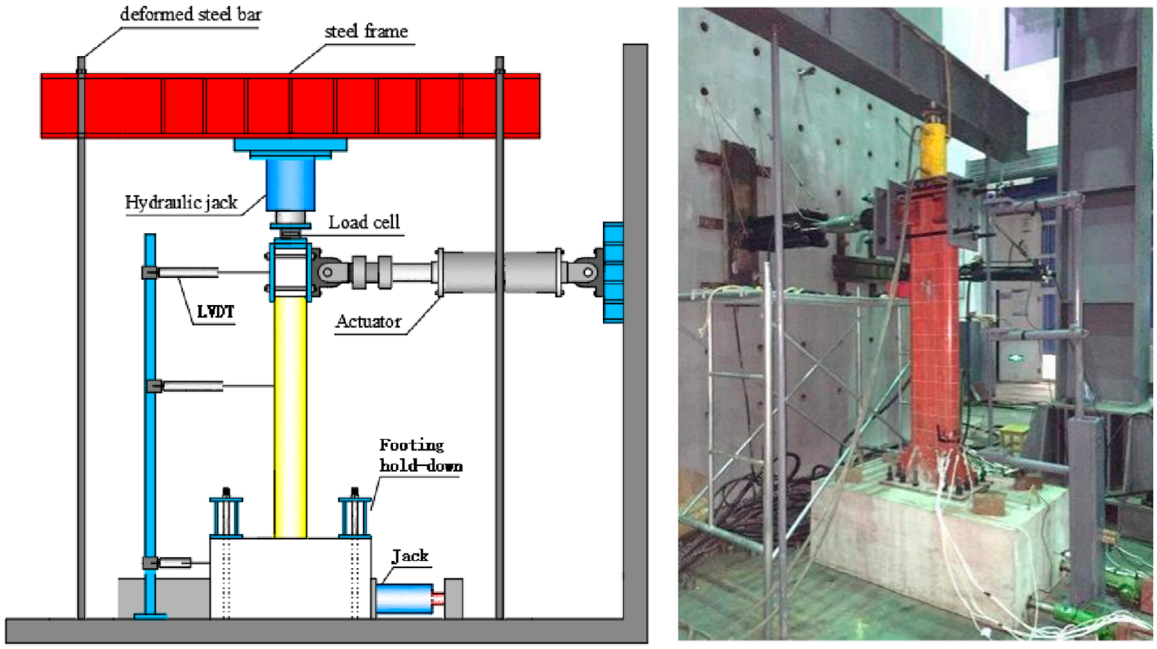

FIGURE 3
Experimental setup.

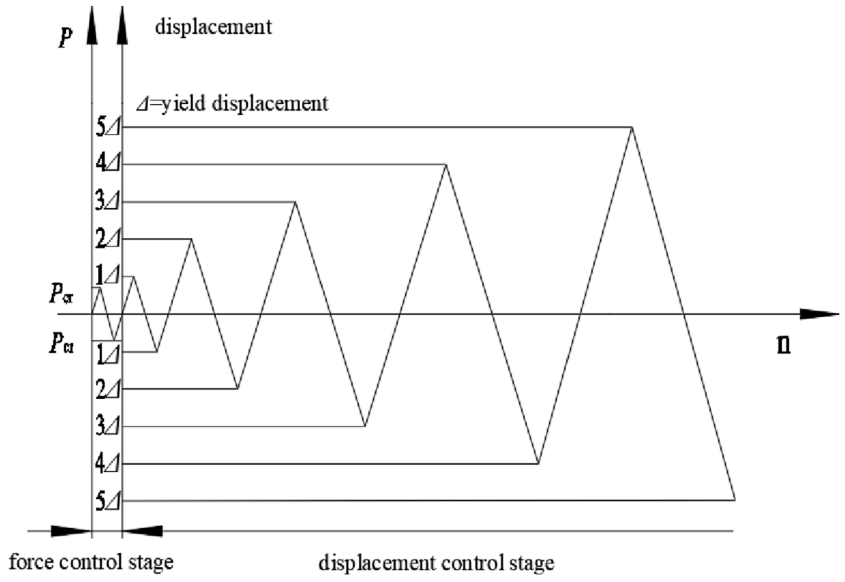

FIGURE 4
Loading protocol.

research on seismic properties is relatively limited, which restricts the application of this type of structure in high seismic-risk areas. Therefore, this study investigates the seismic performance of a CFST column with a multichamber round-ended cross-section. The main objectives of this study are as follows: (i) investigate the seismic performance of 12 CFST columns with a multichamber round-ended cross-section through a quasistatic experimental study and analyze the observed phenomena and failure patterns; (ii) analyze the effects of chamber layout, axial compression ratio, and section width–thickness ratio on the seismic performance, including hysteresis curve, skeleton curve, stiffness degradation, ductility and bearing capacity, and energy dissipation of columns; (iii) recommend reasonable structural measures for CFSTs.

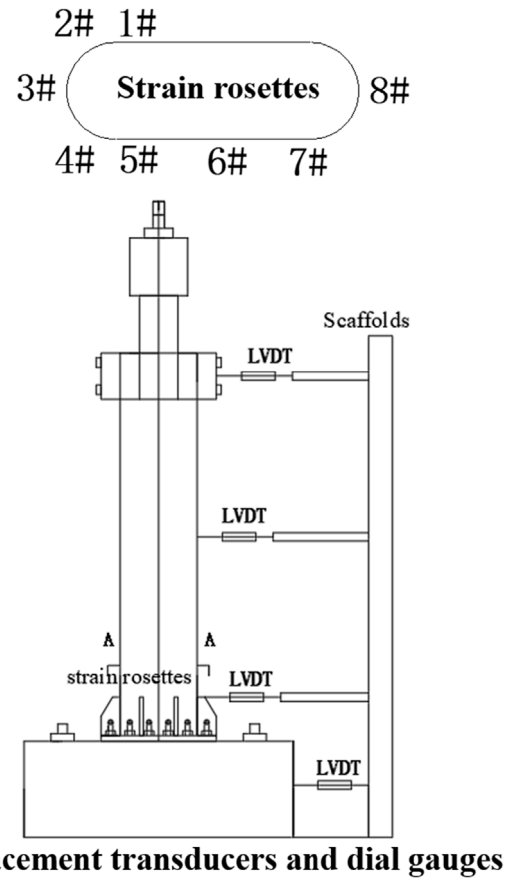

FIGURE 5
Layout of strain measurement.

2 Experimental program

2.1 Specimen design

In accordance with the specification for seismic test of buildings (JGJ101-2015) (GJ101-2015, 2015), a total of 12 CFST columns with a multichamber round-ended cross-section were tested in the current study. The test parameters for the composite columns are presented in Table 1. B is the width of the section, D is the height of the section, H is the height of the column, n is the axial compression ratio of the column, f_{cu} is the cubic compressive strength, f_s is the yield strength of steel tube, and ρ_s is the steel content of the section. Figures 1, 2 show the layouts and cross-section of the specimens, respectively.

During manufacturing, smooth, undistorted cross-sections at both ends of the steel tube must be ensured. A 20 mm-thick steel plate was welded to the bottom of the formed steel tube. Subsequently, concrete was poured and compacted by vibration after being pumped into the tube from the top. After 28 days of curing, the concrete had hardened completely and achieved its compressive strength. Then, the cover plate was welded to the top of the steel tube. For convenience of observation and recording of failure mode, red paint was sprayed on the external surface of the steel tube, and 50 mm × 50 mm white grids were plotted on the surface.

Commercial concrete (grade C40) was adopted for all the specimens, and the 28-day compressive strength obtained from nine standard concrete cubes with a dimension of 150 mm × 150 mm × 150 mm was measured as 45.2 MPa. The measured yield strength of the steel tube was 359 MPa, as listed in Table 1.

2.2 Instrumentation and loading scheme

In this test, a pseudostatic test loading scheme was employed. The composite column test loading device is shown in Figure 3, and the loading process is shown in Figure 4. Specifics are outlined below:

(1) Before the test, approximately 30% of the axial force was applied to verify the stability of the connections among the jack, distribution beam, and specimen. The chuck of the specimen and the specimen itself must be properly secured. The designed axial compression load was applied to the specimen, maintaining a constant axial force value throughout the loading period.

(2) After the trial began, the control loads were 0.2 and 0.4 P_u; P_u represents the limit value of the horizontal load. Load control is employed until the specimen reaches the yield load, after which control is switched to deformation-based loading. Increments of $1\Delta_y$, $2\Delta_y$, $3\Delta_y$, $4\Delta_y$, $5\Delta_y$, $6\Delta_y$, $7\Delta_y$, $8\Delta_y$, and $9\Delta_y$ were used for loading, where $\Delta_y = P_u/K_{sec}$, Δ_y is the yield displacement of the specimen. K_{sec} is the secant stiffness of the load–displacement curve when the load reaches $0.4P_u$.

2.3 Measuring point arrangement

The measurements taken in this test primarily included horizontal load, vertical load, horizontal displacement at the top of the specimen, and strain on the steel tube's surface. The main measurement points are arranged as follows:

2.3.1 Displacement measurement

Vertical load was applied to the specimen using a hydraulic jack. Three displacement meters are positioned along the column, and four displacement meters were placed on the concrete base. Figure 5 displays the displacement observations of the specimen.

2.3.2 Strain measurement

Eight strain gauges were affixed 100 mm above the stiffener to measure the longitudinal and transverse strains on the surface of the steel tube during low-cycle loading, and data were collected by the DH3818. The locations of the strain measuring points on the steel tube section are illustrated in Figure 5.

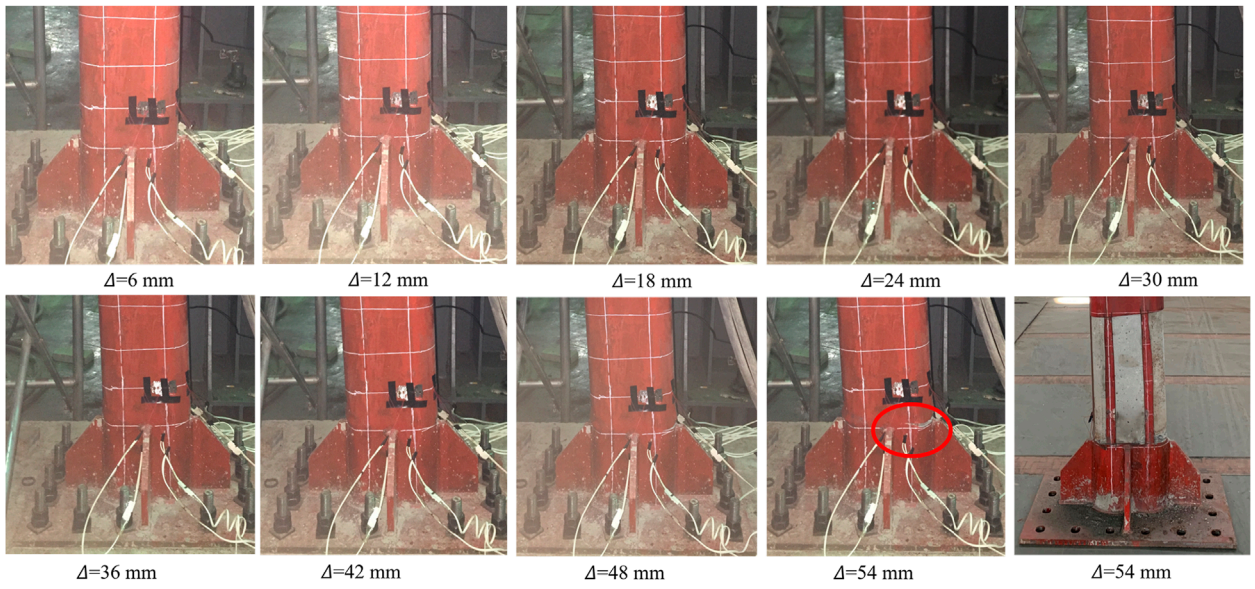

FIGURE 6
Failure process of specimen.

3 Experimental results and discussions

3.1 Failure pattern

The test results indicate that the failure modes of the specimens are essentially the same, characterized by bending failure. To illustrate the failure process of the specimen, we use CFST-C3 as an example, as depicted in Figure 6. Δ represents the maximum displacement at various loading cycles.

Before Δ = 24 mm, no local buckling of the steel tube was observed on the surface of the steel tube. When the load exceeded the yield point, local buckling began to occur within 70 mm of the stiffener's upper end at the specimen's bottom. As the load increased, bulging appeared in the bottom part of the member, and surface deformation of the steel tube rapidly intensified as the specimen approached failure. The sound of the steel tube tearing and the crushing sound of the core concrete (e.g., at Δ = 24 mm) were audible, indicating that the strain in the steel tube had reached its ultimate limit, and its tensile strength had been fully utilized.

The end of the CFST-C1–CFST-C12 test is shown in Figure 7. The fewer the chambers, the more severe the damage to the core concrete. In the case of single-cavity arranged steel tube concrete columns, the failure surface penetrates the entire concrete cross-section, while the presence of multicavity steel tubes constrains the failure of the core concrete in other specimens within their respective steel tube areas. Multicavity constraints can effectively delay and even prevent the occurrence of local buckling in steel tubes and concrete damage.

3.2 Complete curve analysis

The hysteresis curve provides a comprehensive reflection of the seismic performance of structures, indicating deformation characteristics, stiffness degradation, and energy dissipation capacity under pseudostatic loading. The test results reveal that the columns exhibit the same failure mode, characterized by bending failure. As the load surpasses the yield point, local buckling initiates within 100 mm of the upper end of the stiffener ribs at the bottom of the specimens. Therefore, the entire loading process can be divided into three stages: the elastic stage, the elastic–plastic stage, and the failure stage. To illustrate the complete loading procedure, we use CFST-C1 as an example, as shown in Figure 8.

(1) Elastic Stage (OA): In the initial loading stage, all the columns were in the elastic stage, as evidenced by the fact that the load–deflection curves closely followed a linear trend. The residual deformation was nearly zero after unloading. The flexural stiffness of the specimens remained relatively constant during this stage, indicating that the load increased rapidly while the horizontal deflection and strain increase were limited. Subsequently, as the horizontal deflection increased, the steel tube began to yield at point A.

(2) Elastic–Plastic Stage (AB): As the imposed load reached approximately 60% of the ultimate load or when the steel tube began to yield at point A, the load–deflection curves of all the columns began to deviate considerably from their initial linearity, exhibiting elastic–plastic behavior. In this phase, visible local buckling of the steel tube initially occurred above the stiffening ribs. Subsequently, the extent

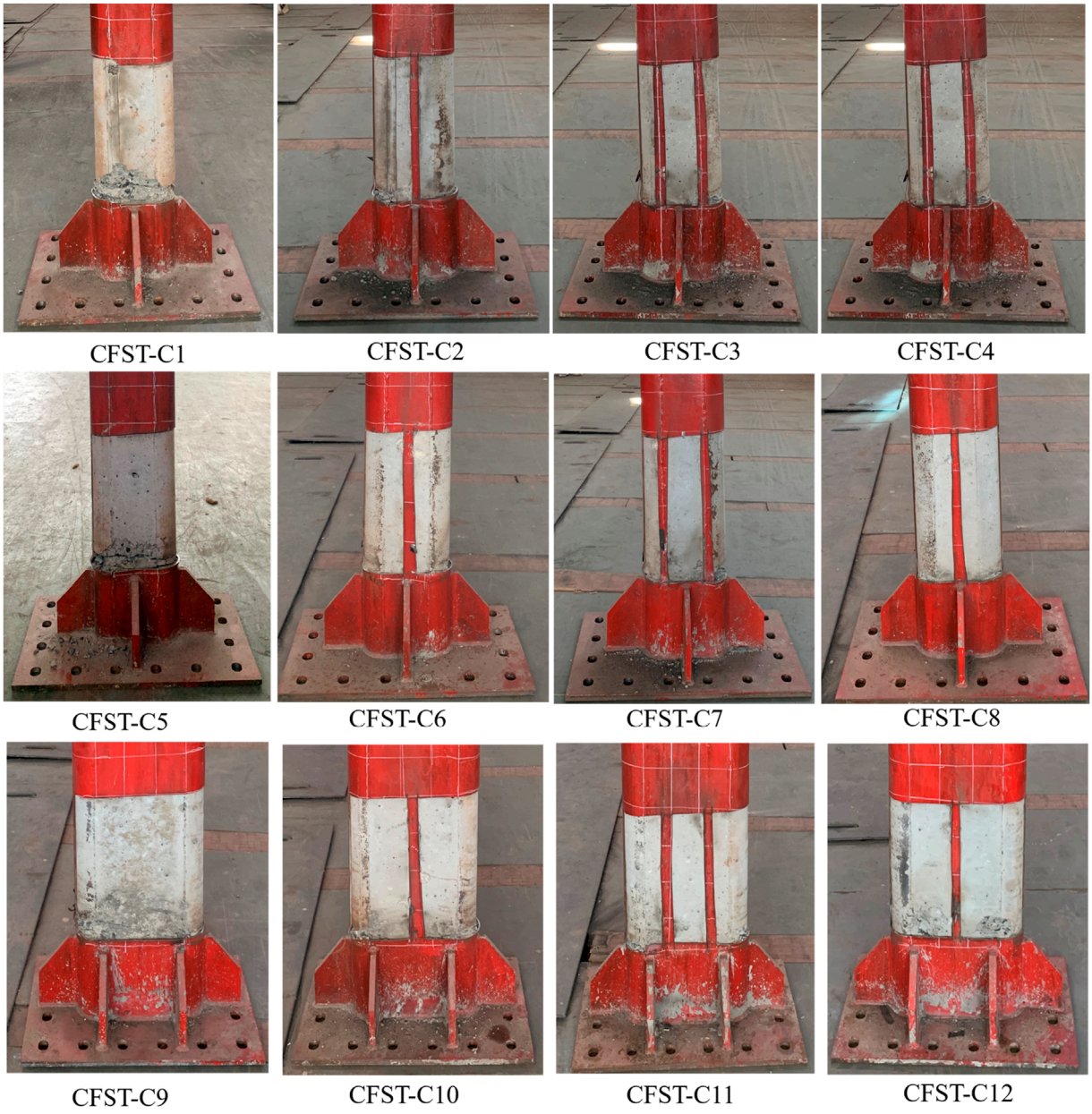

FIGURE 7
Failure modes.

and severity of local buckling increased. At this point, a slight residual displacement became evident, and the stiffness of the specimens gradually degraded. The chamber arrangement and number considerably affected the hysteretic behavior of the columns. The greater the number of chambers, the later and less pronounced the local buckling of the steel tube becomes.

(3) Failure Stage (BC): Once the ultimate bearing capacity was reached (at point B), the maximum capacity at different loading cycles continuously decreased as the loading cycles increased. The flexural stiffness noticeably decreased, and the residual displacement increased rapidly. During this stage, the local buckling of the steel tube gradually spread to both sides, eventually forming a plastic hinge region as the loading cycles increased. Theoretically, the test was terminated when the load dropped below 85% of the peak load because of the accumulated damage to the core concrete and the increased local deformation of the steel tube.

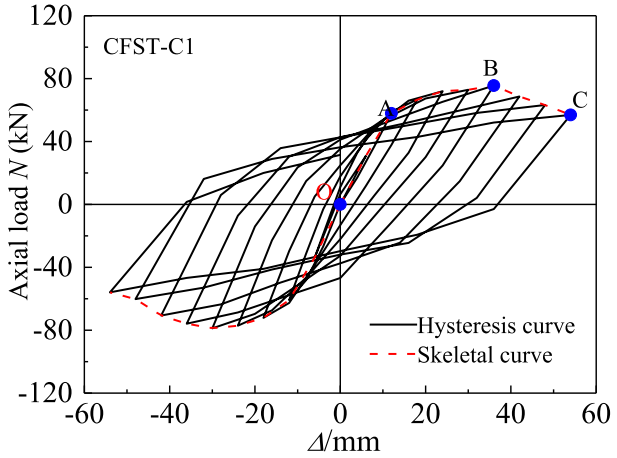

FIGURE 8
Typical skeleton curve of CFST-C1 columns under hysteretic loading.

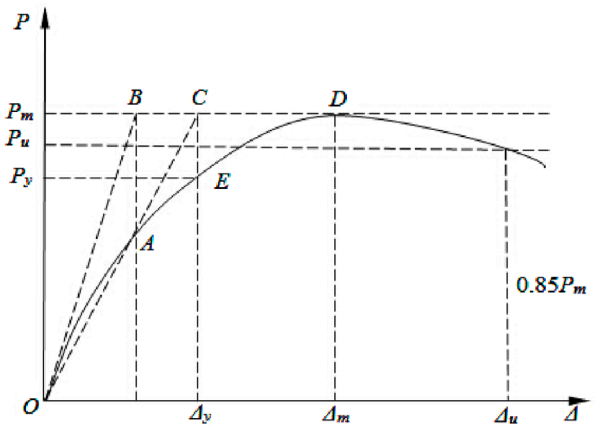

FIGURE 9
GMM method for searching the approximate yield point.

3.3 Effects of parameters on seismic property

3.3.1 Indexes for evaluating seismic performance

Horizontal ultimate bearing capacity (*P*u), displacement ductility index (*DI*), stiffness degradation (K_i), and energy absorption (*E*) are primarily analyzed in this study. The ultimate bearing capacity (P_u) is an important index for investigating the seismic behavior of the columns, as established in extensive previous research. This value can be directly obtained from the experimental results, as shown in Figure 9. All other indices are calculated from the lateral load (*P*)-deflection (*Δ*?) hysteresis and skeleton curves, which will be discussed in detail.

The displacement ductility index (*DI*) is also a critical parameter for understanding the hysteretic behavior of the columns. Therefore, it must be thoroughly investigated. *DI* is defined as the ratio

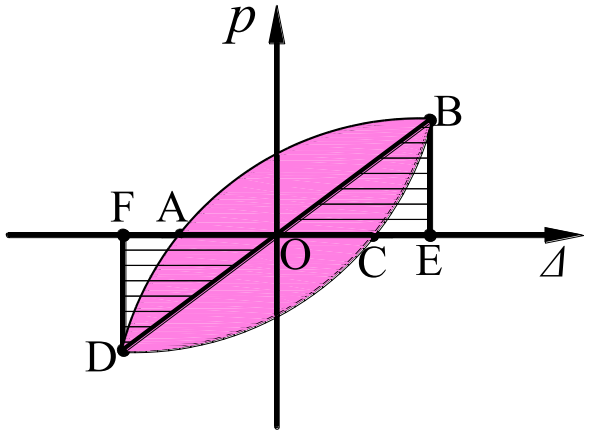

FIGURE 10
Experimental setup.

of failure displacement (Δ_u) to yield displacement (Δ_y), as shown in Eq. 1:

$$DI = \Delta_u/\Delta_y. \tag{1}$$

The general yield moment method proposed in Ref (Ding et al., 2018). Is adopted to determine the yield displacement (Δ_y) or load (P_y) for hysteretic curve envelopes without apparent yield point, as shown in Figure 9. In particular, the tangent lines of the curves at origin O and peak point D intersect at point B. A vertical line through point B intersected with a curve at point A. The line through points O and A intersected with the curve's tangent through peak point D at point C. The vertical line through point C intersected with the curve at point E, the approximate yield point. Δ_u is the ultimate displacement corresponding to the load of $0.85P_{max}$ in the postultimate stage.

Stiffness degradation refers to the phenomenon in which component stiffness decreases continuously with the increase in cycle times and displacement. Parameters such as chamber arrangement, axial compression ratio, and section width–thickness ratio affect the stiffness degradation rule of specimens. The ring stiffness of the specimen can be obtained through Eq. 2.

$$K_i = \frac{\sum_{i=1} P_j^i}{\sum_{i=1}^{n} \Delta_j^i}, \tag{2}$$

where K_i is the ring stiffness, P^i_j is the peak load for the *i*th loading cycle at the *j*th displacement ductility ratio, Δ^i_j is the corresponding peak displacement for the *i*th loading cycle at the *j*th displacement ductility ratio, and *n* is the cycle number.

The energy dissipation performance reflects the absorptive capacity of a structure under seismic load, which is usually measured by the area surrounded by the load–displacement hysteresis curve in the test. With the deformation conditions unchanged, the larger the area contained by the hysteresis curve, the better the energy dissipation performance of the specimen. Figure 10 shows the calculation figure of an equivalent viscous damping index. Many indexes can be used to measure energy dissipation

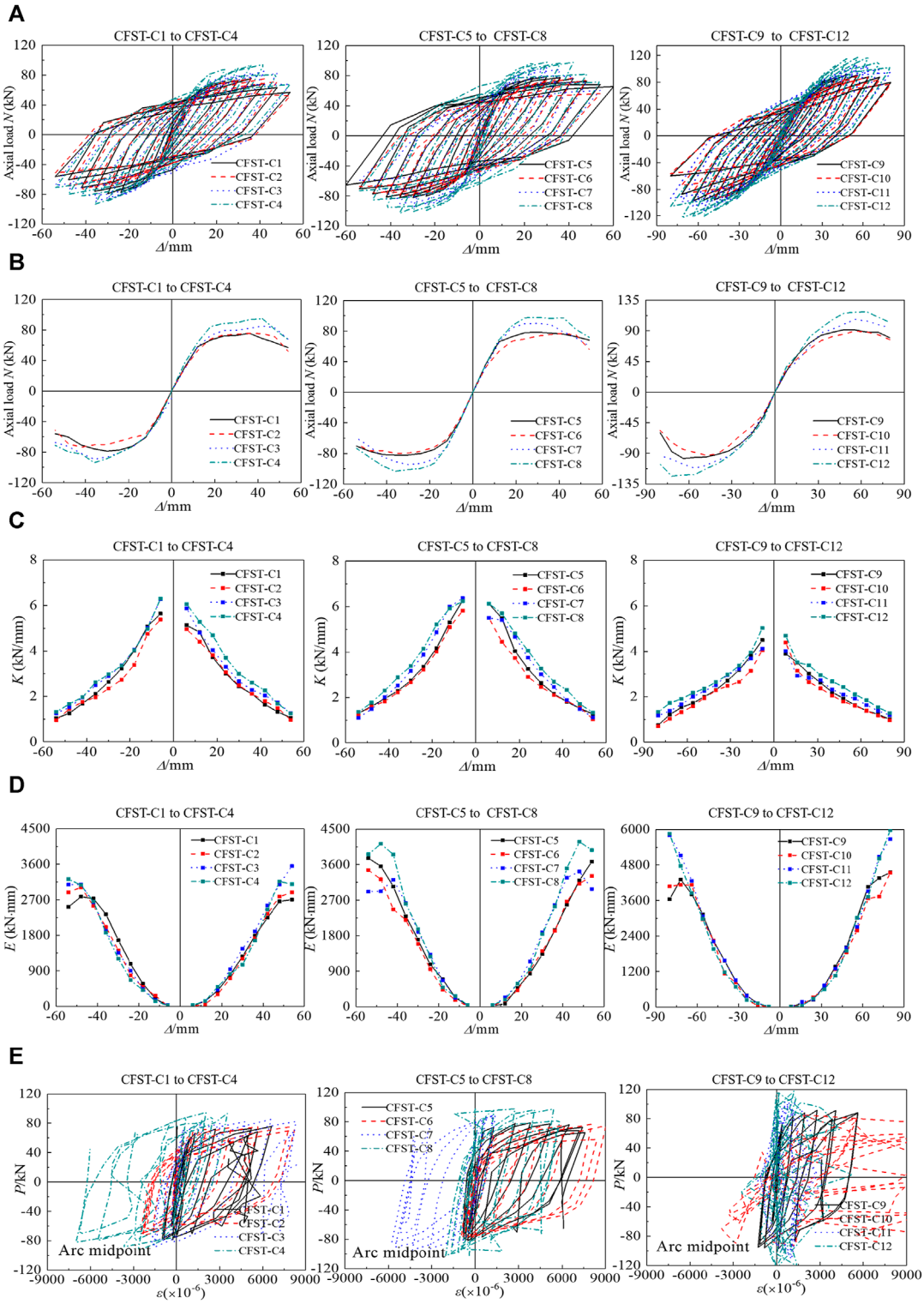

FIGURE 11
Effect of chamber arrangement on seismic property. **(A)** Hysteresis curve. **(B)** Skeletal curve. **(C)** Stiffness degradation. **(D)** Energy absorption. **(E)** Hoop strain.

capacity (e.g., energy dissipation coefficient and equivalent viscous damping coefficient). The energy dissipation factor E can be measured by the hysteretic energy dissipation in a single week, as defined in Eq. 3:

$$E = S_{ABCDA}. \tag{3}$$

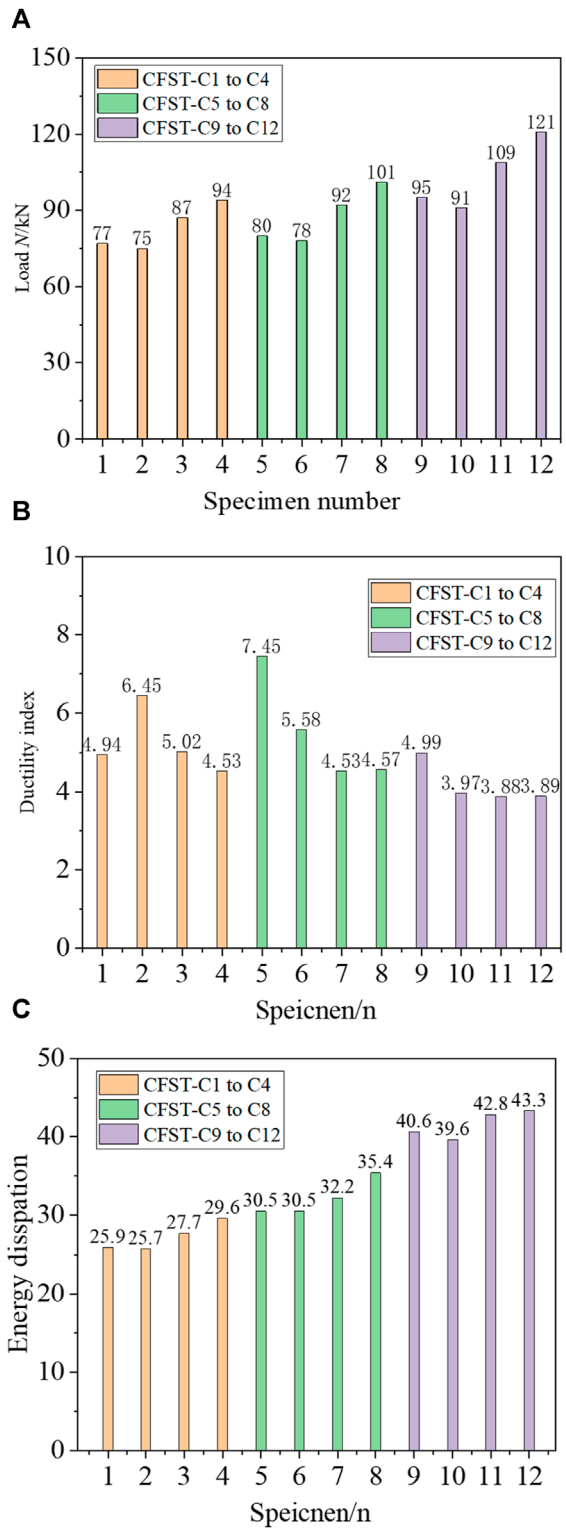

FIGURE 12
Comparisons of capacity, ductility, and energy dissipation. **(A)** Capacity. **(B)** Ductility index. **(C)** Energy dissipation.

3.3.2 Effect of chamber arrangement

Figure 11 shows the effect of chamber arrangement on seismic properties. Figure 12 illustrates comparisons of capacity, ductility, and energy dissipation index.

(1) The hysteretic curves of all specimens are relatively full, with no pinching phenomenon, indicating good seismic performance. The chamber layout considerably influences the hysteresis curve. The more chambers there are, the fuller the hysteresis curve becomes, and the better the seismic energy dissipation. The displacement ductility coefficient ranges from 3.88 to 7.45.

(2) Compared with the bending bearing capacity of single-cavity columns, three-cavity, and four-cavity columns increased by 14.7%, and 25.2%, respectively, while that of the two-cavity columns decreased by 3.1% because the intermediate steel plate in the two-chamber arrangement is located near the neutral axis in the bending area, which has minimal influence on the section's bending bearing capacity. The higher the axial compression ratio, the greater the bearing capacity.

(3) More chambers in the arrangement lead to greater elastic stiffness. The flexural stiffness could be obtained from the load–deflection curves under monotonic loading, while under dynamic cyclic loading, the flexural stiffness could be attained as the secant stiffness at 0.6 times the ultimate load using the skeletal curve. Compared with the single-cavity column, two-cavity, three-cavity, and four-cavity columns were larger by 3.1%, 11.0%, and 14.1%, respectively, because the elastic modulus of steel is much greater than that of concrete, and the increase in steel content can remarkably increase the flexural stiffness of the member. As displacement increases, the specimen's stiffness gradually decreases.

(4) The more chambers the specimen has, the greater the energy dissipation. This relationship reflects the influence of chamber layout on structural energy dissipation. Compared with the single-cavity column, the energy dissipation of the three-cavity, and four-cavity columns were larger by, 5.9%, and 11.6%, respectively. However, the energy dissipation of two-cavity columns decreased by 1.0%

(5) The midpoint of the arc is selected to minimize the influence of welding on the strain measurement points. The axial stress–strain curves of the steel tube at each point of the model exhibit certain hysteresis under different chamber conditions.

3.3.3 Effect of axial compression ratio

Figure 13 shows the effect of axial compression ratio on seismic property.

(1) The hysteresis curves of specimens with axial compression ratio n = 0.3 are fuller than those with axial compression ratio n = 0.1. The higher the axial compression ratio, the larger the bearing capacity of the specimen. The average bearing capacity of CFST-C5–CFST-C8 is 5.2% larger than that of CFST-C1–CFST-C4. A high axial compression ratio of the specimen corresponds to high stiffness.

(2) The axial compression ratio considerably influences the plastic energy dissipation of specimens. CFST-C5–CFST-C8 is 18.2% larger than CFST-C1–CFST-C4, which aligns with the full

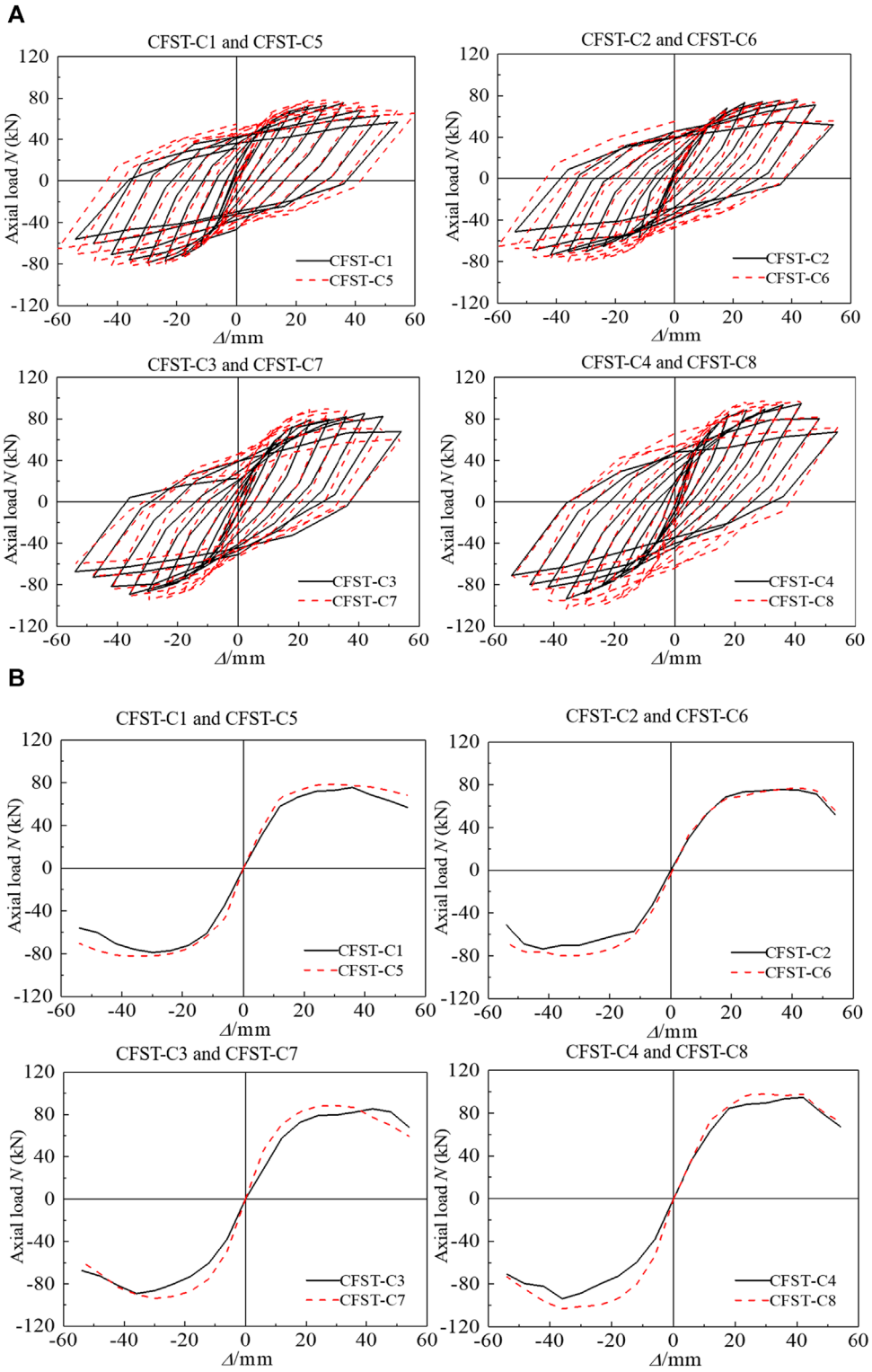

FIGURE 13
(Continued).

hysteresis curve. Increasing the axial compression ratio of specimens can enhance their seismic energy dissipation performance.

(3) The relation curve between axial compression ratio load and circumferential strain of the steel tube is displayed. In the cases of CFST-C3 and CFST-C7, under the two axial

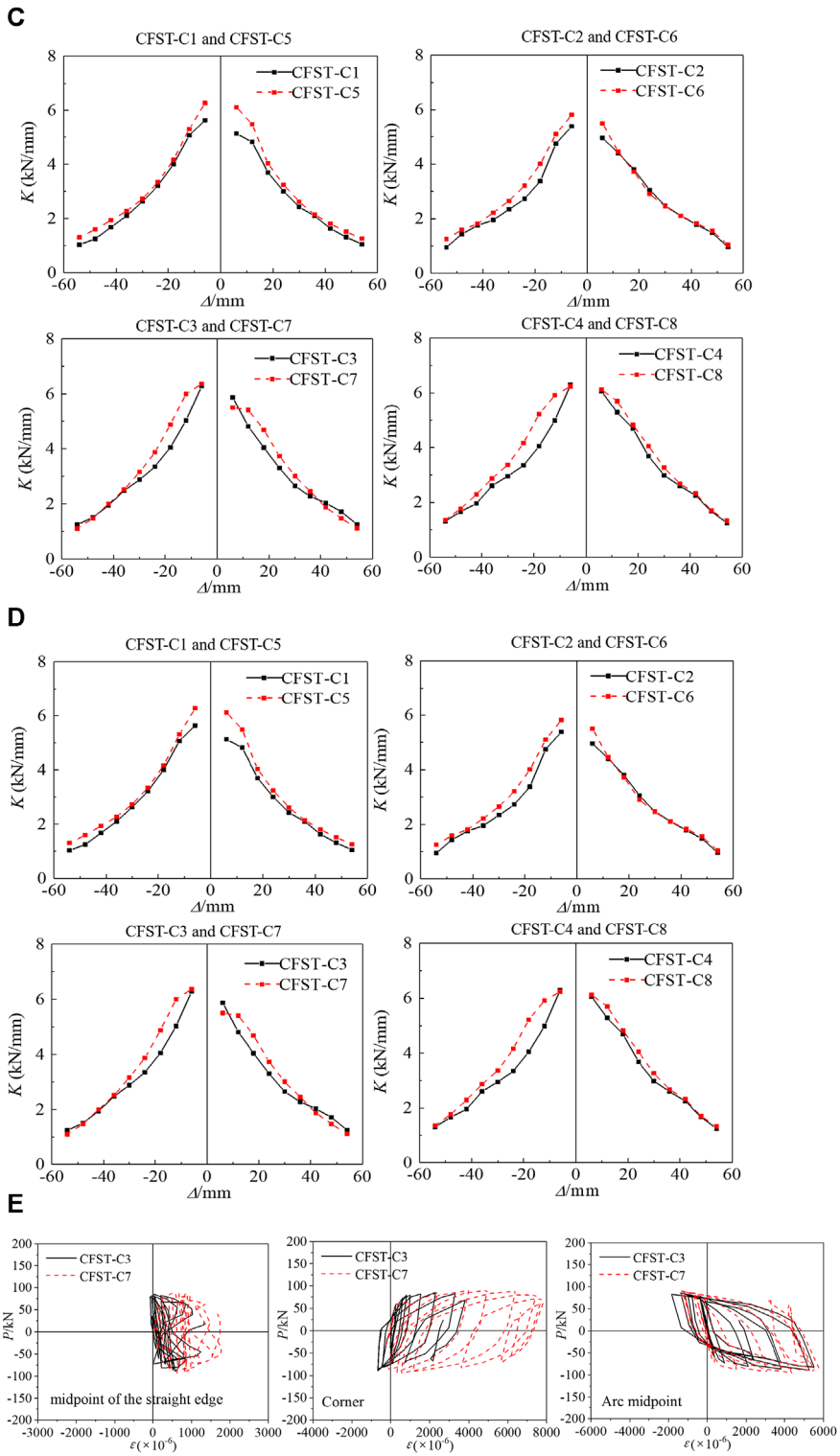

FIGURE 13
(Continued). Effect of axial compression ratio on seismic property. **(A)** Hysteresis curve. **(B)** Skeletal curve. **(C)** Stiffness degradation. **(D)** Energy absorption. **(E)** Hoop strain.

compression ratios, the axial stress–strain curves of the steel tube at each point of the model exhibit some hysteresis. The strain at the midpoint of the straight edge of the specimen is smaller than that at the corner and the midpoint of the arc of the round-ended steel tube. This finding confirms that the constraints at the arc of the steel pipe are stronger

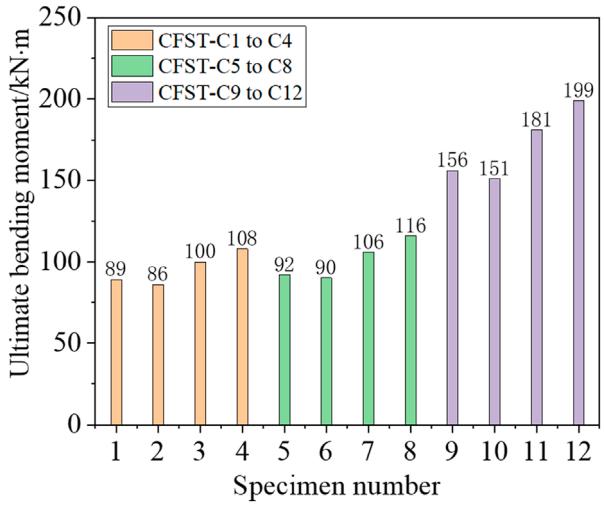

FIGURE 14
Comparisons of ultimate bending moment.

than those at the straight edge. Under low-cycle reciprocating load, the surface transverse deformation coefficient of CFST-C3 steel tube is smaller than that of CFST-C7, indicating that an appropriate increase in axial compression ratio helps improve the lateral constraint effect of the steel tube, which is consistent with the trend of increasing the bearing capacity of the specimen.

3.3.4 Effect of width–thickness ratio

The width–thickness ratios of specimens CFST-C1–CFST-C4 and CFST-C9–CFST-C12 are 2:1 and 3:1, respectively. Given the inconsistency in the height of specimens, the bending moment at the bottom of specimens is compared. Figure 14 shows the effect of the width–thickness ratio on the ultimate bending moment. The bearing capacity of CFST-C9–CFST-C12 is 75.9%, 75.4%, 79.9%, and 83.8% higher than that of CFST-C1–CFST-C4, respectively. The section width–thickness ratio considerably affects the bearing capacity of the specimen.

Figure 15 shows the effect of the width–thickness ratio on hoop strain. The results show that under low cyclic load, the surface transverse deformation coefficient of model CFST-C1 steel tube in the midpoint of the straight edge is greater than that of model CFST-C9, indicating that the larger the aspect ratio, the weaker the constraining effect of steel tube on concrete. Under different aspect ratios, the load–circumferential strain curves of steel tubes at each point of the model show certain hysteresis.

4 Conclusion

This study investigates the seismic behavior of a CFST column with a multichamber round-ended cross-section. A total of 12 composite columns were included in the experiments, and the investigated parameters included chamber layout, axial compression ratio, and section width–thickness ratio. From this study, the following conclusions can be drawn:

(1) The CFST columns with a multichamber round-ended cross-section exhibit excellent seismic performance under pseudostatic load, and the skeleton curves remain horizontal or show a weak decline section in the late loading period. The specimen showed bending shear failure, and no pinch phenomenon was observed.
(2) The more chambers arranged, the fuller the hysteresis curve and the higher the horizontal bearing capacity. The stiffness degradation trend of all specimens decreases with an increase in the number of cycles. The displacement ductility coefficient of all specimens ranges from 3.88 to 7.44, which meets the seismic design requirements.
(3) The more chambers the specimen has, the greater the energy dissipation. This relationship reflects the influence of chamber layout on structural energy dissipation. Compared with the single-cavity column, the energy dissipation of the three-cavity, and four-cavity columns were larger by 5.9%, and 11.6%, respectively. The higher the axial compression ratio, the larger the energy dissipation. The energy dissipation of CFST-C5–CFST-C8 is 18.2% larger than that of CFST-C1–CFST-C4.

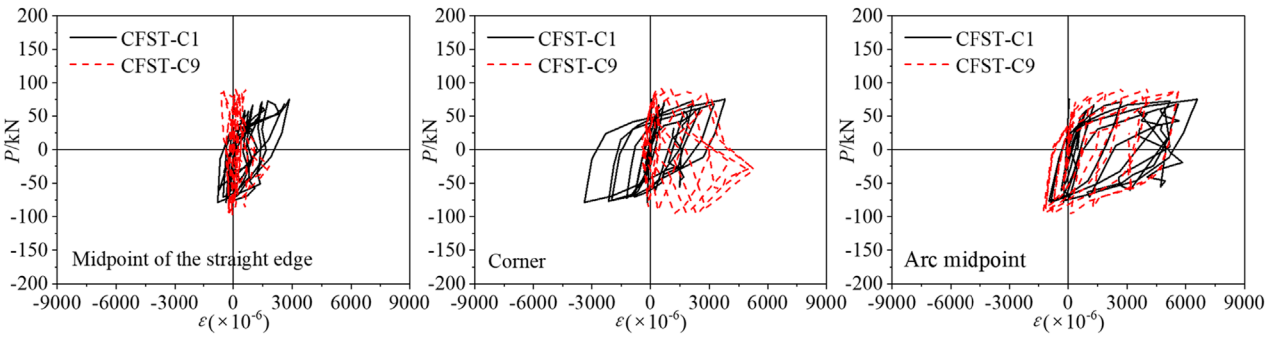

FIGURE 15
Effect of width-thickness ratio on hoop strain.

(4) Based on the test results, for multicavity confined circular CFST columns with a large length–width ratio, the chamber arrangement should bring the long and short sides closer together.

Data availability statement

The original contributions presented in the study are included in the article/Supplementary material, further inquiries can be directed to the corresponding author.

Author contributions

JL: Formal Analysis, Funding acquisition, Investigation, Methodology, Project administration, Supervision, Validation, Visualization, Writing–original draft, Writing–review and editing. WY: Data curation, Validation, Visualization, Writing–original draft. YF: Writing–review and editing. ZP: Data curation, Validation, Visualization, Writing–original draft.

Funding

The author(s) declare financial support was received for the research, authorship, and/or publication of this article. This research is financially supported by the National Natural Science Foundation of China (Grant No. 52008159), Hunan Education Department Foundation Funded Project (Grant No. 21A0504), Natural Science Foundation of Hunan Province (Grant No. 2022JJ30112), Aid program for Science and Technology Innovative Research Team in Higher Educational Institutions of Hunan Province.

Conflict of interest

The authors declare that the research was conducted in the absence of any commercial or financial relationships that could be construed as a potential conflict of interest.

Publisher's note

All claims expressed in this article are solely those of the authors and do not necessarily represent those of their affiliated organizations, or those of the publisher, the editors and the reviewers. Any product that may be evaluated in this article, or claim that may be made by its manufacturer, is not guaranteed or endorsed by the publisher.

References

Alatshan, F., Osman, S. A., Hamid, R., and Mashiri, F. (2020). Stiffened concrete-filled steel tubes: a systematic review. *Thin-walled Struct.* 148 (3), 106590. doi:10.1016/j.tws.2019.106590

Chen, H. R., Wang, L., Chen, H. T., and Cui, W. (2021). Experimental study on the seismic behavior of prefabricated L-shaped concrete-filled steel tube with rectangular multi-cell columns under different lateral loading directions. *J. Constr. Steel Res.* 177 (8), 106480. doi:10.1016/j.jcsr.2020.106480

Ding, F. X., Fu, L., Liu, X. M., and Liu, J. (2016). Mechanical performances of track-shaped rebar stiffened concrete-filled steel tubular (SCFRT) stub columns under axial compression. *Thin-Walled Struct.* 99 (2), 168–181. doi:10.1016/j.tws.2015.11.022

Ding, F. X., Liu, J., Liu, X. M., Zhi-wu, Y., and Yong-suo, L. (2018). Experimental investigation on hysteretic behavior of simply supported steel-concrete composite beam. *J. Constr. Steel Res.* 144 (5), 153–165. doi:10.1016/j.jcsr.2018.01.018

Fei, L., Goto, Y., Kawanishi, N., and Xu, Y. (2020). Three-dimensional numerical model for seismic analysis of bridge systems with multiple thin-walled partially concrete-filled steel tubular columns. *J. Struct. Eng.* 146 (1), 04019164. doi:10.1061/(asce)st.1943-541x.0002451

GJ101-2015 (2015). *Code for seismic test method of building*. Beijing, China: China Building Industry Press.

Hassanein, M. F., and Patel, V. I. (2018). Round-ended rectangular concrete-filled steel tubular short columns: FE investigation under axial compression. *J. Constr. Steel Res.* 140 (1), 222–236. doi:10.1016/j.jcsr.2017.10.030

Hu, R., Fang, Z., Benmokrane, B., and Xu, B. D. (2022a). Experimental behavior of UHPC shear walls with hybrid reinforcement of CFRP and steel bars under lateral cyclic load. *J. Compsites Constr.* 26 (2), 04022011. doi:10.1061/(asce)cc.1943-5614.0001203

Hu, R., Fang, Z., and Xu, B. D. (2022b). Cyclic behavior of ultra-high-performance concrete shear walls with different axial-load ratios. *ACI Struct. J.* 119 (2), 233–246. doi:10.14359/51734339

Qiao, Q. Y., Li, X. Y., Cao, W. L., and Dong, H. (2018). Seismic behavior of specially shaped concrete-filled steel tube columns with multiple cavities. *Struct. Des. Tall Build.* 27 (12), 1–15. doi:10.1002/tal.1485

Ren, Z. G., Wang, D. D., and Li, P. P. (2022). Axial compressive behaviour and confinement effect of round-ended rectangular CFST with different central angles. *Compos. Struct.* 285, 115193. doi:10.1016/j.compstruct.2022.115193

Shen, Q. H., Wang, F. Q., Wang, J. F., and Ma, X. (2022). Cyclic behaviour and design of cold-formed round-ended concrete-filled steel tube columns. *J. Constr. Steel Res.* 190, 107089. doi:10.1016/j.jcsr.2021.107089

Shen, Q. H., Wang, J. F., Liew, R., Gao, B., and Xiao, Q. (2020). Experimental study and strength evaluation of axially loaded welded tubular joints with round-ended oval hollow sections. *Thin-Walled Struct.* 154, 106846. doi:10.1016/j.tws.2020.106846

Wang, J. F., and Shen, Q. H. (2023). Numerical analysis and design of thin-walled RECFST stub columns under axial compression. *Thin-Walled Struct.* 129, 166–182. doi:10.1016/j.tws.2018.03.024

Wang, K. H. (2015). *Seismic research of bridge*. Beijing, China: China Railway Publishing House. (in Chinese).

Wu, H. P., Cao, W. L., Qiao, Q. Y., and Dong, H. (2016). Uniaxial compressive constitutive relationship of concrete confined by special-shaped steel tube coupled with multiple cavities. *Materials* 86 (9), 86–19. doi:10.3390/ma9020086

Wu, H. P., Qiao, Q. Y., Cao, W. L., Dong, H., and Zhang, J. (2017). Axial compressive behavior of special-shaped concrete filled tube mega column coupled with multiple cavities. *Steel and Compos. Struct.* 23 (6), 633–646. doi:10.12989/scs.2017.23.6.633

Yin, F., Xue, S. D., Cao, W. L., Dong, H. Y., and Wu, H. P. (2020). Experimental and analytical study of seismic behavior of special-shaped multicell composite concrete-filled steel tube columns. *J. Struct. Eng.* 146 (1), 04019170. doi:10.1061/(asce)st.1943-541x.0002442

Zhang, Q., and FuXu, L. L. (2020). An efficient approach for numerical simulation of concrete-filled round-ended steel tubes. *J. Constr. Steel Res.* 170, 106086. doi:10.1016/j.jcsr.2020.106086

Zhou, Z., Denavit, M. D., and Zhou, X. H. (2023). New cross-sectional slenderness limits for stiffened rectangular concrete-filled steel tubes. *Eng. Struct.* 280, 115689. doi:10.1016/j.engstruct.2023.115689

Zhou, Z., Gan, D., Denavit, M. D., and Zhou, X. H. (2022). Seismic performance of square concrete-filled steel tubular columns with diagonal binding ribs. *J. Constr. Steel Res.* 189, 107074. doi:10.1016/j.jcsr.2021.107074

Zhou, Z., Gan, D., and Zhou, X. H. (2019). Improved composite effect of square concrete-filled steel tubes with diagonal binding ribs. *J. Struct. Eng.* 145 (10), 04019112. doi:10.1061/(asce)st.1943-541x.0002400

frontiers | Frontiers in Materials

TYPE Original Research
PUBLISHED 10 July 2024
DOI 10.3389/fmats.2024.1413620

OPEN ACCESS

EDITED BY
Jianping Lin,
Huaqiao University, China

REVIEWED BY
Shan Gao,
Harbin Institute of Technology, China
Jingkuang Liu,
Guangzhou University, China

*CORRESPONDENCE
Binyu Su,
julia_721@sina.com

RECEIVED 07 April 2024
ACCEPTED 11 June 2024
PUBLISHED 10 July 2024

CITATION
Chen J, Wu H, Su B and Li W (2024), Strategies for effective reuse of waste from abandoned buildings under sustainable development . *Front. Mater.* 11:1413620.
doi: 10.3389/fmats.2024.1413620

Strategies for effective reuse of waste from abandoned buildings under sustainable development

Jie Chen[1], Hua Wu[2], Binyu Su[3]* and Weiqing Li[1]

[1]School of Arts, Xiamen University, Xiamen, China, [2]School of Art Design, Fuzhou Technology and Business University, Fuzhou, China, [3]Minnan Science and Technology College, Quanzhou, China

Introduction: In the continuous advancement of urbanization, abandoned buildings are a huge challenge in achieving sustainable development goals. If these legacy buildings are not properly handled, they will cause a huge burden on society, economy, and the environment. Based on the material flow analysis method, an evaluation index system was constructed for legacy building resources, and a systematic study was conducted on the reuse pathways of their waste.

Methods: This study focuses on the material flow, reuse pathways, and resource utilization strategies of legacy construction waste, aiming to improve the reuse efficiency of waste building materials and promote the achievement of sustainable development goals. In the study, indicator design was used to quantify the obstacles to the reuse of legacy construction waste, and social and economic costs were analyzed to ensure the comprehensiveness and scientificity of the research.

Results: The experimental results show that the waste recycling rate under the implementation of this strategy reached 82.7%, and the resource utilization rate increased by 50.1%. For the obstacles to the reuse of construction waste, the network density reaches 0.052, and the overall network structure shows a lack of concentration, indicating that the current management methods for construction waste reuse have further optimization space.

Discussion: The study effectively promotes the sustainable utilization of legacy buildings in cities, which is of great significance for improving the quality of urban space and promoting sustainable social development.

KEYWORDS

sustainable development, material flow, reuse pathways, abandoned buildings, indicator design

1 Introduction

Abandoned buildings not only solidify historical moments, but also have strong reuse value in modern urban development (Zou and Wang, 2021). In the global wave of sustainable development, the reuse strategy of abandoned buildings has become particularly important. The effective reuse of construction waste, as a byproduct of urban development, is directly related to the substantive progress of sustainable development and the closed-loop of resource recycling (McAtackney, 2022; Xu et al., 2024). Research on the material flow of construction waste can reveal its resource potential and environmental impact. The refined management of these material flows is a prerequisite for achieving the reduction

and resource utilization of construction waste (Glatt et al., 2021). The reuse approach of abandoned buildings involves specific methods of converting waste into building materials or other functional products, with the significance of endowing abandoned buildings with new vitality (Dixit et al., 2022; Shooshtarian et al., 2022). The resource utilization strategy for abandoned buildings is a macro concept that encompasses the entire process from policy formulation to technological application, aiming to optimize the reuse efficiency of abandoned buildings, reduce environmental loads, and promote coordinated development of the economy, society, and environment. Under the background of the rapid development of urbanization, the management practice of construction and demolition waste faces many challenges, among which how to efficiently reuse the remaining construction waste, reduce the impact on the environment, and achieve resource conservation and sustainable development has become a key issue to be solved. In response to this problem, the study aims to explore and solve the following research questions: 1) What deficiencies exist in current management practices of legacy construction waste, resulting in inefficient resource recovery and reuse? 2) How to identify and quantify the obstacle factors in the recycling process of legacy construction waste through a systematic method? 3) Based on material flow analysis, how to construct an effective recycling strategy for legacy construction waste to improve recycling efficiency? In order to solve the research problems, the objectives set by the research are as follows: 1) To establish a comprehensive evaluation index system to evaluate the recycling potential of the construction waste. 2) Systematically analyze the generation, collection, transportation and treatment process of construction waste through material flow analysis method. 3) Identify and quantify the main obstacles affecting the reuse of legacy construction waste, and propose targeted improvement measures.

The study is divided into four parts. The first part provides a brief overview of sustainable development strategies and the reuse of abandoned buildings. The second part elaborates on the utilization strategies of construction waste under sustainable development, including material flow analysis of construction waste, analysis of reuse barriers, and construction of waste resource utilization strategy. The third part validates the research method, including material flow analysis, networked analysis of obstacles to the reuse of abandoned buildings, and the effectiveness of the reuse strategy model. The fourth part is a summary, and outlook of the research content. The research technology roadmap is shown in Figure 1.

2 Related works

In the construction industry of modern urban development, sustainable development strategy requires a certain level of environmentally friendly materials, energy saving and emission reduction technologies and renewable energy. These methods can mainly reduce the life cycle cost and ecological footprint of buildings, thus promoting environmental protection and efficient use of resources. Some scholars have conducted relevant research on the construction engineering under the sustainable development strategy. Q. Li provided guidance on the direction of green building design based on climate friendly ideas for sustainable architectural design. Green Finance refers to financial activities that support environmental objectives such as environmental improvement, climate change mitigation and resource efficiency. It proved the effectiveness of green finance in supporting climate change adaptive design (Li, 2023). Feng et al. (2021) proposed a bi-directional green promotion framework for the application of 6G and AI technologies in green development. Two-way green promotion framework refers to the mutual promotion and common development of technologies through the integration of green technologies and emerging technologies such as 6G and artificial intelligence in the process of technology development and application. Studies have shown that this framework effectively promotes the promotion of sustainable development strategies (Feng et al., 2021). Hammond et al. (2021) proposed a multi-perspective integration theoretical model to address the low adoption rate of green buildings. The multi-perspective fusion theoretical model is a systematic analysis method that combines perspectives and theories from different disciplines to comprehensively analyze the low adoption rate of green buildings. The systematic analysis of its promotion obstacles was achieved, providing direction guidance for sustainable development (Hammond et al., 2021). Pham et al. (2023) investigated the impact of transformational leadership on sustainable development needs in the construction supply chain and developed a sustainable development supply chain framework based on transformational leadership, achieving a sustainable development strategy in the supply chain. The study demonstrated the effectiveness of the improved framework (Pham et al., 2023). Chakravarthy et al. (2022) conducted a study on management barriers and practices in sustainable development of construction projects. The sustainable development management process of construction projects was optimized, achieving a comprehensive analysis of obstacles and best practices in construction project management. The study identified obstacles and promoted the further application of sustainable development strategies in construction projects (Chakravarthy et al., 2022). Wang et al. (2024) analyzed resources for sustainable development in the construction industry. A new resource utilization framework based on competitive relationships was proposed, achieving a deep understanding of the competitive relationships in resource utilization that supported green and low-carbon transformation. Its importance in promoting sustainable development and transformation in the industry was verified (Wang et al., 2024).

In the process of urban construction and renewal, there are a large number of legacy buildings, which have various materials and Spaces that can be reused. Efficient reuse of legacy buildings can reduce environmental damage and waste of resources, thereby supporting sustainable development. Some scholars have also conducted relevant research on architectural reuse. M. A. T. Alsheyab analyzed the impact of construction waste recycling from the perspective of construction and demolition waste recycling, evaluated its impact on climate change and sustainable development, and proved that recycling activities have A positive effect on reducing environmental deterioration (Alsheyab, 2022). Umar et al. (2021) evaluated the effectiveness of implementing construction and demolition waste management practices in Malaysia, targeting the reuse management practices

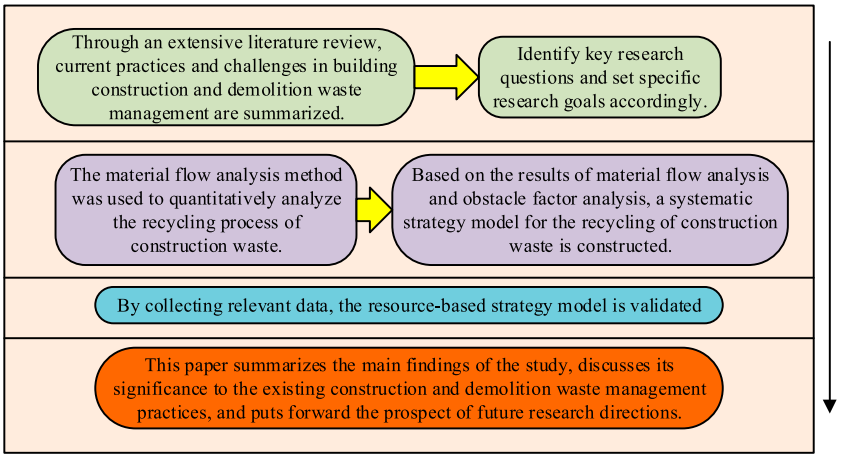

FIGURE 1
Technology roadmap.

of abandoned buildings in Malaysia. It proved the contribution of these practices to improving resource utilization and environmental protection (Umar et al., 2021). Whittaker et al. (2021) conducted in-depth research on the methods and uses of building reuse and demolition waste to improve the efficiency of abandoned building reuse. A comprehensive solution was proposed, effectively improving its reuse efficiency. The research demonstrated the effectiveness of this innovative treatment method in promoting the reuse and recycling of abandoned buildings (Whittaker et al., 2021). J. Liu proposed a policy support policy based on tax incentives to address the lack of economic benefits for enterprises in the reuse of abandoned buildings. It realized the economic benefit analysis of abandoned building reuse projects under tax incentives. Tax incentives could significantly enhance the economic benefits of recycling and reusing abandoned buildings (Liu et al., 2022). Lamba et al. (2022) studied the recycling of plastic waste in abandoned buildings based on sustainable development principles. The impact of plastic waste on the sustainable development and utilization of building materials was evaluted. This recycling and reuse had a positive impact on environmental and social sustainability (Lamba et al., 2022). Marinho et al. (2022) conducted a comprehensive analysis of the reuse and recycling practices of construction and demolition waste in Portugal. The current situation of the management practices for the reuse of abandoned buildings in the country was thoroughly evaluated, providing reference and technical support for specific practices in the reuse of abandoned buildings (Marinho et al., 2022). In order to improve the reliability of reuse of legacy buildings, J. Duan et al. (2021) proposed an ICA-XGBoost model to achieve accurate prediction of compressive strength of recycled aggregate concrete, which has been proved to be of great value in improving the use efficiency of recycled materials (Duan et al., 2021).

Some scholars have conducted relevant research on construction waste management. Liu et al. (2021), aiming at the circular economy problem in construction waste management, proposed a method combining social network analysis. In the process, the management mechanism and effect of chemical recycling were analyzed with Guangzhou as the main research area. This study provides theoretical guidance for the transformation of the construction industry from recycling to energy conservation (Liu et al., 2021). Liu J and his research team proposed a combined sorting model for the management and control of urban construction waste. In the process, the relationship between unused construction waste and carbon emissions is explored, and the carbon emission effects of different policies are collected. The experimental results provide technical support for the government to introduce construction waste management models and policies (Liu et al., 2023). Aiming at the sustainable development of the construction industry, Wang Z and other scholars put forward a method using the environmental Kuznets curve. In the process, carbon emissions of 30 provinces in China were extracted and the relationship between them and economic growth was analyzed. The experimental results provide data support for construction waste management (Wang et al., 2023).

Although existing studies have extensively explored multiple aspects of reuse of legacy buildings, including resource utilization, environmental impact assessment, and economic incentive policies, most studies focus on single-dimensional analysis, lacking systematic consideration of the whole life cycle of legacy buildings. In addition, the research on the strategy of recycling construction waste in the existing literature mainly focuses on the technical and policy aspects, while the comprehensive analysis of market mechanism and social and cultural factors is insufficient. Therefore, the paper proposes an efficient reuse strategy for legacy buildings based on sustainable development goals. Through in-depth analysis of the entire life cycle of buildings from construction to demolition, combined with existing policies and regulations, the paper analyzes the reuse obstacles of legacy buildings, and proposes targeted reuse strategies for legacy buildings. Through the implementation of these strategies, it is expected to open up new ways for the use of legacy buildings, improve their economic and environmental benefits, and contribute to the sustainable development of the city, so as to achieve multi-win social, economic and environmental benefits.

3 Reuse strategies for abandoned buildings under sustainable development

To effectively combine sustainable development goals with the reuse of abandoned buildings, a comprehensive three-step strategy is adopted in the study. Firstly, regarding the entire lifecycle of abandoned buildings, the waste material flow is analyzed. Identifying the resource consumption and generated waste in these processes can reveal potential opportunities for resource conservation and waste reduction. Then, based on existing regulations and policies, the obstacles to the reuse of abandoned buildings are analyzed. These obstacles have been systematically analyzed, aiming to find breakthroughs and develop targeted strategies for the reuse of abandoned buildings. Finally, the resource utilization strategy model for abandoned buildings is constructed. Based on the analysis results of the first two steps, a systematic reuse strategy and measures are designed to maximize the reuse of abandoned buildings, thereby implementing the circular economy.

3.1 Material flow analysis of abandoned construction waste

The waste generated during the demolition and renovation process of abandoned buildings may include recyclable materials and substances that pose potential hazards to the environment. To achieve efficient utilization of abandoned building resources and sustainable environmental development, based on the entire lifecycle of abandoned buildings, a material flow analysis of abandoned building waste is conducted, including the construction and demolition stages of the buildings. During the construction phase, the utilization efficiency of raw materials and the proportion of waste generated during construction are analyzed. In the demolition stage, the focus is on analyzing the waste material flow generated during the dismantling of the building structures and non-structural parts. Based on the data of new construction projects in a certain region from 2022 to 2023, data collection and model calculation are used to estimate the proportion of waste in different life cycle stages. The proportion of waste generated during building demolition and construction is shown in Figure 2.

Figure 2 shows the proportion of various components of waste generated during construction and demolition of buildings. During the construction phase, the proportion of waste varies from high to low, including cement, waste bamboo and wood, asphalt, steel bars, mortar, and bricks. This is because cement is one of the most commonly used materials in the construction, which is used in the production of concrete, masonry and other processes. Waste bamboo and wood come in second place, mainly from temporary facilities such as templates and scaffolding. The proportion of asphalt, steel reinforcement, mortar, and bricks is relatively low, but they are also indispensable materials in the construction process. In the stage of building demolition, the proportion increases from high to low, and the waste is concrete, bricks, mortar, metal, plastic, crushed stone, etc. In the stage of building demolition, the proportion of waste from high to low is concrete, bricks, mortar, metal, plastic, crushed stone, etc. The proportion of concrete is the highest, because concrete is the main constituent material of modern

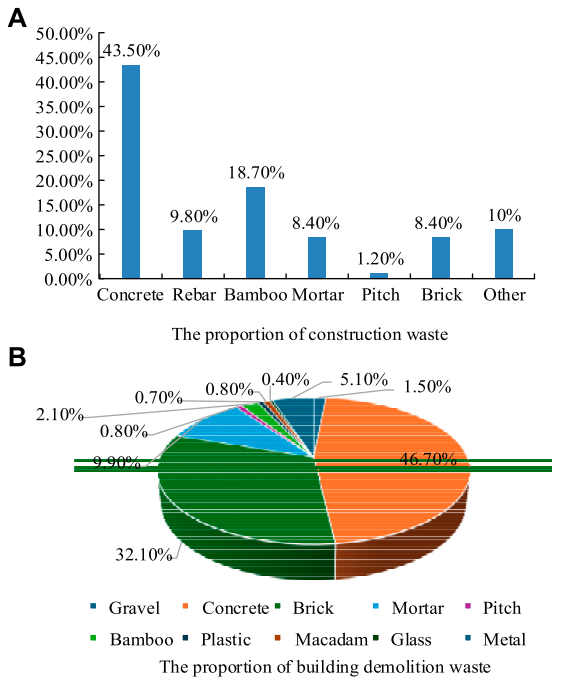

FIGURE 2
Schematic diagram of the proportion of construction and demolition waste. **(A)** The proportion of construction waste **(B)** The proportion of building demolition waste.

buildings. A large amount of concrete waste is generated during the demolition process of buildings. The proportion of waste bricks and mortar is also relatively high, which is related to the construction of the building (Oh, 2023). The materials such as metals, plastics, and crushed stones are relatively low, but they are also common materials in buildings (Ma et al., 2023). After analyzing the composition of construction waste, it can be found that there are various types and huge quantities of waste generated during the construction and demolition. If these wastes are not properly handled, they will cause serious pollution to the environment. Therefore, this study further conducts material flow analysis on the reuse of abandoned construction waste. Based on the different types of materials, they are classified into inorganic non-metallic materials, organic non-metallic materials, and metal materials. Then a framework for the material flow of abandoned building resource utilization is constructed. For inorganic non-metallic materials, physical methods such as crushing, screening, and cleaning can usually be used for pretreatment, and then converted into secondary materials suitable for new construction projects according to specific technical requirements (Shao et al., 2022). The reuse process of waste metal materials is relatively complex. For example, bamboo and wood, after being crushed and sliced, are used to make artificial boards or as biomass fuel. Plastic can be processed into new plastic products through thermoplastic processing (Lu et al., 2022). Figure 3 shows the constructed material flow framework for the resource utilization of abandoned buildings, as well as an example of the reuse of waste concrete.

Figure 3 shows the constructed material flow framework for the resource utilization of abandoned buildings, as well as an

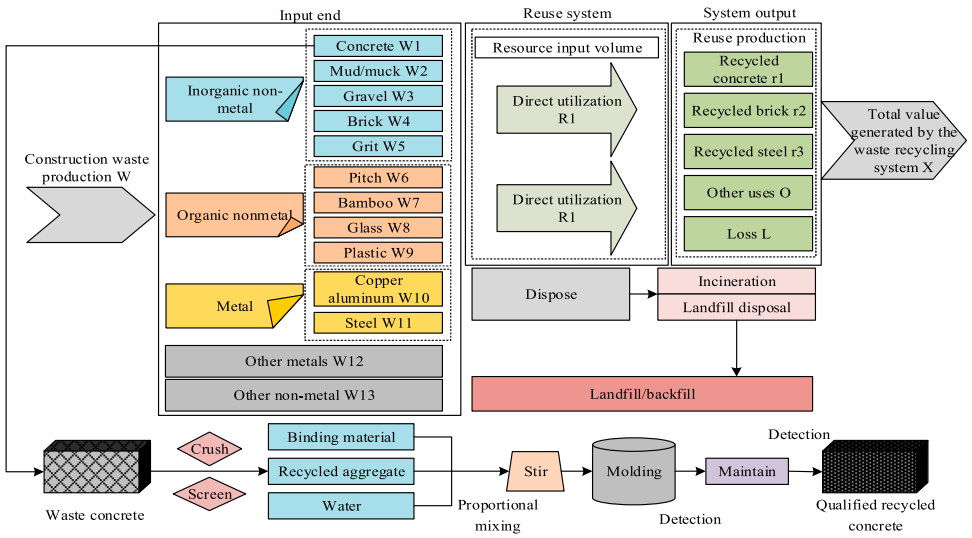

FIGURE 3
Schematic diagram of recycling process of recycled material flow frame and waste concrete for abandoned buildings.

TABLE 1 Explanation of material flow analysis and calculation formula of abandoned buildings.

No.	Index	Formula	Detail
1	System balance accounting	$System\ balance = \sum_{i=1}^{13} W_i = O + L + \sum_{i=1}^{3} r_i + C$ (1)	The input to the system is equal to the output
2	Waste production volume (W)	$W = \sum_{i=1}^{13} W_i$ (2)	
3	Reuse system waste input volume	$R1 + R2$ (3)	Mainly equal to the amount of reuse plus recycling
4	Recycling system waste recovery rate	$\frac{(R1+R2)}{\sum_{i=1}^{13} W_i}$ (4)	Mainly related to waste inventory and waste production
5	Total value generated by the waste recycling system (X)	$\sum_{i=1}^{3} r_i + O$ (5)	Mainly related to rebio yield and other uses
6	Total material output	$\sum_{i=1}^{3} r_i$ (6)	Mainly related to rebio yield
7	Reuse system loss rate	$\frac{L}{R1+R2}$ (7)	Mainly associated with mass loss level resource utilization system
8	Productivity of construction waste	$\frac{\sum_{i=1}^{3} r_i}{R1+R2}$ (8)	Related to the total value of the system and the amount of input
9	Regional construction waste production intensity	$\frac{W}{Gross\ regional\ product}$ (9)	
10	System waste conversion efficiency	$\frac{\sum_{i=1}^{3} r_i}{R1+R2}$ (10)	Related to the amount of material output and input
11	Reuse rate of construction waste	$\frac{\sum_{i=1}^{3} r_i}{\sum_{i=1}^{13} W_i - W2}$ (11)	Related to actual recycled product weight and waste production, mud/muck is not considered

example process for the reuse of waste concrete. Among them, waste concrete is first crushed and screened to obtain recycled aggregates, then added with cementitious materials and water, and mixed and stirred in proportion to form. After passing the test, recycled concrete with useable value can be obtained (Nagalli et al., 2021; Usman and Abdullah, 2023). To refine the material flow analysis of abandoned buildings and further calculate their main indicators in detail, the specific calculation formulas and explanations are shown in Table 1.

In Table 1, all variables correspond to Figure 3. Among them, W_i represents the corresponding waste. r_i represents recycled products. L represents loss. C represents backfilling, In material flow analysis, backfilling refers to the process of reusing construction waste, where a portion of the material may not be directly used for new construction projects or other purposes due to various reasons, but instead be used to backfill the land, which usually occurs at construction sites or other places (Gao et al., 2021). By calculating the backfill rate, it is possible to understand the proportion of

materials in the reuse system that are not effectively utilized but are treated as waste. X represents the total value generated by the waste recycling system. $R1$ represents direct utilization. $R2$ represents indirect utilization. $\sum_{i=1}^{13} W_i$ represents the sum of the masses of 13 types of waste. $\sum_{i=1}^{3} r_i$ represents the sum of the quality of the three recycled products. Material flow analysis of abandoned buildings can comprehensively understand the types, quantities, and potential value of materials contained within them. The results of material flow analysis can provide important basis for the reuse plan of abandoned buildings. Mastering information on the types, quantities, and quality of recyclable materials can develop targeted recycling plans, and select appropriate recycling pathways and processing techniques. Then, to further improve the efficiency and effectiveness of the reuse of abandoned buildings, an analysis is conducted on the obstacles that may be encountered during the reuse process.

3.2 Analysis of obstacles to the reuse of abandoned buildings

To fully evaluate the obstacles to the reuse of abandoned buildings, this study conducts a semi-structured analysis based on current literature, starting from stakeholders. Firstly, through a systematic review of existing literature, it is possible to comprehensively understand the research status and progress of the reuse of abandoned buildings, thereby identifying the key influencing factors in the process of reuse of abandoned buildings (Gao et al., 2023). Analyzing the content and implementation effects of these policies can identify the advantages and disadvantages of existing policies, and propose targeted improvement suggestions. Once again, the industrial structure and market environment involved in the reuse of abandoned buildings also need to be considered. Understanding the characteristics and interrelationships of each link in the industrial chain can identify the opportunities and challenges faced by the reuse of abandoned buildings, evaluate their commercial feasibility and promotion prospects. This analysis specifically includes government, design units, material suppliers, construction units, transportation units, demolition units, resource reuse enterprises, waste landfills, research institutes, and the public. The specific obstacles to the reuse of abandoned buildings are shown in Table 2.

A comprehensive and systematic analysis of the obstacles to the reuse of abandoned buildings can identify specific problems at multiple levels, including regulations, economy, technology, and socio-culture. Then, to effectively promote the resource utilization of abandoned buildings and fully tap into their social, cultural, and economic potential, this study further constructs a strategy model for the resource utilization of abandoned buildings.

3.3 Construction of resource utilization strategy model for abandoned buildings

To promote the efficient reuse of abandoned building resources, considering the increasingly severe global problems such as resource depletion and environmental pollution, combined with the analysis of material flow and reuse obstacles of abandoned buildings, a strategy model for the resource utilization of abandoned buildings is constructed. Based on the principles of resource conservation and environmental friendliness, the fundamental difference between traditional linear economy ("take-make-use-waste" model) and circular economy (emphasizing resource regeneration and recycling) is considered. To promote sustainable development, a strategy model for resource utilization of abandoned buildings based on circular economy is constructed. Figure 4 shows the process of traditional linear economy and circular economy.

Figure 4 shows the process of traditional linear economy and circular economy. The main difference between traditional linear economy and circular economy lies in the utilization and processing mode of resources. In the traditional linear economic model, the resource follows a unidirectional order of "extraction-manufacturing-use-disposal". This model has led to the consumption and waste of a large number of resources, environmental pollution and permanent loss of resources. In the circular economy, the principle of "reduction-reuse-recovery-regeneration" is mainly followed. It breaks through the traditional linear economic model, emphasizing the maximization of resource utilization and circular reuse throughout the entire industrial chain. The effective recycling and reuse of resources are considered in the product design stage. After the end of the product's service life, resources can be reused through remanufacturing, repair, or recycling, forming a closed-loop system to minimize resource loss and environmental impact. Therefore, the study combines circular economy to construct a business model for the resource utilization of abandoned buildings, as shown in Figure 5.

As shown in Figure 5, in order to promote the resource utilization of construction waste in the circular economy system, overcome obstacles such as logistics, costs, and regulations, an innovative business model has been proposed. Enterprises should establish cooperation with all parties in the supply chain, including transportation, equipment supply, scientific research and construction units, to ensure raw material supply, reduce costs, promote technological innovation, and sell recycled products. At the same time, by creating interdisciplinary R&D departments and combining academic, industrial, and government resources, we promote knowledge transfer and technological progress. Promote prefabricated buildings to achieve rapid material recycling and closed-loop utilization. Utilize information platforms such as BIM to achieve data sharing and quantitative management of the entire industry chain. Provide cost-effective products for different market segments while creating social value, including land conservation, environmental protection, environmental awareness enhancement, and promoting industrial development. Adopt customized cooperation and marketing strategies, such as strategic alliances, public-private partnerships, and point discounts, to maintain customer relationships. To ensure the effective reuse of abandoned buildings and achieve maximum resource utilization, promote sustainable environmental development, and respond to the concept of circular economy, promote a win-win situation between economic benefits and environmental protection, the reuse and promotion strategy

10.3389/fmats.2024.1413620

TABLE 2 Details of barriers to reuse of abandoned buildings.

Related object	Serial number	Obstacle factors	Related object	Serial number	Obstacle factors
Government	G1	Lack of regulation	Transportation enterprise	T2	Lack of control
	G2	Lack of commitment		T3	Lack of circularity
	G3	Lack of vision	Demolition enterprise	E1	Lack of site supervision
	G4	Lack of data		E2	Lack of sort processing
	G5	Lack of quality standards		E3	Lack of circularity
	G6	Lack of regulation	Reuse enterprise	R1	Lack of raw materials
	G7	Lack of usage rules		R2	Invalid processing
	G8	Lack of policy support		R3	Equipment limitation
	G9	Lack of publicity		R4	Blind production
	G10	Lack of official demonstration		R5	Lack of integration strategy
Architect	D1	Lack of green design		R6	Fund shortage
	D2	Lack of circularity		R7	Excessive cost
Material supply	M1	Lack of production responsibility		R8	Size limitation
	M2	Lack of circularity		R9	Unreasonable price
Construction unit	C1	Lack of reuse		R10	Higher admission fees
	C2	Lack of recycled product quality		R11	Unreasonable site selection
	C3	High regeneration cost		R12	Lack of publicity
	C4	Lack of circularity	Landfill	L1	Space problem
Construction organization	O1	Lack of construction standards		L2	Lack of circularity
	O2	Lack of recycling	Scientific institute	S1	Funding problem
	O3	Exorbitant cost		S2	Lack of research
	O4	Lack of sort processing		S3	Lack of cycle planning
	O5	Lack of regeneration		S4	Lack of loop optimization
	O6	Lack of recycled product quality		S5	Lack of research on barriers
	O7	Excessive regeneration price	The public	P1	Lack of quality recognition
	O8	Lack of regeneration		P2	Biased primary material
Transportation enterprise	T1	Direct landfill		P3	High regeneration price

of abandoned buildings has been deeply analyzed. Therefore, starting from the three main subjects, the study analyzes the promotion strategies for the reuse of abandoned buildings, as shown in Figure 6.

Based on the analysis of the reuse of abandoned buildings, to effectively promote the recycling of resources, improve environmental quality, stimulate economic vitality, and ensure the protection and inheritance of cultural heritage, this study combines

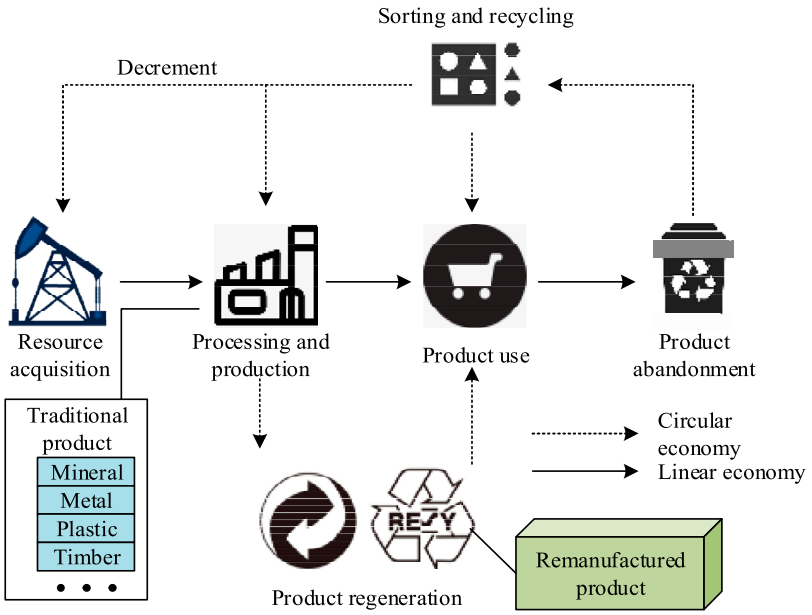

FIGURE 4
Schematic diagram of traditional linear economy and circular economy process.

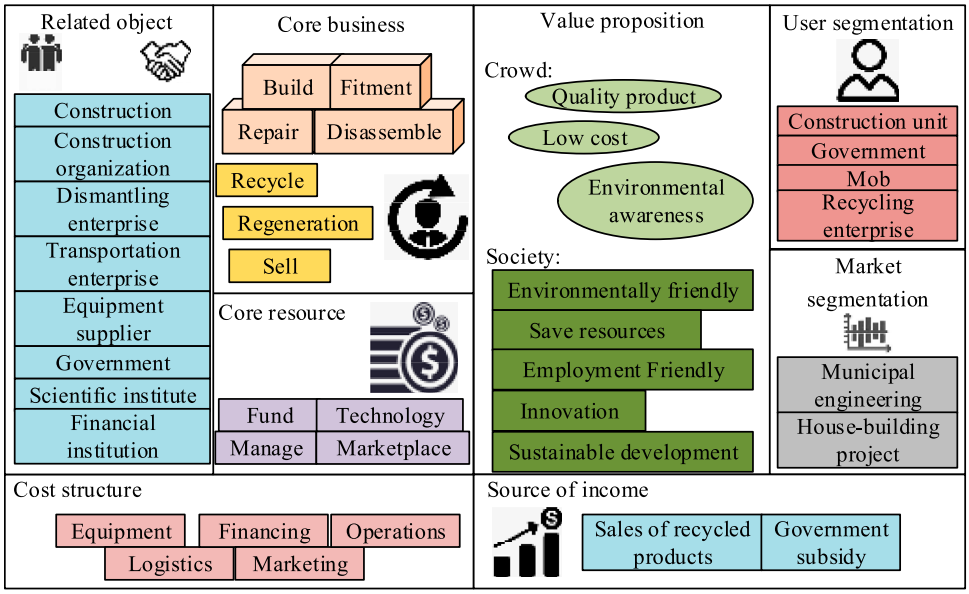

FIGURE 5
Schematic diagram of the business model of recycling of abandoned buildings.

the perspective of the government to construct a phased strategy model for the reuse of abandoned buildings. It is specifically divided into production stage, recycling stage, reuse stage, and promotion and use stage. The specific reuse strategy model for the constructed abandoned buildings is shown in Figure 7.

Figure 7 shows a strategy model for the reuse of abandoned buildings. The goal of the strategic model is to achieve efficient recycling and reuse of construction waste, reduce the impact of waste on the environment, and transform it into valuable resources. Firstly, in the production stage, the main sources of waste are construction, demolition, and decoration. After on-site classification and sorting, it enters the recycling stage and arrives at the landfill and resource utilization enterprises through transportation enterprises. In the recycling stage, with the support of equipment manufacturers, research institutes, and testing institutions, renewable resource products are produced. Finally, it is transported to the construction unit, and the public. The reuse of residual construction waste is completed.

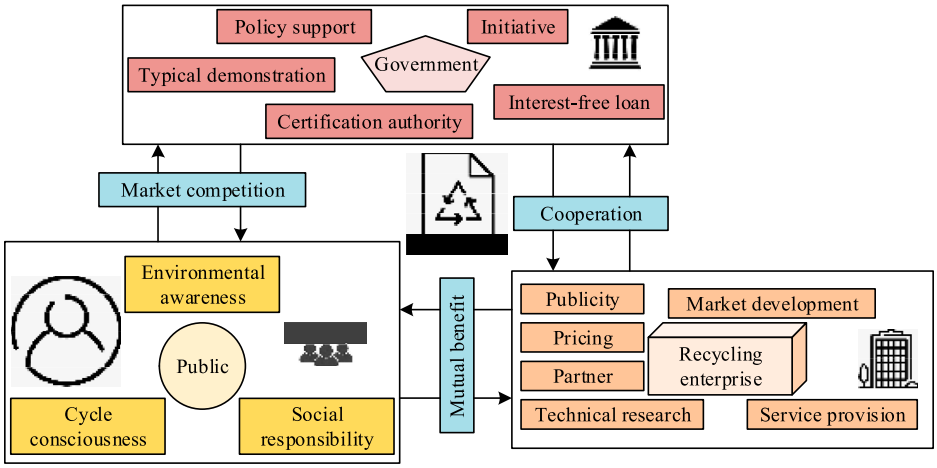

FIGURE 6
Analysis diagram of the reuse and promotion strategy of abandoned buildings based on the three main bodies.

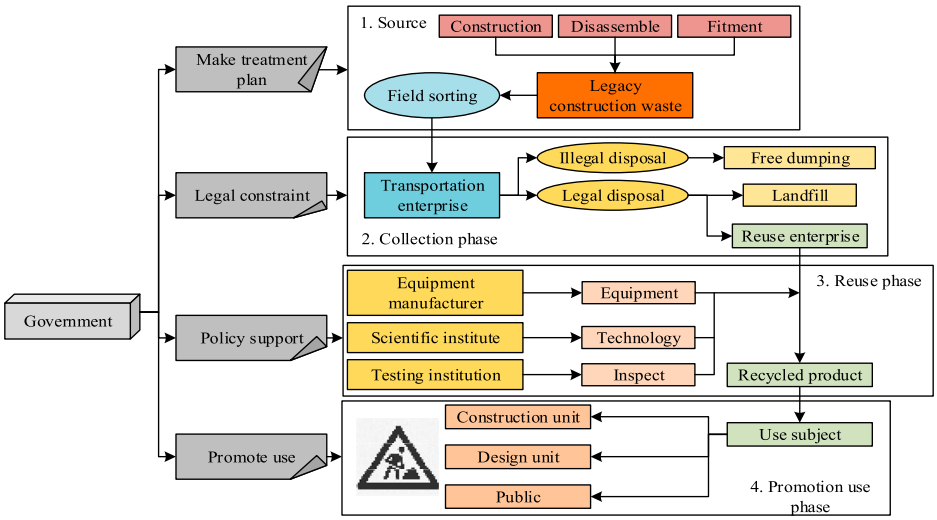

FIGURE 7
Schematic diagram of reuse strategy model for abandoned buildings.

4 Verification of the resource utilization strategy model for construction waste

4.1 Material flow analysis of abandoned construction waste

To better understand the potential of the flow and recycling of leftover construction waste, considering the limited resources and environmental protection needs, this study conducts material flow analysis of leftover construction waste based on the principles of circular economy. To obtain the data, statistical data and official reports published by government agencies and construction industry associations were collected. Through on-site research, first-hand data were obtained directly from construction sites, waste treatment centers and recycling enterprises, including the types, quantities and disposal methods of waste. Through literature review, academic studies, case studies and theoretical models related to construction and demolition waste management are collected, which provide theoretical basis and empirical data from previous studies. The collected data will be integrated and cross-verified to ensure the consistency and accuracy of the data, and then the statistical analysis method is used to conduct in-depth analysis of the data. The professional SubStance Flow Analysis software is used to analyze the flow in construction waste systems. Based on the constructed classification system above, statistical analysis is conducted on the flow of waste at different treatment stages. A detailed analysis of the material flow of construction waste is shown in Figure 8. From Figure 8, there was significant room for optimization in the current reuse pathways of construction waste.

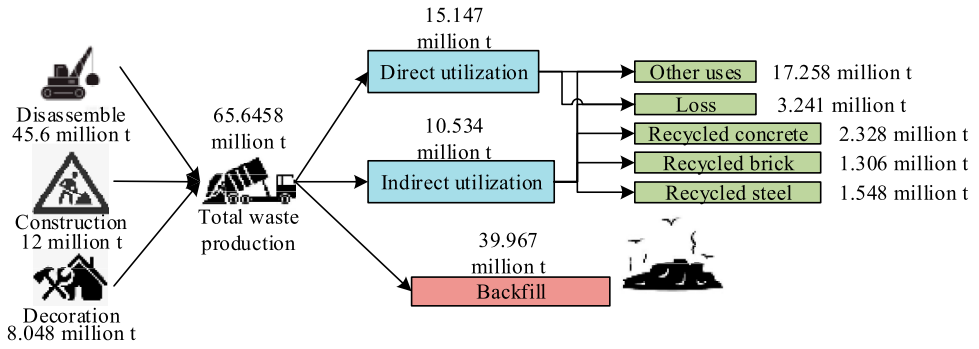

FIGURE 8
Schematic diagram of material flow analysis of construction waste.

Based on the above analysis, it is possible to conduct a thorough analysis of the material flow of construction waste. On this basis, effective management strategies are formulated to improve resource recycling and minimize environmental impact.

4.2 Network analysis of recycling barriers for abandoned construction waste

This study further delves into the problems and potential improvement opportunities in the recycling network of construction waste. Considering the complex relationships and interactions among participants in the network, Ucinet6 software is used to conduct a detailed quantitative analysis for the network indicators of obstacles to the recycling of construction waste, and to visualize the network relationships. The first step in conducting centrality analysis on Ucinet6 is to ensure that network data is correctly imported into Ucinet6, and necessary cleaning and formatting have been carried out. Secondly, select appropriate centrality indicators based on the research objectives. Then, select the corresponding command or tool in Ucinet6 to perform centrality analysis. At the same time, analyze the results of centrality indicators and identify key obstacles in the network. Finally, use Ucinet6's visualization tools to display the analysis results, helping to intuitively understand the network structure and the role of obstacles.

Ucinet6 quantifies the importance and influence of various obstacles in the network by calculating indicators such as degree centrality, proximity centrality, and betweenness centrality. Degree centrality determines the influence of nodes based on their number of connections, and is applicable to both undirected and directed graphs; Proximity centrality measures the average distance between a node and all other nodes in the network, reflecting the speed of information dissemination; Quantify the intermediate frequency of nodes in the shortest path of the network based on betweenness centrality, and identify the role of bridges; PageRank is based on the random walk algorithm, considering the link relationships and importance transfer between nodes. As shown in Table 3.

Table 3 shows the degree centrality, proximity centrality, betweenness centrality, and PageRank values of obstacles, all presented to two decimal places. The cost issue scored 0.41 on degree centrality, indicating a significant direct connection with other obstacles in the network. The betweenness centrality of regulatory restrictions is 0.52, indicating its pivotal role in information flow. The PageRank value for the cost issue is 0.52, confirming its importance in the network. Although the market acceptance score is 0.24 in terms of degree centrality, its PageRank value of 0.32 indicates that its influence cannot be ignored. In Figure 9, the network analysis of the obstacles to the recycling of construction waste is presented. From Figure 8, the five obstacles with high centrality are O5, C1, R1, T1, and O4, respectively, from high to low. Among them, O5 indicates a lack of reuse awareness in construction organization. C1 refers to the lack of direct reuse by the construction unit. R1 indicates a shortage of raw materials in the recycling industry. T1 is the direct landfill behavior of transportation enterprises. O4 indicates a lack of classification in construction organization.

Then, to further identify and understand the key obstacles and their interactions that affect the recycling process of construction waste resources, the centrality values of each obstacle factor are tested and analyzed. Centrality analysis is an important social network analysis indicator that can be used to evaluate the importance of a node in a network. A high centrality indicates that it can have a greater impact on the overall information flow of the network. The test results are shown in Figure 10. From Figure 10, the center value of O8 was the highest, far greater than the second ranked node. C1 and O2 were second. In practice, the focus should be on analyzing O8, which is the lack of reuse behavior in construction organization.

To effectively solve the problems in the recycling process of construction waste resources and optimize the efficiency of the entire system, based on the obtained data, the correlation between obstacle factors is calculated. Obstacle factors are subjected to network clustering. Network clustering can help identify groups of obstacle factors with similar features or strong correlations, thereby providing strategic basis for the structural optimization and obstacle removal of the entire resource recovery network. The study conducted correlation analysis on 54 obstacles to the resource utilization of construction waste using the CONCOR program of Ucinet software, and then implemented clustering processing. This process divides obstacle factors into eight different groups based on the similarity of network structure. The equivalence of the positions of obstacle factors within each group in the network indicates that they are structurally similar.

TABLE 3 Centrality analysis data.

Obstacle name	Degree centrality	Proximity centrality	Betweenness centrality	PageRank
Regulatory restrictions (A)	0.37	0.68	0.52	0.47
Technical limitations (B)	0.28	0.59	0.39	0.35
Cost issue (C)	0.41	0.71	0.63	0.52
Lack of awareness (D)	0.34	0.64	0.47	0.41
Market acceptance (E)	0.24	0.56	0.29	0.32

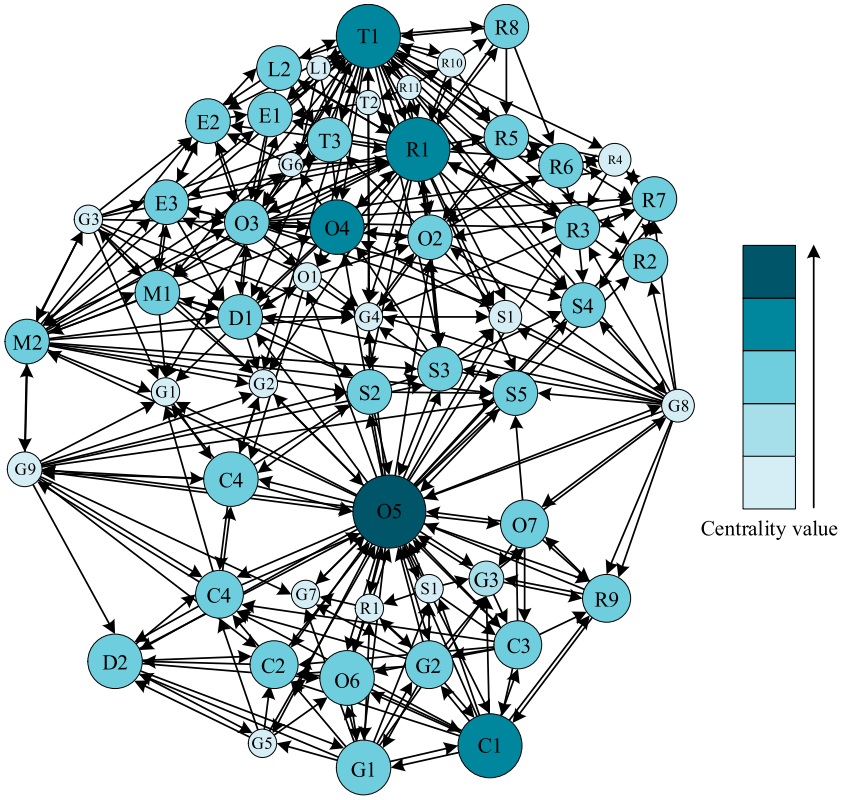

FIGURE 9
Network analysis of barriers to recycling of abandoned construction waste.

The specific clustering of obstacle factor networks is shown in Table 4.

To further understand the distribution and overall impact of obstacle factors in the recycling of construction waste resources, based on the completed network clustering, Ucinet 6 software is used to analyze the density matrix of obstacle factors. The density matrix of obstacle factors is shown in Table 4. From Table 4, the correlation between Zone B and Zone C was the highest, followed by Zone B and Zone D. Meanwhile, the network density was 0.052, but the concentration was insufficient. The Ucinet software automatically calculates key indicators such as network density, and users only need to input network data. In this study, the software determined a network density value of 0.052, indicating that the actual number of edges is much lower than the potential maximum value, indicating that the network structure needs to be optimized and may lack centralized coordination. To gain a deeper understanding of this value, it should be compared to the density values of other networks in the literature: a high-density value close to 1 indicates a concentrated network, while a low-density value indicates loose network connections. The low density value of this study reflects that although there are connections between nodes, the overall connectivity is insufficient, which may weaken the information flow and coordination efficiency of building waste resource utilization. The density matrix of specific obstacle factors is detailed in Table 5. The density matrix of obstacle factors is shown in Table 5.

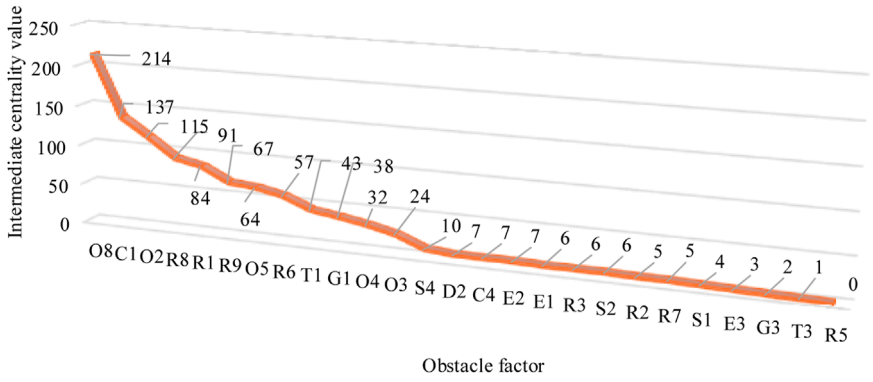

FIGURE 10
Centrality analysis of barriers to reuse of abandoned buildings.

TABLE 4 Network node partition of barriers to reuse of abandoned buildings.

Subzone	Include obstacles
Zone A	G1, G2, G9, G4, G8
Zone B	G7, G5, G10, R12
Zone C	D2, C2, C4, O8, P2, C1, P1, O6, O5
Zone D	R9, P3, C3, O7
Zone E	G6, R11, G3, L1, T2, R10, O1
Zone F	R8, R6, O2, T3, R5, T1, E1, E2
Zone G	O3, L2, O4, RI2, RI3, RI1, D1, E3, M1, M2, RI4, RI5
Zone H	R1, R4, R7, R2, R3

TABLE 5 Network node density matrix of barriers to reuse of abandoned buildings.

-	A	B	C	D	E	F	G	H
A	0.000	0.000	1.262	0.912	0.000	1.142	1.569	0.396
B	0.000	0.000	2.457	1.597	0.000	0.000	0.000	0.000
C	0.000	0.000	0.872	0.099	0.000	0.024	0.049	0.000
D	0.000	0.000	0.821	1.502	0.000	0.000	0.000	0.000
E	0.000	0.000	0.039	0.000	0.000	0.721	0.392	0.357
F	0.000	0.000	0.000	0.000	0.000	0.527	0.069	0.912
G	0.000	0.000	0.000	0.000	0.000	0.129	0.114	0.279
H	0.000	0.000	0.000	0.000	0.000	0.316	0.000	0.668
Network density = 0.052								

To comprehensively evaluate and solve the obstacles in the recycling leftover construction waste, as well as their relative positions and roles in the overall network, the image matrix of the obstacle factor network is further analyzed. The image matrix analysis of obstacle factors is shown in Figure 11. From Figure 11, zones A, B, and E were the core locations, which had a significant impact on the obstacle factor network.

4.3 Analysis of the recycling rate of residual construction waste

To verify the actual effectiveness of the optimization scheme for the recycling of construction waste resources proposed in the research, a quantitative analysis is conducted on the recycling rate based on current data to measure the effectiveness of the optimization measures. The analysis results are shown in Figure 12. From Figure 12, after implementing the optimization scheme, the recovery rate reached 82.7%, indicating that the scheme has substantially improved the resource recovery efficiency of construction waste. In addition, the growth rate of recycling rate also showed a rapid improvement, reflecting the positive driving force of optimization measures in promoting resource recovery. Compared with traditional schemes, the increase in recovery rate reached 67.4%. This significant improvement demonstrates the enormous potential and practical benefits of the optimization scheme.

4.4 Analysis of resource utilization rate of construction waste

To comprehensively evaluate the effectiveness of the optimization scheme in improving the resource utilization of construction waste, a quantitative analysis is further conducted on the resource utilization rate. The analysis results are shown in Figure 13. After implementing the optimization scheme, the resource utilization rate significantly increased to 92.7%, indicating

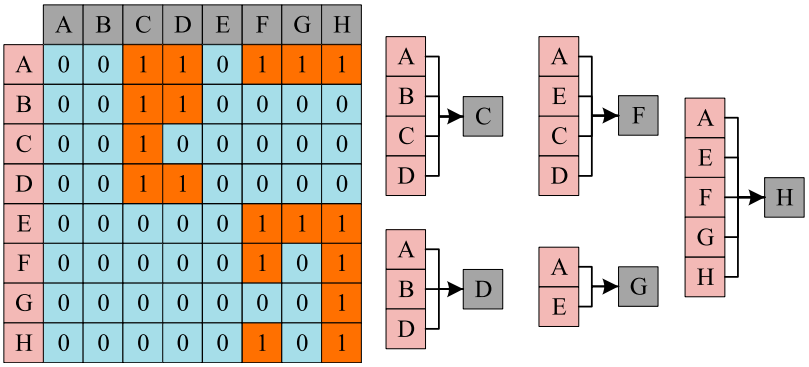

FIGURE 11
Network image matrix of barriers to reuse of abandoned buildings.

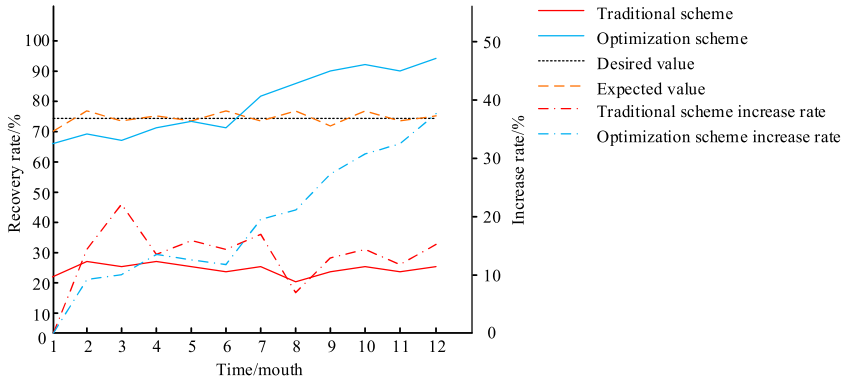

FIGURE 12
Recovery rate test of construction waste.

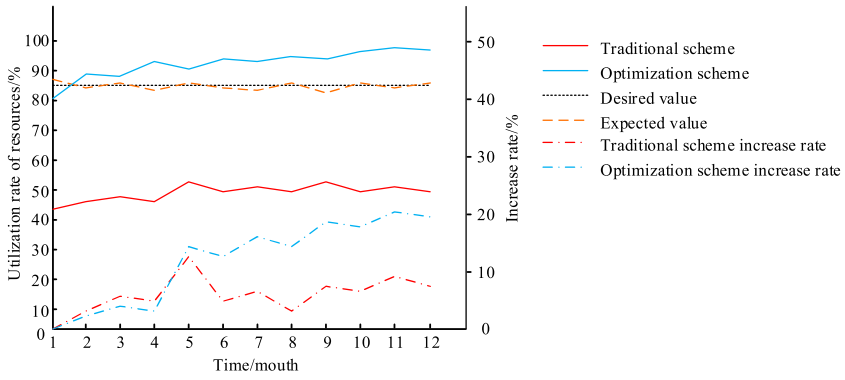

FIGURE 13
Resource utilization test of residual construction waste.

that the plan efficiently converted waste into useful resources. Compared with traditional solutions, it has increased by 50.1%, demonstrating the enormous potential of the optimization scheme in optimizing resource circulation and enhancing environmental sustainability.

4.5 Discussion

The research is supported by the theory of circular economy, which holds that by reducing resource consumption and waste generation, and promoting resource reuse and recycling, economic

activities can be sustainable. Through the material flow analysis and the construction of the resource strategy model, the theory of circular economy provides the theoretical basis for the analysis of the construction and demolition waste management practice, and guides the construction of the resource strategy model. The research results show that by optimizing the sorting, collection and treatment of building construction and demolition waste, the maximum utilization of resources and the minimization of environmental impact are achieved, which echoes the multi-perspective fusion theoretical model proposed by Hammond et al. (2021), which comprehensively analyzes the low adoption rate of green buildings through a systematic analysis method. The study also draws on other scholars' research on the obstacles to the reuse of construction waste. For example, Pham et al. (2023) explored the impact of transformative leadership in the construction supply chain and developed a sustainable supply chain framework based on transformative leadership. Through empirical analysis, this study verified that improving stakeholder awareness and participation, as well as developing targeted policies and incentives, can significantly improve the reuse rate of building construction and demolition waste, which is consistent with the research results of Pham et al. (2023) To sum up, this study not only compares and analyzes different viewpoints on building construction and demolition waste management, but also clarifies the supporting role of circular economy theory and change management theory in this study, and verifies these theories through empirical research results. It provides theoretical basis and practical guidance for effective management of construction and demolition waste and sustainable development of construction industry.

5 Conclusion

In the development of urbanization, the reuse of abandoned buildings has a positive significance for resource conservation and sustainable development. To overcome the difficulties of reuse and optimize the existing strategies for the reuse of abandoned buildings, the material flow and obstacle analysis of abandoned building waste were carried out, aiming to further improve the resource recovery and utilization rate. The theoretical contribution of the research is that through in-depth analysis of the management practice of building construction and demolition waste, combined with the theory of circular economy, a set of systematic resource strategy model is proposed, which not only enriches the existing theoretical system of building construction and demolition waste management, but also provides a theoretical basis for realizing the efficient recycling and reuse of construction waste. On this basis, network clustering and density analysis were carried out to carry out targeted optimization strategies. The network analysis results showed that the network density reached 0.052, indicating that there was significant optimization space in the current reuse network. Further testing was conducted on the effectiveness of the optimization strategy. The test results showed that the waste recovery rate of the improved strategy reached 82.7%. Compared with the traditional scheme, the recovery rate increased rapidly, with an increase of 67.4%. In addition, the resource utilization rate increased by 50.1% compared with traditional schemes. The practical guiding significance of the research is that the resource strategy model provides specific operational framework and implementation steps for the management of construction and demolition waste, and provides clear action guidelines for the construction industry practitioners, policy makers and relevant stakeholders to help them make more effective decisions in the actual operation. It indicates that the optimization scheme has effectively promoted sustainable resource utilization. Although this strategy has achieved significant results in improving recovery rates and resource utilization, the lack of centralized network structure still needs to be further addressed. Future work will focus on optimizing the network structure, enhancing the connectivity and role of core nodes, thereby stimulating the potential of the entire recycling network and further promoting the sustainable development. Through continuous research and practice, it is expected to provide a more solid theoretical foundation and practical guidance for maximizing the utilization of abandoned building resources and sustainable urban ecological construction.

Data availability statement

The original contributions presented in the study are included in the article/Supplementary Material, further inquiries can be directed to the corresponding author.

Author contributions

JC: Investigation, Writing–original draft. HW: Investigation, Writing–review and editing. BS: Supervision, Writing–review and editing. WL: Investigation, Writing–original draft.

Funding

The author(s) declare that no financial support was received for the research, authorship, and/or publication of this article.

Conflict of interest

The authors declare that the research was conducted in the absence of any commercial or financial relationships that could be construed as a potential conflict of interest.

Publisher's note

References

Alsheyab, M. A. T. (2022). Recycling of construction and demolition waste and its impact on climate change and sustainable development. *Int. J. Environ.* 19 (3), 2129–2138. doi:10.1007/s13762-021-03217-1

Chakravarthy, P. R. K., Suganya, R., Nivedhitha, M., Parthiban, A., and Sivaganesan, S. (2022). Barriers and project management practices in green buildings. *Mat. Today Proc.* 52 (1), 1131–1134. doi:10.1016/j.matpr.2021.11.007

Dixit, S., Arora, R., Kumar, K., Basnsal, S., Vatin, N., Araszkiewicz, K., et al. (2022). Replacing E-waste with coarse aggregate in architectural engineering and construction industry. *Mat. Today Proc.* 56 (1), 2353–2358. doi:10.1016/j.matpr.2021.12.154

Duan, J., Asteris, P. G., Nguyen, H., Bui, X. N., and Moayedi, H. (2021). A novel artificial intelligence technique to predict compressive strength of recycled aggregate concrete using ICA-XGBoost model. *Eng. Comput-Germany.* 37 (4), 3329–3346. doi:10.1007/s00366-020-01003-0

Feng, H., Cui, Z., Han, C., Ning, J., and Yang, T. (2021). Bidirectional green promotion of 6G and AI: architecture, solutions, and platform. *IEEE Netw.* 35 (6), 57–63. doi:10.1109/MNET.101.2100285

Gao, S., Guo, Z., Guo, L., Zhou, L., and Yuan, K. (2021). Utilization of coal gangue as coarse aggregates in structural concrete. *Constr. Build. Mater.* 268, 121212. doi:10.1016/j.conbuildmat.2020.121212

Gao, S., Li, W., Yuan, K., and Rong, C. (2023). Properties and application of thixotropic cement paste backfill with molybdenum tailings. *J. Clean. Prod.* 391, 136169. doi:10.1016/j.jclepro.2023.136169

Glatt, M., Sinnwell, C., Yi, L., Donohoe, S., Ravani, B., and Aurich, J. C. (2021). Modeling and implementation of a digital twin of material flows based on physics simulation. *J. Manuf. Syst.* 58 (2), 231–245. doi:10.1016/j.jmsy.2020.04.015

Hammond, S. F., Gajendran, T., Savage, D. A., and Maund, K. (2021). Unpacking the problems behind the limited green construction adoption: towards a theoretical model. *Eng. Constr. Archit. Ma.* 28 (4), 833–844. doi:10.1108/ECAM-06-2020-0410

Lamba, P., Kaur, D. P., Raj, S., and Sorout, J. (2022). Recycling/reuse of plastic waste as construction material for sustainable development: a review. *Environ. Sci. Pollut. R.* 29 (57), 86156–86179. doi:10.1007/s11356-021-16980-y

Li, Q. (2023). Green financing role on climate change-supportive architectural design development: directions for green architectural designs. *Environ. Sci. Pollut. R.* 30 (19), 56984–56997. doi:10.1007/s11356-023-26229-5

Liu, J., Gong, E., and Wang, X. (2022). Economic benefits of construction waste recycling enterprises under tax incentive policies. *Environ. Sci. Pollut. R.* 29 (9), 12574–12588. doi:10.1007/s11356-021-13831-8

Liu, J., Li, Y., and Wang, Z. (2023). The potential for carbon reduction in construction waste sorting: a dynamic simulation. *Energy* 275, 127477. doi:10.1016/j.energy.2023.127477

Liu, J., Wu, P., Jiang, Y., and Wang, X. (2021). Explore potential barriers of applying circular economy in construction and demolition waste recycling. *J. Clean. Prod.* 326, 129400. doi:10.1016/j.jclepro.2021.129400

Lu, W., Du, L., and Feng, Y. (2022). Decision making behaviours and management mechanisms for construction and demolition waste recycling based on public–private partnership. *Environ. Sci. Pollut. R.* 29 (54), 82078–82097. doi:10.1007/s11356-022-21221-x

Ma, M., Tam, V. W., Le, K. N., Butera, A., Li, W., and Wang, X. (2023). Comparative analysis on international construction and demolition waste management policies and laws for policy makers in China. *J. Civ. Eng. Manag.* 29 (2), 107–130. doi:10.3846/jcem.2023.16581

Marinho, A. J. C., Couto, J., and Camões, A. (2022). Current state, comprehensive analysis and proposals on the practice of construction and demolition waste reuse and recycling in Portugal. *J. Civ. Eng. Manag.* 28 (3), 232–246. doi:10.3846/jcem.2022.16447

McAtackney, L. (2022). A suitable place to remember? Derelict Magdalen Laundries as possible sites of conscience in contemporary Ireland. *Space Cult.* 25 (2), 266–281. doi:10.1177/12063312211065560

Nagalli, A., Oliveira, L. O. S., Schamne, A. N., Barros, B. P., Hochleitner, H. D., and Oliveira, C. J. D. (2021). BIM plug-in technology for construction waste quantification. *Rev. Bras. Gestão Ambient. Sustentabilidade* 8 (20), 1605–1619. doi:10.21438/rbgas(2021)082021

Oh, C. (2023). Exploring the way to harmonize sustainable development assessment methods in article 6.2 cooperative approaches of the Paris agreement. *GLCE* 1 (3), 121–129. doi:10.47852/bonviewGLCE32021065

Pham, H. T., Pham, T., Truong Quang, H., and Dang, C. N. (2023). Impact of transformational leadership on green learning and green innovation in construction supply chains. *Eng. Constr. Archit. Ma.* 30 (5), 1883–1901. doi:10.1108/ECAM-05-2021-0379

Shao, Z., Li, M., and Yu, D. (2022). Bibliometric analysis of construction and demolition waste recycling: review and prospects. *P I Civ. Eng.* 175 (6), 283–292. doi:10.1680/jensu.21.00089

Shooshtarian, S., Maqsood, T., Caldera, S., and Ryley, T. (2022). Transformation towards a circular economy in the Australian construction and demolition waste management system. *SUSTAIN Prod. CONSUMP* 30 (1), 89–106. doi:10.1016/j.spc.2021.11.032

Umar, U. A., Shafiq, N., and Ahmad, F. A. (2021). A case study on the effective implementation of the reuse and recycling of construction and demolition waste management practices in Malaysia. *Ain Shams Eng. J.* 12 (1), 283–291. doi:10.1016/j.asej.2020.07.005

Usman, A. M., and Abdullah, M. K. (2023). An assessment of building energy consumption characteristics using analytical energy and carbon footprint assessment model. *GLCE* 1 (1), 28–40, Mar. doi:10.47852/bonviewGLCE3202545

Wang, B., Yang, Y., and Cao, J. (2024). Analysis of resource utilization competition relationship supporting green low-carbon transformation development of the construction industry. *Int. J. Low-Carbon Technol.* 19 (1), 544–550. doi:10.1093/ijlct/ctad147

Wang, Z., Han, F., Xia, B., Liu, J., and Zhang, C. (2023). Regional differences and heterogeneity of construction and demolition waste with economic growth: evidence from China. *Constr. Manag. Econ.* 41 (1), 44–59. doi:10.1080/01446193.2022.2137882

Whittaker, M. J., Grigoriadis, K., Soutsos, M., Sha, W., Klinge, A., Paganoni, S., et al. (2021). Novel construction and demolition waste (CDW) treatment and uses to maximize reuse and recycling. *Adv. Build.* 15 (2), 253–269. doi:10.1080/17512549.2019.1702586

Xu, Y., Lin, T., Du, P., and Wang, J. (2024). An innovative interval grey model for construction waste forecasting. *Appl. Math. Model.* 126 (1), 22–51. doi:10.1016/j.apm.2023.10.013

Zou, S., and Wang, L. (2021). Detecting individual abandoned houses from google street view: a hierarchical deep learning approach. *ISPRS J. Photogramm.* 175 (1), 298–310. doi:10.1016/j.isprsjprs.2021.03.020

frontiers | Frontiers in Materials

TYPE Original Research
PUBLISHED 08 October 2024
DOI 10.3389/fmats.2024.1490006

OPEN ACCESS

EDITED BY
Biao Hu,
Shenzhen University, China

REVIEWED BY
Amir Ali Shahmansouri,
Washington State University, United States
Zeyu Lu,
University of Macau, China

*CORRESPONDENCE
Qingxin Zhao,
Submission_tju@126.com

RECEIVED 02 September 2024
ACCEPTED 19 September 2024
PUBLISHED 08 October 2024

CITATION
He Z, Wu Z, Niu W, Wang F, Zhong S, Han Z and Zhao Q (2024) A machine learning model for predicting the mechanical strength of cement-based materials filled with waste rubber modified by PVA.
Front. Mater. 11:1490006.
doi: 10.3389/fmats.2024.1490006

A machine learning model for predicting the mechanical strength of cement-based materials filled with waste rubber modified by PVA

Zhengfeng He[1], Zhuofan Wu[2], Wenjun Niu[2], Fengcai Wang[1], Shunjie Zhong[3], Zeyu Han[1] and Qingxin Zhao[4]*

[1]Cangzhou Qugang Expressway Construction Co., Ltd., Hebei, China, [2]School of Civil Engineering, Tianjin University, Tianjin, China, [3]Fujian Zhanglong Construction Investment Group Co., Ltd., Fujian, China, [4]School of Civil Engineering and Mechanics, Yanshan University, Hebei, China

As demand for sustainable building materials rises, the use of waste rubber in civil engineering is gaining attention. This study proposes a method to modify waste rubber using polyvinyl alcohol (PVA) to enhance its material properties and expand its applications. A dataset was created focusing on the mechanical strength of cementitious materials incorporating PVA-modified waste rubber, and multiple machine learning methods were used to develop regression prediction models, particularly evaluating the support vector regression (SVR) model. Results show that the SVR model outperforms others, achieving mean squared errors of 1.21 and 0.33, and mean absolute errors of 2.06 and 0.15. Analysis indicates a negative correlation between waste rubber content and the water-to-cohesive ratio (w/c) with strength indexes, while a positive correlation exists between curing age and PVA. Notably, waste rubber content significantly affects strength. The mechanical strength of cementitious materials was notably enhanced by PVA-modified waste rubber, likely due to PVA's dispersion and bridging effects. This study presents a novel approach to sustainably recycle waste rubber, highlighting its potential in construction materials.

KEYWORDS

waste rubber, PVA, mechanical strength, machine learning, robustness

1 Introduction

The rapid economic development in our country has resulted in it becoming the world's largest consumer and producer of rubber and rubber products, leading to a significant increase in the generation of waste rubber (Xiao et al., 2009; Ossola and Wojcik, 2014; Thomas and Gupta, 2015; Chen et al., 2019). In the construction field, waste rubber has been proven to be an effective additive for preparing construction materials with specific applications (Lisi et al., 2004; Sukontasukkul, 2009; Richardson et al., 2011). However, the incorporation of waste rubber can impair the mechanical properties of cement-based materials (Eldin and Senouci, 1993; Mendis et al., 2017; Li et al., 2020; Steyn et al., 2021; Mhaya et al., 2021). Recent research has focused on improving rubberized concrete

TABLE 1 Chemical and mineral composition of OPC.

Component	SiO_2	$Al2O_3$	Fe_2O_3	CaO	MgO	SO_3	K_2O	LOI
%	22.95	8.9	3.3	57.36	2.36	2.75	1.67	0.65

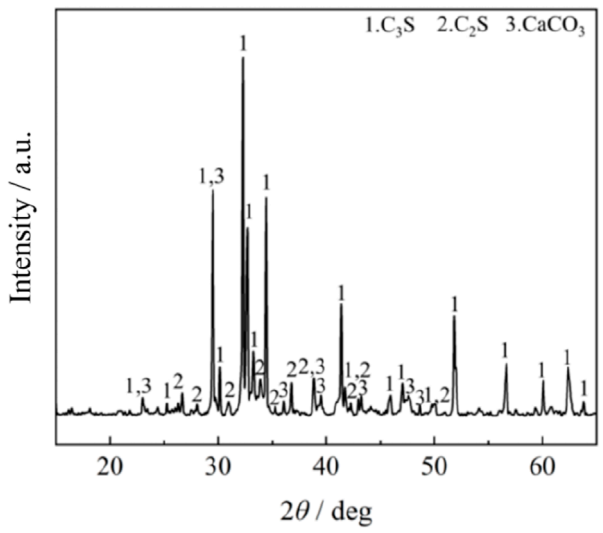

FIGURE 1
XRD analysis results of OPC.

by surface treatments of waste rubber. Dong et al. applied silane coupling agents to enhance performance of rubber (Dong et al., 2013). Kumar et al. found sulfuric acid treatment improved the bonding of rubber with cement paste (Kumar and Dev, 2021), while He et al. validated urea, sulfonation, and NaOH modifications for better bonding (He et al., 2021). Notably, studies have shown that PVA, widely used as a construction adhesive in the building industry, not only adsorbed rubber molecules effectively but was also non-toxic and environmentally friendly (Fan et al., 2019; Yu et al., 2020). Therefore, to further enhance the application of PVA-modified waste rubber in the construction industry, it is crucial to conduct research aimed at improving its mechanical properties.

Additionally, to better guide engineering practices, many researchers are now using machine learning models to develop and analyze regression prediction models (Tu et al., 2022). In the field of civil engineering, the in-depth application of machine learning has greatly advanced the discipline (Papazek et al., 2020; Zhou, 2022). The most frequent research involving machine learning focuses on establishing regression models for the mechanical properties of concrete, such as compressive strength and flexural strength (Konstantopoulos et al., 2020; Cook et al., 2021; Zhang et al., 2021). (Li et al., 2024) used ultra-high performance concrete (UHPC) as the target object and identified cement, silica fume, steel fibers, mineral powder, water-reducing agents, defoamers, and water as the feature factors, then developed a nonlinear regression model to predict the 28-day compressive strength of UHPC. They employed Random Forest Regression (RF), Support Vector Machine Regression (SVR), and Multi-Layer Perceptron Regression (MLP) models, and found that the SVR and MLP models outperformed the RF model, with predictions falling within a 5% confidence interval. Asteris et al. (2021) established a large database considering the age of mortar, water-cement ratio, particle size distribution, plasticizers, and cement grade, and discussed the applicability of SVR, RF, Decision Tree (DT), AdaBoost, and k-Nearest Neighbors (KNN) models in predicting the compressive strength behavior of cement mortar, concluding that RF and AdaBoost models demonstrated the best regression prediction capabilities. Huang et al. (2021) were the first to use machine learning methods to predict the mechanical properties of carbon nanotube (CNT)-reinforced cement-based composites, and they extensively tuned the model parameters to achieve optimal prediction results. Sensitivity analysis using the Jacobian matrix indicated that the length of CNTs had the most significant effect on the compressive strength of the composites, while curing time had the greatest impact on the flexural strength, providing a solid basis for future experimental mix optimization and condition design. Guan et al. (2022) proposed a machine learning framework to predict the hardness, transverse rupture strength, and fracture toughness of WC-Co alloys, analyzing the prediction accuracy of KNN, MLP, RF, SVR, and Stacking Regressor (STK) models. Their report showed that the MLP model outperformed other models in predicting fracture performance. The results reaffirm the remarkable significance of machine learning in guiding the design of new materials (Lunt, 2015).

Therefore, this paper proposed a method utilizing PVA-modified waste rubber to establish a strength index database for cement-based materials filled with PVA-modified waste rubber and used various machine learning methods to develop regression prediction models. It analyzed the robustness of different feature factors on strength, thereby providing theoretical guidance for engineering practice. This research not only achieved the harmless disposal of waste tire rubber but also expanded the application range of waste rubber in civil engineering, carrying substantial practical significance.

2 Materials and methodology

2.1 Materials

2.1.1 Ordinary portland cement (OPC)

The cement used in this study is P.O 42.5 cement produced by Tianjin Jidong Cement Co., Ltd., which conformed to the national standard GB175-2007. The cement exhibited a deep gray granular appearance. The chemical composition was provided in Table 1, and the XRD analysis results were presented in Figure 1.

2.1.2 Waste rubber particles

The waste rubber particles used in this study were produced by Tianjin Kewei Rubber Factory, with an apparent density of

TABLE 2 Chemical and mineral composition of the waste rubber particles.

Component	Rubber hydrocarbons	Carbon black	Acetone extract	Isoprene	Ash	Water	Fiber	Metal	Others
%	45.20	25.80	14.20	12.10	0.90	0.80	0.50	0.08	0.42

FIGURE 2
The morphology of the waste rubber particles.

1,050 kg/m^3. The maximum particle size of the waste rubber was 2.5 mm, with over 80% of the particles having a size between 1 and 2 mm. Additionally, the chemical composition of the waste rubber particles was detailed in Table 2, and their morphology was shown in Figure 2.

2.1.3 Polyvinyl alcohol (PVA) powder

The PVA used in this study was produced by Shandong Yousuo Chemical Technology Co., Ltd. and was characterized by low water solubility. The macroscopic appearance of the PVA was a white powder with a mesh size of 160, while the microscopic morphology exhibited a particulate structure, as shown in Figure 3.

2.1.4 Other chemical reagents

The chemical reagent used in this study was primarily isopropanol, employed to terminate the cement hydration process. Detailed information was provided in Table 3.

2.2 Macro-experimental methodology

2.2.1 Preparation of PVA solution

The modifier used in this study was a PVA solution with a mass fraction of 0.1%. However, PVA was not readily soluble in water at room temperature. Therefore, the preparation of the PVA solution was carried out using a constant-temperature magnetic stirrer, with the temperature set at 75°C, as shown in Figure 4.

2.2.2 Tests for mechanical properties

The fundamental performance of cement-based materials was the mechanical properties. In this study, the mechanical properties of the specimens were tested using a YAW-300C fully automatic compression testing machine produced by Jinan Shidai Test Machine Co., Ltd. The strength indicators obtained from the experiments (compressive strength and flexural strength) were used as the dataset for the machine learning models.

2.3 Machine learning models

2.3.1 Least-squares linear regression

Linear regression (LR) is one of the most basic and straightforward regression models, which considers a linear relationship between the objective function and various influencing factors. The schematic representation of LR regression was shown in Figure 5 (Lunt, 2015; Cai et al., 2020). In the LR algorithm, a series of coefficient values corresponding to different influencing factors were provided to represent the feature values through a linear combination. The mathematical expression is given below:

$$\hat{y}(\omega, x) = \omega_0 + \omega_1 x_1 + \cdots + \omega_p x_p$$

Where, $\hat{y}$ represents the predicted value, ω_0, ω_1, ., ω_p represent the weight coefficients of different eigenvalues, and x_1, ., x_p represent the eigenvectors corresponding to different eigenvalues.

In LR algorithms, the least squares method is one of the most common and fundamental approaches. It addresses the following mathematical problem by minimizing the sum of the squared residuals between the observed targets from experimental data and the predicted targets obtained through linear regression:

$$\omega = \left(\omega_1, \cdots, \omega_p\right)$$

$$\min_{\omega} \|X\omega - y\|_2^2$$

Where, ω represents the weight coefficients, X represents the eigenvectors and y represents the true values.

2.3.2 Support vector machine regression

Support Vector Machine Regression (SVR) is a supervised learning algorithm that constructs a hyperplane or a set of hyperplanes in a high-dimensional or infinite-dimensional space to perform regression and outlier detection on experimental data (Moguerza and Muñoz, 2006). For a given set of regression data, its computational form was illustrated in Figure 6 (Yu et al., 2018; Biswas et al., 2023). It was generally believed that good separation was achieved by maximizing the margin between the hyperplane and the nearest training data points (known as the functional margin) in any class. Typically, a larger margin resulted in lower generalization error of the classifier.

For a specific set of feature vectors (consisting of experimental data in this study), SVR can solve the following mathematical form of the problem:

$$\min_{\omega,b,\xi,\xi^*} \frac{1}{2}\omega^T\omega + C\sum_{i=1}^{n} \xi_i + \xi_i^*$$

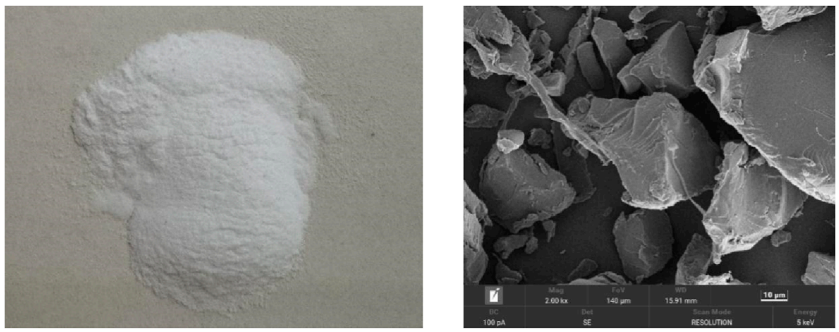

(a) (b)

FIGURE 3
The morphology of PVA: **(A)** macro-morphology; **(B)** micro-morphology, ×2000.

TABLE 3 Detailed information of the isopropanol.

Item	Chemical formula	Purity	Manufacturer
Isopropanol	$CH_3CHOHCH_3$	AR	Myriad Shanghai

FIGURE 4
The constant-temperature magnetic stirrer.

With certain restrictions:

$$y_i - \omega^T \Phi(x_i) - b \le \varepsilon + \xi_i$$

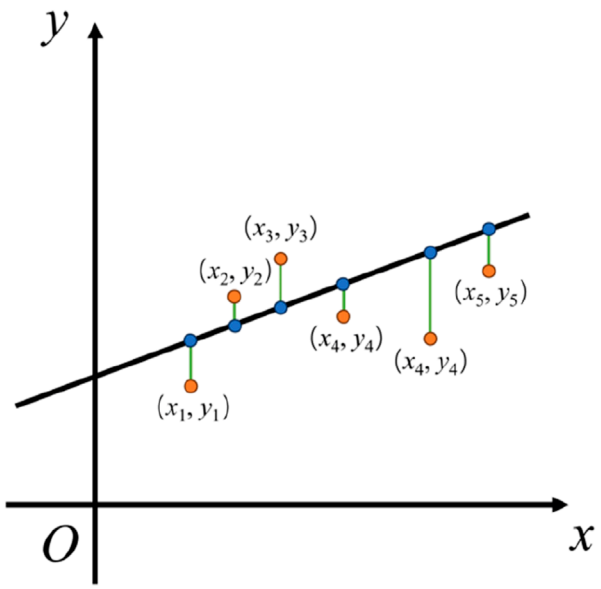

FIGURE 5
Schematic diagram of LR calculation.

$$\omega^T \Phi(x_i) + b - y_i \le \varepsilon + \xi_i^*$$

$$\xi_i, \xi_i^* \ge 0, i = 1, \cdots, n$$

Where, ω represents the weight coefficient of the eigenvalues, b represents the deviation coefficient, C represents the penalty factor, ε is the given interval, ξ_i and $\xi_i{}^*$, represents the introduction of slack variables.

In the SVR regression calculation process, the core component is the use of a kernel function for analytical computation. A kernel function is a type of function that takes vectors from the original space as input and returns the dot product of vectors in the feature space (where the transformed data space may be high-dimensional). The choice of kernel function significantly affects the

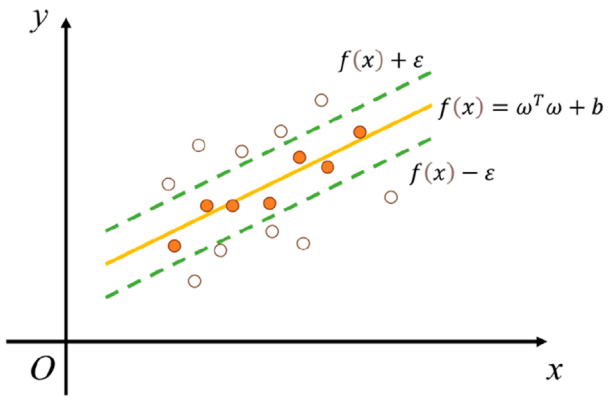

FIGURE 6
Schematic diagram of SVR calculation.

final computation results and prediction accuracy in SVR. Common kernel functions include the Linear kernel function, Polynomial kernel function, Gaussian Radial Basis Function (RBF), and Sigmoid function. Their functional expressions are as follows.

(1) Linear kernel function:

$$k(x,x') = \langle x,x' \rangle$$

(2) Polynomial function:

$$k(x,x') = (\gamma\langle x,x' \rangle + r)^d, \qquad \gamma > 0$$

Where, γ is the tuning parameter of the polynomial function, r is an optional constant, and d is the highest order term of the polynomial function.

(3) Gaussian radial basis function:

$$k(x,x') = \exp\left(-\gamma\|x-x'\|^2\right), \qquad \gamma > 0$$

Where, γ is the tuning parameter.

(4) Sigmoid function:

$$k(x,x') = \tanh\left(\gamma\langle x,x' \rangle + r\right)$$

Where, γ is the tuning parameter, r is an optional constant.

2.3.3 Random forest regression

Random Forest Regression (RF) is an averaging algorithm based on random decision trees (Lund et al., 2011; Liu K. et al., 2023). Unlike random decision trees, RF is not determined by specific feature values or combinations, thereby enhancing randomness and achieving better ensemble performance, resulting in lower variance and further mitigating overfitting issues during the fitting process (as shown in Figure 7) (Cook et al., 2021; Surehali et al., 2024). In a random forest, each tree is constructed from samples drawn with replacement (i.e., bootstrap samples) from the training set. When splitting each node, the best split is found from a randomly selected subset of all input features or their sizes. This approach enables RF to handle nonlinear data effectively and provides faster processing speeds. Additionally, RF can assess the interactions between feature factors during training and further analyze the importance of different feature factors, thus offering better guidance for engineering practice.

2.3.4 Integrated algorithmic regression

The implementation of Ensemble Regression involves combining multiple individual models to enhance machine learning performance, often resulting in better predictive outcomes compared to single models (Nilsen et al., 2019; Yang et al., 2024). In this study, the ensemble method employed involves simultaneously training the aforementioned SVR and RF models using the same training data. The final regression analysis decision is made based on a voting mechanism, where the principle of majority rule is applied to determine the outcome. This approach is used to evaluate the accuracy and effectiveness of the machine learning models under the ensemble regression framework (Han et al., 2020; Lapeyre et al., 2021).

2.3.5 Multilayer prceptron-artificial neural network regression

Artificial Neural Networks (ANNs) represent a category of machine learning models based on the neural synaptic networks of animals, used for distributed parallel information processing algorithms (Zhang, 2016; Kumar et al., 2024). The constructed neural network relies on the complexity of the system and adjusts the connections between internal data to achieve the intended information processing goals (Murthy et al., 2024; Liu et al., 2024).

The Multilayer Perceptron (MLP) is a fundamental type of artificial neural network. As a feedforward neural network, it consists of multiple layers of neurons and is commonly used for solving classification and regression problems. As shown in Figure 8, the most basic structure of an MLP comprises a single input layer, a single hidden layer, and a single output layer, with each layer consisting of one or more neurons. Each neuron performs a weighted sum of input values and produces an output through an activation function. During this process, MLP utilizes a backpropagation algorithm to recalculate the weights and biases between neurons, aiming to minimize the error between the predicted and actual outputs to achieve higher accuracy. During training, the gradient of the loss with respect to the weights is expressed as follows:

$$Loss(\hat{y},y,W) = \frac{1}{2n}\sum_{i=0}^{n}\|\hat{y}_i - y_i\|_2^2 + \frac{\alpha}{2n}\|W\|_2^2$$

2.4 Machine learning models

The evaluation of different machine learning models can be carried out through various evaluation metrics, including having

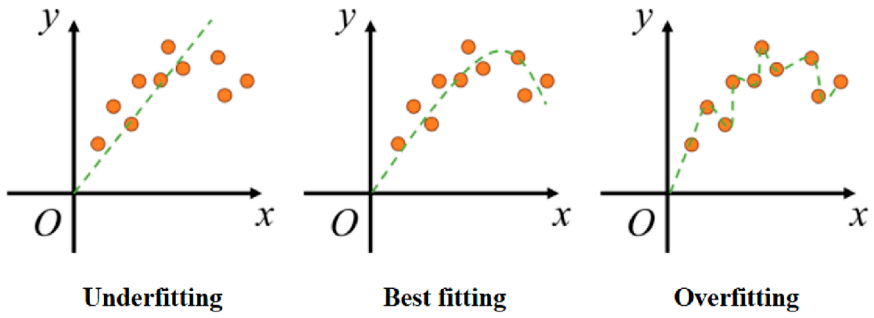

FIGURE 7
Fitting problems of machine learning models.

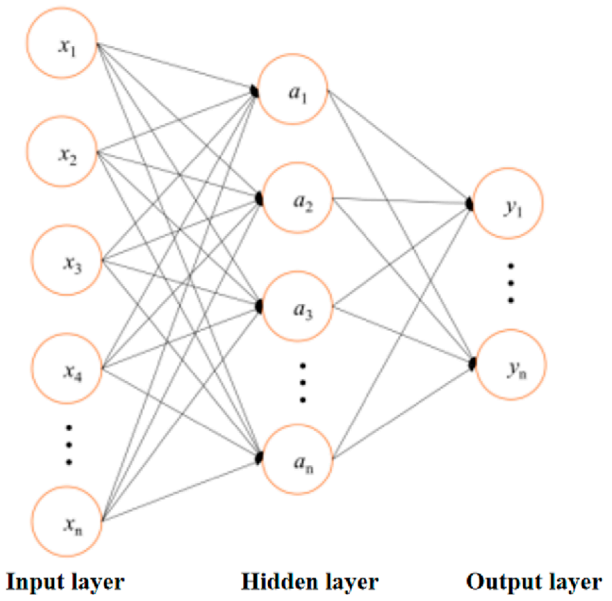

FIGURE 8
Basic structure of MLP-ANN.

TABLE 4 Descriptive statistics of dataset characteristics.

Parameters	Unit	Minimum	Maximum	Average
Rubber content	%	0	25	12.5
w/c ratios		0.3	0.4	0.35
Ages	Day	3	28	13
PVA		1	2	1.5
Compressive strength	MPa	21.5	63.3	40.09
Flexural strength	MPa	4.4	13.9	8.93

mean absolute error (*MAE*), mean square error (*MSE*), root mean square error (*RMSE*), and correlation coefficient R^2, which are mathematically expressed as follows:

$$MAE = \frac{1}{n}\sum_{i=1}^{n}|\hat{y}_i - y_i|$$

$$MSE = \frac{1}{n}\sum_{i=1}^{n}(\hat{y}_i - y_i)^2$$

$$RMSE = \sqrt{\frac{1}{n}\sum_{i=1}^{n}(\hat{y}_i - y_i)^2}$$

$$R^2 = 1 - \frac{RSS}{TSS} = 1 - \frac{\sum_{i=1}^{n}(\hat{y}_i - y_i)^2}{\sum_{i=1}^{n}(\bar{y}_i - y_i)^2}$$

Where, y_i represents the true value, $\hat{y}_i$ represents the predicted value, $\bar{y}_i$ represents the mean of the true value, and n represents the number of samples.

3 Models establishment

3.1 Establishment of data sets

The data used in this study was derived from the compressive strength and flexural strength of cement-based materials filled with PVA-modified waste rubber. The influencing factors, or input features, include rubber content, water-to-cement (w/c) ratio, age, and the presence of PVA. Compressive strength and flexural strength were considered as the output variables. The rubber content values are 0%, 5%, 10%, 15%, 20%, and 25%; the w/c ratio were 0.3, 0.35, and 0.4; the ages were 3, 7, 14, and 28 days; and the presence of PVA was denoted by one and 2, representing 0% PVA and 0.1% PVA, respectively. Table 4 presented the characteristics of the collected data, including units, maximum values, minimum values, and averages. Figures 9, 10 illustrated the distribution of data in the compressive strength and flexural strength datasets, respectively.

The accuracy of machine learning models is influenced by the input features; thus, it is necessary to conduct a correlation analysis of the influencing factors for both compressive strength and flexural

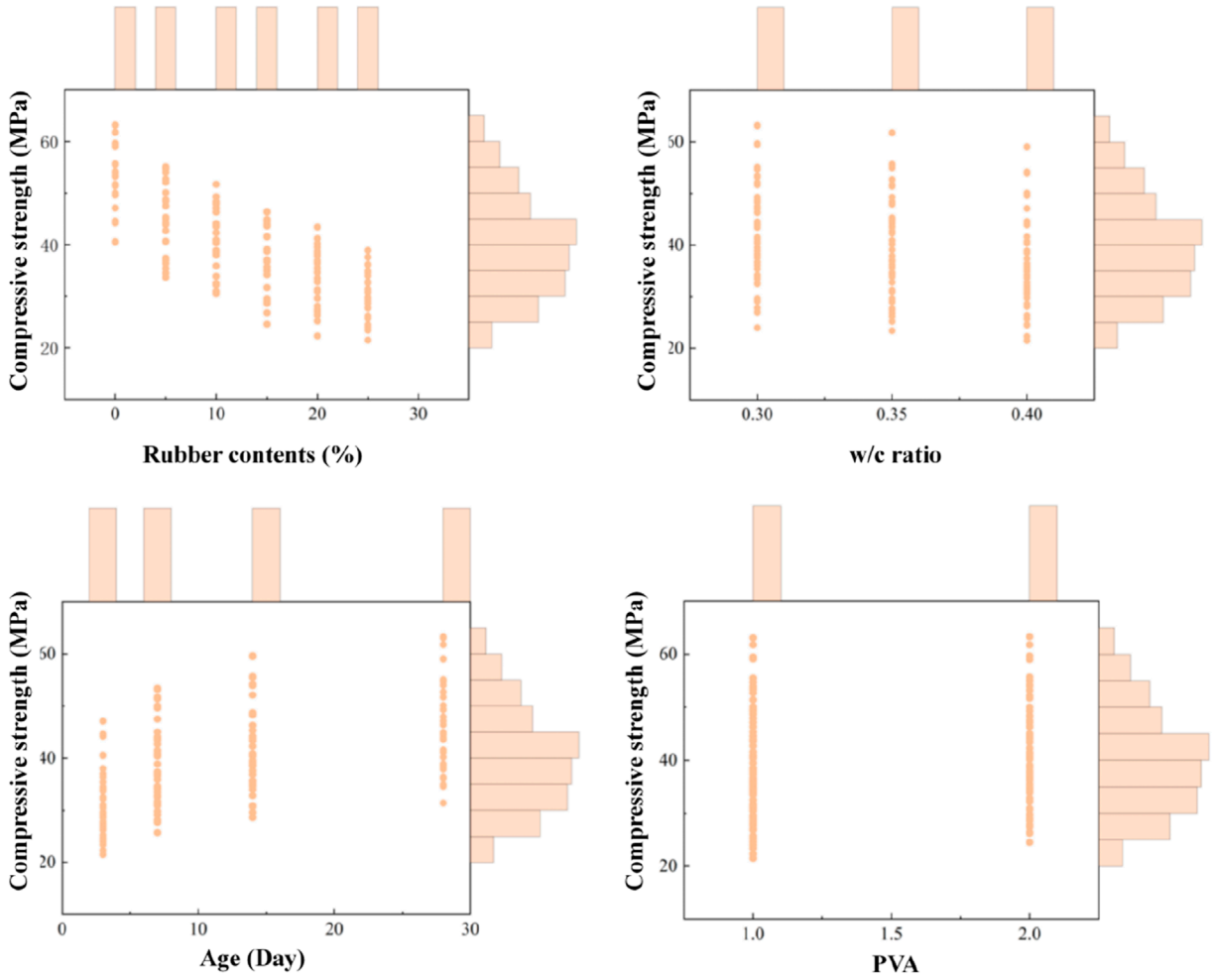

FIGURE 9
Distribution of data in the compressive strength dataset.

strength models to verify their validity (Serban et al., 2024). In this study, Pearson correlation coefficients were used to analyze the correlations between the influencing factors (input features), with results presented in Figures 11, 12. The Pearson correlation analysis showed that, for both compressive strength and flexural strength models, the correlation coefficients between different influencing factors were close to 0, indicating that there was no significant correlation between the factors and that each factor was necessary and non-negligible (Janiesch et al., 2021).

For both compressive strength and flexural strength, the rubber content was identified as the most influential factor, with correlation coefficients of −0.76 and −0.81, respectively. In contrast, the effect of PVA on compressive strength and flexural strength was relatively minor, with correlation coefficients of 0.13 and 0.17, respectively. Among the four influencing factors, rubber content and w/c ratio were negatively correlated with both compressive strength and flexural strength, while age and PVA exhibited a positive correlation with these properties. Specifically, an increase in rubber content and w/c ratio decreased the mechanical properties of PVA-modified waste rubber-filled cement-based materials, whereas an increase in age and the presence of PVA enhanced the mechanical properties of cement-based materials, consistent with the experimental results discussed earlier.

3.2 Development and tuning of machine learning models

In this study, the model was developed with a ratio of 1:3 between the test set and the training set, using 25% of the compressive strength and flexural strength dataset to evaluate the model's accuracy and generalization ability.

Furthermore, considering the substantial mean differences among various influencing factors (as shown in Table 4), it was essential to standardize the dataset before training to ensure the effectiveness and accuracy of the machine learning models. The formula for data standardization was as follows:

$$x' = \frac{x - \mu}{\sigma}$$

Where, μ represents the mean of the feature data and σ represents the standard deviation of the feature data.

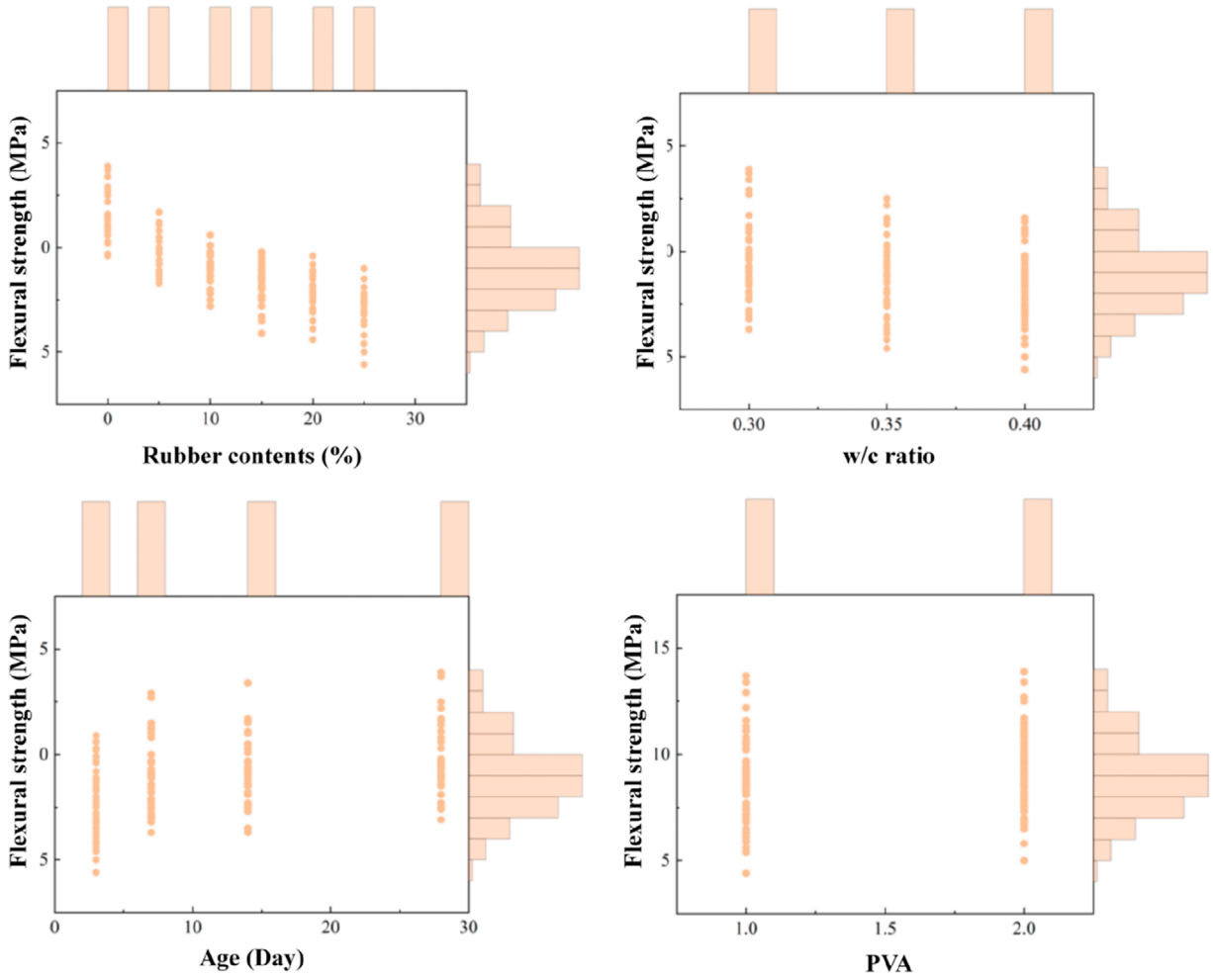

FIGURE 10
Distribution of data in the flexural strength dataset.

In each model, some hyperparameters needed to be adjusted to achieve superior predictive performance. In this study, hyperparameters were optimized using learning curves and grid search, considering cross-validation while exploring the given parameter combinations. Ten-fold cross-validation was employed in this study to iteratively adjust the hyperparameters of each model, improving the accuracy of the predictions to meet our requirements.

Figure 13 illustrated the principle of cross-validation. The 10-fold cross-validation used in this study involved randomly dividing the sample dataset into 10 subsets, using one subset as the test set while the remaining subsets were used as the training set. The mean squared error (MSE) of each iteration was averaged to evaluate the parameter adjustments and assess the accuracy of the model under the current hyperparameters, ultimately determining the optimal combination of hyperparameters.

In summary, the steps of a complete machine learning model implementation were shown in Table 5.

4 Results and discussion

4.1 Model hyper-parameterization

Based on the results of 10-fold cross-validation, the final model parameters for this study, after multiple adjustments, were summarized in Table 6. The hyperparameters listed in Table 6 were determined using learning curves and grid search, while the hyperparameters for other models and those not listed were set to the default values. Notably, during the hyperparameter tuning of the SVR model, we observed that the gamma value for the compressive strength model was lower than that for the flexural strength model, whereas the C value was higher. This suggested that the SVR model was more prone to overfitting when predicting compressive strength, which adversely affected the prediction accuracy. Indeed, during model validation, overfitting was more prevalent in the predictions of compressive strength compared to flexural strength. Nevertheless, the issue was effectively addressed by 10-fold cross-validation.

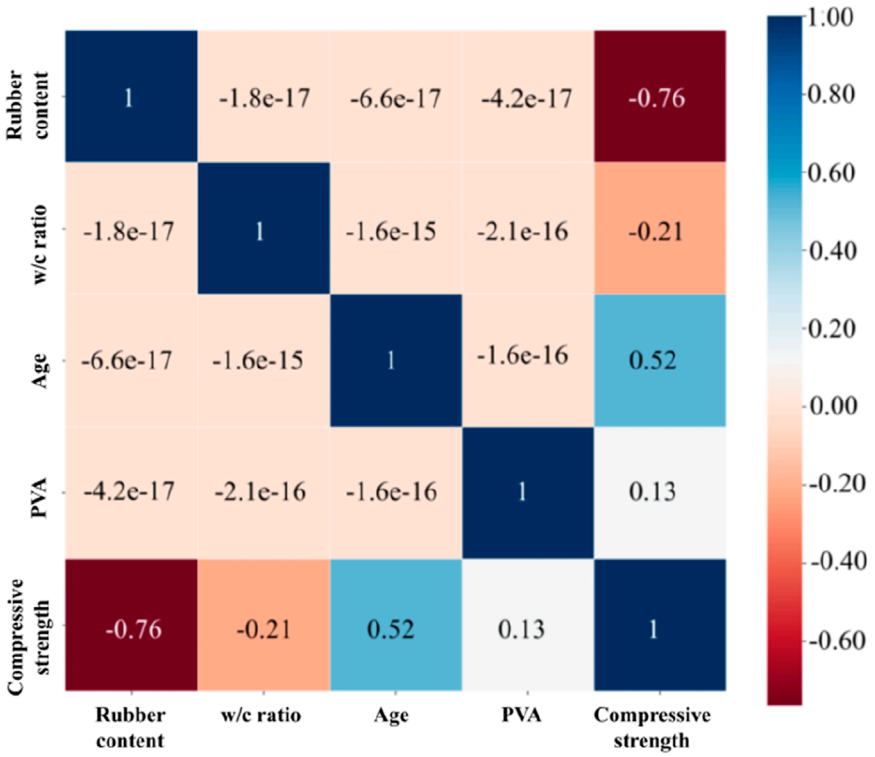

FIGURE 11
Analysis of Pearson's correlation coefficient in compressive strength modeling.

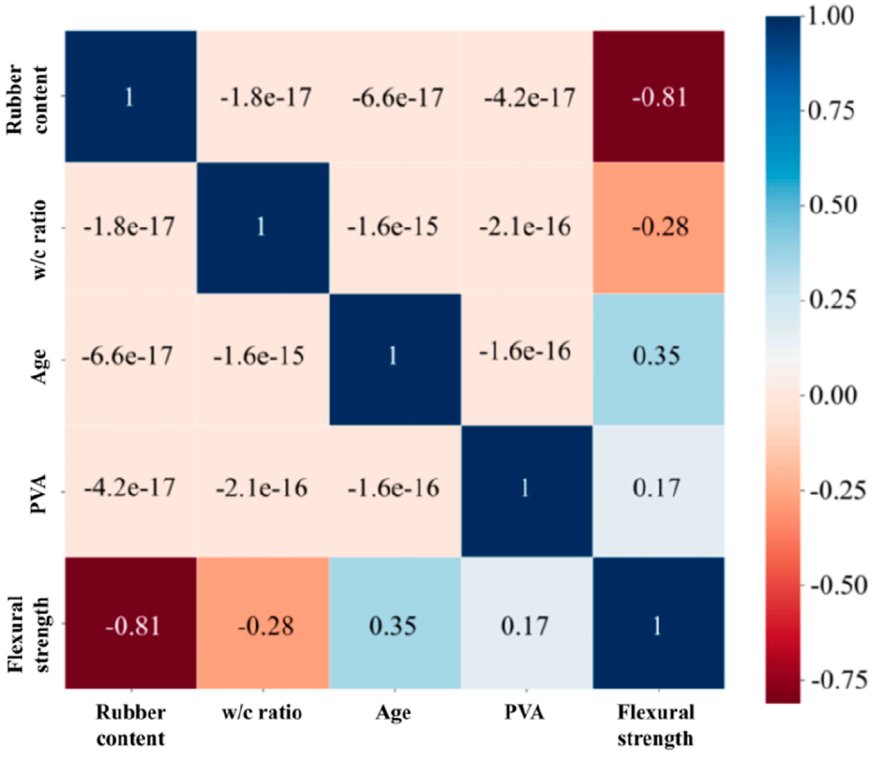

FIGURE 12
Analysis of Pearson's correlation coefficient in flexural strength modeling.

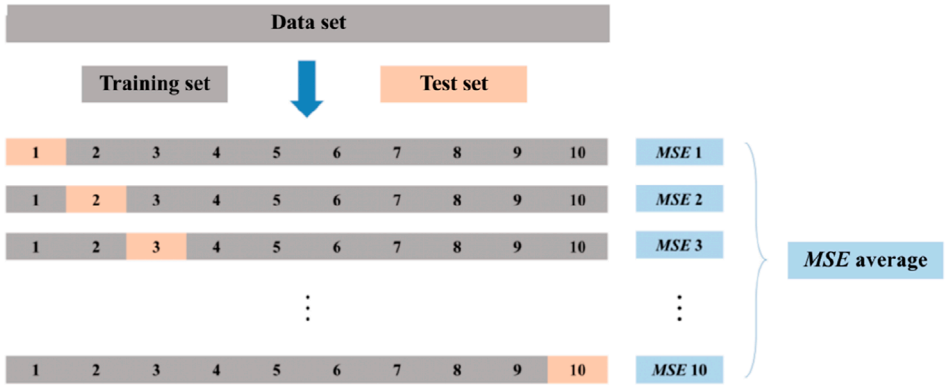

FIGURE 13
Schematic of 10-fold cross-validation.

TABLE 5 Steps in machine learning model establishment.

Steps	Processes
1	Load various module packages required by the model
2	Read pre-prepared data files
3	Divide the training set and test set according to a certain ratio
4	Normalize the data set.
5	Instantiate the model after parameter tuning and train on the training set.
6	Perform prediction on the divided test set.
7	Calculate and output each model evaluation index

TABLE 6 Machine learning model hyper-parameterization.

Model	Parameters	Value_ compressive	Value_ flexural
SVR	kernel	rbf	rbf
	gamma	0.081	0.098
	C	77.89	47.03
	epsilon	0.01	0.042
RF	n_estimators	20	125
	max_depth	8	-
MLP-ANN	solver	lbfgs	lbfgs
	hidden_layer_ sizes	(204)	(172)
	activation	tanh	logistic

4.2 Comparison of actual and predicted values

The actual values from the test set were compared with the predicted values generated by each model to visually assess the accuracy of the machine learning models' predictions. Figures 14, 15 showed that, whether in the compressive strength regression prediction model or the flexural strength regression prediction model, all machine learning models exhibited excellent regression prediction capabilities. Specifically, all predicted values in the test set fall within ±20% of the actual values, with no outliers detected, indicating that the machine learning models demonstrated excellent regression prediction performance and were suitable for application and promotion in engineering practice.

4.3 Evaluation metrics analysis

Table 7 summarized the final evaluation metrics for the compressive strength and flexural strength regression prediction models to clearly analyze the regression prediction capabilities of different models.

For the compressive strength regression prediction model, the SVR, Ensemble, and MLP-ANN models exhibited high R^2 values of 0.98 on the test set, indicating excellent accuracy and generalization ability in predicting compressive strength. Among these, SVR and MLP-ANN models performed the best, with the smallest *MAE*, *MSE*, and *RMSE*, and the highest R^2. Specifically, the evaluation metrics for the SVR model were 1.21, 2.06, 1.43, and 0.98, respectively, while those for the MLP-ANN model were 1.05, 2.14, 1.46, and 0.98, showing clear superiority over other models.

In the flexural strength regression prediction model, the SVR, Ensemble, and MLP-ANN models also stood out, with R^2 values exceeding 0.95 in the flexural strength test set. The SVR model performed the best, with the smallest MAE, MSE, and RMSE, and the highest R^2 values of 0.33, 0.15, 0.39, and 0.96, respectively, which indicated that the SVR model achieved the highest prediction accuracy and generalization ability in the flexural strength regression model.

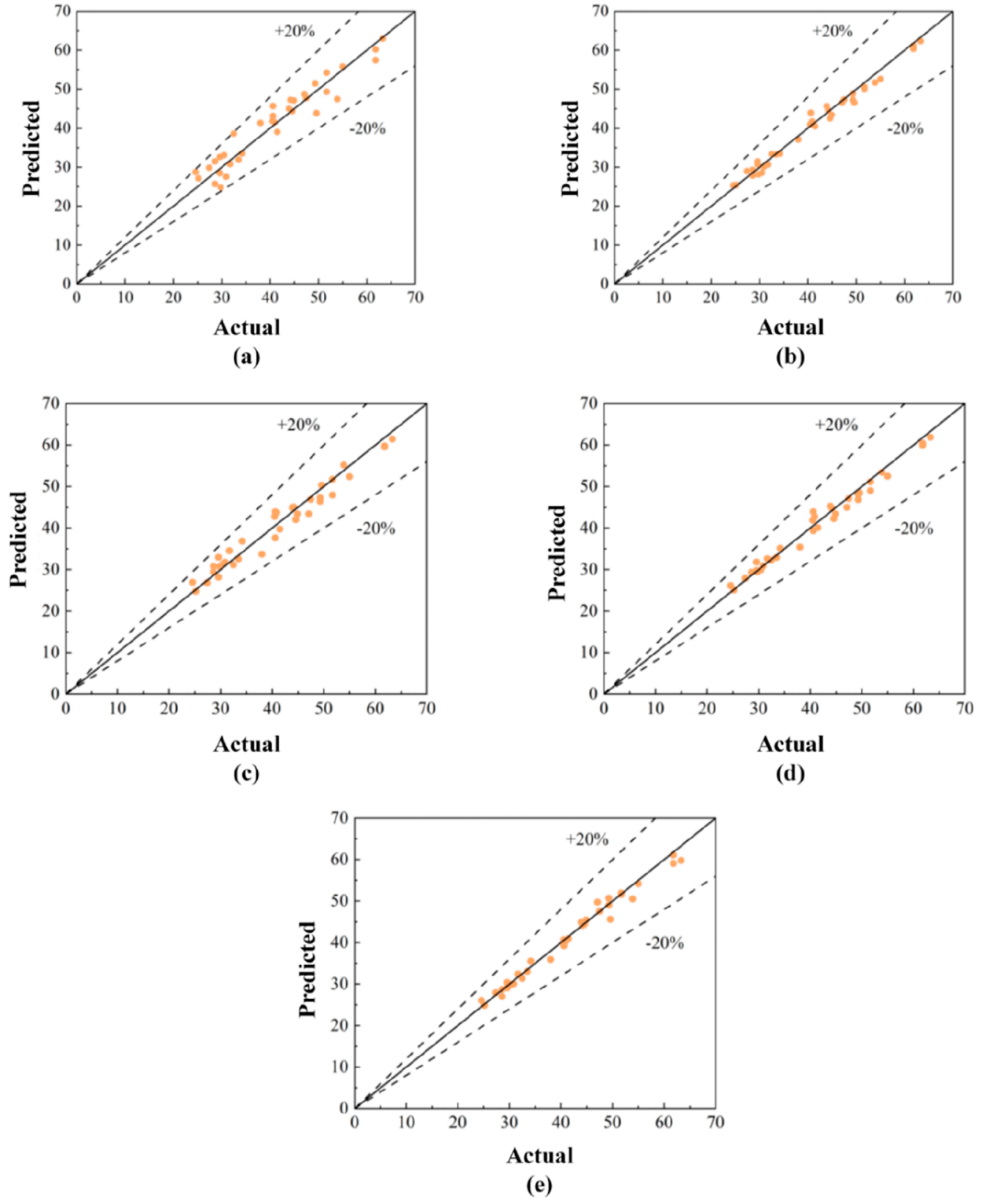

FIGURE 14
Comparison of actual and predicted values in the regression prediction model of compressive strength: **(A)** LR; **(B)** SVR; **(C)** RF; **(D)** Ensemble; **(E)** MLP-ANN.

Conversely, the LR model performed the worst in both the compressive strength and flexural strength regression prediction models. This may be due to the dataset exhibiting more non-linearity, making simple linear fitting less effective in capturing the relationships between influencing factors and output features. Nevertheless,

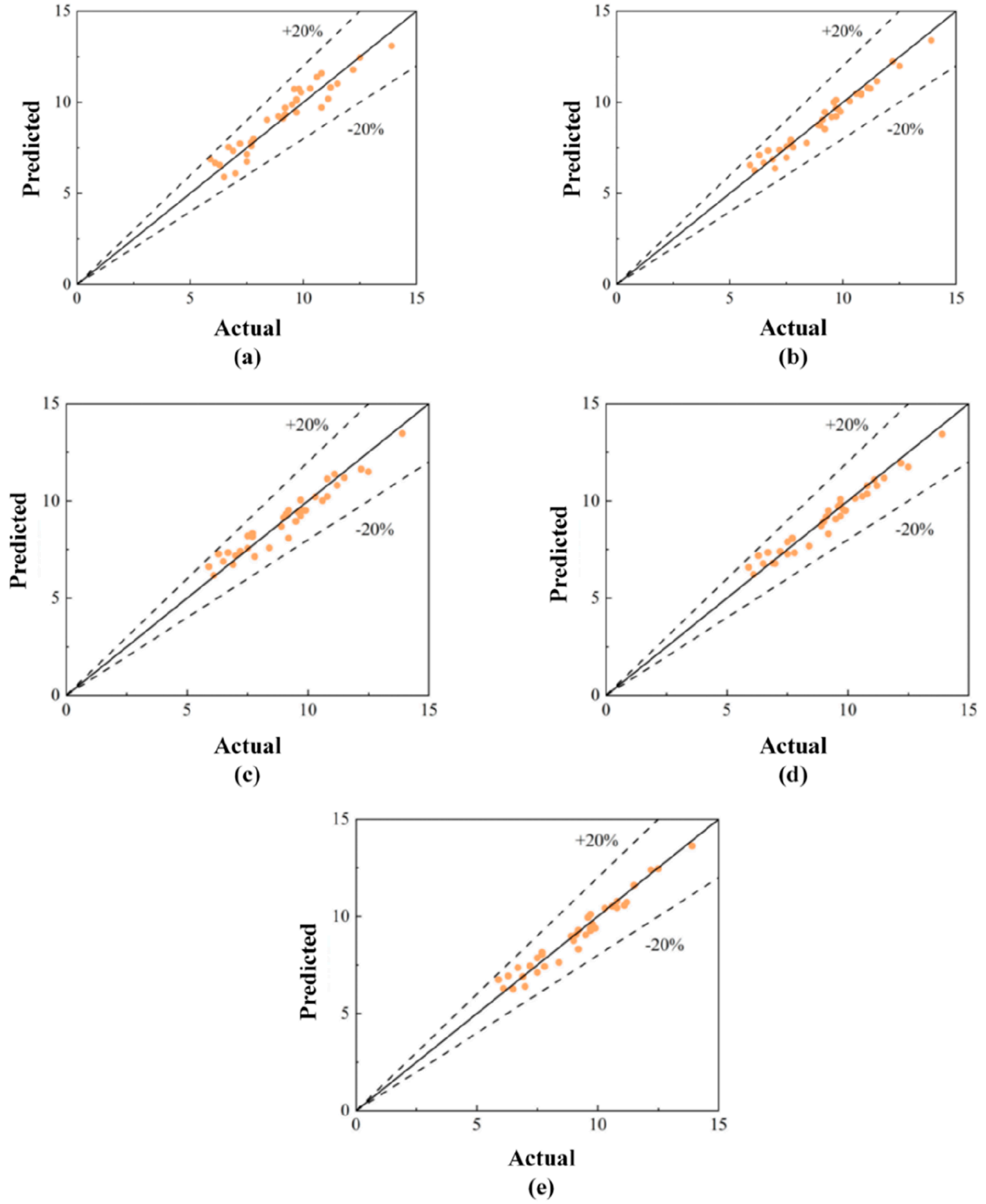

FIGURE 15
Comparison of actual and predicted values in the regression prediction model of flexural strength: **(A)** LR; **(B)** SVR; **(C)** RF; **(D)** Ensemble; **(E)** MLP-ANN.

the LR model's R^2 values were still greater than 0.90, reflecting its reasonably good regression prediction capability in an absolute sense. Therefore, the LR calculation results were retained in this study and used for the robustness analysis of the influencing factors in subsequent sections.

TABLE 7 Summary of machine learning model evaluation metrics.

Models	Compressive strength				Flexural strength			
	MAE	*MSE*	*RMSE*	R^2	*MAE*	*MSE*	*RMSE*	R^2
LR	2.52	9.01	3.00	0.92	0.52	0.36	0.60	0.90
SVR	1.21	2.06	1.43	0.98	0.33	0.15	0.39	0.96
RF	1.91	4.77	2.18	0.96	0.44	0.26	0.51	0.93
Ensemble	1.26	2.29	1.51	0.98	0.35	0.18	0.42	0.95
MLP-ANN	1.05	2.14	1.46	0.98	0.34	0.17	0.41	0.95

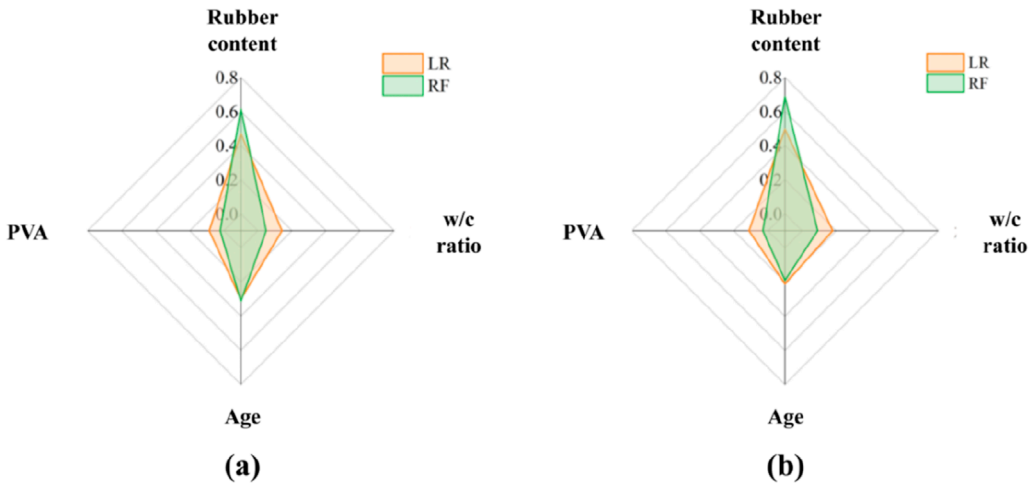

FIGURE 16
Characteristic importance analysis based on line model (LR) and tree model (RF): **(A)** compressive strength; **(B)** flexural strength.

4.4 Characteristic importance analysis

Feature importance analysis in machine learning models can effectively assess the impact of different influencing factors (input features) on the dependent variable (output feature). In the LR model, a series of fitting coefficients for the influencing factors were provided, where the magnitude of these coefficients' absolute values could directly reflect the level of influence of each factor. In the RF model, feature importance was evaluated based on how frequently different influencing factors were used in the tree model or their importance in splitting decisions. Figure 16 presented the normalized importance values of these factors. In both the compressive strength and flexural strength regression prediction models, the feature importance rankings given by the LR and RF models were consistent. The importance rankings for the influencing factors were as follows: rubber content > age > w/c ratio > PVA. The results indicated that rubber content and age were the two most significant variables affecting the compressive and flexural strengths of PVA-modified waste rubber-filled cement-based materials, while the w/c ratio and PVA have relatively smaller effects. The predictions aligned with the findings of Zvonarić et al. (2024) and Liu L. et al. (2023). This served to validate the reliability of the model.

However, not all machine learning models provided self-ranking of features like LR and RF models. Therefore, it was necessary to introduce a special calculation method applicable to any model. In this study, SHAP values were used for additional feature importance analysis. SHAP, which stood for SHapley Additive exPlanations, originated from cooperative game theory (Wang et al., 2024). For each sample to be predicted, the model generated a prediction value, and SHAP values represented the contribution of each feature to this prediction for each sample. The key advantage of SHAP was its ability to reflect the degree of influence of each feature on every sample and to indicate the direction of the feature's effect (positive or negative).

Figure 17 presented the SHAP value analysis for the compressive strength and flexural strength regression models, respectively. For PVA-modified waste rubber-filled cement-based materials, rubber content and age were identified as the two most significant factors, consistent with the feature importance results from the LR and RF models. Additionally, the SHAP values for rubber content and w/c ratio were negative, while age and PVA had positive impacts on the output features. The results suggested

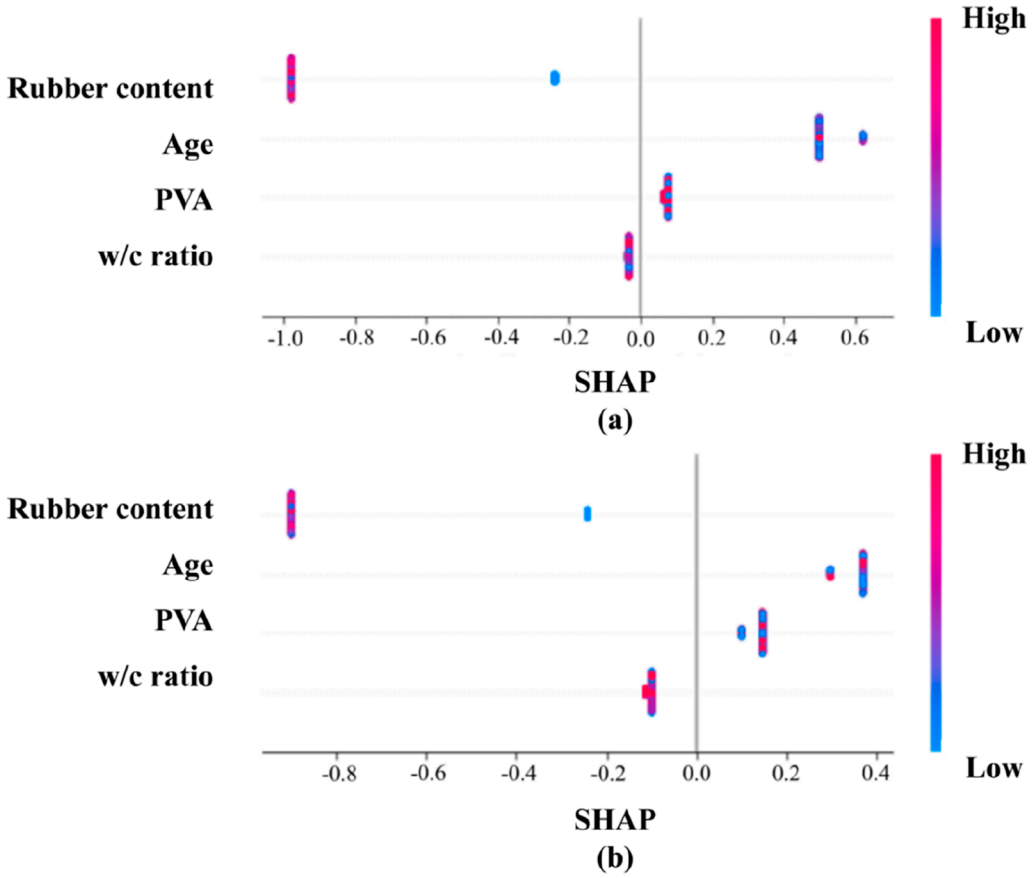

FIGURE 17
Summary charts for SHAP interpretation: **(A)** Compressive strength; **(B)** Flexural strength.

that increasing rubber content and w/c ratio negatively affected the mechanical properties of PVA-modified waste rubber-filled cement-based materials, whereas increasing age and adding PVA significantly positively influence the mechanical properties of the materials. The positive effects of PVA were encouraging. Lotfy et al. (2024) observed that the enhancement in mechanical properties may be attributed to the function of the modified material as a dispersant, which improved the wettability of cement-based materials and accelerated the hydration rate. Conclusions similar to those presented here were reached by Zhu et al. (2024). These findings indicated that the application of PVA represents a novel approach for the modification of rubber-cement-based materials. Indeed, prior research conducted by Niu and colleagues demonstrated that PVA can enhance the toughness of rubber-cement-based materials through a "bridging effect," as substantiated by digital image correlation (DIC) technology (Zhang et al., 2023).

5 Conclusion

Based on experimental data, this study investigated the compressive and flexural strength of cement-based materials filled with PVA-modified waste rubber. The following main conclusions were drawn from the construction and evaluation of various machine learning regression prediction models.

(1) All employed machine learning models demonstrated good performance in predicting the compressive and flexural strength of cement-based materials modified with waste rubber and PVA. Specifically, the Support Vector Regression (SVR) model exhibited superior performance with a mean squared error (*MSE*) of 1.21 and 0.33, and a mean absolute error (*MAE*) of 2.06 and 0.15 on the test set. The prediction errors for this model were consistently within 20%. Overall evaluation metrics indicated that the SVR model achieved the best prediction accuracy and generalization ability compared to other models.

(2) The use of PVA-modified waste rubber significantly enhanced the mechanical strength of cement-based materials. This modification approach provides a means to enhance material performance in practical engineering applications, while also effectively utilizing waste rubber resources, thereby reducing environmental impact. Economically, the application of modified waste rubber can lower material costs and improve the overall performance of the materials.

(3) Analysis using model-internal evaluation metrics and SHAP values revealed that rubber content and water-to-cement ratio negatively correlated with both compressive

and flexural strength, while curing age and PVA showed positive correlations with these strength indicators. Among all influencing factors, rubber content had the most significant impact. Our study indicates that the application of PVA-modified waste rubber in cement-based materials has significant engineering implications and practical value. The SVR model excelled in predicting these effects but attention should be given to the model's sensitivity to certain conditions.

It is worth noting that the model presented in this study may have certain limitations, such as potential overfitting and biases due to hyperparameter tuning, a dataset that may not be sufficiently large due to computational constraints, and a more comprehensive sensitivity analysis of hyperparameters. These limitations will be addressed in future work.

Data availability statement

The original contributions presented in the study are included in the article/supplementary material, further inquiries can be directed to the corresponding author.

Author contributions

ZhH: Writing–original draft, Writing–review and editing. ZW: Investigation, Writing–review and editing. WN: Data curation, Validation, Writing–original draft. FW: Formal Analysis, Investigation, Writing–review and editing. SZ: Data curation, Resources, Writing–original draft. ZeH: Methodology, Validation, Writing–review and editing. QZ: Methodology, Resources, Validation, Writing–review and editing.

Funding

The author(s) declare that no financial support was received for the research, authorship, and/or publication of this article.

Acknowledgments

Financial support from the National Natural Science Foundation of Tianjin under the grant of 21JCZDJC00410 is gratefully acknowledged.

Conflict of interest

Authors ZH, FW, and ZH were employed by Cangzhou Qugang Expressway Construction Co., Ltd.

Author SZ was employed by Fujian Zhanglong Construction Investment Group Co., Ltd.

The remaining authors declare that the research was conducted in the absence of any commercial or financial relationships that could be construed as a potential conflict of interest.

Publisher's note

References

Asteris, P. G., Koopialipoor, M., Armaghani, D. J., Kotsonis, E. A., and Lourenço, P. B. (2021). Prediction of cement-based mortars compressive strength using machine learning techniques. *Neural Comput. Appl.* 33 (19), 13089–13121. doi:10.1007/s00521-021-06004-8

Biswas, R., Kumar, M., Singh, R. K., Alzara, M., El Sayed, S. B. A., Abdelmongy, M., et al. (2023). A novel integrated approach of Runge Kutta optimizer and ANN for estimating compressive strength of self-compacting concrete. *Case Stud. Constr. Mater.* 18, e02163. doi:10.1016/j.cscm.2023.e02163

Cai, R., Han, T., Liao, W., Huang, J., Li, D., Kumar, A., et al. (2020). Prediction of surface chloride concentration of marine concrete using ensemble machine learning. *Cem. Concr. Res.* 136, 106164. doi:10.1016/j.cemconres.2020.106164

Chen, Z., Li, L., and Xiong, Z. (2019). Investigation on the interfacial behaviour between the rubber-cement matrix of the rubberized concrete. *J. Clean. Prod.* 209, 1354–1364. doi:10.1016/j.jclepro.2018.10.305

Cook, R., Han, T., Childers, A., Ryckman, C., Khayat, K., Ma, H., et al. (2021). Machine learning for high-fidelity prediction of cement hydration kinetics in blended systems. *Mater. and Des.* 208, 109920. doi:10.1016/j.matdes.2021.109920

Dong, Q., Huang, B., and Shu, X. (2013). Rubber modified concrete improved by chemically active coating and silane coupling agent. *Constr. Build. Mater.* 48, 116–123. doi:10.1016/j.conbuildmat.2013.06.072

Eldin, N. N., and Senouci, A. B. (1993). Observations on rubberized concrete behavior. *Cem. Concr. Aggregates* 15 (1), 74–84. doi:10.1520/cca10590j

Fan, J., Li, G., Deng, S., and Wang, Z. (2019). Mechanical properties and microstructure of polyvinyl alcohol (PVA) modified cement mortar. *Appl. Sci.* 9 (11), 2178. doi:10.3390/app9112178

Guan, Z., Li, N., Zhang, W., Wang, J., Wang, C., Shen, Q., et al. (2022). A multiple loops machine learning framework to predict the properties of WC–Co based cemented carbides. *Int. J. Refract. Metals Hard Mater.* 104, 105798. doi:10.1016/j.ijrmhm.2022.105798

Han, T., Siddique, A., Khayat, K., Huang, J., and Kumar, A. (2020). An ensemble machine learning approach for prediction and optimization of modulus of elasticity of recycled aggregate concrete. *Constr. Build. Mater.* 244, 118271. doi:10.1016/j.conbuildmat.2020.118271

He, L., Cai, H., Huang, Y., Ma, Y., Van Den Bergh, W., Gaspar, L., et al. (2021). Research on the properties of rubber concrete containing surface-modified rubber powders. *J. Build. Eng.* 35, 101991. doi:10.1016/j.jobe.2020.101991

Huang, J. S., Liew, J. X., and Liew, K. M. (2021). Data-driven machine learning approach for exploring and assessing mechanical properties of carbon nanotube-reinforced cement composites. *Compos. Struct.* 267, 113917. doi:10.1016/j.compstruct.2021.113917

Janiesch, C., Zschech, P., and Heinrich, K. (2021). Machine learning and deep learning. *Electron. Mark.* 31 (3), 685–695. doi:10.1007/s12525-021-00475-2

Konstantopoulos, G., Koumoulos, E. P., and Charitidis, C. A. (2020). Testing novel portland cement formulations with carbon nanotubes and intrinsic properties revelation: nanoindentation analysis with machine learning on microstructure identification. *Nanomater. (Basel)* 10 (4), 645. doi:10.3390/nano10040645

Kumar, R., and Dev, N. (2021). Mechanical and microstructural properties of rubberized concrete after surface modification of waste tire rubber crumb. *Arabian J. Sci. Eng.* 47 (4), 4571–4587. doi:10.1007/s13369-021-06154-w

Kumar, S., Kumar, R., Rai, B., and Samui, P. (2024). Prediction of compressive strength of high-volume fly ash self-compacting concrete with silica fume using machine learning techniques. *Constr. Build. Mater.* 438, 136933. doi:10.1016/j.conbuildmat.2024.136933

Lapeyre, J., Han, T., Wiles, B., Ma, H., Huang, J., Sant, G., et al. (2021). Machine learning enables prompt prediction of hydration kinetics of multicomponent cementitious systems. *Sci. Rep.* 11 (1), 3922. doi:10.1038/s41598-021-83582-6

Li, X., Ling, T.-C., and Hung Mo, K. (2020). Functions and impacts of plastic/rubber wastes as eco-friendly aggregate in concrete – a review. *Constr. Build. Mater.* 240, 117869. doi:10.1016/j.conbuildmat.2019.117869

Li, Y., Shen, J., Li, Y., Wang, K., and Lin, H. (2024). The data-driven research on the autogenous shrinkage of ultra-high performance concrete (UHPC) based on machine learning. *J. Build. Eng.* 82, 108373. doi:10.1016/j.jobe.2023.108373

Lisi, R. D., Park, J. K., and Stier, J. C. (2004). Mitigating nutrient leaching with a sub-surface drainage layer of granulated tires. *Waste Manag.* 24 (8), 831–839. doi:10.1016/j.wasman.2004.03.012

Liu, K., Zhang, L., Wang, W., Zhang, G., Xu, L., Fan, D., et al. (2023a). Development of compressive strength prediction platform for concrete materials based on machine learning techniques. *J. Build. Eng.* 80, 107977. doi:10.1016/j.jobe.2023.107977

Liu, L., Wang, C., Liang, Q., Chen, F., and Zhou, X. (2023b). A state-of-the-art review of rubber modified cement-based materials: cement stabilized base. *J. Clean. Prod.* 392, 136270. doi:10.1016/j.jclepro.2023.136270

Liu, W., Liu, G., and Zhu, X. (2024). Applicability of machine learning algorithms in predicting chloride diffusion in concrete: modeling, evaluation, and feature analysis. *Case Stud. Constr. Mater.* 21, e03573. doi:10.1016/j.cscm.2024.e03573

Lotfy, V. F., Basta, A. H., and Shafik, E. S. (2024). Assessment of the effect of different pulping by-products on enhancing the reuse of rubber waste in producing of cement-mortar. *Int. J. Biol. Macromol.* 256 (Pt 1), 128205. doi:10.1016/j.ijbiomac.2023.128205

Lund, B. C., Abrams, T. E., Gravely, A. A., Carlson, K., and Spoont, M. (2011). Validity of PTSD diagnoses in VA administrative data: comparison of VA administrative PTSD diagnoses to self-reported PTSD Checklist scores. *J. Rehabil. Res. Dev.* 48 (1), 21–30. doi:10.1682/jrrd.2009.08.0116Available at: http://www.rehab.research.va.gov/jour/11/481/pdf/gravely.pdf.

Lunt, M. (2015). Introduction to statistical modelling: linear regression: fig. 1. *Rheumatol. Oxf.* 54 (7), 1137–1140. doi:10.1093/rheumatology/ket146

Mendis, A. S. M., Al-Deen, S., and Ashraf, M. (2017). Behaviour of similar strength crumbed rubber concrete (CRC) mixes with different mix proportions. *Constr. Build. Mater.* 137, 354–366. doi:10.1016/j.conbuildmat.2017.01.125

Mhaya, A. M., Fahim Huseien, G., Faridmehr, I., Razin Zainal Abidin, A., Alyousef, R., and Ismail, M. (2021). Evaluating mechanical properties and impact resistance of modified concrete containing ground Blast Furnace slag and discarded rubber tire crumbs. *Constr. Build. Mater.* 295, 123603. doi:10.1016/j.conbuildmat.2021.123603

Moguerza, J. M., and Muñoz, A. (2006). Support vector machines with applications. *Stat. Sci.* 21 (3). doi:10.1214/088342306000000493

Murthy, Y. I., Meena, K. B., and Patel, N. (2024). Machine learning for predicting the half cell potential of cathodically protected reinforced cement concrete slabs subjected to chloride ingress. *Eng. Appl. Artif. Intell.* 137, 109090. doi:10.1016/j.engappai.2024.109090

Nilsen, V., Pham, L. T., Hibbard, M., Klager, A., Cramer, S. M., and Morgan, D. (2019). Prediction of concrete coefficient of thermal expansion and other properties using machine learning. *Constr. Build. Mater.* 220, 587–595. doi:10.1016/j.conbuildmat.2019.05.006

Ossola, G., and Wojcik, A. (2014). UV modification of tire rubber for use in cementitious composites. *Cem. Concr. Compos.* 52, 34–41. doi:10.1016/j.cemconcomp.2014.04.004

Papazek, P., Schicker, I., Plant, C., Kann, A., and Wang, Y. (2020). Feature selection, ensemble learning, and artificial neural networks for short-range wind speed forecasts. *Meteorol. Z.* 29 (4), 307–322. doi:10.1127/metz/2020/1005

Richardson, A., Coventry, K., Dave, U., and Pienaar, J. (2011). Freeze/thaw performance of concrete using granulated rubber crumb. *J. Green Build.* 6 (1), 83–92. doi:10.3992/jgb.6.1.83

Serban, A., van der Blom, K., Hoos, H., and Visser, J. (2024). Software engineering practices for machine learning — adoption, effects, and team assessment. *J. Syst. Softw.* 209, 111907. doi:10.1016/j.jss.2023.111907

Steyn, Z. C., Babafemi, A. J., Fataar, H., and Combrinck, R. (2021). Concrete containing waste recycled glass, plastic and rubber as sand replacement. *Constr. Build. Mater.* 269, 121242. doi:10.1016/j.conbuildmat.2020.121242

Sukontasukkul, P. (2009). Use of crumb rubber to improve thermal and sound properties of pre-cast concrete panel. *Constr. Build. Mater.* 23 (2), 1084–1092. doi:10.1016/j.conbuildmat.2008.05.021

Surehali, S., Han, T., Huang, J., Kumar, A., and Neithalath, N. (2024). On the use of machine learning and data-transformation methods to predict hydration kinetics and strength of alkali-activated mine tailings-based binders. *Constr. Build. Mater.* 419, 135523. doi:10.1016/j.conbuildmat.2024.135523

Thomas, B. S., and Gupta, R. C. (2015). Long term behaviour of cement concrete containing discarded tire rubber. *J. Clean. Prod.* 102, 78–87. doi:10.1016/j.jclepro.2015.04.072

Tu, P., Li, X., Cao, L., Zhong, M., Xie, Z., and Wu, Z. (2022). Machine learning and BP neural network revealed abnormal B cell infiltration predicts the survival of lung cancer patients. *Front. Oncol.* 12, 882018. doi:10.3389/fonc.2022.882018

Wang, Z., Liu, H., Amin, M. N., Khan, K., Qadir, M. T., and Khan, S. A. (2024). Optimizing machine learning techniques and SHapley Additive exPlanations (SHAP) analysis for the compressive property of self-compacting concrete. *Mater. Today Commun.* 39, 108804. doi:10.1016/j.mtcomm.2024.108804

Xiao, F., Wenbin Zhao, P. E., and Amirkhanian, S. N. (2009). Fatigue behavior of rubberized asphalt concrete mixtures containing warm asphalt additives. *Constr. Build. Mater.* 23 (10), 3144–3151. doi:10.1016/j.conbuildmat.2009.06.036

Yang, S., Sun, J., and Zhifeng, X. (2024). Prediction on compressive strength of recycled aggregate self-compacting concrete by machine learning method. *J. Build. Eng.* 88, 109055. doi:10.1016/j.jobe.2024.109055

Yu, J., Wang, N., Wang, M., Zhang, J., and Hou, D. (2020). Recyclable rubber-cement composites produced by interfacial strengthened strategy from polyvinyl alcohol. *Constr. Build. Mater.* 264, 120541. doi:10.1016/j.conbuildmat.2020.120541

Yu, Y., Li, W., Li, J., and Nguyen, T. N. (2018). A novel optimised self-learning method for compressive strength prediction of high performance concrete. *Constr. Build. Mater.* 184, 229–247. doi:10.1016/j.conbuildmat.2018.06.219

Zhang, J., Niu, W., Yang, Y., Hou, D., and Dong, B. (2023). Research on the mechanical properties of polyvinyl alcohol-modified waste rubber-filled cement paste using digital image correlation technology. *Compos. Struct.* 320, 117164. doi:10.1016/j.compstruct.2023.117164

Zhang, W., Lee, D., Lee, J., and Lee, C. (2021). Residual strength of concrete subjected to fatigue based on machine learning technique. *Struct. Concr.* 23 (4), 2274–2287. doi:10.1002/suco.202100082

Zhang, Z. (2016). A gentle introduction to artificial neural networks. *Ann. Transl. Med.* 4 (19), 370, Oct. doi:10.21037/atm.2016.06.20

Zhou, Z. H. (2022). Open-environment machine learning. *Natl. Sci. Rev.* 9 (8), nwac123. doi:10.1093/nsr/nwac123

Zhu, Z., Zhou, M., Wang, B., and Xu, X. (2024). Enhancing permeability and mechanical properties of rubber cement-based materials through surface modification of waste tire rubber powder. *Constr. Build. Mater.* 425, 136098. doi:10.1016/j.conbuildmat.2024.136098

Zvonarić, M., Barišić, I., and Dokšanović, T. (2024). Effect of rubber granules and rubber threads on mechanical properties of cement-bound base course. *Constr. Build. Mater.* 437, 137094. doi:10.1016/j.conbuildmat.2024.137094

frontiers | Frontiers in Materials

TYPE Original Research
PUBLISHED 16 October 2024
DOI 10.3389/fmats.2024.1490442

OPEN ACCESS

EDITED BY
Biao Hu,
Shenzhen University, China

REVIEWED BY
Chuanqing Fu,
Zhejiang University of Technology, China
Weichao Guo,
Yanshan University, China
Muhan Wang,
Qingdao University of Technology, China

*CORRESPONDENCE
Yang Jiapeng,
1472401892@qq.com

RECEIVED 03 September 2024
ACCEPTED 30 September 2024
PUBLISHED 16 October 2024

CITATION
Shusen Z, Jiapeng Y, Yiyang L, Zhenyu W, Shunjie Z, Liling Z and Tao W (2024) Study on the adhesive property of sludge-modified magnesium phosphate cement reinforcement coating for steel bars.
Front. Mater. 11:1490442.
doi: 10.3389/fmats.2024.1490442

Study on the adhesive property of sludge-modified magnesium phosphate cement reinforcement coating for steel bars

Zhang Shusen[1], Yang Jiapeng[2]*, Li Yiyang[2], Wang Zhenyu[1], Zhong Shunjie[3], Zhuang Liling[3] and Wang Tao[1]

[1]Cangzhou Qugang Expressway Construction Co., Ltd., Cangzhou, Hebei, China, [2]School of Civil Engineering, Tianjin University, Tianjin, China, [3]Fujian Zhanglong Construction Investment Group Co., Ltd., Zhangzhou, Fujian, China

The synergistic interaction inreinforced concrete systems originates from the strong bond between steel reinforcement and concrete, enabling them to collaborateunder load and optimize structural performance. This study applied various sludge-modified magnesium phosphate cement mixtures to the surfaces of plain round steel bars and ribbed steel bars to prepare steel-reinforced concrete specimens. The characterization of the bond performance of the sludge-modified magnesium phosphate cement reinforcement coating for steel bars and concrete was achieved through analyzing the failure modes, bond strength, and slip values of different groups. Microscopic analysis was performed using a scanning electron microscope. The results revealed that the primary failure mode of the steel-reinforced concrete specimens was steel bar pull-out, with some specimens exhibiting concrete splitting failure. Coating application on plain round steel bars increased bond strength, while on ribbed steel bars, it decreased bond strength. The application of the coating slightly reduced slip values to some extent.

KEYWORDS

magnesium phosphate cement, reinforcement coating, adhesive property, sludge, mechanical properties

1 Introduction

The reinforced concrete system can form a good working system cooperation work because there is a good bond between the steel bar and the concrete. The steel bar and concrete can work together when the force is loaded, and the best structural performance of the system can be observed. Good adhesive properties guarantee the most basic safety, shock resistance, durability, maintenance, and operating costs of reinforced concrete structures and quality control during construction. There is a good bond stress between the reinforcement and concrete, which is generally provided by the following aspects (Zhao and Jin, 2002; Yang et al., 2013; Haque and Chen, 2019; Nobre et al., 2020).

In reinforced concrete structures, bonding stress between the concrete and steel reinforcement is primarily facilitated by chemical adhesion, mechanical

bite force, and friction. Chemical adhesion results from the hydration reaction of cement with steel surfaces, forming a solid interface. Mechanical bite force, especially crucial for ribbed steel bars, relies on surface properties and internal pressure to enhance the bond strength. Friction force, generated when concrete envelops steel bars and resists relative movement, is influenced by extrusion pressure, surface roughness, and concrete shrinkage. Chemical bonding is typically minimal, with round bars relying more on friction and ribbed bars on mechanical bite force for effective bonding (Jiang and Qiu, 2012; Yang, 2018; Szewczak et al., 2020).

Magnesium phosphate cement (MPC) differs from traditional Portland cement, possessing unique hydration and hardening characteristics (Bodong et al., 2023; Xiangrui et al., 2023; Xin et al., 2022). Due to its ceramic-like properties, MPC is also referred to as chemically bonded magnesium phosphate ceramics. MPC is typically produced through an acid–base neutralization reaction between calcined magnesium oxide and water-soluble acid phosphate. It offers several advantages, including rapid setting and hardening, high early strength, good volumetric stability, strong bond strength, and excellent resistance to chloride and sulfate ions. These properties make MPC widely applicable in structural repair and reinforcement, bioceramics, radioactive and hazardous waste containment, manufacturing embedded mold materials, and protective coatings. MPC is particularly favored for use in protective coatings due to its unique combination of fast hardening, strong adhesion, and superior fire and corrosion resistance. Recent studies have further demonstrated that MPC exhibits a high degree of similarity with ordinary Portland cement in terms of the thermal expansion coefficient and volume compatibility. As a result, MPC is well-suited for producing anti-corrosion coatings to protect reinforced concrete from degradation (Wang et al., 2021; Jun et al., 2019; Kytinou et al., 2020; Xiaoming et al., 2023; Zhang et al., 2023).

Yang Haiyan applied a magnesium phosphate cement coating with a thickness of approximately 500 μm on the surface of Q235 steel (Yang, 2018). Through electrochemical tests and salt spray tests, it was proven that the magnesium phosphate cement coating has a good anti-corrosion protection effect on Q235 steel, and the magnesium phosphate cement coating with the combination of silica ash and Al_2O_3 is better in corrosion resistance. Li studied the sulfate attack resistance of concrete coated with coating, magnesium phosphate cement coating, and epoxy coating, and the results indicated that the structure and composition of the MPC coating changed under the sulfate attack environment. The MPC coating made concrete bonds more tightly, and the structure was more compact than in other environments, which significantly corroded the sulfate protection effect of concrete. The MPC coating can significantly improve the sulfate resistance of concrete than epoxy coating (Jun et al., 2019). Tang studied the protective effect of magnesium phosphate cement on steel corrosion in the restoration of reinforced concrete structures, and the results indicated that MPC has a good protective effect on steel corrosion, which might be due to the newly formed protective film on the steel surface. In addition, the related reactions between phosphate and Fe^2+ ions may play an important role in the formation of the protective film and effectively reduce the corrosion rate (Tang et al., 2020). Yang Quan Bing studied the ability of magnesium phosphate cement mortar, ordinary Portland cement, and slag cement to prevent corrosion of steel bars. The results indicated that after six dry–wet cycles, the corrosion rate of magnesium phosphate cement mortar was only 0.18%, which was only 22.8% of that of ordinary Portland cement and 48.6% of that of slag cement (Yang et al., 2000). Xiangdong made a reinforced concrete specimen coated with epoxy coating. By controlling the steel bar diameter and effective bond length, the influence on the bond performance of the specimen was analyzed, and the relevant bond strength calculation formula was proposed (Yang, 2018). Jones analyzed and studied the influence of various factors on the bond strength between epoxy-coated steel bars and high-performance concrete. Based on the analysis of these data, he put forward relevant suggestions for modifying the current formula (Jones and Ramirez, 2016). Zhang conducted a pull-out test on the bond performance of FRP bars and concrete and analyzed the bond slip constitutive model of ribbed FRP bars and plain bars. The failure forms of the specimens are sliding and pulling out of FRP bars and breaking of FRP bars. With the decrease in the surface reinforcement and anchorage length of FRP bars and the increase in concrete strength, the average bond strength between FRP bars and concrete increases (Yongkang and Xiaoming, 2012).

Sludge, as an inert admixture, can be used to modify magnesium phosphate cement, effectively extending its setting time and enhancing its early mechanical properties. Additionally, sludge can be applied directly as an anti-corrosion coating on the surface of steel bars, providing significant protection and improving their corrosion resistance. However, there is limited research on the adhesive properties between sludge-modified magnesium phosphate cement coatings and concrete. Therefore, this study employs pull-out tests as the core experimental framework to evaluate and analyze the adhesive properties of modified magnesium phosphate cement coatings with varying sludge contents by preparing pull-out test specimens (Ryu et al., 2024; Guan et al., 2024; Furong et al., 2024; Pavlíková et al., 2020).

2 Materials and methods

2.1 Experimental material

The re-fired magnesia produced by Jinan Ludong Refractory Material Co., Ltd. is calcined and ground into magnesia powder at 1700°C for the preparation of magnesia phosphate cement. The powder is brownish yellow. Potassium dihydrogen phosphate (KH_2PO_4) produced by Sinophosphate Chemical Reagent Co., LTD. is a white powder, easily soluble in water at room temperature. Prior to experimentation, the sludge obtained from the desiccation project at Yuecheng Reservoir in Cixian County, Handan City, Hebei Province, requires activation. The activation process involves drying the sludge in a drying box, followed by ball milling to produce a brown and yellow powder. Subsequently, the powder undergoes calcination in a high-temperature furnace before being subjected to ball milling again. The chemical composition of the resulting material is detailed in the table below. The chemical composition of the material is shown in Tables 1, 2 (Lv et al., 2024a; Lv et al., 2024b; Lv et al., 2024c).

P.O.42.5 ordinary Portland cement, produced by the Tangshan Yanshan Cement Factory, was selected for the concrete preparation.

TABLE 1 Chemical composition of MgO (%).

MgO	SiO_2	CaO	Fe_2O_3	Al_2O_3	Loi
89.65	5.18	2.94	1.04	1.04	1.03

Crushed stone and river sand were used as aggregates, with the stone having a uniform particle size range of 5–25 mm and the river sand featuring continuous grading with a maximum particle size of 5 mm. The chemical composition of the cement is presented in Table 3 below.

2.2 Mix ratio design

Due to the small particle size of the sludge, even a small amount can significantly affect the flow behavior of the MPC system. Therefore, in this study, while varying the sludge content in different groups, the flowability of each group was kept consistent. The MG-P molar ratio of the magnesium phosphate cement in the sludge-free group was maintained at 8.5, and the combined mass of the sludge and MgO in the sludge-containing groups was controlled to 2.5, ensuring uniform fluidity across all groups. The specific proportions of MPC with varying sludge contents used in the experiment are presented in Table 4. Additionally, uncoated steel bars (Group C) were prepared as a control group.

The concrete design strength of the drawing specimen is C40 concrete, and the mix ratio per cubic meter of concrete is calculated according to JG55-2011"Ordinary Concrete Mix ratio Design Regulations", as shown in Table 5 below.

2.3 Specimen preparation

Production of magnesium phosphate cement: Magnesium phosphate cement is prepared according to the modified mix ratio detailed in Table 4. Initially, the required amounts of magnesium oxide, phosphate, and sludge are weighed according to the ratios specified. These materials are then placed into a cement slurry mixer and mixed at a slow speed for 60 s to ensure thorough and uniform blending of the dry components. Next, water, measured according to the mix ratio, is added to the mixer and stirred at a slow speed for another 60 s. The mixing is paused, and any remaining material adhering to the blade and walls of the pot is scraped down into the mixer by using a shovel. The mixture is then stirred for an additional 60 s to achieve uniform consistency. After mixing, the modified magnesium phosphate cement is ready for use.

Coating steel bar production: Given the rapid setting and hardening characteristics of magnesium phosphate cement, the coating process must be executed promptly. First, the prepared magnesium phosphate cement is introduced into a semi-circular PVC pipe. The steel bar is then rotated within the PVC pipe to ensure a complete and even coating of the magnesium phosphate cement on its surface. Finally, the mixing pot and PVC pipe are thoroughly cleaned to remove any residual material.

Coating of steel bars: Due to the rapid setting and hardening of MPC, the coating process should be performed swiftly, with the entire operation completed within 5 min. First, the prepared MPC is placed into a semi-circular PVC pipe, and the steel bar is rotated within the PVC pipe to ensure that the surface is uniformly coated with MPC. The consistent flowability of the slurry ensures a uniform coating thickness of approximately 1 mm. The coated steel bars are then cured under indoor air conditions (25°C ± 2°C, RH 70% ± 5%). Finally, the mixing bowl and PVC pipe are thoroughly cleaned.

Drawing test piece production: For the preparation of drawing test pieces for reinforced concrete, use steel bars with a diameter of 10 mm and a length of 500 mm, and pour concrete into molds to create cubes measuring 150 mm × 150 mm × 150 mm. Insert one end of the steel bar into the mold to a depth of 100 mm, with the other end extending 250 mm, and set the protective layer thickness to 75 mm. To minimize experimental errors, place a PVC pipe of 50 mm length at each end of the steel bar. The effective bonding length between the steel bar and concrete is set to 5 d (where d is the diameter of the steel bar; thus, 5 d equals 50 mm). The specific mold is depicted in Figure 1. First, apply a release agent to the inside of the plastic mold. Next, accurately weigh the required amounts of cement, aggregate, and sand according to the mix ratio, and combine them in the concrete mixing pot. Perform a dry mix for 90 s to ensure uniform distribution of the dry materials. Add the measured water, and mix until the concrete achieves the desired flow and consistency. Pour the mixed concrete into the pre-oiled plastic mold, position the mold in the center of a shaking table, and use a scraper to remove excess concrete while vibrating the mold to ensure proper compaction.

2.4 Experimental method

The central drawing test device used a WAW-1000A microcomputer controlled electro-hydraulic servo universal testing machine to load the specimen and customized the drawing fixture with matching size according to the specifications of the loading device. Before loading, the specimen was passed through the drawing fixture, the upper end of the loading test machine tightened the fixture, and the lower end of the clamping steel bar loading device is shown in Figure 2 below. The loading mode was set as displacement loading, and a dial gage was fixed at the free end of the reinforced concrete specimen to test the relative slip between the reinforcement and concrete. During the experiment, when the free slip end exceeds the specified value, the concrete cracks or the steel bar is pulled apart, the loading is stopped and the load and the dial indicator are recorded at this time, and then the loading of the next specimen is continued.

Scanning electron microscopy (SEM) was used to analyze the magnesium phosphate cement modified with different amounts of sludge and to explain the influence on the adhesive properties at the microscopic level. The EDS point spraying method was used to analyze the chemical element composition of the modified magnesium phosphate cement and to explain the effect of the modified magnesium phosphate cement with different amounts of sludge.

TABLE 2 Chemical composition of sludge (%).

Al_2O_3	SiO_2	Fe_2O_3	CaO	MgO	CO_2	Na_2O	Loi
17.3	56.1	7.9	9.2	3.3	5.9	0.3	5.9

TABLE 3 Chemical composition of cement (%).

Al_2O_3	SiO_2	Fe_2O_3	CaO	MgO	SO_3	f-CaO	Loi
5.03	20.58	3.38	63.32	2.01	2.06	0.68	1.76

TABLE 4 Design of the mixing ratio of sludge-modified magnesium phosphate cement.

Number	MgO (%)	Sludge (%)	Water cement ratio	MgO + sludge/KH_2PO_4
MS-0	100	0	0.23	2.5
MS-5	95	5	0.235	
MS-10	90	10	0.24	
MS-15	85	15	0.25	
MS-20	80	20	0.26	
MS-25	75	25	0.27	
MS-30	70	30	0.275	

TABLE 5 Concrete mix design (kg/m^3).

Cement	Pebble	Sand	Water
500	750	900	200

FIGURE 1
Specimen mold.

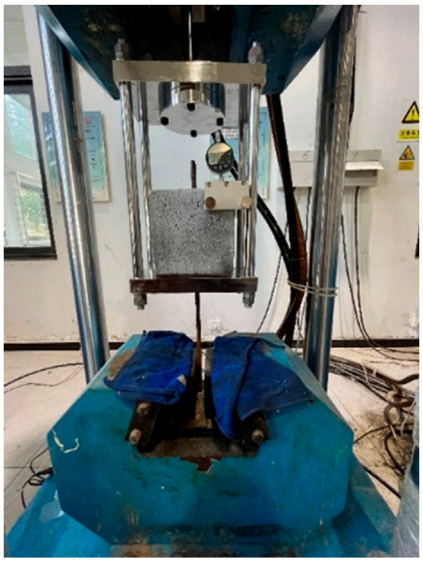

FIGURE 2
Experimental loading.

FIGURE 3
Center pull-out failure.

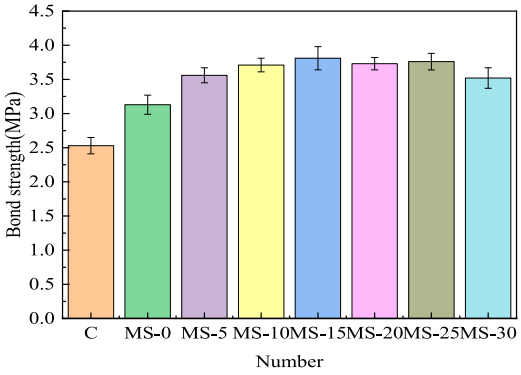

FIGURE 4
Bond strength of the round steel bar.

3 Results and discussion

3.1 Failure mode

During the experimental loading, all 24 pull-out specimens of circular steel bars exhibited central pull-out failure, as illustrated in Figure 3. This indicates that there was a slip between the steel bars and the concrete, and the PVC pipes at both ends of the steel bars also experienced some degree of slip. This failure mode suggests that the friction force between the steel bars and the concrete was insufficient to overcome the applied tensile stress, leading to the direct pull-out of the steel bars due to low bond strength. For the 24 ribbed steel bar pull-out specimens, those with a coating on the surface also displayed central pull-out failure. However, the specimens with uncoated surfaces exhibited splitting failure, primarily due to the high mechanical bite force between the ribs of the ribbed steel bars and the concrete. This high bond strength between the steel bars and concrete is maintained until the tensile stress of the concrete exceeds its tensile and cracking strength, resulting in splitting failure. When the surface of the ribbed steel bars is coated, the mechanical bite force between the ribs and the steel bars is disrupted. In all groups, there was no evidence of peeling or detachment between the magnesium phosphate cement coating and the steel bars, indicating that the bond strength between the magnesium phosphate cement and the steel bars is robust. This suggests that the coating adheres well to the steel bar surface, providing effective protection (Yang et al., 2002; Li et al., 2021).

3.2 Bond strength

Since the central drawing test was used for test loading in all experiments and the length of the bonding section between reinforcement and concrete was small, the bonding stress between the reinforcement and concrete was approximately regarded as uniformly distributed, and the following Formula 1–1 was used to calculate the bonding stress. The labels MS-0, MS-5, MS-10, MS-15, MS-20, MS-25, and MS-30 represent the sludge contents of 0, 5%, 10%, 15%, 20%, 25%, and 30%, respectively.

$$\tau = \frac{P}{\pi dl}. \quad (1)$$

In the above formula, τ represents the calculated bond stress, and the unit is MPa.

P represents the measured drawing force, and the unit is N.

d represents the diameter of the coated steel bar, expressed in mm.

l is the length of the effective bonding section, expressed in mm.

The bond strength of modified magnesium phosphate cement with varying sludge contents, applied to smooth round steel bars, is illustrated in Figure 4. Without the magnesium phosphate cement coating, the bond strength of the smooth round steel bar is the lowest, at 2.53 MPa. With the addition of sludge at 0%, 5%, 10%, 15%, 20%, 25%, and 30%, the bond strengths increased to 3.13 MPa, 3.56 MPa, 3.71 MPa, 3.81 MPa, 3.73 MPa, 3.76 MPa, and 3.52 MPa, respectively. The corresponding bond strength increases were 23.7%, 40.7%, 46.6%, 50.6%, 47.4%, 48.6%, and 39.1%, respectively. These data indicate that the inclusion of sludge significantly enhances the bond strength between the modified magnesium phosphate cement-coated steel bars and concrete, with the optimal bond performance achieved at a sludge content of 15%. However, further increases in sludge content have a diminishing effect on bond performance. The observed improvement in bond strength with the magnesium phosphate cement coating is primarily due to the increased friction force between the smooth steel bars and the concrete, which is related to the roughness of the contact surface. The coating introduces surface irregularities and pores, which enhance bond strength. Additionally, research by Tang Hao supports these findings, highlighting that magnesium phosphate cement exhibits strong adhesive properties with steel bars and forms a dense bonding layer on the steel surface, further contributing to the increased bond strength observed with the coating (Tang et al., 2020).

The bond strength of modified magnesium phosphate cement applied to ribbed steel bars with varying sludge contents is depicted in Figure 5. The data clearly show that the bond strength behavior

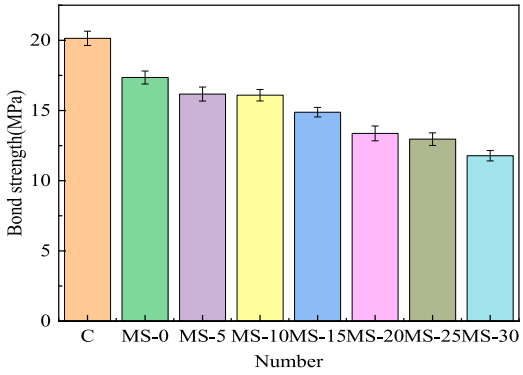

FIGURE 5
Bond strength of the ribbed steel bar.

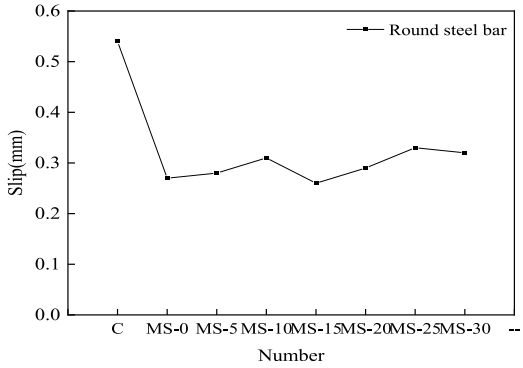

FIGURE 6
Slip of the round steel bar.

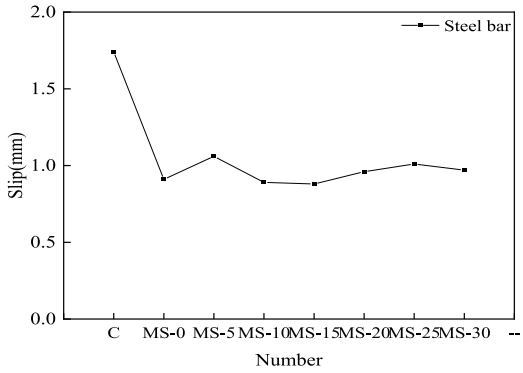

FIGURE 7
Slip of the ribbed steel bar.

of ribbed steel bars is opposite to that of smooth round steel bars. For ribbed steel bars without coating, the bond strength is the highest at 21.83 MPa. As sludge is added, the bond strength of the ribbed steel bars gradually decreases. Specifically, with sludge contents of 0%, 5%, 10%, 15%, 20%, 25%, and 30%, the bond strengths are 17.35 MPa, 16.17 MPa, 16.09 MPa, 14.88 MPa, 13.37 MPa, 12.96 MPa, and 11.78 MPa, respectively. The reductions in bond strength are 20.5%, 25.9%, 26.3%, 31.8%, 38.8%, 40.6%, and 46.0%, respectively. The significant reduction in the bond strength of coated ribbed steel bars is attributed to the disruption of the mechanical biting force between the ribs and the concrete. In uncoated ribbed steel bars, the bond strength is primarily supported by this mechanical biting force. However, when the modified magnesium phosphate cement coating is applied, it interferes with the biting force, leading to a reliance on friction force and the diminished mechanical bite force, ultimately reducing the overall bond strength (Mathern and Yang, 2021; Chen et al., 2023).

Comparing the two types of steel bars reveals that the adhesive properties of smooth round steel bars improve with the application of modified magnesium phosphate cement coating. Conversely, the adhesive properties of ribbed steel bars decrease with the same coating. This difference is primarily related to the nature of the bond between each type of steel bar and the concrete. While coating ribbed steel bars in engineering applications can enhance their corrosion protection, it may also lead to a reduction in bond strength. Therefore, a careful evaluation and analysis are necessary to balance the benefits of improved corrosion resistance with the potential decrease in bond strength during application.

3.3 Slippage

Figure 6 illustrates the slippage of smooth round steel bars coated with modified magnesium phosphate cement containing varying sludge contents. For smooth round steel bars, the bond stress between the steel bar and the concrete is primarily provided by friction force. The data show that the slip amount for uncoated steel bars is the largest, reaching 0.54 mm. When modified magnesium phosphate cement is applied, the slip amount decreases significantly. Specifically, for sludge contents of 0%, 5%, 10%, 15%, 20%, 25%, and 30%, the slip amounts are 0.27 mm, 0.28 mm, 0.31 mm, 0.26 mm, 0.29 mm, 0.33 mm, and 0.32 mm, respectively. Analysis of the different sludge contents indicates that there is minimal variation in the slip amount across the different groups, suggesting that the sludge content has little impact on the slip of the modified magnesium phosphate cement-coated round steel bars. During the test loading process, there is no significant slip observed in the initial stages; however, as loading progresses, the uncoated group experiences substantial slip due to inadequate bonding force between the steel bar and the concrete. Coating the steel bar surface improves the roughness of the contact surface, thereby reducing slip when the maximum load is reached. Overall, applying a modified magnesium phosphate cement coating to the surface of smooth round steel bars effectively enhances the bond strength between the steel bar and concrete, reducing relative slip. This treatment not only improves the corrosion resistance of the steel bars but also increases the bond strength with the concrete (Xiang and Yang, 2023; He and Lu, 2024a).

Figure 7 illustrates the slippage of ribbed steel bars coated with modified magnesium phosphate cement containing various sludge contents. For ribbed steel bars, the bond stress is primarily provided by the mechanical biting force between the ribs and the

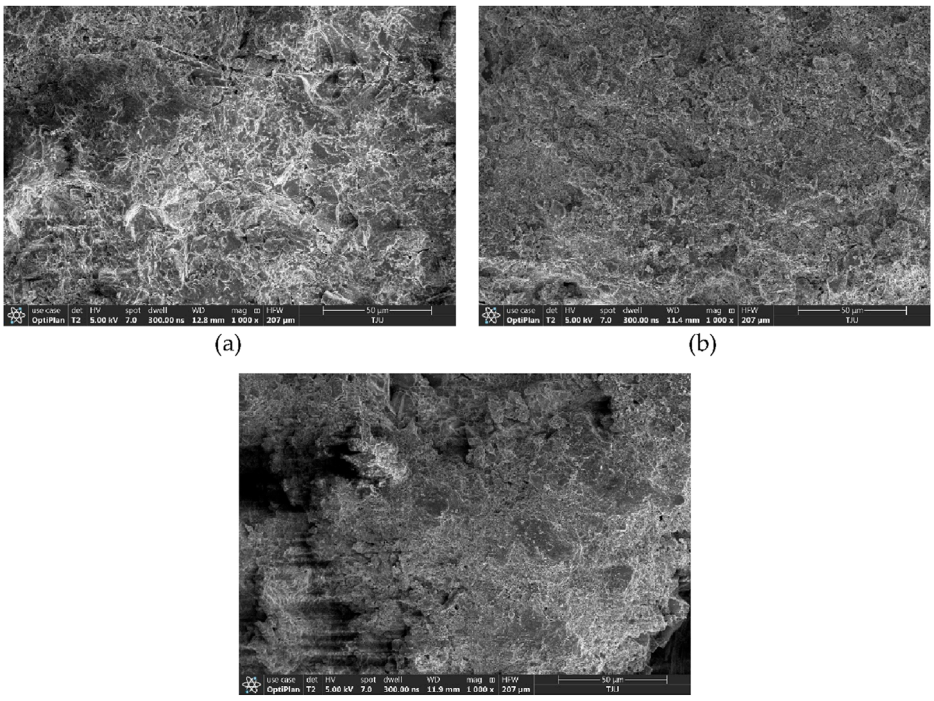

FIGURE 8
SEM images of MPC modified by sludge **(A)** 0%; **(B)** 15%; and **(C)** 30%.

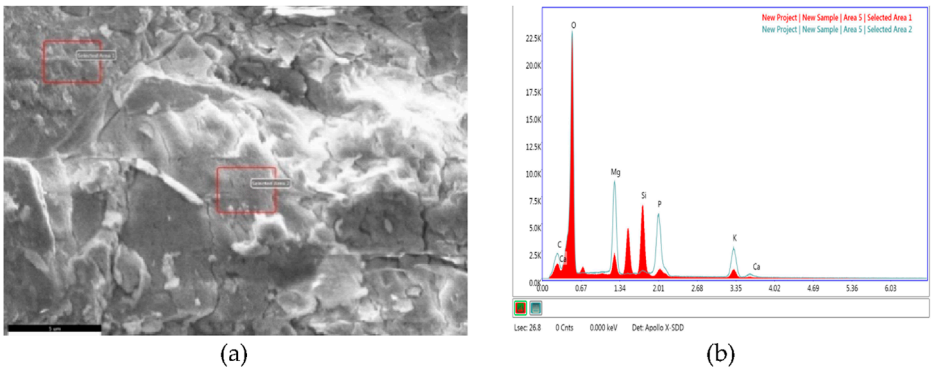

FIGURE 9
EDS test **(A)** test area and **(B)** elemental analysis.

concrete. The slip amount for the uncoated group is 1.74 mm. With the application of modified magnesium phosphate cement coating, the slip amount decreases to some extent. Specifically, with sludge contents of 0%, 5%, 10%, 15%, 20%, 25%, and 30%, the slip amounts are 0.91 mm, 1.06 mm, 0.89 mm, 0.88 mm, 0.96 mm, 1.01 mm, and 0.97 mm, respectively. The sludge content has a minimal effect on the slippage of ribbed steel bars, similar to the trend observed with smooth round steel bars. Ribbed steel bars, due to their threaded surface, generate significant mechanical biting force with the concrete. However, when the surface of the steel bars is coated, the uniform coating reduces the mechanical biting force between the coated steel bars and the concrete, which diminishes the bond performance and decreases slip amount. Consequently, the slip amount is reduced when the maximum load is reached (He et al., 2024; He and Lu, 2024b).

When smooth round and ribbed steel bars are uncoated, the slip amount of the smooth round steel bar is relatively small. This is due to the lower bond strength between the smooth round steel bar and the concrete, resulting in minimal slip when the loading process reaches its maximum load. After coating, the slippage of both types of steel bars decreases, indicating that the coating effectively reduces the relative slippage between the steel bars and the concrete. This reduction in slip contributes to improved structural stability.

3.4 Microanalysis

Figure 8 displays SEM images of modified magnesium phosphate cement with varying sludge contents. The images reveal that struvite, the primary hydration product of magnesium phosphate cement, predominantly exhibits a sheet-like structure. The overall structure consists of a spatial arrangement formed by magnesium oxide and struvite, which has not undergone further hydration. Comparison of SEM images across different sludge contents shows that pure magnesium phosphate cement has notable voids and large pores. At a sludge content of 15%, the overall compaction of the structure significantly improves. However, as the sludge content increases to 30%, the amount of struvite decreases, and some voids and pores become evident. This phenomenon is primarily due to the fact that the main component of sludge is inactive quartz (SiO_2), and the sludge particles are small. On one hand, the inactive sludge can adhere fully to the surface of magnesium oxide, extending the time the water remains in contact with the material, which enhances the hydration reaction. This leads to the formation of more guanolite, increasing the density and reducing porosity. On the other hand, the small particle size of the sludge allows it to function as an inactive filler material, filling gaps between struvite and magnesium oxide. This increases the overall density of the structure and further reduces porosity. However, when the sludge content is too much, it will replace part of the amount of magnesium oxide, resulting in insufficient reaction material and a reduction in the amount of struvite as a hydration product. Through SEM analysis, it is explained that the bond strength of the smooth round steel bar reaches the maximum when the sludge content is 15%, but decreases when the sludge content is 30%.

Figure 9 presents the correlation analysis of modified magnesium phosphate cement with 30% sludge content, conducted via EDS point scanning. The analysis reveals that as the sludge content increases, the proportion of silicon (Si) in the cement matrix increases. This is attributed to the high SiO_2 content in the sludge, which causes a decrease in the magnesium-to-phosphorus (Mg/P) ratio. After 7 days of curing, the Si content in region 1 of the sample with 30% sludge is 18.46%. This indicates that excessive sludge can displace magnesium oxide, leading to an insufficient amount of magnesium oxide and resulting in inadequate hydration reactions. Consequently, there is a reduced formation of struvite, leading to a less complete structure with numerous pores and cracks. Additionally, the excess sludge negatively impacts structural densification and reduces the bond strength of the smooth round steel bars.

4 Conclusion

(1) The primary failure mode of the reinforced concrete specimens is reinforcement pull-out failure, with some groups exhibiting concrete splitting failure. This occurs mainly because the friction between the circular steel bars (both coated and uncoated) and the concrete is insufficient to overcome the applied tensile stress, leading to pull-out failure. However, ribbed steel bars experience splitting failure due to the high mechanical interlock force between the ribs and the concrete.

(2) Based on the bond strength analysis of each group, the bond strength of smooth round steel bars improves after coating, primarily due to the increased roughness of the contact surface, which enhances friction and bond strength. In contrast, coating ribbed steel bars reduces their bond strength, as the coating disrupts the mechanical interlock between the ribs and the concrete, weakening the bond.

(3) Analysis of the slip amounts for each group shows that applying a modified coating to the steel bar surface reduces slippage to some extent. However, the sludge content generally has little impact on slip amounts, as the coating alters the friction and mechanical interlock between the steel bar and concrete, which in turn affects slippage.

(4) According to SEM/EDS microscopic analysis, the main components of magnesium phosphate cement are magnesium oxide and struvite. The addition of sludge acts as a filler, reducing porosity and increasing the densification of the cement. However, excessive sludge can introduce cracks and voids. EDS spectrum analysis indicates that as sludge content increases, the proportion of silicon (Si) also increases, which leads to reduced magnesium oxide content and an incomplete hydration reaction, resulting in insufficient struvite formation.

Data availability statement

The original contributions presented in the study are included in the article/Supplementary Material; further inquiries can be directed to the corresponding author.

Author contributions

ZaS: conceptualization, methodology, project administration, visualization, and writing–review and editing. YJ: conceptualization, resources, supervision, and writing–review and editing. LY: funding acquisition and writing–original draft. WZ: validation and writing–original draft. ZoS: validation and writing–original draft. ZL: data curation, validation, and writing–original draft. WT: validation, visualization, and writing–review and editing.

Funding

The author(s) declare that financial support was received for the research, authorship, and/or publication of this article. This research was funded by the Natural Science Foundation of Tianjin Municipality, grant numbers (21jczdjc00410 and 22jcybjc00620).

Conflict of interest

Authors ZaS, WZ, and WT were employed by Cangzhou Quangang Expressway Construction Co., Ltd. Authors ZoS and ZL were employed by Fujian Zhanglong Construction Investment Group Co., Ltd.

The remaining authors declare that the research was conducted in the absence of any commercial or financial relationships that could be construed as a potential conflict of interest.

Publisher's note

References

Bodong, F., Zhuojun, H., Tao, S., Yanming, L., Xian, W., Daping, Y., et al. (2023). Research progress on the properties and applications of magnesium phosphate cement. *Ceram. Int.* 49 (3), 4001–4016. doi:10.1016/j.ceramint.2022.11.078

Chen, Y., Wang, Z., Lin, Y., Wang, H., and Hua, L. (2023). Theoretical modeling and experimental verification of the bending deformation of fiber metal laminates. *Materials* 16 (9), 3486. doi:10.3390/ma16093486

Furong, L., Guoxing, C., Guizhong, X., and Yongyi, W. (2024). An experimental study on the compressive dynamic performance of polypropylene fiber reinforced concrete for retaining structure under automobile collision magnitude. *Adv. Civ. Eng.* 2020. doi:10.1155/2020/8826006

Guan, G., Wang, X., Xin, M., Sun, C., Zhang, Q., and He, J. (2024). Study on the bonding performance of BFRP bars with seawater sand concrete. *Materials* 17 (3), 543. doi:10.3390/ma17030543

Haque, M. A., and Chen, B. (2019). Research progresses on magnesium phosphate cement: a review. *Constr. Build. Mater.* 211, 885–898. doi:10.1016/j.conbuildmat.2019.03.304

He, R., and Lu, N. (2024a). Air void system and freezing-thawing resistance of concrete composite with the incorporation of thermo-expansive polymeric microspheres. *Constr. Build. Mater.* 419, 135535. doi:10.1016/j.conbuildmat.2024.135535

He, R., and Lu, N. (2024b). Hydration, fresh, mechanical, and freeze-thaw properties of cement mortar incorporated with polymeric microspheres. *Adv. Compos. Hybrid Mater.* 7 (3), 92. doi:10.1007/s42114-024-00899-2

He, R., Nantung, T., and Lu, N. (2024). Unraveling microstructural evolution in air-entrained mortar and paste: insights from MIP and micro-CT tomography amid cyclic freezing-thawing damage. *J. Build. Eng.* 94, 109922. doi:10.1016/j.jobe.2024.109922

Jiang, D., and Qiu, H. (2012). Test study on bonding performance of reinforced concrete anchorage zone under repeated loads, 33(9), 127–135.

Jones, J., and Ramirez, J. A. (2016). Bond of reinforcement in high-strength concrete. *ACI Struct. J.* 113 (3), 549–556. doi:10.14359/51688620

Jun, L., Yongsheng, J., Linglei, Z., and Benlin, L. (2019). Resistance to sulfate attack of magnesium phosphate cement-coated concrete. *Constr. Build. Mater.* 195, 156–164. doi:10.1016/j.conbuildmat.2018.11.071

Kytinou, V. K., Chalioris, C. E., and Karayannis, C. G. (2020). Analysis of residual flexural stiffness of steel fiber-reinforced concrete beams with steel reinforcement. *Materials* 13 (12), 2698. doi:10.3390/ma13122698

Li, H., Guo, X., and Duan, J. (2021). Numerical simulation of steel-reinforced reactive powder concrete beam based on bond-slip. *Materials* 14 (15), 4176. doi:10.3390/ma14154176

Lv, T., Zhang, J., Hou, D., Long, W.-J., and Dong, B. (2024a). Mechanical properties and microstructural characteristics of seawater-mixed sintered sludge cement paste. *Constr. Build. Mater.* 414, 134996. doi:10.1016/j.conbuildmat.2024.134996

Lv, T., Zhang, J., Xu, L., Hou, D., Long, W.-J., and Dong, B. (2024c). Hydration behavior and chloride binding of seawater-mixed sintered sludge cement paste: experimental and thermodynamic study. *Constr. Build. Mater.* 426, 136170. doi:10.1016/j.conbuildmat.2024.136170

Lv, T., Zhang, J., Zhao, M., Yang, J., Hou, D., and Dong, B. (2024b). Utilization of sintered sludge ash with different mechanical–thermal activation parameters as a supplementary cementitious material: mechanical properties and life cycle assessment of cement-based paste. *Materials* 17 (16), 4101. doi:10.3390/ma17164101

Mathern, A., and Yang, J. (2021). A practical finite element modeling strategy to capture cracking and crushing behavior of reinforced concrete structures. *Materials* 14 (3), 506. doi:10.3390/ma14030506

Nobre, J., Ahmed, H., Bravo, M., Evangelista, L., and de Brito, J. (2020). Magnesia (MgO) production and characterization, and its influence on the performance of cementitious materials: a review. *Materials* 13 (21), 4752. doi:10.3390/ma13214752

Pavlíková, M., Pivák, A., Záleská, M., Jankovský, O., Reiterman, P., and Pavlík, Z. (2020). Magnesium oxychloride cement composites lightened with granulated scrap tires and expanded glass. *Materials* 13 (21), 4828. doi:10.3390/ma13214828

Ryu, J.-C., Lee, C.-J., Shin, D.-H., and Ko, D.-C. (2024). Prediction of the interface behavior of a steel/CFRP hybrid Part Manufactured by stamping. *Materials* 17 (17), 4291. doi:10.3390/ma17174291

Szewczak, I., Rzeszut, K., Rozylo, P., and Snela, M. (2020). Laboratory and numerical analysis of steel cold-formed sigma beams retrofitted by bonded CFRP Tapes—extended research. *Materials* 13 (21), 4960. doi:10.3390/ma13214960

Tang, H., Qian, J., Ji, Z., Dai, X., and Li, Z. (2020). The protective effect of magnesium phosphate cement on steel corrosion. *Constr. Build. Mater.* 255, 119422. doi:10.1016/j.conbuildmat.2020.119422

Wang, H., Yan, P., and Guan, Y. (2021). Robust heterojunctions of metallic alloy and carbon fiber-reinforced composite induced by laser processing. *Materials* 14 (23), 7469. doi:10.3390/ma14237469

Xiang, D., and Yang, Y. (2023). Study on calculation of bond-slip performance and strength of C50 concrete epoxy coating steel bars. *Industrial Saf. Environ. Prot.* 39 (09), 39–43.

Xiangrui, M., Yu, J., Bing, C., and Liyan, W. (2023). Research progress on the setting time and solidification mechanism of magnesium phosphate cement: a review. *Constr. Build. Mater.* 408, 133612. doi:10.1016/j.conbuildmat.2023.133612

Xiaoming, H., Guodong, L., Yangzezhi, Z., and Haoyuan, L. (2023). The performance of magnesium phosphate cement in negative temperature environment: a state-of-the-art review. *J. Build. Eng.* 76, 107278. doi:10.1016/j.jobe.2023.107278

Xin, W., Xiang, H., Jianming, Y., Linlin, C., and Caijun, S. (2022). Research progress on interfacial bonding between magnesium phosphate cement and steel: a review. *Constr. Build. Mater.* 342 (PB), 127925. doi:10.1016/j.conbuildmat.2022.127925

Yang, H. (2018). Preparation and Modification of magnesium phosphate cement anticorrosive coating on Q235 Steel Surface. *Southwest Jiaot. Univ.*

Yang, N., Shi, C., Yang, J., and Chang, Y. (2013). Research progresses in magnesium phosphate cement–based materials. *J. Mater. Civ. Eng.* 26 (10), 04014071. doi:10.1061/(asce)mt.1943-5533.0000971

Yang, Q., Zhang, S., and Wu, X. (2002). Deicer-scaling resistance of phosphate cement-based binder for rapid repair of concrete. *Cem. Concr. Res.* 32 (1), 165–168. doi:10.1016/s0008-8846(01)00651-2

Yang, Q., Zhang, S., Yang, Q., and Wu, X. (2000). Performance of new fast hardening phosphate repair material. *Concr. Cem. Prod.* 04, 8–11.

Yongkang, Z., and Xiaoming, G. (2012). Study on bond performance test of fiber reinforced plastics(FRP) bar and concrete. *Urban Roads Bridg. and Flood Control.*

Zhang, W., Dai, M., Liang, X., Wang, X., Wei, W., and Zhou, Z. (2023). Interfacial enhancement by CNTs grafting towards high-performance mechanical properties of carbon fiber-reinforced epoxy composites. *Materials* 16 (10), 3825. doi:10.3390/ma16103825

Zhao, Y., and Jin, W. (2002). Test study on bond stress-slip relationship of concrete and steel bar. *J. Build. Struct.* 01, 32–37.

frontiers | Frontiers in Materials

TYPE Original Research
PUBLISHED 13 November 2024
DOI 10.3389/fmats.2024.1509077

OPEN ACCESS

EDITED BY
Biao Hu,
Shenzhen University, China

REVIEWED BY
Cong Lu,
Southeast University, China
Yanshuai Wang,
Shenzhen University, China

*CORRESPONDENCE
Qingxin Zhao,
l1220805317@qq.com

RECEIVED 10 October 2024
ACCEPTED 28 October 2024
PUBLISHED 13 November 2024

CITATION
Wang H, Li C, Gao H, Zhao Y, Xia H, Zhou C, Zhong S and Zhao Q (2024) Improvement of dispersants on nano carbon black-modified cement paste: performance, microstructure and carbon footprint.
Front. Mater. 11:1509077.
doi: 10.3389/fmats.2024.1509077

Improvement of dispersants on nano carbon black-modified cement paste: performance, microstructure and carbon footprint

Hui Wang[1], Chenjiang Li[2], Haixiang Gao[1], Yan Zhao[3], Handuo Xia[3], Cong Zhou[1], Shunjie Zhong[4] and Qingxin Zhao[5]*

[1]Cangzhou Qugang Expressway Construction Co., Ltd., Cangzhou, China, [2]State Key Laboratory of Hydraulic Engineering Intelligent Construction and Operation, Tianjin University, Tianjin, China, [3]China Mcc22 Group Corporation Ltd., Tangshan, China, [4]Fujian Zhanglong Construction Investment Group Co., Ltd., Zhangzhou, China, [5]State Key Laboratory of Metastable Materials Science and Technology, Yanshan University, Qinhuangdao, China

The agglomeration of nano carbon black (NCB), driven by its high specific surface energy, limits the fundamental performance of cementitious materials and hinders the broader application of functional cementitious materials in engineering domains. NCB-modified cement (NC) has a low snow-melting efficiency, resulting in high energy consumption and excessive CO_2 emissions. Herein, this study innovatively proposed a method of using dispersants to overcome the above issue and systematically introduced the effects of three dispersants, polycarboxylic acid superplasticizer (PCE), tannic acid (TA), and sodium dodecyl sulfate (SDS), on NC. The dispersity of dispersant-NCB suspension was analyzed firstly, and then the performance of fresh paste, mechanical properties, resistivity, snow-melting speed and LCA of NC were explored. Experimental results indicated that, in terms of suspension stability, SDS was the most effective, followed by TA, while PCE exhibited the least efficacy. Furthermore, all three dispersants improved the fluidity of NC to varying degrees. However, PCE and TA demonstrated a retardation effect on the setting time, whereas SDS facilitated a reduction in the setting time of NC. From the point of view of mechanical properties, the use of these dispersants not only augmented the mechanical strength of the NC but also decreased its electrical resistivity. The uniform dispersion of SDS at the microstructural level of NCB had also been found. When the PCE content is 0.2%, TA content is 0.4%, and SDS content is 0.4%, the mechanical strength and resistivity of NC were the best. NC with dispersant TA melted snow three times faster than the control group, reducing snow-melting energy consumption. Moreover, LCA analysis showed that the addition of dispersants also reduced carbon emissions.

KEYWORDS

nano carbon black, cement paste, dispersant, electrical properties, CO_2 emissions

1 Introduction

In winter, high altitude areas of north and west China face significant challenges due to seasonal temperature changes and heavy snowfall, which increase snow thickness and lead to frequent icing on roads, bridges, and airports (Li et al., 2022; Julitta et al., 2014). Early snowfall and melting can create thin layers of frozen ice on highways and runways, reducing friction and posing safety risks as these surfaces can appear similar to wet roads (Wang et al., 2022). If not addressed promptly, this ice can severely impede vehicle movement, causing traffic paralysis and complicating infrastructure maintenance, accompanied by high costs (Pytka, 2010). To tackle these issues, various deicing and snow melting technologies have been employed (Zhao et al., 2024; Xu et al., 2021; Ma et al., 2016; Huang et al., 2021; Pei et al., 2021). Mechanical deicing and snow removal methods are effective but resource-intensive, while traditional salt-sprinkling methods can lead to environmental pollution and damage to concrete surfaces, including corrosion of steel in bridges. Therefore, there is an urgent need for efficient and environmentally friendly deicing solutions that can reduce reliance on human resources and minimize the negative impact on the durability of road structures and bridges.

In recent years, the emergence of multi-functional cement-based materials has also provided new ideas for solving road engineering problems (Zhai et al., 2023; Zhan et al., 2020; Han et al., 2015). As a multi-functional cement-based material, electro-thermal concrete has been used in the field of deicing and snow-melting of pavement due to its good mechanical properties and excellent electric heating ability. The excellent electrothermal property of electro-thermal concrete is reflected in the fact that it can heat up buildings or concrete pavement by external power supply voltage in winter snow and ice weather, so that the temperature rises and maintains a relatively stable value, so that the buildings or pavement can be kept in a state without snow and ice in a long period of cooling and snowfall weather, which can effectively prevent adverse situations (Li et al., 2013). Over the past decade or so, carbon materials have attracted much attention due to their high specific surface area and high strength. A large number of studies have shown that the addition of carbon materials to cement-based materials can greatly improve their mechanical and electrical properties, such as carbon nanotubes (Pan et al., 2020; Yıldırım et al., 2018), graphene (Bai et al., 2018; Yoo et al., 2017; liu et al., 2019) and nano carbon black (NCB) (Gong et al., 2009; Hong et al., 2018; Keal et al., 2024), etc., which are often used as fillers for conductive concrete. In contrast, NCB is a more cost-effective option and has a very broad practical application prospect. In addition, studies have shown that NCB can not only effectively repair micro-cracks in cement, but also accelerate the hydration degree of cement, thereby improving the mechanical properties of cement.

However, due to the high specific surface energy of NCB, it is easy to aggregate under the action of van der Waals force (Geim and Novoselov, 2007; Zhu et al., 2010; Chuah et al., 2018), and the direct addition of NCB often leads to poor fluidity and low mechanical strength of cement-based materials (Sobolkina et al., 2012; Xu et al., 2018). The low snow-melting efficiency of NC has led to increased electricity consumption, resulting in a significant amount of CO_2 emissions. In order to avoid the restriction of caking when NCB is applied in cement, a uniform and stable dispersion is required. Many researchers have conducted a lot of research, and currently there are two main dispersion treatment methods: physical dispersion (Nan et al., 2023) and chemical treatment (Kishore et al., 2023). Physical dispersion technology usually uses grinding, ball milling, ultrasonic and microwave radiation methods to achieve uniform suspension of particles. Although the physical technology is simple and fast, it also has a big disadvantage: it is not enough to achieve long-term stable dispersion. The chemical treatment technology is mainly to modify the particles by surfactants and realize non-covalent functionalization to improve their hydrophilicity, so that the particles can be stably dispersed into the solvent. In summary, how to improve the dispersion stability of NCB in cement hydration environment and reduce the CO_2 emissions from NC snow-melting have become key problems. Therefore, it is particularly important to disperse NCB better, improve its application effect in cement-based materials and reduce the CO_2 emissions from NC snow-melting.

Based on the existing problems, and in order to better play the application of NCB in cement-based materials, three different surfactants, sodium dodecyl sulfate (SDS), polycarboxylic acid superplasticizer (PCE) and tannic acid (TA), were selected as dispersants to disperse NCB. Starting with NCB suspension, the effects of three dispersants on the dispersion stability of NCB in aqueous solution were investigated by ultraviolet spectrophotometry. Subsequently, the performance of NC was investigated, and the influence of three dispersants on the new mixing performance of NC was demonstrated according to the test of fluidity and setting time. Then, on the surface of NC, the effects of three dispersants on the physical and electrical properties of NC were analyzed by compressive and flexural strength and resistivity tests. The effect of SDS on the microstructure of NC-paste also been studied. Finally, the snow-melting speed of NC with different dispersants was studied through the test of snow-melting. Meanwhile the life cycle assessment of each group was made to judge their CO_2 emissions. The reliable experimental data were obtained, which laid a foundation for practical engineering application.

2 Material and methods

2.1 Raw materials

The cement was P.O 42.5 ordinary Portland cement produced by Tianjin Jinyu Zhenxing Cement Factory, and its chemical composition is shown in Table 1. Carbon black was NCB with high specific surface area and low resistivity provided by Tianjin Huaran Chemical Co., LTD. NCB was prepared by gas phase method, and its related performance parameters are shown in Table 2. The dispersant SDS was from Shanghai Sigma Aldrich Trading Co., LTD. The water reducing agent was the third generation PCE with water reduction rate ≥25%. The purity of TA used was AR grade, provided by Hunan Beekman Biotechnology Co., LTD. For the convenience of reading, the abbreviations in this article are summarized in Table 3.

2.2 Sample preparation

In order to better study the modification effect of various dispersants on NCB cement-based composites, cement paste

TABLE 1 Chemical composition of cement (%).

CaO	SiO_2	Al_2O_3	Fe_2O_3	MgO	SO_3	K_2O	Loi
62.8	21.56	4.67	3.31	2.38	3.25	1.25	0.78

without coarse or fine aggregate was used in this study. The water-cement ratio of the cement-based composite prepared by the test is fixed at 0.45. The specific ratio is shown in Table 4. Firstly, a suspension of dispersant mixed with NCB was prepared, and then the NCB suspension was prepared for the preparation of cement paste.

(1) Preparation of dispersant-NCB suspension: Take the preparation standard of NCB/SDS solution as an example to illustrate (PCE and TA preparation methods were consistent with SDS). Firstly, 0.1 g NCB and 50 mL SDS solution with different mass fractions (0%, 0.2%, 0.4%, 0.6%) were added into 100 mL beaker, mechanically stirred for 5 min and ultrasonic dispersion for 15 min to obtain NCB/SDS suspension.
(2) Preparation of cement paste sample: A total of 300 mL of PCE/TA/SDS and NCB suspensions were prepared, mechanically stirred for 5 min, and ultrasonically dispersed for 15 min. Weighed cement was added to the mixer, followed by the 300 mL NCB suspension, and mixed for 1.5 min. After a 30-second pause, 264 g of water was gradually added while stirring, and mixing continued for another 1.5 min. The paste was then poured into a lubricated steel mold (40 × 40 × 160 mm). After shaking for 30 s, the surface was covered with polyethylene film to prevent water loss. The mold was removed after 24 h and placed in a standard curing room for further testing.

The preparation method of the specimen for the electrical conductivity test was roughly the same as that for the mechanical properties of the specimen, the only difference was that the electrical conductivity test uses the four-electrode method to determine the resistivity, so it was necessary to prepare 40 × 50 mm copper mesh as the measuring electrode.

2.3 Test methods

2.3.1 Absorbance test

The dispersion of dispersant NCB suspension was evaluated by ultraviolet spectrophotometry. The PE Lambda 750 s spectrophotometer was selected to measure the absorbance (ABS) within 24 h at 270 nm wavelength (Lavagna et al., 2021). The test mix ratio was consistent with that described in Section 1.3. The strength of absorbance can be expressed by the following Formula 1:

$$A = Kbc \tag{1}$$

where: A is absorbance; K is the molar absorption coefficient, which is related to the properties of the absorbing material and the wavelength λ of the incident light. b is the thickness of the absorption layer; c is the concentration of the light-absorbing substance in mol/L. In this test, the molar absorption coefficient K and the thickness of the absorption layer b are fixed. At this time, the absorbance A of the solution is positively correlated with the concentration c of the dispersant in the suspension, which can be used to quantitatively describe the dispersion effect of NCB in the solution.

2.3.2 Fresh cement paste performance test

In order to determine the effect of dispersant on the new mixing performance of NC, the fluidity and initial and final setting time of paste at room temperature (20°C ± 2°C) were measured by NLD 3 electric cement paste fluidity tester and Vicar meter. For specific test steps, refer to GB/T 1346–2011 "Test Method for Water Consumption, Setting Time and Stability of Cement Standard Consistency", the test was carried out three times, and the average value was taken as the test result.

2.3.3 Mechanical properties test

YAW-300C automatic bending testing machine was used to measure the compressive strength and flexural strength of the specimens, and the test method in GB/T17671-1999 "Cement mortar Strength Inspection Method (ISO method)" was used as the standard.

2.3.4 Electrical performance test

The main function of conductive phase filler NCB was to significantly improve the electrical conductivity of cement-based materials, and the direct measurement of sample resistance by instrument and electric meter was easy to produce a large error. Therefore, the four-electrode method was selected to measure the resistivity of the sample in this experiment. The current and voltage were measured by the multifunctional electric meter produced by Tianlilong Technology Co., LTD. The DC regulated power supply provided by Youlide was used as the voltage input terminal. The copper mesh was provided by Hebei Hengshui Furun Filter Co., LTD., with a diameter of 0.7 mm and low error and resistivity. The four-electrode measurement method is shown in Figure 1. The test piece was subjected to direct current of 0 ~ 30 V to measure its voltage and current, and the resistivity of early and late hydration was calculated by Formula 2, 3.

The calculation formula is as follows:

$$R = \frac{U}{I} \tag{2}$$

$$\rho = \frac{RS}{L} \tag{3}$$

Where: U represents the actual measured voltage, V; I represents the actual measured current, mA; R represents the calculated resistance between the middle two electrodes, Ω; rrepresents the resistivity of the sample, Ω·cm; L represents the distance between the middle two electrodes, mm; S represents the cross-sectional area of the sample, mm^2.

2.3.5 Snow-melting test

Snow-melting test was to observe the change of ice mass with time under certain temperature conditions. First, add 100 g of water into the beaker and freeze it in the refrigerator at −18°C for more than 12 h until the water was completely frozen. The ice cube was a cylinder with a diameter of 30 mm on the bottom side. The ice

TABLE 2 NCB performance index.

Particle size (nm)	Iodine absorption value (g/kg)	D.B.P absorption value (ml/100 g)	Electrical resistivity (Ω•m)	pH	Heating decrement (%)	Ash content (%)	Ctab surface area (m2/g)	Impurity
30	820	380	0.9	7.2	0.2	0.1	150	no

TABLE 3 Description of abbreviations used.

Abbreviation	Description
NCB	Nano carbon black
NC	NCB-modified cement
PCE	Polycarboxylic acid superplasticizer
TA	Tannic acid
SDS	Sodium dodecyl sulfate
SEM	Scanning electron microscopy
XRD	X-ray diffraction
AFt	Ettringite
C-S-H	Calcium Silicate Hydrate

cube was placed in the middle of the specimen, and the voltage was connected to each group of NC in the same way as the electrical performance test. Quickly measure the mass of the ice every 5 min. High snow-melting efficiency led to lower electricity consumption and reduced CO_2 emissions.

2.3.6 Microscopic characterization tests

Scanning electron microscopy (SEM) was employed to analyze the microscopic distribution of NCB. Specimens measuring 10 mm × 10 mm × 10 mm were cut from the cement paste and vacuum-dried to avoid carbonation from CO_2 exposure. The dried samples were then subjected to SEM testing after being coated with gold. The Czech TESCAN MIRA LMS was utilized for the SEM analysis and energy spectrum testing. X-ray diffraction (XRD) was used to determine the crystalline structure of materials. The sample was finely powdered and placed on a sample stage, where X-rays were directed at it. As the X-rays interact with the crystal lattice, they produced a diffraction pattern that can be analyzed to reveal information about the crystallographic phases present in the materials.

2.3.7 Life cycle assessment analysis

The purpose of the life cycle assessment analysis was to analyze and evaluate the environmental load generated by NC with different dispersant, so as to facilitate the quantitative calculation and comparison the effect of different dispersants. In this paper, a process-based inventory analysis method was used to classify NC with different dispersant into four processes: raw material mining, mixing, transportation and snow-melting, and the CO_2 emissions of each process was quantified. Finally, the global warming potential (GWP) impact category was selected (Nayır et al., 2024), and the results of inventory analysis were quantitatively evaluated to determine the impact on the external environment.

3 Result and discussion

3.1 Absorbance of dispersant-NCB suspension

Figure 2 shows the change of absorbance of NCB suspension in each group with time after ultrasonic dispersion. The results of quantitative analysis showed that the absorbance of the suspension without dispersant was 1.732 at the beginning, and decreased significantly by 1.28 in the first 2 h and to 0.1 after 12 h, with a decrease of 94%, indicating that the dispersion and stability of pure NCB suspension were poor. The reason was that the interfacial effect between NCB and aqueous solution led to the increase of interfacial tension, and the force imbalance between solid and liquid forms clumps, resulting in the condensation of NCB. In addition, the non-polar characteristics of NCB surface limited its dispersion ability in water, and it was difficult for functional groups such as hydroxyl groups to form strong interactions with water, which further promoted the formation of clumps.

Figures 2A–C show the changes in UV-visible absorptance of NCB suspension at different concentrations of PCE, TA and SDS within 24 h. The overall curve showed that the addition of PCE, TA and SDS significantly affected the initial absorbance of suspension with the same NCB content. When the concentration of PCE was 0.2%, 0.4% and 0.6%, the absorbance was 1.777, 1.859 and 2.016, respectively. When the concentration of TA was 0.2%, 0.4%, 0.6%, the absorbance was 2.067, 2.359, 2.476. When SDS concentration was 0.2%, 0.4%, 0.6%, absorbance was 2.067, 2.259, 2.376. The results showed that PCE, TA and SDS can all improved the dispersion effect of NCB in water, PCE effect was the least, while TA and SDS effect were similar. With the increase of standing time, the absorbance of all groups decreased, but tended to balance after 12 h. In terms of suspension stability, SDS was the best, followed by TA, and PCE was the worst. The addition of SDS made the absorbance decrease slowly by about 0.55, indicating that the dispersion and stability of SDS to NCB was better than that of TA. In addition, the change of SDS concentration had little effect on the dispersion of NCB, possibly because 0.2% SDS concentration was enough to cover the dispersion of NCB, and further increasing the concentration would only lead to

TABLE 4 Sample ratios for test.

Sample number	Cement(g)	NCB(g)	Water(g)	PCE/TA/SDS suspension (g/mL)	
				Water(g)	PCE/TA/SDS(g)
0	1,254	40	264	300	0
PCE-0.2	1,254	39.5	264	300	0.4
PCE-0.4	1,254	39	264	300	0.8
PCE-0.6	1,254	38.7	264	300	1.1
TA-0.2	1,254	39.6	264	300	0.6
TA-0.4	1,254	39.1	264	300	1.1
TA-0.6	1,254	38.6	264	300	1.7
SDS-0.2	1,254	39.8	264	300	0.5
SDS-0.4	1,254	39.2	264	300	1.1
SDS-0.6	1,254	38.3	264	300	1.6

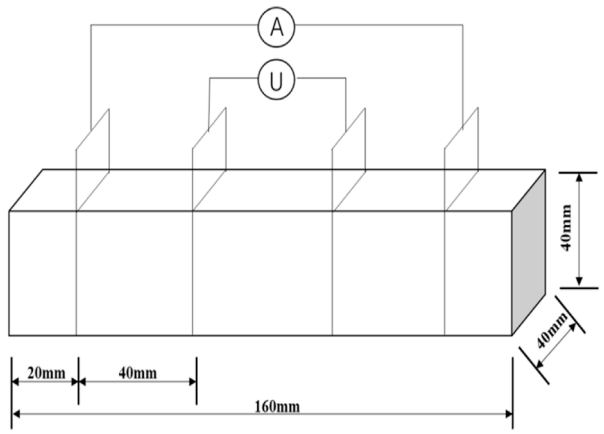

FIGURE 1
Four-electrode method.

susaturation of the solution and could not significantly improve the dispersion effect.

3.2 Fresh property analysis

Figures 3A–C show the flow and setting time of freshly mixed NC with different PCE, TA and SDS contents, respectively. On the whole, the three dispersants all improved the fluidity of NC to different degrees, but their performance in setting time was different.

On the whole, with the increase of dispersant content, the diffusion diameter of NC gradually increased, indicating that the addition of dispersant improved its fluidity. The diffusion diameter of the samples without dispersant was 16.8 cm, while the diffusion diameter of CPE-0.2, CPE-0.4 and CPE-0.6 increased by 20.8%, 35.1% and 59.5%, respectively. TA-0.2, TA-0.4 and TA-0.6 increased by 13.7%, 26.8% and 34.5%, respectively. SDS-0.2, SDS-0.4 and SDS-0.6 increased by 9%, 23% and 15%, respectively. It can be seen that the fluidity of PCE and TA increased with the increase of dosage, while SDS increased first and then decreased. Compared with the three dispersants, under the same dosage, PCE had the greatest improvement on fluidity, TA followed, and SDS had the least. The fluidity of PCE be due to its comb molecular structure, which formed a thicker adsorption layer, releasee free water between cement particles, and also had a certain dispersion effect on NCB. TA and SDS released encapsulated free water mainly by preventing NCB from accumulating, but TA performed slightly better in cement paste than SDS.

From the point of view of setting time, with the increase of dispersant content, the setting time of NC would be different due to the action of different dispersants. Both PCE and TA had retarding effect on NC, and TA had a more significant effect, which had also been reflected in previous Portland cement studies (Sokołowska et al., 2024). On the contrary, SDS shortened the setting time of the paste, which indicated that the action mechanism of different dispersants in NC was different. The initial and final setting times of NC without dispersant were 4.08 h and 5.33 h, respectively, while those of CPE-0.6 were 5.42 h and 6.82 h, respectively, and the time interval was slightly extended. This was because the hydroxyl, carboxyl and amino groups in PCE molecules form complexes with calcium ions in NC, which hindered the hydration process of cement. The initial and final setting times of TA-0.6 samples were 6.62 h and 8.47 h, respectively, and the time intervals were further extended, which could be explained by the theory of the formation of complexes between TA and calcium ions. In contrast, the initial and final setting time of SDS-0.6 sample were shortened to 3.65 h and 4.62 h, respectively, and the time interval was reduced, indicating that SDS

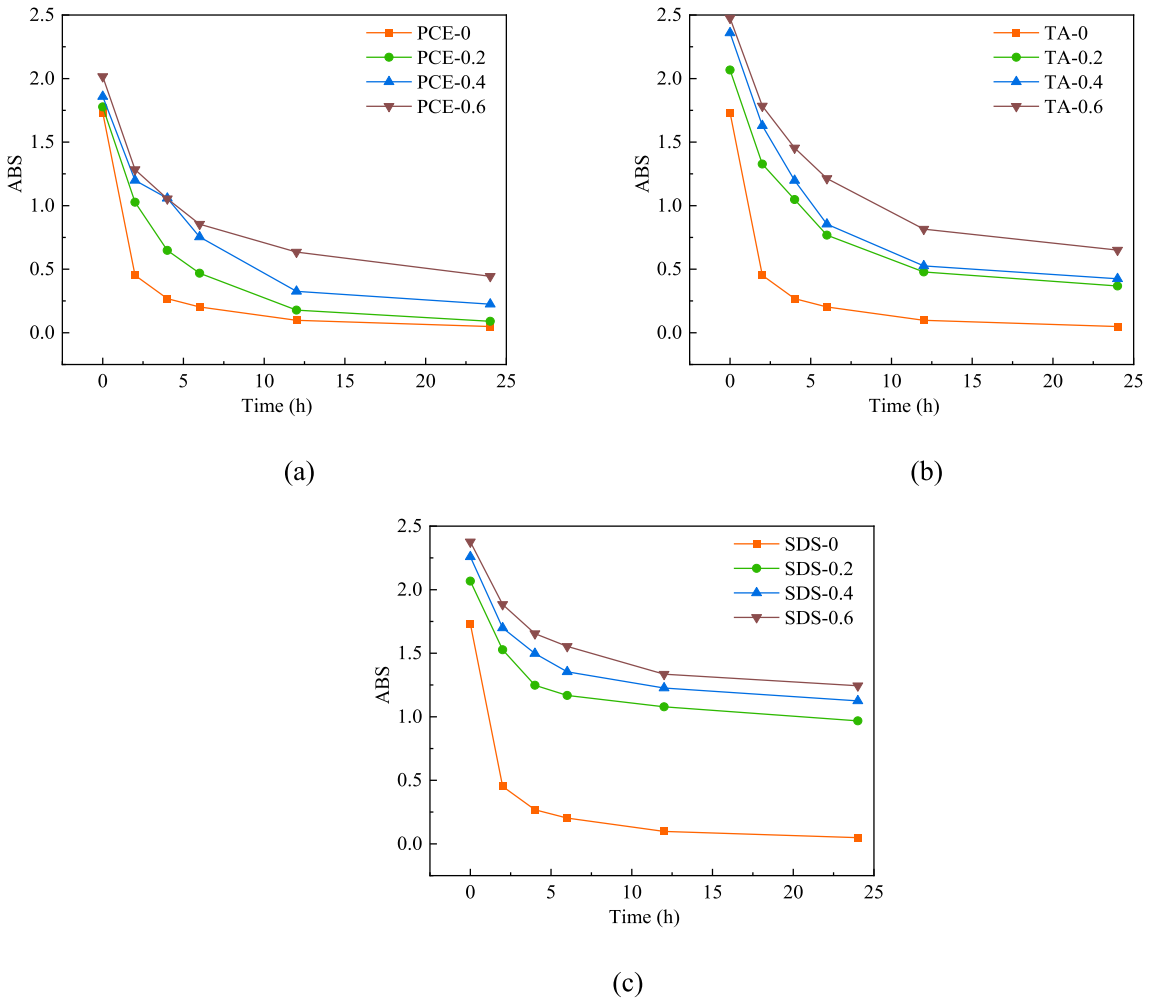

FIGURE 2
ABS *versus* time **(A)** PCE, **(B)** TA and **(C)** SDS.

accelerated the hardening process of cement. This may be because SDS was unable to form a complex with calcium ions, its main role was to prevent NCB agglomeration, and the interaction with the cement paste was weak.

3.3 Mechanical properties of NC

3.3.1 Flexural strength

Figures 4A–C show the flexural strength of NC with different PCE, TA and SDS contents at early hydration stage (3 days) and late hydration stage (28 days), respectively. As can be seen from the figure, the flexural strength of NC without dispersant at 3 days and 28 days was 5.2 MPa and 7.2 MPa, respectively. The flexural strength of NC after adding dispersant was higher than that of the sample without dispersant in the early and late stages of hydration, indicating that the three dispersants all increased the flexural strength to varying degrees, and showed a trend of first increasing and then decreasing.

With the increase of PCE content, the flexural strength of PCE-0.2, PCE-0.4 and PCE-0.6 increased by 32.7%, 26.9% and 7.7%, respectively, compared with that of PCE-0 at 3 days. The early flexural strength of NC was improved best when the content of PCE was 0.2%. At 28 days, the flexural strength of CPE-0.2, CPE-0.4 and CPE-0.6 increased by 19.4%, 16.7% and 12.5%, respectively, indicating that the influence of PCE content on the flexural strength at the later stage of hydration was small, which may be due to the delay of hydration of cement particles coated by PCE in the early stage and the gradual release of cement particles in the later stage. The difference in flexural strength was reduced. Their behavior was different. At 3 days, the flexural strength of TA-0.2, TA-0.4 and TA-0.6 increased by 5.8%, 13.5% and 3.8% compared with TA-0, respectively, indicating that 0.4% TA content contributed the most to the early flexural strength of NC. However, the flexural strength changes of TA-0.2, TA-0.4 and TA-0.6 at 28 days were 0%, 8.3% and −4.2%, respectively, indicating that too much TA was not beneficial to the growth of flexural strength, which may be related to its retarding effect. For SDS, the flexural strength of SDS-0.2, SDS-0.4 and SDS-0.6 increased by 15.4%, 19.2% and 5.8%, respectively,

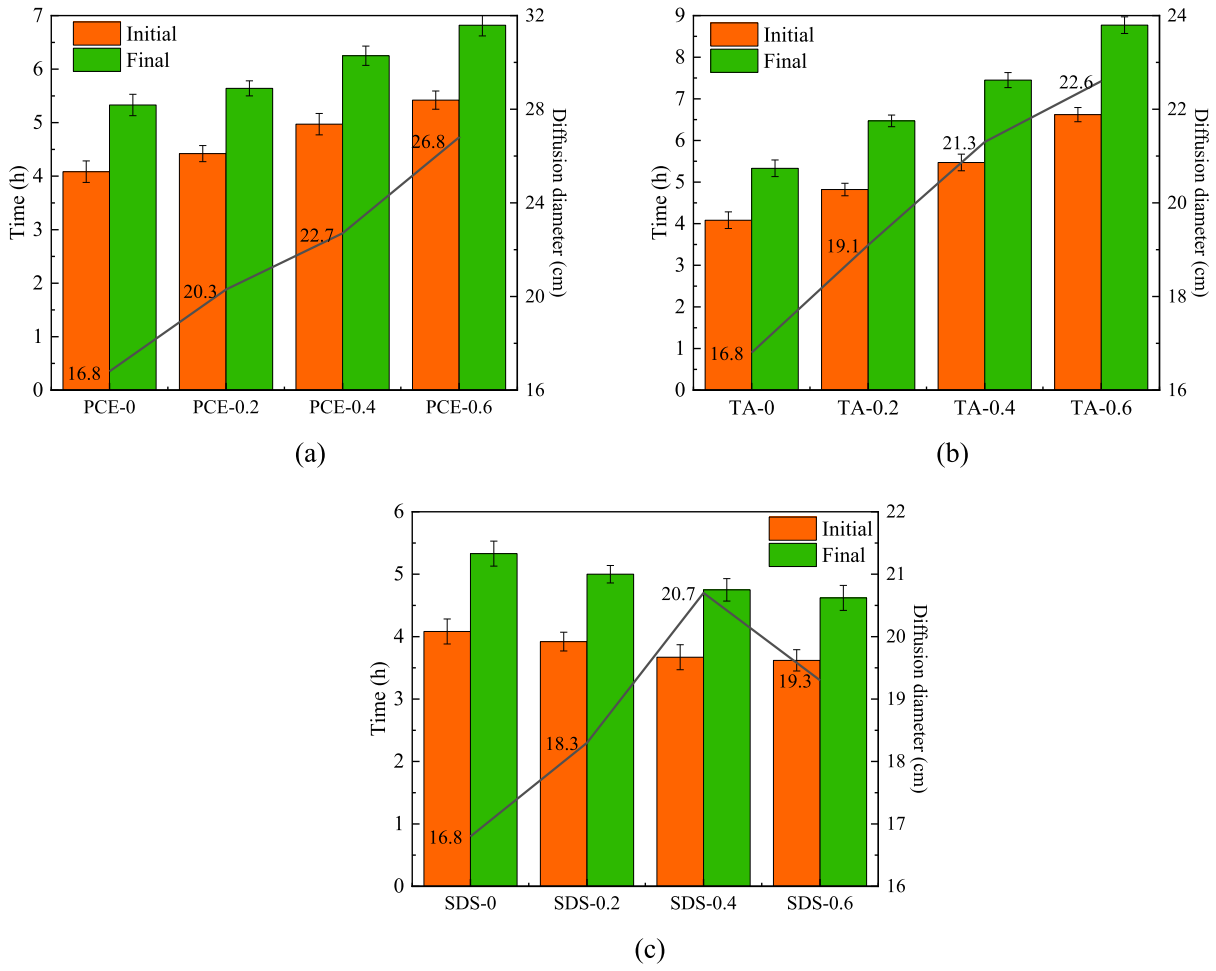

FIGURE 3
Fresh NC fluidity and setting time **(A)** PCE, **(B)** TA and **(C)** SDS.

compared with SDS-0 at 3 days, indicating that 0.4% SDS content contributed the most to the early flexural strength. At 28 days, the flexural strength increased by 8.3%, 12.5% and 1.4%, respectively.

3.3.2 Compressive strength

Figures 5A–C show the compressive strength of NC with different PCE, TA and SDS contents at early hydration stage (3 days) and late hydration stage (28 days), respectively. As can be seen from the figure, the compressive strength of NC without dispersant at 3 days and 28 days was 22.3 MPa and 32.6 MPa, respectively. The law of compressive strength was the same as that of flexural strength mentioned above.

As for PCE, the compressive strength of PCE-0.2, PCE-0.4 and PCE-0.6 at 3 days increased by 37.7%, 27.8% and 14.3%, respectively, compared with that of PCE-0, with the increase of PCE-0.2 on the early compressive strength being the most significant. At 28 days, the compressive strength of CPE-0.2, CPE-0.4 and CPE-0.6 increased by 34.4%, 30.9% and 20.2%, respectively, compared with that of CPE-0, indicating that PCE had a significant effect on the compressive strength of NC, especially CPE-0.2 and CPE-0.4. This may be due to the fact that PCE improved paste fluidity, reduced internal bubbles and pores, and enhanced compressive strength. However, excessive PCE can cause retardation and segregation, leading to negative effects. The influence trend of TA and SDS on compressive strength was similar, and both reached the peak value when the dosage was 0.4%. Without dispersant, NCB easily aggregated in cement and reduced compressive strength. In TA-0.4 and SDS-0.4 samples, uniformly dispersed NCB promoted the nucleation of hydration products and improved the structural densification, thus enhancing compressive strength. However, excessive TA and SDS will increase the internal defects of the paste and reduce the compressive strength.

3.4 Resistivity of NC

Figures 6A–C show the resistivity of NC with different PCE, TA and SDS contents in early hydration (3 days) and late hydration (28 days), respectively. It can be seen from the figure that the resistivity of NC without dispersant was 8.31 MPa and 8.54 MPa at 3 days and 28 days, respectively. The reason for the increase of resistivity in the late hydration period was the loss of pore water, which reduced the electron conduction path. In general, the resistivity of NC mixed with dispersant was higher than that of samples without dispersant in the early and late stages

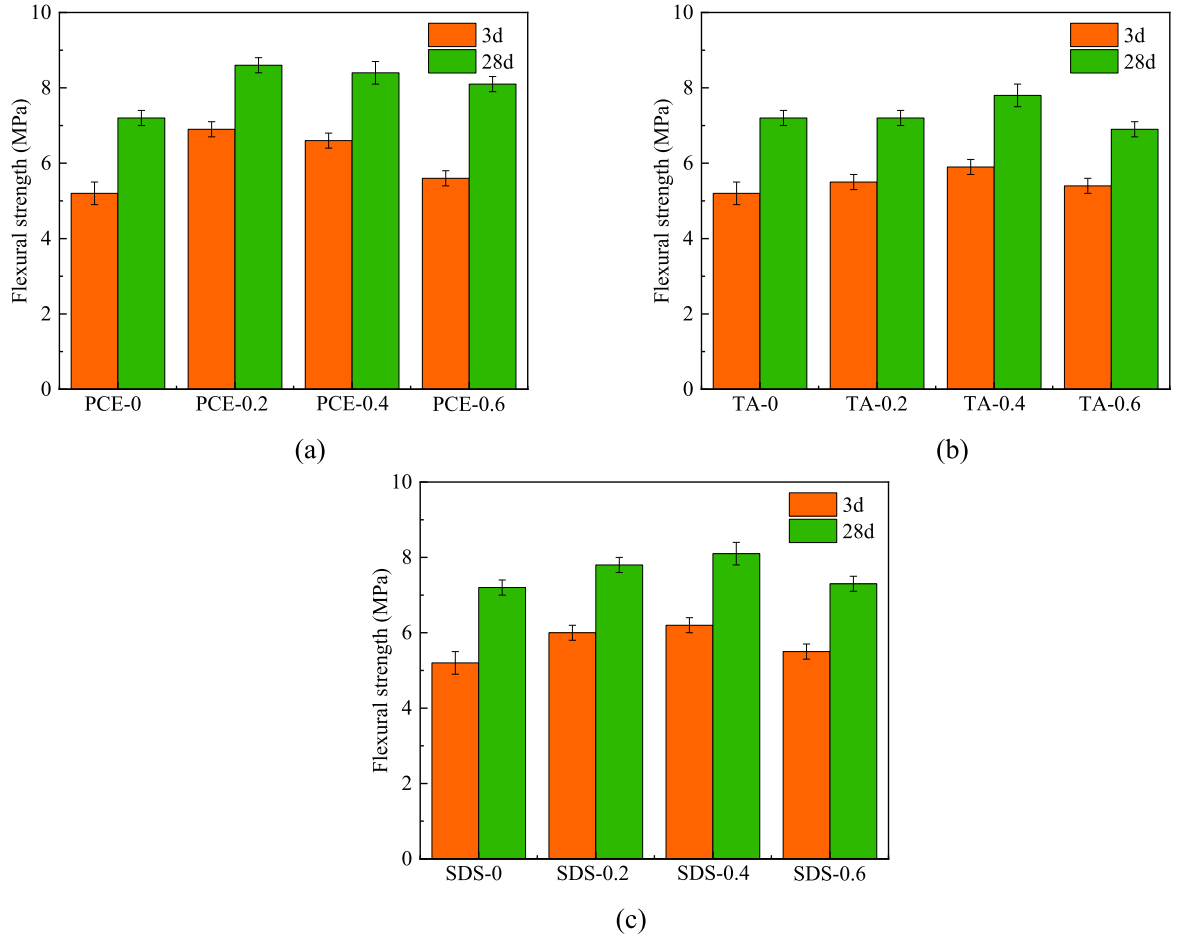

FIGURE 4
The flexural strength of NC **(A)** PCE, **(B)** TA, and **(C)** SDS.

of hydration, indicating that the three dispersants reduced the resistivity to different degrees, and the resistivity showed a trend of first decreasing and then increasing.

For PCE, the resistivity of PCE-0.2, PCE-0.4 and PCE-0.6 at 3 days decreased by 9.3%, 7.5% and 6.3%, respectively, as the content of PCE increased. When the PCE content was 0.2%, it made the greatest contribution to the reduction of the early resistivity of NC. At 28 days, the resistivity of CPE-0.2, CPE-0.4 and CPE-0.6 decreased by 10.4%, 7.4% and 6.6%, respectively, similar to the reduction in the early stage of hydration. The effect of PCE-0.2 was the best, but too much incorporation would lead to slow solidification and segregation of cement paste, which was not conducive to the performance of cement paste. For TA, the resistivity of TA-0.2, TA-0.4 and TA-0.6 decreased by 17.5%, 23.5% and 19.8% in 3 days compared with that of TA-0, respectively, and the best effect was achieved when the content of TA was 0.4%. At 28 days, the decrease of resistivity was basically the same as that at 3 days, and too much TA inclusion would increase the internal defects of the cement paste, resulting in an increase in resistivity. For SDS, the resistivity of SDS-0.2, SDS-0.4 and SDS-0.6 at 3 days was reduced by 11.3%, 17.3% and 11.2%, respectively, compared to SDS-0. With the increase of SDS content, the dispersion effect of NCB in cement was enhanced, and the resistance decreased first and then increased, reaching the lowest value at SDS-0.4. However, the high content of SDS would increase the porosity of cement matrix, but increased the resistivity.

With the increase of hydration time, the resistivity of the samples with different dispersants increased, but the overall trend remained unchanged. The reason was that the cement hydration was not complete in the early stage, and the resistivity of NC was affected by two aspects: First, NCB formed a conductive network conducive to electron transport in the cement matrix; The second was the conduction of electrons and ions in the pore liquid. At 28 days, the hydration of cement was basically completed, the pore liquid was reduced, and the electrical conductivity of ions was weakened, resulting in an increase in resistivity (He et al., 2018).

3.5 Microscopic characterization of NC

3.5.1 Types of hydration products

The XRD patterns displayed in Figure 7 provide a comparative analysis of the hydration products formed in the samples PCE-0.4, TA-0.4, SDS-0.4, and the Ctrl. The crystalline hydration products identified in the NC were $Ca(OH)_2$, $CaCO_3$, and $CaSO_4$.

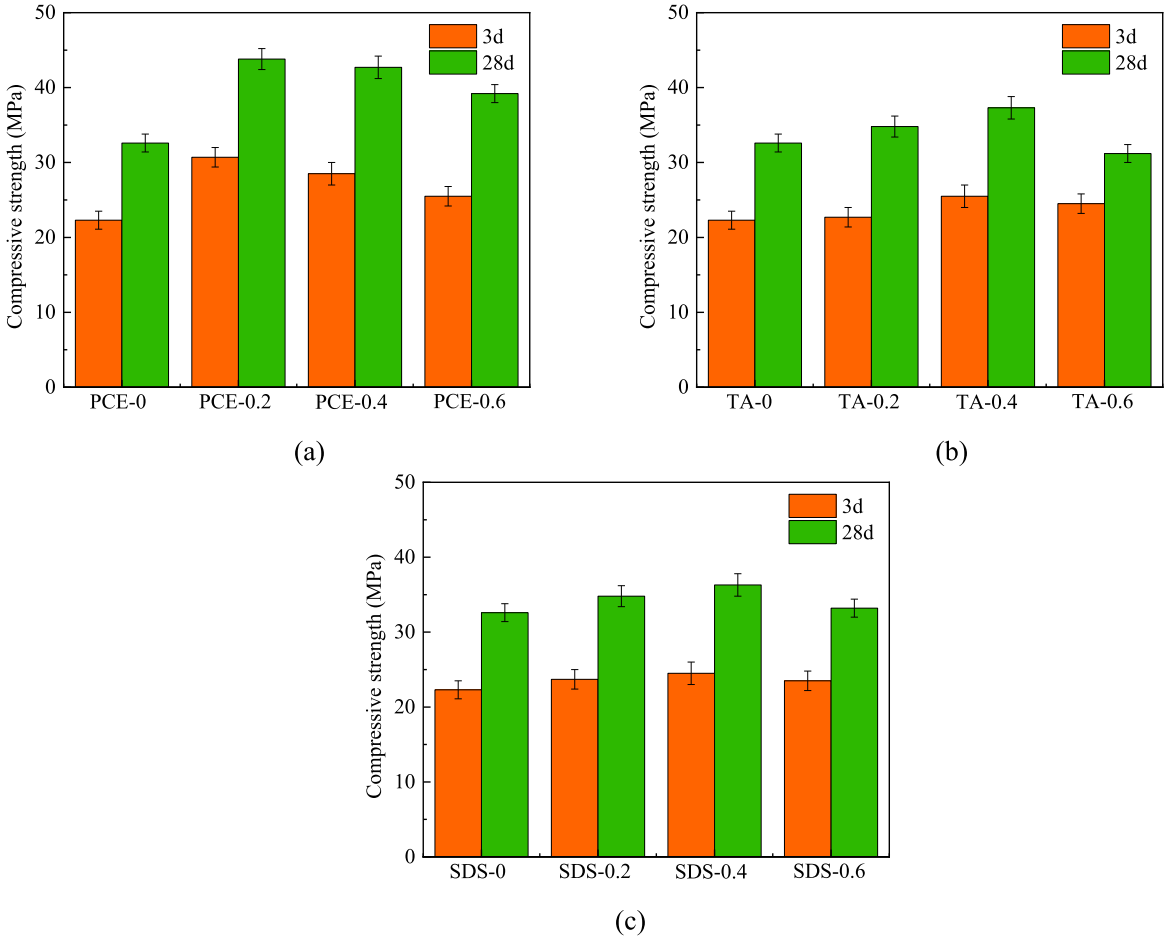

FIGURE 5
The compressive strength of NC **(A)** PCE, **(B)** TA, and **(C)** SDS.

It was noteworthy that the introduction of various dispersants, PCE, TA, and SDS, did not appear to alter the fundamental types of hydration products generated during the hydration process. This indicated that while the dispersants may play a role in improving the dispersion and workability of the NCB, they did not influence the chemical composition of the hydration products.

3.5.2 Distribution and morphology of hydration products

SEM images revealed the effect of NCB on the microstructure of the cement paste. As shown in Figure 8, the dispersion of NCB under SEM significantly affected the characteristics of the cement paste. In Figure 8A, the hydration products of NCB were sparsely distributed. This distribution was mainly due to the high surface energy of NCB itself and the lack of sufficient dispersant, which made it difficult to combine with cement particles, thus limiting its promotion effect on hydration. Some incomplete granular products were unevenly dispersed and not tightly connected. As a result, unmodified NCB may form new pores and defects in the cement, reducing the fluidity of the material and the compactness of the overall structure. With the addition of SDS dispersant, as shown in Figure 8B, the agglomeration of NCB in cement almost disappeared. The dispersed particles exhibited a uniform and continuous network distribution, which helped to promote the formation of C-S-H. At the same time, the hydration product was wrapped on the surface of NCB, which increased the crystallization degree of the hydration product, filled the micropores, and improved the compactness of the cement. NCB was surrounded by hydration products and acts as a nucleation site for C-S-H (Lu et al., 2019; Chen et al., 2024), facilitating the formation of a more dense and homogeneous cement structure. In Figure 8C, the distribution of AFt and C-S-H appeared sparse and porous, while in Figure 8D, these products were clustered in cement. This aggregation effectively enhanced the mechanical strength and conductivity of the cement paste, indicating that SDS had successfully achieved the dispersion of NCB in the cement paste. Through the uniformly dispersed NCB, a conductive network was formed, and the tightness of the connection between the hydration products was improved, which provided a preliminary explanation for the improvement of SDS-0.4 in terms of mechanical strength and resistivity. This improvement may be due to the effect of SDS on the interaction between cement particles and NCB, which promoted the effective dispersion of NCB and optimized the microstructure of cement paste.

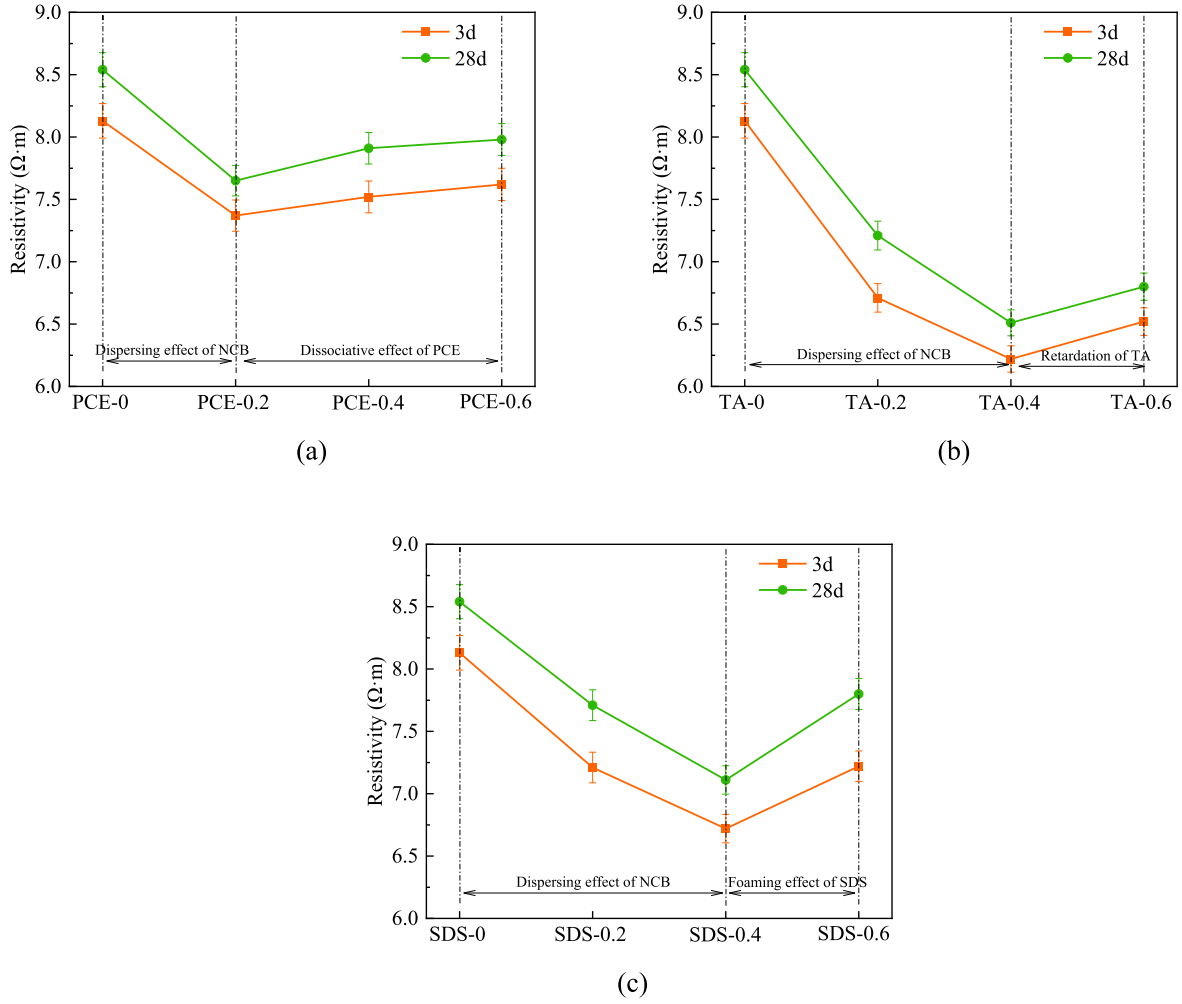

FIGURE 6
Resistivity of NC **(A)** PCE, **(B)** TA, and **(C)** SDS.

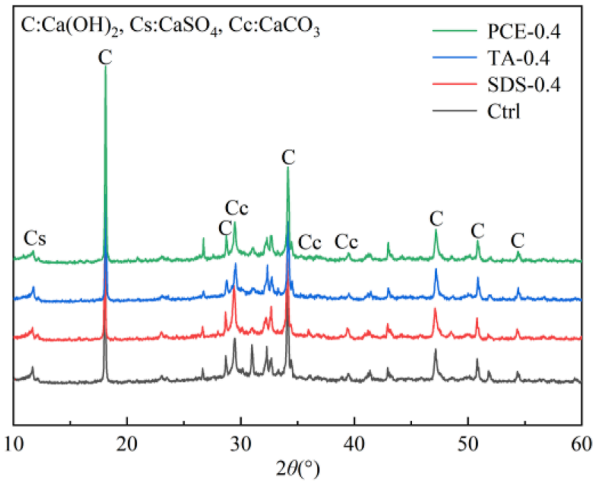

FIGURE 7
XRD of SDS-0 and SDS-0.4.

3.6 Snow-melting speed of NC

As shown in the Figure 9, the addition of three dispersants accelerated the snow-melting rate of NC to different degrees. Among them, TA had the most obvious effect, and the time can be reduced to 1/3; SDS followed, and PCE had the weakest effect. In the TA group, the decrease rate of TA-0.4 was the highest, the optimal dosage of SDS was also 0.4, and the optimal dosage of PCE was 0.2. The results were consistent with the resistivity results. The effect of dispersant directly affected the uniform distribution of NCB in the paste. The better the dispersion effect, the more uniform the distribution of NCB in the cement hardened paste, the lower the resistance, the better the conductivity, the higher the ice melting efficiency, and the lower the energy consumption. The reduction in electricity consumption of the TA group directly led to a reduction in CO_2 emissions.

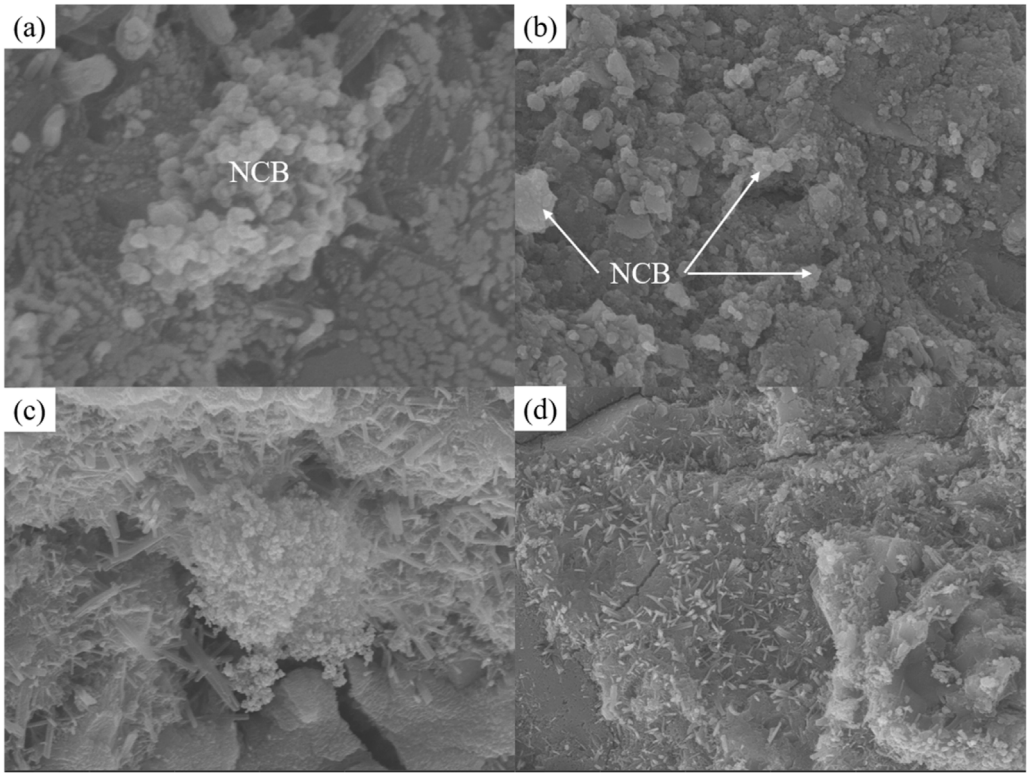

FIGURE 8
SEM of **(A) (C)** SDS-0 and **(B) (D)** SDS-0.4.

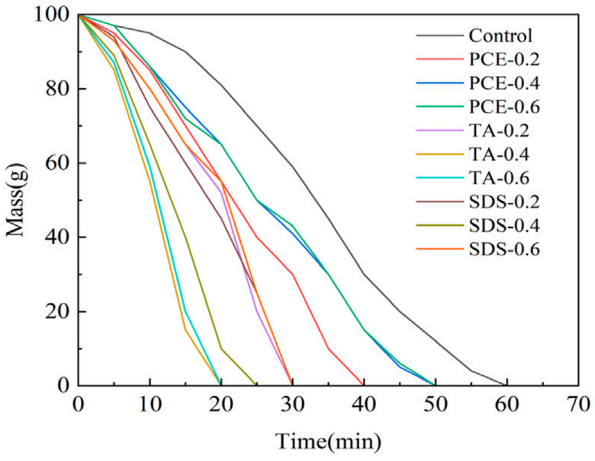

FIGURE 9
Ice mass loss of NC with different dispersants.

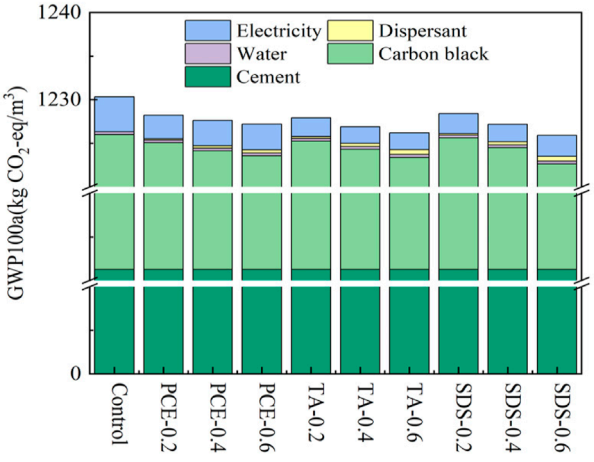

FIGURE 10
NC environmental impact assessment.

3.7 LCA analysis

Figure 10 shows GWP100a values of NC with different PCE, TA and SDS contents. The CO_2 emissions of NC was mainly concentrated in cement and carbon black. Secondly, it was the electric energy required in the snow-melting process, it can be found that the electric energy of TA was the least, mainly because TA improved the ice melting efficiency of NC, SDS was in the middle, and the NC with PCE had the highest snow-melting energy consumption. CO_2 was the main pollutant causing global warming, so while improving the efficiency of snow-melting and deicing of cement paste, carbon emissions should also be controlled.

According to the comprehensive analysis, the impact of NCB on the environmental load of cement paste is as follows: PCE was the largest, SDS was the second, TA was the least. In conclusion, the CO_2 emissions of NC with TA were the lowest.

4 Conclusion

In order to solve the problem of poor dispersion of NCB in cement paste and low snow-melting efficiency of NC, three dispersants, PCE, TA and SDS, were used in this paper to modify NC, which not only improved its dispersion, but also enhanced its mechanical and electrical properties, reduced CO_2 emissions of NC. Meanwhile, snow-melting speed and life cycle assessment analysis of NC with different dispersants were investigated. The main conclusions are as follows:

(1) All three dispersants can improve the dispersion stability of NCB suspension. PCE improved the dispersion stability of NCB suspension the least, the effect of TA and SDS was similar. Under the same dosage, PCE had the most significant improvement on fluidity, TA was the second, SDS was the least. PCE and TA both delayed the setting time, TA effect was more obvious, while SDS shortened the setting time.

(2) The influence of PCE, TA and SDS on the compressive and flexural strength of NC was similar, which firstly increased and then decreased. The three dispersants all improved the mechanical strength of NC to varying degrees. The highest contribution to the mechanical strength was PCE-0.2, TA-0.4 and SDS-0.4, respectively.

(3) The three dispersants can reduce the resistivity of NC at different hydration stages, and showed a trend of first decreasing and then increasing. PCE-0.2 can effectively reduce the resistivity of the sample, but excessive use will cause retarding and segregation, resulting in increased resistivity. TA-0.4 had the best effect on the improvement of resistivity, reducing the resistivity by 23.8% at 28 days, but excess can also cause retarding and increased resistivity. SDS-0.4 can minimize the resistivity, but excessive will lead to foaming and increase the porosity of the cement matrix.

(4) The three dispersants all accelerated the snow-melting speed of NC by dispersing NCB, among which the snow-melting speed of NC with TA was the fastest. From the perspective of global warming potential, the three dispersants all reduced the CO_2 emissions of NC. The impact of different dispersants NC on environmental load is as follows: PCE had the largest impact, followed by SDS, and TA had the least impact.

In this paper, low cost and high conductivity NCB was used to modify the cement paste, and the advantages of the structure and performance of the material were used in the test and the ideal results were obtained. Subsequently, the thermal conductivity of composite materials can be studied to provide a new idea for road deicing and snow removal in northern and western high-altitude areas in winter.

Data availability statement

The original contributions presented in the study are included in the article/supplementary material, further inquiries can be directed to the corresponding author.

Author contributions

HW: Conceptualization, Methodology, Writing–original draft. CL: Data curation, Investigation, Writing–original draft. HG: Software, Supervision, Writing–original draft. YZ: Formal Analysis, Investigation, Writing–review and editing. HX: Supervision, Validation, Writing–review and editing. CZ: Methodology, Supervision, Writing–review and editing. SZ: Investigation, Methodology, Writing–review and editing. QZ: Conceptualization, Funding acquisition, Writing–review and editing.

Funding

The author(s) declare that financial support was received for the research, authorship, and/or publication of this article. This study was financially supported by the National Joint Foundation for Regional Innovation and Development of China (U22A20228).

Conflict of interest

Authors HW, HG, and CZ were employed by Cangzhou Qugang Expressway Construction Co., Ltd. Authors YZ and HX were employed by China Mcc22 Group Corporation Ltd. Author SZ was employed by Fujian Zhanglong Construction Investment Group Co., Ltd.

The remaining authors declare that the research was conducted in the absence of any commercial or financial relationships that could be construed as a potential conflict of interest.

Generative AI statement

The author(s) declare that no Generative AI was used in the creation of this manuscript.

Publisher's note

References

Bai, S., Jiang, L., Xu, N., Jin, M., and Jiang, S. (2018). Enhancement of mechanical and electrical properties of graphene/cement composite due to improved dispersion of graphene by addition of silica fume. *Constr. Build. Mater.* 164, 433–441. doi:10.1016/j.conbuildmat.2017.12.176

Chen, X., Liu, T., Guo, J., Nie, K., Yang, X., Zhang, L., et al. (2024). C–S–H-PCE nanoparticles and anionic surfactants as nucleation agent in cement based materials: focus on the antagonism. *Cem. Concr. Compos.* 152, 105644. doi:10.1016/j.cemconcomp.2024.105644

Chuah, S., Li, W., Chen, S. J., Sanjayan, J. G., and Duan, W. H. (2018). Investigation on dispersion of graphene oxide in cement composite using different surfactant treatments. *Constr. Build. Mater.* 161, 519–527. doi:10.1016/j.conbuildmat.2017.11.154

Geim, A. K., and Novoselov, K. S. (2007). The rise of graphene. *Nat. Mater.* 6 (3), 183–191. doi:10.1038/nmat1849

Gong, H., Li, Z., Zhang, Y., and Fan, R. (2009). Piezoelectric and dielectric behavior of 0-3 cement-based composites mixed with carbon black. *J. Eur. Ceram. Soc.* 29 (10), 2013–2019. doi:10.1016/j.jeurceramsoc.2008.11.014

Han, B., Zhang, L., Sun, S., Yu, X., Dong, X., Wu, T., et al. (2015). Electrostatic self-assembled carbon nanotube/nano carbon black composite fillers reinforced cement-based materials with multifunctionality. *Compos. Part A Appl. Sci. Manuf.* 79, 103–115. doi:10.1016/j.compositesa.2015.09.016

He, R., Ma, H., Hafiz, R. B., Fu, C., Jin, X., and He, J. (2018). Determining porosity and pore network connectivity of cement-based materials by a modified non-contact electrical resistivity measurement: experiment and theory. *Mater. and Des.* 156, 82–92. doi:10.1016/j.matdes.2018.06.045

Hong, Y., Li, Z., Qiao, G., Ou, J., and Cheng, W. (2018). Pressure sensitivity of multiscale carbon-admixtures–enhanced cement-based composites. *Nanomater. Nanotechnol.* 8, 184798041879352. doi:10.1177/1847980418793529

Huang, K., Liu, J., Wang, J., and Shi, X. (2021). Characterization and mechanism of a new superhydrophobic deicing coating used for road pavement. *Crystals* 11, 1304. doi:10.3390/cryst11111304

Julitta, T., Cremonese, E., Migliavacca, M., Colombo, R., Galvagno, M., Siniscalco, C., et al. (2014). Using digital camera images to analyse snowmelt and phenology of a subalpine grassland. *Agric. For. Meteorology* 198-199, 116–125. doi:10.1016/j.agrformet.2014.08.007

Keal, M. E., Clewlow, L., Roberts, E., and Rees, N. V. (2024). Electrochemical recovery of ruthenium via carbon black nano-impacts. *Electrochimica Acta* 507, 145185. doi:10.1016/j.electacta.2024.145185

Kishore, K., Pandey, A., Wagri, N. K., Saxena, A., Patel, J., and Al-Fakih, A. (2023). Technological challenges in nanoparticle-modified geopolymer concrete: a comprehensive review on nanomaterial dispersion, characterization techniques and its mechanical properties. *Case Stud. Constr. Mater.* 19, e02265. doi:10.1016/j.cscm.2023.e02265

Lavagna, L., Nisticò, R., Musso, S., and Pavese, M. (2021). Functionalization as a way to enhance dispersion of carbon nanotubes in matrices: a review. *Mater. Today Chem.* 20, 100477. doi:10.1016/j.mtchem.2021.100477

Li, G., Qin, J.-m., Yu, H.-x., and Huang, N. (2022). Wind-tunnel experimental studies of the spatial snow distribution over grass and bush surfaces. *J. Hydrodynamics* 34 (1), 85–93. doi:10.1007/s42241-022-0009-4

Li, H., Zhang, Q. Q., and Xiao, H. G. (2013). Self-deicing road system with a CNFP high-efficiency thermal source and MWCNT/cement-based high-thermal conductive composites. *Cold Regions Sci. Technol.* 86, 22–35. doi:10.1016/j.coldregions.2012.10.007

liu, X., Song, A., Chen, S., Li, Q., Sun, R., Yang, J., et al. (2019). Conductive mechanism of CNTs enhanced conductive magnetic fluid. *Mater. Lett.* 252, 110–113. doi:10.1016/j.matlet.2019.05.088

Lu, Z., Chen, B., Leung, C. Y., Li, Z., and Sun, G. (2019). Aggregation size effect of graphene oxide on its reinforcing efficiency to cement-based materials. *Cem. Concr. Compos.* 100, 85–91. doi:10.1016/j.cemconcomp.2019.04.005

Ma, T., Geng, L., Ding, X., Zhang, D., and Huang, X. (2016). Experimental study of deicing asphalt mixture with anti-icing additives. *Constr. Build. Mater.* 127, 653–662. doi:10.1016/j.conbuildmat.2016.10.018

Nan, Z., Ma, P., Yang, Z., Fang, Y., and Zhang, Z. (2023). Physical dispersion method and mechanism of graphene. *J. Superhard Mater.* 45 (3), 186–191. doi:10.3103/s1063457623030218

Nayır, S., Bahadır, Ü., and Toğan, V. (2024). Investigation of global warming potential of concrete with silica fume and blast furnace slag. *Iran. J. Sci. Technol. Trans. Civ. Eng.* 48 (4), 1965–1975. doi:10.1007/s40996-023-01264-x

Pan, H., She, W., Zuo, W., Zhou, Y., Huang, J., Zhang, Z., et al. (2020). Hierarchical toughening of a biomimetic bulk cement composite. *ACS Appl. Mater. and Interfaces* 12 (47), 53297–53309. doi:10.1021/acsami.0c15313

Pei, Z., Yi, J., Li, Y., Cheng, P., Zhu, Y., and Feng, D. (2021). Material design and performance analysis of the anti-ice and antiskid wear layer on pavement. *Constr. Build. Mater.* 282, 122734. doi:10.1016/j.conbuildmat.2021.122734

Pytka, J. (2010). Determination of snow stresses under vehicle loads. *Cold Regions Sci. Technol.* 60 (2), 137–145. doi:10.1016/j.coldregions.2009.10.002

Sobolkina, A., Mechtcherine, V., Khavrus, V., Maier, D., Mende, M., Ritschel, M., et al. (2012). Dispersion of carbon nanotubes and its influence on the mechanical properties of the cement matrix. *Cem. Concr. Compos.* 34 (10), 1104–1113. doi:10.1016/j.cemconcomp.2012.07.008

Sokołowska, J. J., Łukowski, P., and Bączek, A. (2024). Mortars with polypropylene fibers modified with tannic acid to increase their adhesion to cement matrices. *Appl. Sci.* 14, 2677. doi:10.3390/app14072677

Wang, T., Dra, Y. A. S. S., Cai, X., Cheng, Z., Zhang, D., Lin, Y., et al. (2022). Advanced cold patching materials (CPMs) for asphalt pavement pothole rehabilitation: state of the art. *J. Clean. Prod.* 366, 133001. doi:10.1016/j.jclepro.2022.133001

Xu, S., Zhou, Z., Feng, L., Cui, N., and Xie, N. (2021). Durability of pavement materials with exposure to various anti-icing strategies. *Processes* 9, 291. doi:10.3390/pr9020291

Xu, Y., Zeng, J., Chen, W., Jin, R., Li, B., and Pan, Z. (2018). A holistic review of cement composites reinforced with graphene oxide. *Constr. Build. Mater.* 171, 291–302. doi:10.1016/j.conbuildmat.2018.03.147

Yıldırım, G., Sarwary, M. H., Al-Dahawi, A., Öztürk, O., Anıl, Ö., and Şahmaran, M. (2018). Piezoresistive behavior of CF- and CNT-based reinforced concrete beams subjected to static flexural loading: shear failure investigation. *Constr. Build. Mater.* 168, 266–279. doi:10.1016/j.conbuildmat.2018.02.124

Yoo, D.-Y., You, I., and Lee, S.-J. (2017). Electrical properties of cement-based composites with carbon nanotubes, graphene, and graphite nanofibers. *Sensors* 17, 1064. doi:10.3390/s17051064

Zhai, S., Zhou, X., Zhang, Y., Pang, B., Liu, G., Zhang, L., et al. (2023). Effect of multifunctional modification of waste rubber powder on the workability and mechanical behavior of cement-based materials. *Constr. Build. Mater.* 363, 129880. doi:10.1016/j.conbuildmat.2022.129880

Zhan, M., Pan, G., Zhou, F., Mi, R., and Shah, S. P. (2020). *In situ*-grown carbon nanotubes enhanced cement-based materials with multifunctionality. *Cem. Concr. Compos.* 108, 103518. doi:10.1016/j.cemconcomp.2020.103518

Zhao, X., Zhang, Y., and Zheng, M. (2024). Enhancing the efficiency of ice-resistant materials in asphalt road surfaces: a comprehensive performance analysis. *Coatings* 14, 37. doi:10.3390/coatings14010037

Zhu, Y., Murali, S., Cai, W., Li, X., Suk, J. W., Potts, J. R., et al. (2010). Graphene and graphene oxide: synthesis, properties, and applications. *Adv. Mater.* 22 (35), 3906–3924. doi:10.1002/adma.201001068

frontiers | Frontiers in Materials

TYPE Original Research
PUBLISHED 19 November 2024
DOI 10.3389/fmats.2024.1499691

OPEN ACCESS

EDITED BY
Biao Hu,
Shenzhen University, China

REVIEWED BY
Pan Wang,
Qingdao University of Technology, China
Zeyu Lu,
University of Macau, China
Xiongfei Liu,
Hebei University of Technology, China

*CORRESPONDENCE
Jiayang Zhang,
15620218044@163.com

RECEIVED 21 September 2024
ACCEPTED 28 October 2024
PUBLISHED 19 November 2024

CITATION
Ning X, Zhang J, Zhuang C, Su Q and Zhong S (2024) Investigation of the performance and life cycle assessment of alkali-activated sintered sludge-slag-based permeable concrete.
Front. Mater. 11:1499691.
doi: 10.3389/fmats.2024.1499691

Investigation of the performance and life cycle assessment of alkali-activated sintered sludge-slag-based permeable concrete

Xiangbo Ning[1], Jiayang Zhang[2]*, Can Zhuang[3], Qunyong Su[4] and Shunjie Zhong[3]

[1]China MCC22 Group Corporation Ltd., Hebei, China, [2]School of Civil Engineering, Tianjin University, Tianjin, China, [3]Fujian Zhanglong Construction Investment Group Co., Ltd., Zhangzhou, Fujian, China, [4]Zhangzhou Municipal Engineering Center, Zhangzhou, Fujian, China

As urbanization continues to accelerate, the application of permeable concrete is becoming an increasingly prevalent practice. Nevertheless, the carbon dioxide emission issue associated with traditional permeable concrete cannot be overlooked. In this study, alkali-activated sintered sludge and slag were employed as raw materials to prepare alkali-activated sintered sludge-slag-based permeable concrete. The effects of sludge calcination temperature, sludge content, and binder-to-aggregate ratio on the compressive strength, porosity, and permeability coefficient of the permeable concrete were investigated through the implementation of one-way experiments. The formation mechanism of permeable concrete materials was analyzed using scanning electron microscopy-energy dispersive spectroscopy (SEM-EDS), and a carbon emission assessment was performed. The findings indicated that an increase in sludge content resulted in a notable decline in the 28-day compressive strength, accompanied by a reduction in the Ca/Si ratio of the C-A-S-H hydration products, from 1.08 to 0.35. Conversely, the carbon emission assessment demonstrated that abiotic losses declined markedly with an increase in sludge content, effectively mitigating the carbon emission burden associated with construction materials.

KEYWORDS

alkali-activated permeable concrete, sludge, slag, formation mechanism, carbon emissions

1 Introduction

Globally, the acceleration of urbanization and increase in industrial activities lead to the production of a significant amount of construction waste and industrial by-products, the disposal of which has become a serious environmental issue (Jiang et al., 2024; Duan and Wang, 2022; Sharma et al., 2023). Moreover, traditional cement has notable deficiencies in urban drainage and rainwater management (Adresi et al., 2023; Isukuru et al., 2024). Although its high strength and durability make it widely used in construction, the high carbon emissions from cement production severely limit its

environmental friendliness. The large amounts of carbon dioxide released during the cement production process not only exacerbate global warming but also make traditional permeable concrete unsustainable in addressing urban drainage challenges, particularly in managing rainwater permeation and reducing surface runoff. The high carbon footprint of traditional cement contradicts its environmental requirements, necessitating the search for greener alternatives (Zaid et al., 2024; Basyouni and Mahmoud, 2024; Khan and McNally, 2024).

Permeable concrete is a special type of concrete material characterized by high permeability due to large voids between aggregates, which effectively reduces surface runoff, alleviates the burden on urban drainage systems, and quickly eliminates standing water, thus mitigating urban flooding issues (Pour et al., 2020). Additionally, it aids in groundwater recharge, improves water quality, and helps alleviate urban heat island effects, providing a comfortable living environment for citizens (Florentin et al., 2024; Al Jurdi et al., 2023). This material is widely used in parking lots, sidewalks, and pathways, with relatively simple construction and maintenance requirements (Rumbach et al., 2022). However, the high cement content in traditional permeable concrete leads to significant carbon emissions, which is a pressing issue in the current global environmental context. To further reduce environmental impacts, improvements in material formulations and production processes are needed to find more sustainable solutions (Wu et al., 2024; Salami et al., 2024).

Sludge and slag are two widely available and potential supplementary cementitious materials, whose application not only helps in resource recycling but also significantly reduces the carbon footprint of building materials (Yang et al., 2024). Sludge mainly comes from urban sewage treatment plants and is a solid waste precipitated during the sewage treatment process. It contains a large amount of minerals (such as silicates, bauxite, and iron ores) and organic matter. Its chemical composition allows it to exhibit good cementitious properties when properly treated (Guo et al., 2024). By drying, crushing, and chemically processing sludge, it can be transformed into a reactive material. This material can chemically react with alkaline solutions in alkali-activated reactions, forming high-strength gel bodies, thereby partially replacing traditional cement, reducing reliance on cement, and effectively reducing waste (Zhao et al., 2024; Jin et al., 2024). Studies have explored ultra-fine kaolin, water glass, and sodium hydroxide for alkali activation, with different amounts of accelerators to produce optimal geopolymer composite materials. The results indicated that at an accelerator amount of 5%, the geopolymer exhibited the best apparent density, porosity, and enhancement effects, and the strength of geopolymers with accelerators was higher than those without when the accelerator dosage was increased within a certain range. Slag is a by-product of the metallurgical industry, mainly originating from the smelting of iron ores and other metal ores (Đorđević et al., 2024). The slag produced during smelting is rich in silicates, bauxite, and lime, which exhibit good cementitious properties after grinding. Slag can also react with alkaline solutions to form a high-strength and stable cementitious material, making it an eco-friendly alternative material in construction engineering, reducing the use of traditional cement (Cui et al., 2024).

Meanwhile, sludge and slag are ideal precursors for alkali-activated reactions. Alkali-activated reactions utilize strong alkaline solutions (such as sodium hydroxide or calcium hydroxide) to activate the minerals in these materials, forming high-performance cementitious products. These alkali-activated products exhibit excellent physical and chemical properties, including high strength, low permeability, and good chemical corrosion resistance (Yuan et al., 2024). Studied the effects of different cement and alkali contents on the mechanical properties of cementitious materials. Their research indicated that increasing the amounts of cement and alkali led to higher strength in the cementitious materials (Yu et al., 2024). Notably, variations in alkali content had a more pronounced effect on the early strength of the materials. However, when the cement content exceeded 10%, the mechanical properties began to decline. By this method, sludge and slag can be converted into effective building materials, greatly reducing the demand for traditional cement, thus lowering the carbon emissions during the production of building materials and promoting the development of sustainable building materials (Kuoribo et al., 2024). Although alkali-activated materials have shown good application prospects in the construction industry, research on alkali-activated permeable concrete is still relatively limited. Most existing studies focus on the performance and environmental impacts of traditional permeable concrete, lacking in-depth discussions on alkali-activated permeable concrete, and research on aspects such as life cycle assessment of alkali-activated permeable concrete is not yet complete (Salami et al., 2024).

This paper mainly investigates the effects of sludge calcination temperature, the content of sintered sludge, and the aggregate-to-binder ratio on the compressive strength, connectivity porosity, and permeability coefficient of alkali-activated permeable concrete. It also analyzes the formation mechanism of the permeable concrete material using scanning electron microscopy-energy dispersive spectroscopy (SEM-EDS) testing methods. Additionally, a life cycle assessment (LCA) study is conducted to explore its environmental impact. By systematically evaluating the mechanical properties, permeability, and durability of alkali-activated sintered sludge-slag-based permeable concrete, this research aims to provide a scientific basis for its application in urban infrastructure. Furthermore, this study will combine the LCA method to comprehensively analyze the environmental impact of this material, thus offering theoretical support and practical guidance for the development and application of green building materials.

2 Materials and methods

2.1 Raw materials

The sludge used in this study was sourced from Baiyangdian in Hebei, while the slag was obtained from a steel mill in Hunan. The main components include SiO_2, CaO, and Al_2O_3, as shown in Table 1. The coarse aggregate used was ordinary limestone crushed stone with a particle size of 4.75–9.5 mm from the Hengji Stone Factory in Jilin City. The particle grading, particle size, mud content, crushing index, and void ratio of the coarse aggregate all meet the requirements of the "Pebbles and Crushed Stone for Building Use" (GB/T 14685-2022) and "Technical Specifications for Permeable Cement Concrete Pavement" (CJJ/T 135-2009) (Zhang et al., 2024). The water glass solution came from a chemical plant in Handan,

TABLE 1 Chemical composition of sludge.

Oxide (%)	CaO	SiO_2	Al_2O_3	Fe_2O_3	SO_3	MgO	K_2O	TiO_2
Sludge	6.25	58.95	19.01	6.27	0.28	2.75	2.96	0.82
Slag	39.23	35.56	15.45	0.71	4.22	8.21	0.45	0.82

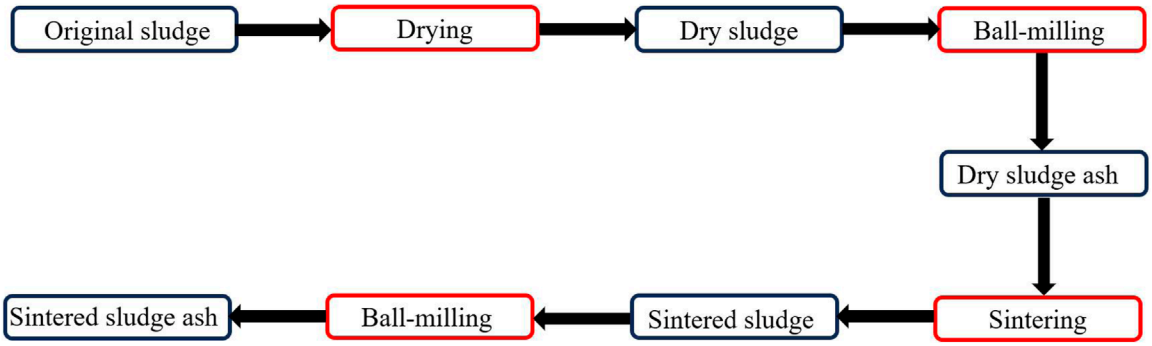

FIGURE 1
The calcination activation process of sludge.

Hebei Province, with a modulus of 3.1, a SiO_2 mass fraction of 27.54%, and a Na_2O mass fraction of 9.35%. Solid sodium hydroxide, with a purity of 98.9%, was sourced from a chemical plant in Luoyang, Henan Province.

2.2 Mix proportion design

Preliminary experiments were conducted to explore the characteristics of the raw materials and the performance requirements of the permeable concrete to be satisfied, and the general range for the alkali equivalence and the sludge to slag ratio was determined. In the experiments, the water to binder ratio was fixed at 0.4, the modulus of the water glass was consistently 3.1 M, and the alkali content referred to the percentage of Na_2O in the total mass of sludge and slag.

The sludge was treated by calcination: first, the sludge blocks were placed in an oven and dried at 150°C. The dried blocky sludge was then ground in a ball mill for 6 min to produce powdered sludge ash. The sludge ash was then placed in a crucible and calcined in a high-temperature furnace, heating at a rate of 10°C/min to temperatures of 400°C, 600°C, and 800°C, then held at these temperatures for 120 min to produce sintered sludge, which was finally ground again for 1 min to obtain sintered sludge ash. As shown in Figure 1.

Using the volumetric method to determine the mix ratio of permeable concrete, the speccific steps are as shown in Equations 1–3:

$$\frac{m_s}{\rho_s}+\frac{m_r}{\rho_r}+\frac{m_w}{\rho_w}+\frac{m_a}{\rho_a}+\frac{m_g}{\rho_g}=1 \quad (1)$$

$$\frac{m_w}{m_r+m_s}=0.4 \quad (2)$$

$$\frac{m_r+m_s}{m_g}=0.24 \quad (3)$$

where m_s is the mass of the slag in a dry state (g), m_r is the mass of the slag in a dry state (g), m_w is the mass of water (g), m_a is the mass of the alkaline activator (g), m_g is the mass of coarse aggregate (g), ρ_s is the density of the slag in a dry state (g/cm^3), ρ_r is the density of the slag in a dry state (g/cm^3), ρ_w is the density of water (g/cm^3), ρ_a is the density of the alkaline activator (g/cm^3), ρ_g is the density of the coarse aggregate in a bulk state (g/cm^3).

The experiment was designed with sludge undergoing no calcination treatment and calcination at different temperatures: 400°C, 600°C, 800°C. The sludge content was: 0%, 10%, 30%, 50%, and different binder-aggregate ratios: 0.2, 0.22, 0.24, 0.26, resulting in a total of 12 experimental groups. The experimental mix ratio design is shown in Table 2.

2.3 Specimen preparation

The concrete mix was prepared using a two-charge method, tamped into molds to form 100 mm × 100 mm × 100 mm non-standard test blocks. Sodium hydroxide, water glass, and water were mixed to prepare different moduli of alkali activators, which were then stored indoors to cool for 24 h before use. The pre-moistened coarse aggregate was first put into the mixer, followed by 20%–30% alkali activator solution and mixed for 30 s to ensure the coarse aggregate was sufficiently wet to better adhere to the cementitious materials, then, the pre-mixed sludge and slag were added and mixed for 1 min to evenly coat the aggregate surfaces with cementitious materials, finally, the remaining alkali activator solution was added and mixed for 3 min to fully coat the aggregate. The mixture was loaded in two layers, tamped, and then cured in still water until the age for performance testing.

10.3389/fmats.2024.1499691

TABLE 2 Experimental mix ratios.

Number	Sludge		Slag (kg/m^3)	Aggregate (kg/m^3)	Alkali concentratio (kg/m^3)	Water (kg/m^3)	Binder-to-aggregate ratio (kg/m^3)
	Temperature (°C)	Content (kg/m^3)					
T1	20	83.11	193.93	1154.46	16.62	96.96	0.24
T2	400	83.11	193.93	1154.46	16.62	96.96	0.24
T3	600	83.11	193.93	1154.46	16.62	96.96	0.24
T4	800	83.11	193.93	1154.46	16.62	96.96	0.24
S1	600	0.00	280.37	1168.33	16.82	98.13	0.24
S2	600	27.92	251.33	1163.67	16.75	97.74	0.24
S3	600	83.11	193.93	1154.46	16.62	96.96	0.24
S4	600	137.43	137.43	1145.39	16.49	96.20	0.24
L1	600	71.90	167.77	1198.37	14.38	83.88	0.20
L2	600	77.62	181.11	1175.97	15.52	90.55	0.22
L3	600	83.11	193.93	1154.46	16.62	96.96	0.24
L4	600	88.42	206.33	1133.65	17.68	103.16	0.26

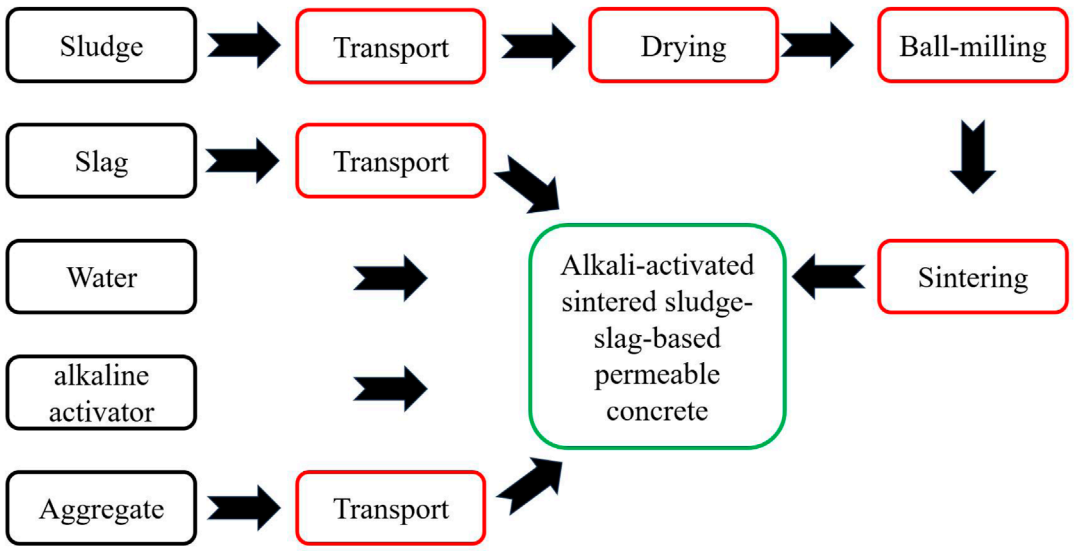

FIGURE 2
System boundary for alkali-activated sintered sludge-slag permeable concrete.

2.4 Experimental methods

2.4.1 Compressive strength

The compressive strength of the specimens was tested using a YAW-300C fully automatic compression testing machine produced by Jinan Shidai Test Gold Testing Machine Co., Ltd., following the standards in GB/T 50081-2019 "Standard for Test Methods of Physical and Mechanical Properties of Concrete." The cured alkali-activated sintered sludge-slag-based permeable concrete blocks were placed on the platform of the testing machine, ensuring good contact between the bottom of the sample and the platform surface. During the compressive strength test, the loading speed was adjusted to 2.4 kN/s. The data recorded were processed by arithmetic average to calculate the compressive strength of the group. If

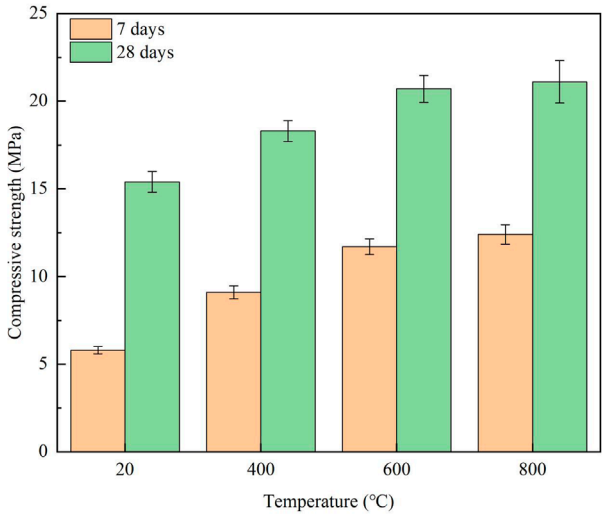

FIGURE 3
Effect of sludge calcination temperature on compressive strength.

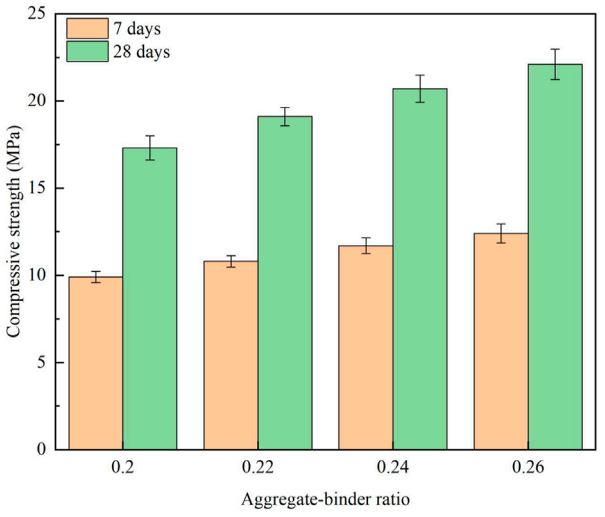

FIGURE 5
Effect of different binder-to-aggregate ratios on compressive strength.

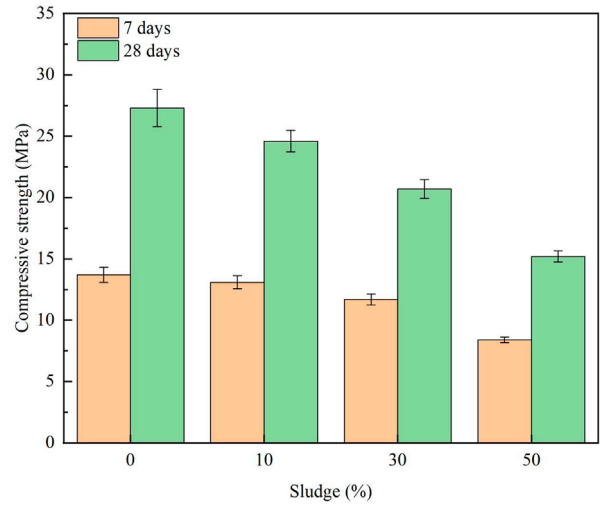

FIGURE 4
Effect of sludge content on compressive strength.

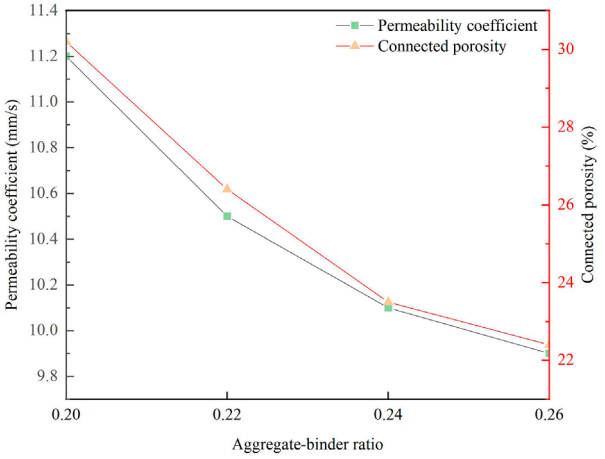

FIGURE 6
Effect of different binder-to-aggregate ratio on porosity and permeability coefficient.

the experimental values in the group had large errors, they were processed again.

2.4.2 Permeability coefficient

The permeability coefficient was tested according to CJJ/T135-2009 (Muauz et al., 2024). The sample size for testing was a cylinder with a base diameter of 100 mm and a height of 50 mm. Calculated according to Equation 4:

$$K_T = \frac{QL}{AHt} \quad (4)$$

where KT is the permeability coefficient (mm/s), T is the water temperature (°C), Q is the volume of water collected in t s (mm^3), L is the thickness of the specimen (mm), A is the surface area of the specimen (mm^2), H is the water level difference (mm), and t is the time (s).

2.4.3 Connected porosity rate

The test for connected porosity rate of permeable concrete specimens was used to evaluate the connectivity of the pores and the overall permeability. Firstly, the permeable concrete specimens, sized 100 mm × 100 mm × 100 mm, were cured under standard conditions for 28 days. After reaching the age, the specimens were placed in an oven and dried to constant weight at a set temperature of (105 ± 5)°C. After removal, the specimens were cooled to room temperature in a cool, dry environment and weighed. Then, they were immersed in water, treated to saturation until no more bubbles emerged from the surface. Following this, the saturated specimens were weighed in water, and their mass was recorded. By comparing

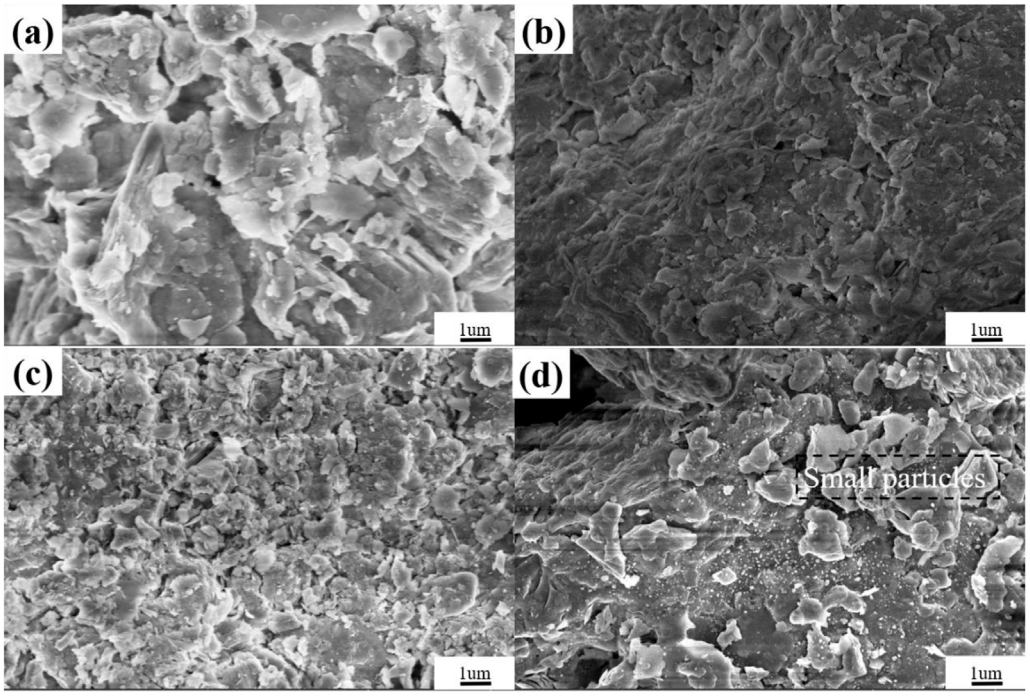

FIGURE 7
Morphology of alkali-activated sintered sludge-slag-based permeable concrete at different temperatures. **(A)** 20°C **(B)** 400°C **(C)** 600°C **(D)** 800°C.

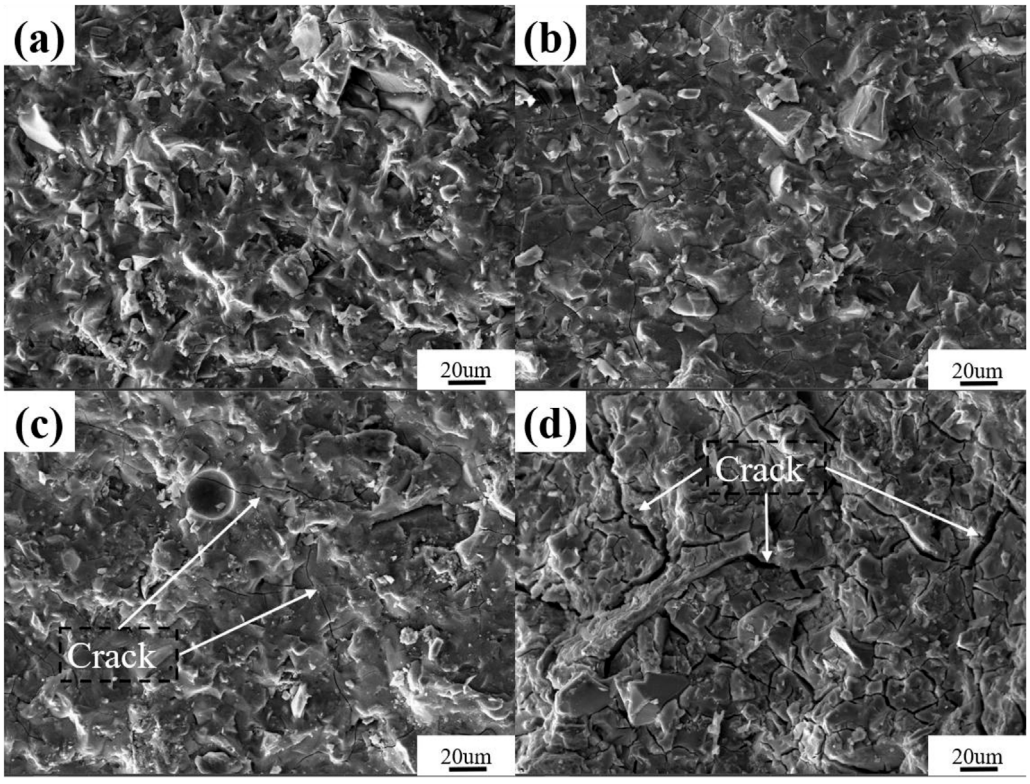

FIGURE 8
Morphology of alkali-activated slag permeable concrete with different content of sintered sludge. **(A)** 0% **(B)** 10% **(C)** 30% **(D)** 50%.

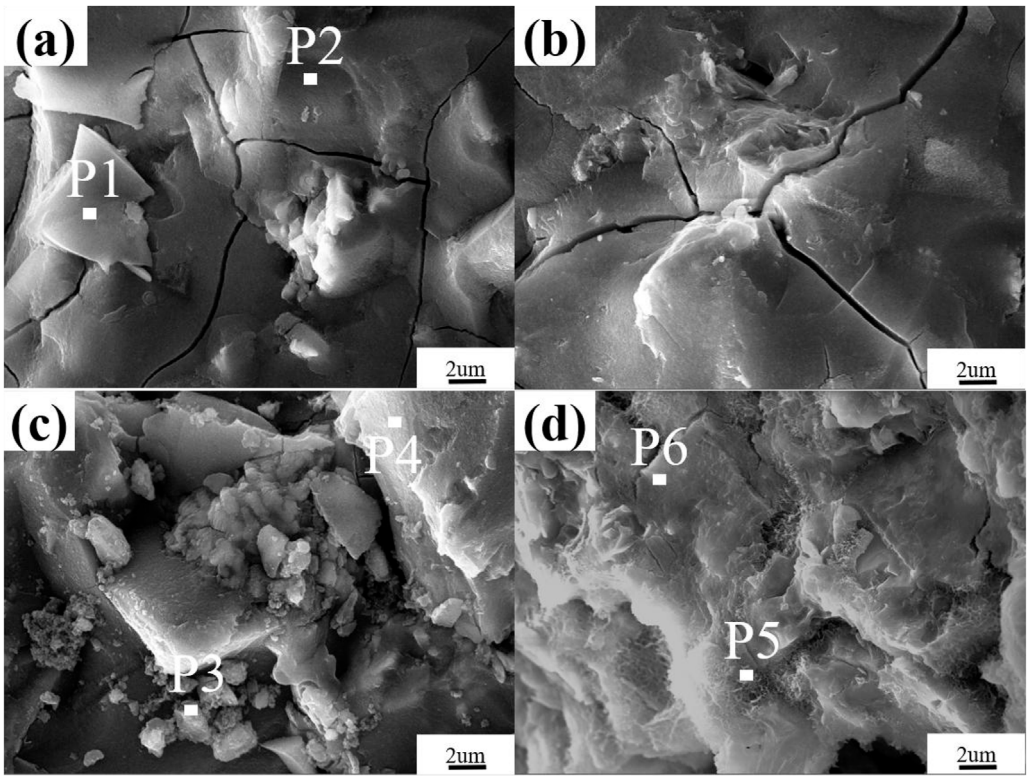

FIGURE 9
Morphology of alkali-activated slag permeable concrete with different amounts of sintered sludge at high magnification. **(A)** 0.20 **(B)** 0.22 **(C)** 0.24 **(D)** 0.26.

the mass of the specimen in the dry state with the mass in the saturated state, the connected porosity can be calculated. Calculated according to Equation 5:

$$P = \left(1 - \frac{m_1 - m_2}{\rho V}\right) \times 100\% \quad (5)$$

where P is the connected porosity rate (%), m_1 is the mass of the specimen in dry state (g), m_2 is the mass of the specimen in saturated state (g), ρ is the density of the specimen (g/cm^3), and V is the volume of the specimen (cm^3).

2.4.4 Scanning electron microscope (SEM)

To observe the microstructure and elemental composition of the hydration products in the alkali-activated sintered sludge-slag-based permeable concrete, a Quanta 250 Field Emission Scanning Electron Microscope (FEI/SEM, Hillsboro, OA, United States) was used. Due to the poor conductivity of the alkali-activated sintered sludge-slag-based permeable concrete, it was necessary to apply conductive adhesive to the sample surface first, followed by gold sputtering to enhance the sample's conductivity.

2.4.5 Life cycle assessment method (LCA)

Life Cycle Assessment (LCA) is a method for analyzing and evaluating the overall resource inputs and emissions outputs throughout the entire lifecycle of a product. This includes everything from raw material extraction, transportation, and processing to the final product's use and eventual disposal (Liang et al., 2024). The assessment process consists of four main components: defining the goal and scope, inventory analysis, impact assessment, and interpretation of the lifecycle results.

In this experiment, the LCA model aimed to quantify the resource and environmental impacts of producing alkali-activated sintered sludge-slag permeable concrete under various material proportions. The research findings will provide substantial evidence and reference for selecting sludge treatment conditions in terms of resource and environmental impacts, aiding decision-making when related research is implemented in real production (Tamoor et al., 2023).

When discussing the standard scope, it is essential to highlight that the majority of moisture in the sludge drying phase is lost during natural air drying. Given sufficient time, this process can even result in complete dryness. The treatment of specimens in an oven was not included in the primary conditions under consideration, as its energy consumption is relatively low compared to the overall process, leading to minimal environmental impact. Consequently, the cut-off principle was applied to exclude this process.

In summary, the system boundary for the production of alkali-activated sintered sludge-slag permeable concrete is illustrated in Figure 2.

This experiment utilizes SimaPro as the software tool for constructing the life cycle assessment model (Herrando et al., 2022). Developed by the Centre for Environmental Science at Leiden University in the Netherlands, SimaPro is currently used in over 80 countries. The software includes a rich set of databases, such as large databases like ecoinvent, ELCD, the U.S. Life Cycle Inventory Database, and the IDEA Japan Inventory Database, as

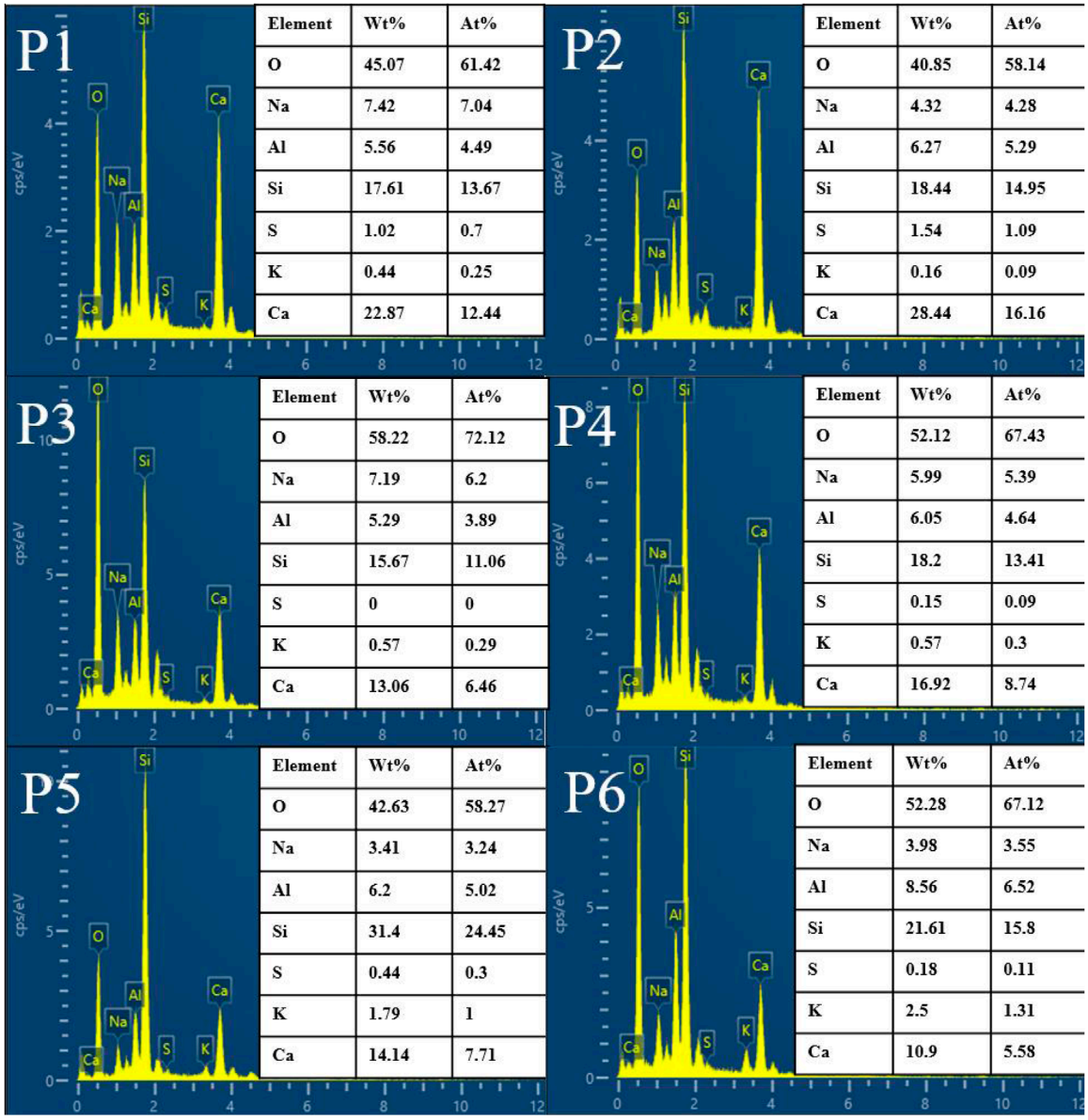

FIGURE 10
EDS energy spectrum analysis of alkali-activated slag permeable concrete with different content of sintered sludge.

well as numerous industry-specific databases like PlasticsEurope, ERASM, and World Steel. The databases related to construction materials, transportation processes, and treatment methods are relatively comprehensive and sufficient to meet the requirements for building the corresponding model.

3 Results and discussion

3.1 Compressive strength analysis

3.1.1 Sludge calcination temperature

Figure 3 showed the compressive strength of permeable concrete at 7 and 28 days under room temperature and various calcination temperatures (20°C, 400°C, 600°C, 800°C) (Yan et al., 2022). It was observed that as the calcination temperature of sludge increases, so did the compressive strength of the permeable concrete. This increase in strength was due to the reduction of organic substances within the sludge, which would otherwise impede hydration reactions and affect the strength of the concrete. The structural changed in the sludge particles after calcination also made them more conducive to bonding with the cement matrix, thereby enhancing the overall strength of the concrete. The influence of temperature on strength showed a more pronounced effect in the early stages, becoming nearly consistent at higher temperatures. At 600°C, almost all organic materials were decomposed, hence the impact on the strength of sludge at 600°C and 800°C was nearly the same.

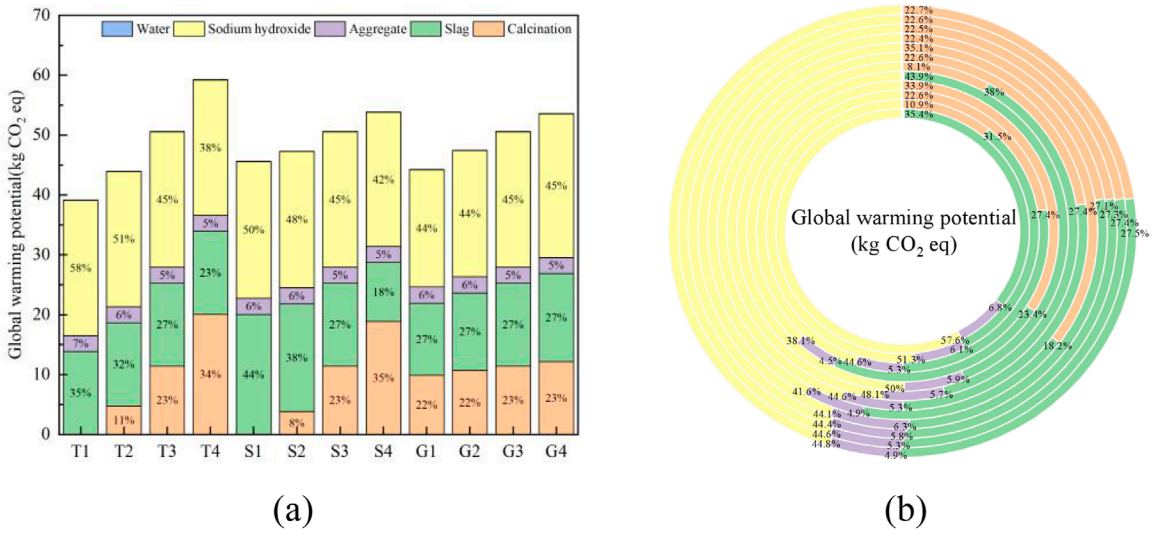

FIGURE 11
The **(A)** eigenvalue and **(B)** composition ratio of GWP.

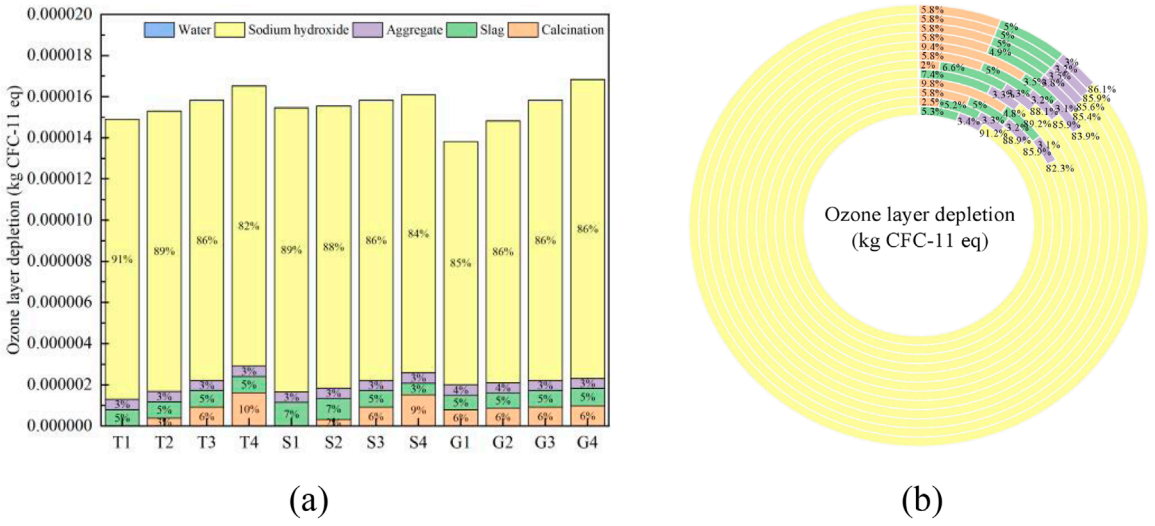

FIGURE 12
The **(A)** eigenvalue and **(B)** composition ratio of OLDP.

3.1.2 Sintered sludge content

Figure 4 illustrated the compressive strength of permeable concrete at 7 and 28 days with different sintered sludge contents (0%, 10%, 30%, 50%). As the sintered sludge content increases, the compressive strength of the permeable concrete decreases. This was because sludge, as an auxiliary cementitious material, offers lower strength than slag. When the sludge contents of 0%–30%, the strength at 7 days changed little, while at 28 days, the strength significantly reduced, indicating that sludge contributes more to the early strength, whereas slag provides better late strength. It was evident that at a sludge content of 50%, there is a sharp drop in strength. This may be due to excessive sludge content reducing the flowability of the permeable concrete, making it difficult to compact during preparation, and creating weak areas, thereby reducing the compressive strength of the concrete. Therefore, sludge content should ideally be kept within 50%.

3.1.3 Binder-to-aggregate ratio

Figure 5 showed the compressive strength of permeable concrete at 7 and 28 days with different binder-to-aggregate ratios (0.2, 0.22, 0.24, 0.26). As the binder-to-aggregate ratio increased, so did the strength at both 7 and 28 days, although the increase was relatively modest. Additionally, the 28 days strength was approximately twice that of the 7 days compressive strength. When the

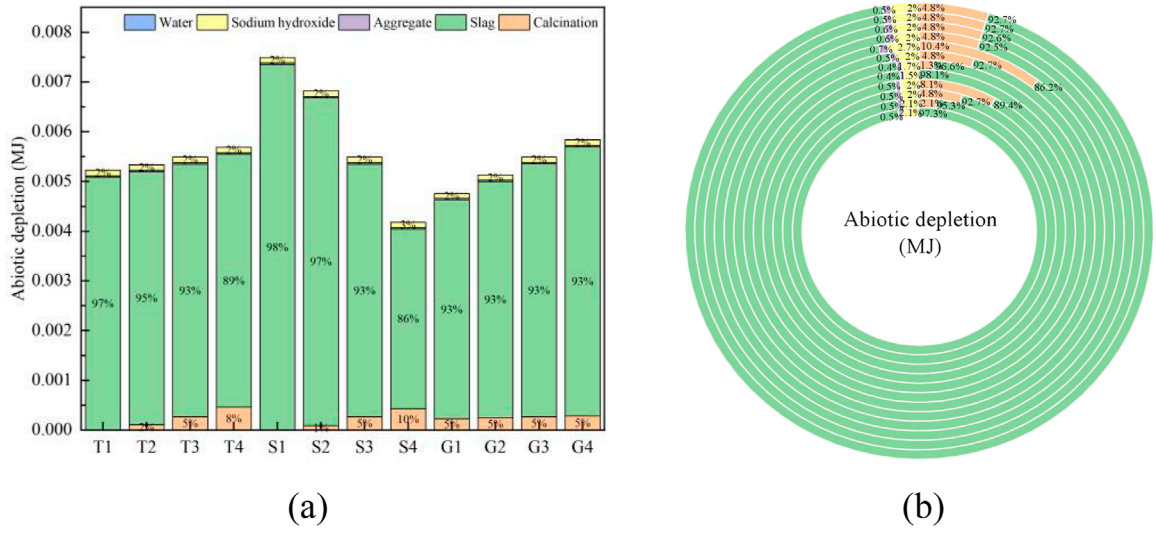

FIGURE 13
The **(A)** eigenvalue and **(B)** composition ratio of ADP.

binder-to-aggregate ratio was low, the cementitious material provided a weaker coating around the aggregates, and the coating layer was thinner. Also, due to more aggregates, the cementitious material may accumulate in clumps, failing to adequately bond all aggregates, thus resulting in lower compressive strength. As the amount of cementitious material increased, both the degree of coating around aggregates and the thickness of the coating improve, and the reduction in aggregate quantity allows the cementitious material to better connect all aggregates, enhancing the compressive strength of the permeable concrete.

3.1.4 Connected porosity and permeability analysis

Figure 6 shows the effect of different binder-to-aggregate ratio on porosity andpermeability coefficient. Comparing the connected porosity and permeability coefficients, a similar trend can be observed, both decreasing as the binder-to-aggregate ratio increases, with the rate of decrease slowing as the ratio increases (Liu et al., 2022). This was because the primary channels for water permeability in permeable concrete were the voids between aggregates rather than the cementitious material itself, thus there was a strong correlation between connected porosity and permeability coefficients. At lower binder-to-aggregate ratios, due to inadequate coating of aggregates by cementitious materials, the connections between aggregates were poor, resulting in more pores. This resulted in higher connected porosity and permeability coefficients. As the cementitious material fully enveloped the aggregates, this phenomenon gradually diminished, significantly reduced both metrics (Shanmuganathan et al., 2023).

3.2 Microscopic morphology

Figure 7 shows the alkali-activated permeable concrete composed of sintered sludge and slag as precursor materials at different calcination temperatures. It is evident that as the calcination temperature increases, the minerals gradually decompose, forming more fine particles. High-temperature calcination activation enhances the reactivity of sludge, contributing to improved strength and durability of permeable concrete (Wang et al., 2024). Moreover, the higher the temperature, the denser the microstructure, forming a more compact network structure, which aids in the mechanical performance of the permeable concrete. However, at 800°C, increased porosity and a looser particle structure were observed, which may be due to recrystallization (Tiwari et al., 2020).

Figure 8 shows the alkali-activated slag permeable concrete with different proportions of sintered sludge at 28 days of age. As the sludge content increased, cracks and pores become more apparent within the cementitious material, indicating that the addition of sintered sludge inhibits the shrinkage ability of the alkali-activated cementitious material. The primary hydration products in the alkali-activated slag reaction are calcium-aluminosilicate hydrates (C-A-S-H) and calcium-aluminate hydrates (C-A-H). C-A-S-H possesses good binding properties, while calcium-aluminate hydrates (C-A-H) formed in a high-alkali environment when aluminum in slag reacted with calcium, enhancing the material's strength and durability (Kosar et al., 2023). Hydration products typically appeared as irregular granular or gel-like structures, which interlace during hydration to form complex networks. The compactness of the alkali-activated slag cementitious material was typically higher. However, the early high hydration degree of alkali-activated cementitious materials can adversely affect the material of sustained development, sludge addition balances the excessive early reaction of slag, achieving the goal of sustained development for permeable concrete cementitious materials (Zhu et al., 2024).

As shown in Figure 9, high-magnification images reveal unreacted calcined sludge particles at point P3 in samples with high sludge content, as evidenced by the spectrum in Figure 10. This

observation indicates that the calcined sludge has not been fully decomposed, suggesting that its reactivity is lower than that of the slag. This incomplete decomposition may result from insufficient processing conditions or inadequate exposure time during the calcination process.

Through the energy spectrum of 2, 4, 6 points in Figure 10, it was found that the content of calcined sludge is from 0% to 30% to 50%, and the Ca/Si of hydration product C-A-S-H was from 1.08 to 0.65 to 0.35. The results were consistent with the high silicon content of calcined sludge. The addition of calcined sludge changed the structure of hydration products and reduced its Ca/Si.

3.3 Life cycle assessment

3.3.1 Global warming potential (GWP)

Global warming potential indicates the likelihood of global warming over 100 years, mainly related to greenhouse gas emissions as shown in the Figure 11. The metric is expressed in kg CO_2 eq. The results showed that the main sources were sodium hydroxide and slag, and as the calcination temperature increased, the impact of calcination also rised (Yan et al., 2022). Considering the effects of calcination temperature on mechanical properties, it was advisable to avoid calcination temperatures above 800°C. Excessive calcination temperatures not only minimally enhance mechanical properties but can also negatively impact the environment. Additionally, as the sludge content increases, the global warming potential also rises, although the changes were minor at lower sludge contents (10%).

3.3.2 Ozone layer depletion

Ozone layer depletion refers to the gradual thinning of Earth's upper atmosphere ozone layer caused by the release of gaseous chlorine or bromine compounds from industrial and other human activities as shown in the Figure 12. The metric is expressed in kg CFC-11 eq (Pradel et al., 2021; Savinykh et al., 2021). As observed, ozone layer depletion slowly increases with higher calcination temperatures due to the destructive effects of the calcination process on the ozone layer. Using sludge in place of slag almost does not change the ozone layer depletion, signifying that substituting slag with sludge can manage solid waste without adding to the destruction of the ozone layer. As the binder-to-aggregate ratio increases, leading to higher usage of cementitious materials, ozone layer depletion also rises (Wang et al., 2023).

3.3.3 Abiotic depletion (fossil fuels)

Abiotic depletion indicates the consumption of non-renewable resources such as fossil fuels, measured in MJ, as shown in the Figure 13 (Wang et al., 2023). With increasing calcination temperature, there is little change in abiotic depletion. However, as the replacement amount of sludge increases, there is a significant decline. At a 50% substitution level, abiotic depletion decreases by nearly 50%. This is primarily because the main source of abiotic depletion is slag, thus, reducing the amount of slag significantly lowers abiotic depletion. Without compromising mechanical strength, increasing the sludge substitution amount can effectively reduce abiotic depletion (Burchart-Korol, 2013).

4 Conclusion

This study provides an in-depth exploration of the performance and life cycle of alkali-activated sintered sludge-slag permeable concrete, leading to the following important conclusions:

(1) Mechanical performance: As the calcination temperature of the sludge increases, the compressive strength of the permeable concrete correspondingly rises. This improvement is primarily attributed to the synergistic effect between the sintered sludge and slag, which forms a stable three-dimensional network structure. However, with an increase in sludge content, the compressive strength decreases because the strength provided by the sludge as an auxiliary binder is lower than that of the slag.

(2) Microscopic features: As the sintering temperature continues to rise, minerals gradually decompose, generating more fine particles. High-temperature calcination activation allows the sludge to exhibit better reactivity, contributing to enhanced strength and durability of the permeable concrete. However, with an increase in sludge content, cracks appear in the binder material, leading to increased porosity, while the calcium-to-silicon ratio of the hydration products initially increases and then decreases.

(3) Environmental impact: Reducing the amount of slag can significantly lower abiotic depletion. At the same time, an increase in sludge content leads to a rise in global warming potential, although the variation is relatively small at lower substitution levels (10%).

Future research can focus on further optimizing the ratio of sintered sludge to slag to achieve the best mechanical performance and economic benefits, particularly in balancing the relationship between sludge content and compressive strength. Additionally, exploring the impact of different sintering temperatures on material properties is crucial for enhancing the long-term durability of permeable concrete. Lastly, while reducing the slag content can significantly decrease abiotic depletion, increasing sludge content raises global warming potential, thus, it is necessary to seek more environmentally friendly material alternatives or additives to mitigate environmental impacts.

Data availability statement

The original contributions presented in the study are included in the article/supplementary material, further inquiries can be directed to the corresponding author.

Author contributions

XN: Investigation, Methodology, Resources, Validation, Writing–original draft, Writing–review and editing. JZ:

Conceptualization, Data curation, Formal Analysis, Resources, Visualization, Writing–original draft, Writing–review and editing. CZ: Conceptualization, Formal Analysis, Methodology, Validation, Writing–original draft. QS: Data curation, Formal Analysis, Investigation, Software, Writing–original draft. SZ: Funding acquisition, Investigation, Project administration, Software, Writing–original draft.

Funding

The author(s) declare financial support was received for the research, authorship, and/or publication of this article. Financial support from the National Natural Science Foundation of Tianjin under the grants of 21JCZDJC00410 is gratefully acknowledged.

Conflict of interest

Author XN was employed by China MCC22 Group Corporation Ltd. Authors CZ and SZ were employed by Fujian Zhanglong Construction Investment Group Co., Ltd.

The remaining authors declare that the research was conducted in the absence of any commercial or financial relationships that could be construed as a potential conflict of interest.

Publisher's note

References

Adresi, M., Yamani, A., Karimaei Tabarestani, M., and Rooholamini, H. (2023). A comprehensive review on pervious concrete. *Constr. Build. Mater.* 407, 133308. doi:10.1016/j.conbuildmat.2023.133308

Al Jurdi, M., Wehbe, R., and Mroueh, H. (2023). Integration of citizens' feelings and feedback into the city information modeling environment. *Sustain. Cities Soc.* 99, 104971. doi:10.1016/j.scs.2023.104971

Basyouni, Y. A., and Mahmoud, H. (2024). Affordable green materials for developed cool roof applications: a review. *Renew. Sustain. Energy Rev.* 202, 114722. doi:10.1016/j.rser.2024.114722

Burchart-Korol, D. (2013). Life cycle assessment of steel production in Poland: a case study. *J. Clean. Prod.* 54, 235–243. doi:10.1016/j.jclepro.2013.04.031

Cui, W., Liu, J., Duan, W., Xie, M., Li, X., and Dong, X. (2024). Study on the synergistic effects and eco-friendly performance of red mud-based quaternary cementitious materials. *Constr. Build. Mater.* 428, 136352. doi:10.1016/j.conbuildmat.2024.136352

Đorđević, T., Tasev, G., Aicher, C., Potysz, A., Nagl, P., Lengauer, C. L., et al. (2024). Mineralogy and environmental stability of metallurgical slags from the Euronickel smelter, Vozarci, North Macedonia. *Appl. Geochem.* 170, 106068. doi:10.1016/j.apgeochem.2024.106068

Duan, L., and Wang, L. (2022). How does the construction of China's ecological civilization affect the health burden of urban and rural residents? *Chin. J. Popul. Resour. Environ.* 20 (4), 369–382. doi:10.1016/j.cjpre.2022.11.007

Florentin, K. M., Onuki, M., and Yarime, M. (2024). Facilitating citizen participation in greenfield smart city development: the case of a human-centered approach in Kashiwanoha international campus town. *Telematics Inf. Rep.* 15, 100154. doi:10.1016/j.teler.2024.100154

Guo, K., Li, Y., Wang, J., Sui, Z., Wang, T., and Pan, W.-P. (2024). A review on selenium in coal-fired power plants: content and forms in coal, determination methods, migration, transformation, and control technologies. *J. Environ. Chem. Eng.* 12 (5), 113579. doi:10.1016/j.jece.2024.113579

Herrando, M., Elduque, D., Javierre, C., and Fueyo, N. (2022). Life Cycle Assessment of solar energy systems for the provision of heating, cooling and electricity in buildings: a comparative analysis. *Energy Convers. Manag.* 257, 115402. doi:10.1016/j.enconman.2022.115402

Isukuru, E. J., Opha, J. O., Isaiah, O. W., Orovwighose, B., and Emmanuel, S. S. (2024). Nigeria's water crisis: abundant water, polluted reality. *Clean. Water* 2, 100026. doi:10.1016/j.clwat.2024.100026

Jiang, Z.-Y., Sun, X.-P., Luo, Y.-Q., Fu, X.-L., Xu, A., and Bi, Y.-Z. (2024). Recycling, reusing and environmental safety of industrial by-product gypsum in construction and building materials. *Constr. Build. Mater.* 432, 136609. doi:10.1016/j.conbuildmat.2024.136609

Jin, J., Chen, Y., Li, M., Liu, T., Qin, Z., Liu, Q., et al. (2024). Preparation of self-consolidating cemented backfill with tailings and alkali activated slurry: performance evaluation and environmental impact. *Constr. Build. Mater.* 438, 137088. doi:10.1016/j.conbuildmat.2024.137088

Khan, M., and McNally, C. (2024). Recent developments on low carbon 3D printing concrete: revolutionizing construction through innovative technology. *Clean. Mater.* 12, 100251. doi:10.1016/j.clema.2024.100251

Kosar, K., de Salles, L. S., Sharifi, N. P., Vandenbossche, J., and Khazanovich, L. (2023). Onsite strength determination for early-opening decision making of high early strength concrete pavement. *J. Traffic Transp. Eng. Engl. Ed.* 10 (2), 291–303. doi:10.1016/j.jtte.2021.12.005

Kuoribo, E., Shokry, H., and Mahmoud, H. (2024). Attaining material circularity in recycled construction waste to produce sustainable concrete blocks for residential building applications. *J. Build. Eng.* 96, 110503. doi:10.1016/j.jobe.2024.110503

Liang, H., Bian, X., and Dong, L. (2024). Towards net zero carbon buildings: accounting the building embodied carbon and life cycle-based policy design for Greater Bay Area, China. *Geosci. Front.* 15 (3), 101760. doi:10.1016/j.gsf.2023.101760

Liu, Q., Hu, R., Hu, L., Xing, Y., Qiu, P., Yang, H., et al. (2022). Investigation of hydraulic properties in fractured aquifers using cross-well travel-time based thermal tracer tomography: numerical and field experiments. *J. Hydrology* 609, 127751. doi:10.1016/j.jhydrol.2022.127751

Muauz, A., Behailu, B., and Bediru, H. (2024). Application of surface geophysical investigations and pumping test data analysis for better characterization of aquifer hydraulic parameters, Upper Awash Sub-Basin, Central Ethiopia. *J. Hydrology Regional Stud.* 55, 101933. doi:10.1016/j.ejrh.2024.101933

Pour, S. H., Wahab, A. K. A., Shahid, S., Asaduzzaman, M., and Dewan, A. (2020). Low impact development techniques to mitigate the impacts of climate-change-induced urban floods: current trends, issues and challenges. *Sustain. Cities Soc.* 62, 102373. doi:10.1016/j.scs.2020.102373

Pradel, M., Garcia, J., and Vaija, M. S. (2021). A framework for good practices to assess abiotic mineral resource depletion in Life Cycle Assessment. *J. Clean. Prod.* 279, 123296. doi:10.1016/j.jclepro.2020.123296

Rumbach, A., Sullivan, E., McMullen, S., and Makarewicz, C. (2022). You don't need zoning to be exclusionary: manufactured home parks, land-use regulations and housing segregation in the Houston metropolitan area. *Land Use Policy* 123, 106422. doi:10.1016/j.landusepol.2022.106422

Salami, B. A., Bahraq, A. A., Haq, M. M. U., Ojelade, O. A., Taiwo, R., Wahab, S., et al. (2024). Polymer-enhanced concrete: a comprehensive review of innovations and pathways for resilient and sustainable materials. *Next Mater.* 4, 100225. doi:10.1016/j.nxmate.2024.100225

Savinykh, V. V., Elansky, N. F., and Gruzdev, A. N. (2021). Interannual variations and long-term trends in total ozone over the North Caucasus. *Atmos. Environ.* 251, 118252. doi:10.1016/j.atmosenv.2021.118252

Shanmuganathan, R., Rath, B., Almoallim, H. S., Alahmadi, T. A., Jhanani, G. K., Lan Chi, N. T., et al. (2023). Utilisation of persistent chemical pollutant incorporating with nanoparticles to modify the properties of geopolymer and cement concrete. *Environ. Res.* 219, 114965. doi:10.1016/j.envres.2022.114965

Sharma, A. K., Sharma, M., Sharma, A. K., Sharma, M., and Sharma, M. (2023). Mapping the impact of environmental pollutants on human health and environment: a systematic review and meta-analysis. *J. Geochem. Explor.* 255, 107325. doi:10.1016/j.gexplo.2023.107325

Tamoor, M., Samak, N. A., and Xing, J. (2023). Life cycle assessment and policy for the improvement of net-zero emissions in China. *Clean. Eng. Technol.* 15, 100663. doi:10.1016/j.clet.2023.100663

Tiwari, A., Mahadik, K. R., and Gabhe, S. Y. (2020). Piperine: a comprehensive review of methods of isolation, purification, and biological properties. *Med. Drug Discov.* 7, 100027. doi:10.1016/j.medidd.2020.100027

Wang, H., Liu, T., Zhang, Z., Zou, D., Zhou, A., and Li, Y. (2024). Durability of SFCB reinforced low-alkalinity seawater sea sand concrete beams in marine environment. *Eng. Struct.* 317, 118616. doi:10.1016/j.engstruct.2024.118616

Wang, T., Tian, W., Lin, Y., Gou, X., Liu, H., Wang, X., et al. (2023). Decadal changes in the relationship between Arctic stratospheric ozone and sea surface temperatures in the North Pacific. *Atmos. Res.* 292, 106870. doi:10.1016/j.atmosres.2023.106870

Wu, L., Sun, Z., and Cao, Y. (2024). Modification of recycled aggregate and conservation and application of recycled aggregate concrete: a review. *Constr. Build. Mater.* 431, 136567. doi:10.1016/j.conbuildmat.2024.136567

Yan, T., Han, Q., Li, Z., Song, Y., Wang, Y., and Zhang, X. (2022). Influence of rare earth doping and calcination temperature on temperature sensitivity of gadolinium molybdate nanoparticle. *J. Alloys Compd.* 907, 164462. doi:10.1016/j.jallcom.2022.164462

Yang, B., Zhang, Y., Zhang, W., Sun, H., Wang, Q., and Han, D. (2024). Recycling lithium slag into eco-friendly ultra-high performance concrete: hydration process, microstructure development, and environmental benefits. *J. Build. Eng.* 91, 109563. doi:10.1016/j.jobe.2024.109563

Yu, Z., Wang, B., Li, T., Fan, C., and Yu, H. (2024). Effect and mechanism of activators on the properties of Yellow River sediment/fly ash/cement-based alkali-activated cementitious materials used for coal mine filling. *Constr. Build. Mater.* 445, 137955. doi:10.1016/j.conbuildmat.2024.137955

Yuan, S., Zhang, S., Pei, L., Liu, Y., Sun, Y., Peng, J., et al. (2024). Elaborating conspicuously low hydrogen permeability EVOH composite membrane upgraded by corrosion protection function. *J. Membr. Sci.* 708, 123050. doi:10.1016/j.memsci.2024.123050

Zaid, O., Alsharari, F., and Ahmed, M. (2024). Utilization of engineered biochar as a binder in carbon negative cement-based composites: a review. *Constr. Build. Mater.* 417, 135246. doi:10.1016/j.conbuildmat.2024.135246

Zhang, L., Song, Y., Shi, T., Zhao, Z., Zhang, X., Liu, Y., et al. (2024). A correlation study between the properties of manufactured sand and tunnel muck. *Case Stud. Constr. Mater.* 21, e03684. doi:10.1016/j.cscm.2024.e03684

Zhao, Y., Zhou, X., Zhou, Q., Zhu, H., Cheng, F., and Chen, H. (2024). Development of full-solid waste environmentally binder for cemented paste backfill. *Constr. Build. Mater.* 443, 137689. doi:10.1016/j.conbuildmat.2024.137689

Zhu, P., Chen, X., Liu, H., Wang, Z., Chen, C., and Li, H. (2024). Recycling of waste recycled aggregate concrete in freeze-thaw environment and emergy analysis of concrete recycling system. *J. Build. Eng.* 96, 110377. doi:10.1016/j.jobe.2024.110377

frontiers | Frontiers in Materials

TYPE Original Research
PUBLISHED 06 January 2025
DOI 10.3389/fmats.2024.1458836

OPEN ACCESS

EDITED BY
Biao Hu,
Shenzhen University, China

REVIEWED BY
Amir Ali Shahmansouri,
Washington State University, United States
Chuanqing Fu,
Zhejiang University of Technology, China
Paolo Di Re,
Sapienza University of Rome, Italy

*CORRESPONDENCE
Hui Qian,
qianhui@zzu.edu.cn
M. Nasir Ayaz Khan,
engr.khannasir@gmail.com

RECEIVED 03 July 2024
ACCEPTED 04 December 2024
PUBLISHED 06 January 2025

CITATION
Umar M, Qian H, Khan MNA, Siddique MS, Almujibah H, A. Elshekh AE, Bashir MO and Vatin NI (2025) Strength and durability of concrete with bentonite clay and quarry dust. *Front. Mater.* 11:1458836. doi: 10.3389/fmats.2024.1458836

Strength and durability of concrete with bentonite clay and quarry dust

Muhammad Umar[1], Hui Qian[1]*, M. Nasir Ayaz Khan[2]*, Muhammad Shahid Siddique[2], Hamad Almujibah[3], Ali. E. A. Elshekh[3], Maaz Osman Bashir[3] and Nikolai Ivanovich Vatin[4]

[1]School of Civil Engineering, Zhengzhou University, Zhengzhou, Henan, China, [2]Department of Structural Engineering, MCE Risalpur Campus, National University of Sciences and Technology, Islamabad, Pakistan, [3]Department of Civil Engineering, College of Engineering, Taif University, Taif, Saudi Arabia, [4]Division of Research and Development, Peter the Great St. Petersburg Polytechnic University, St.Petersburg, Russia

The research object is concrete with supplementary cementitious materials (SCMs) such as bentonite clay and quarry dust. The impact of incorporating these SCMs on fresh concrete properties, compressive, flexural, and split tensile strengths, and acid resistance was investigated. Microstructural analysis using Scanning Electron Microscopy (SEM) and X-ray radiography were used. Varying proportions of SCMs (5%–20%) were incorporated into the concrete mix while maintaining a constant water-to-cement ratio. Key findings reveal a 7.31% increase in compressive strength, a significant 19.7% improvement in flexural strength, and enhanced acid resistance. Utilizing Response Surface Methodology (RSM), the optimal mix design for achieving superior mechanical strength was identified. The quadratic model of RSM indicated that a combination of 10.29% bentonite clay, 7.20% quarry dust, and 8.19% fine aggregate replacement yielded the highest strength. Predictive and experimental results demonstrated strong agreement. Compared to the reference concrete, the optimized samples exhibited significant increases of 18.08%, 33.60%, and 11.15% in compressive, flexural, and tensile strengths, respectively. This research demonstrates the potential of locally available SCMs as viable and sustainable alternatives for concrete production, offering improved performance without compromising strength.

KEYWORDS

bentonite clay, quarry dust, compressive strength, cement, response surface

1 Introduction

The world rests on concrete, the most prevalent construction material globally, serving as the foundation for both developed and developing economies. It has been quantified that producing one metric ton of cement yields an equivalent carbon dioxide emission, totaling one metric ton, into the Earth's atmosphere. It is estimated that the production of Portland cement contributes to approximately 7% of global greenhouse gas emissions (Althoey et al., 2023; da Silva Rego et al., 2023; Soomro et al., 2022; Sousa et al., 2023). Cement production exhibits a growth rate of ten percent annually worldwide. Concrete has three primary constituents: cement, aggregates (fine and coarse materials), and water (Uratani and Griffiths, 2023). In the current production of concrete, there has been a

GRAPHICAL ABSTRACT

remarkable production in the utilization of locally accessible raw materials such as rice husk ash, fly ash, metakaolin, crushed granulated blast furnace slag, waste glass powder, and foundry sand as Supplementary Cementitious Materials (SCM) over the preceding decades (Isaksson et al., 2023; Manjunatha et al., 2021; Qureshi et al., 2020; Nasiru et al., 2021). Incorporating SCM into concrete is associated with various advantages surrounding its inherent cementitious properties, economical cost, and ready availability within proximity. Throwing away these materials without proper care is not just wasteful. It can also pollute the environment and harm plants, animals, and ourselves (Kolawole et al., 2021; Aprianti S, 2017; Zhang et al., 2023).

Supplementary cementitious materials are not widely available across the globe, the global shift towards green energy has led to the closure of coal power plants in certain regions, resulting in a sharp decrease in fly ash production. The availability of SCMs is uneven across different regions, and their production is considerably lower compared to ordinary Portland cement (OPC). As a result, SCMs cannot fully satisfy the demand for high cement replacement in large-scale construction projects (Arrigoni et al., 2020). Additionally, the production quantity and quality of SCMs are impacted by changes in industrial processes, especially within the steel and coal industries. Therefore, researchers are exploring alternative SCMs, such as bentonite clay and quarry dust, which could serve as partial replacements for cement to address these challenges and promote sustainable construction practices (Duchesne, 2021; Raza et al., 2024; Chengfang et al., 2024). A promising alternative is bentonite clay, which is abundantly available in regions of Asia and Africa (Javed et al., 2020).

Bentonite, a clay mineral rich in montmorillonite (a type of hydrous aluminum silicate), forms layered deposits with varying thicknesses, mainly composed of smectite clays. It is classified into swelling (sodium bentonite) or non-swelling (calcium bentonite) types based on its sodium content (Sun et al., 2022). The choice of bentonite clay dictates the characteristics of the resulting concrete, with swelling bentonite yielding a foamy consistency and non-swelling bentonite resulting in a cracked appearance. Bentonite can bind sand particles in the presence of water, forming a plastic paste that helps create a workable concrete mix. This reaction produces magnesium and potassium oxides, contributing to the strength and setting of the concrete (Ahmad et al., 2022). Some types of bentonite may expand when exposed to water due to the reaction with the montmorillonite content, but calcium-rich bentonite has a lower swelling capacity. Significant bentonite reserves are found in various regions, with estimates of approximately 36 million metric tons. Utilizing bentonite is more cost-effective than cement, with one tonne of bentonite priced at Rs-3600 ($12) versus Rs-24000 ($80). Enhanced concrete mixtures containing bentonite exhibit prolonged strength and resistance to acid attacks, improving durability and reliability, crucial factors in seismic regions (Umair et al., 2023; Ashraf et al., 2022; Masood et al., 2020; Mirza et al., 2009).

Moreover, concrete mixtures enhanced with bentonite have demonstrated the ability to maintain strength over extended periods and resist acid attacks. Bentonite enhances the durability and reliability of structural concrete from an earlier age (Xie et al., 2018), increases mortar creep (Fadaie et al., 2019), and introduces siliceous and aluminous compounds into concrete mixtures, offering a range of benefits (Memon et al., 2012). Seismically active areas have experienced substantial structural damage during previous earthquakes, largely due to the use of substandard materials. The economic challenge wherein a significant portion of the population faces extreme poverty renders them unable to afford high-quality cement (Khan et al., 2019). Additionally, recent research highlights the cement industry as the primary contributor to carbon dioxide emissions. Consequently, advocating for the adoption of locally available construction materials will address economic barriers and align with environmental sustainability goals. Encouraging the use of such materials not only facilitates cost-effective construction but also promotes an eco-friendly approach (Khan et al., 2021; Rehman et al., 2020).

The limited accessibility of conventional SCMs employed for cement substitution presents a significant obstacle for the concrete industry, driving the need to identify and implement alternative cementitious binders (Snellings et al., 2023; Ndahirwa et al., 2022). Quarry dust, a waste product from the crushing process, presents itself as a potential SCM for partial cement substitution in mortar and concrete formulations (Dobiszewska et al., 2023; Sundaralingam et al., 2022). Rock dust, a byproduct generated during the comminution of diverse geological rock formations, exhibits potential for optimizing the particle size distribution (PSD) and packing density within concrete composites. A promising approach to sustainable construction involves partially substituting rock dust for cement. It could lead to less CO2 pollution, a smaller environmental footprint, and a decrease in resource and energy consumption (Zhao et al., 2022; Nasier, 2021; Al-Bakri et al., 2022).

The quarrying and crushing of large rocks into smaller fragments culminate in producing aggregates of varying sizes, serving as the originator for quarry dust. Projections indicate that the global construction aggregates market is composed of growth, with an anticipated Compound Annual Growth Rate (CAGR) of approximately 6.7% in the coming years. It was expected to attain an estimated value approaching US$ 393.5 Billion in 2019 (Escavy et al., 2020). This figure alone is compelling evidence of the escalating trajectory within the construction industry. Quarry dust as waste, due to dust fine particle size, has adverse environmental effects (Ali et al., 2023; Shaheen et al., 2023). Quarry dust can be utilized as a filler material (fine aggregate) and as a binding agent, replacing a portion of the customary cement content in concrete mixes (Hemalatha and Sindu, 2020; Kankam et al., 2017; Mugi, 2022).

While there is extensive global research on supplementary cementitious materials (SCMs) as sustainable alternatives in concrete production, most studies have predominantly focused on conventional SCMs like fly ash and slag. However, the combined use of waste materials such as bentonite clay and quarry dust as partial cement replacements remains largely unexplored. To the best of our knowledge, no existing research has comprehensively investigated the combined effect of these two materials as concrete binders. This study fills this knowledge gap by evaluating the mechanical properties of concrete (compressive, flexural, and split tensile strength) and its acid resistance when cement is partially replaced with these SCMs. Furthermore, this work advances current knowledge by utilizing Response Surface Methodology (RSM) to optimize the replacement levels, providing a predictive framework for enhancing concrete performance. The novelty lies not only in the use of these unconventional SCMs but also in the validation of RSM as an effective tool in designing sustainable concrete mixes, thus offering a meaningful contribution to both academic research and industry practice.

2 Materials and methods

2.1 Material used

Various materials are employed during experimental testing, elucidated in the subsequent subsections.

2.1.1 Cement

In this research, ASTM Type 1"Fuji Cement," which was free from clumps and impurities, was utilized. This cement was ordinary Portland cement (OPC) and confirmed to ASTM C150. The cement underwent a physical examination to assess its smoothness and colour. The properties of cement are detailed in Table 1.

2.1.2 Bentonite clay

The Jehangira bentonite deposits are located at 33°59′56″ latitude and 72°12′47″ longitude, as shown in Figure 1 indicated by the Survey of Pakistan topographic sheet 43 C/1 (Karagüzel et al., 2010). The particle size distribution of bentonite clay is shown in Figure 3A and collected from these deposits in small pieces, as depicted in Figures 2A, B. For finer particles, bentonite clay was subjected to grinding in a Los Angeles abrasion machine. Each batch underwent 4,500 revolutions to ensure uniform fineness until fully transformed into powder. The elemental composition of bentonite and quarry dust was determined using an Energy Dispersive X-ray (EDX) at the Centralized Resource Laboratory (CRL), University of Peshawar, Pakistan.

TABLE 1 Properties of Ordinary Portland cement.

Physical properties	Value
Specific gravity, g/cm^3	3.10
Mean particle size, μm	18.98
Consistency, %	29.04
Initial setting time	1 h and 21 min
Final setting time	3 h and 41 min
Fineness, cm^2/g	1.76

2.1.3 Quarry dust

The quarry dust was collected at the crusher facility in Margalla Hills, Islamabad, Pakistan. Large pieces of stone were removed from the location where they were found. The particle sizes ranged from 4.75 mm down to dust sizes of 0.05 mm and smaller; the gradation curve is shown in Figure 2C. Subsequently, the sample was transferred to the laboratory for additional screening and examination. Compared to fine aggregates, Table 2 illustrates that quarry dust has a lower specific gravity and a higher water absorption rate. Table 3 provides information on the chemical characteristics of cement, bentonite, and quarry dust.

The specific gravity and water absorption rates of bentonite clay and quarry dust influence the concrete's mix design, density, and workability. Their water absorption impacts hydration and particle bonding, improving compressive strength. High SiO_2 content in both materials promotes pozzolanic reactions, increasing strength through the formation of calcium silicate hydrate (C-S-H) gel. The Al_2O_3 content in bentonite improves acid resistance, while Fe_2O_3 and MgO enhance binding. The loss on ignition (LOI) values reflect the presence of volatile components that may affect durability. The pozzolanic activity and improved particle packing, driven by these material properties, contribute to the enhanced mechanical properties (compressive, flexural, and tensile strength) of the concrete.

2.1.4 Aggregates

The deposits at Lawrencepur served as the source for collecting fine aggregates. The ASTM C136-04 was employed to determine the fineness modulus. Figure 3A illustrates the gradation curves for fine aggregates of different sizes. Throughout this study, coarse aggregates were sourced from the Margalla hills, widely acknowledged as some of the best in Pakistan (Khan M. I. et al., 2022).

2.1.5 Characterization of bentonite clay and quarry dust

The XRD analysis was conducted to determine the mineralogical composition of bentonite and quarry dust, which were used as partial replacements for cement in this study as shown in Figure 3B.

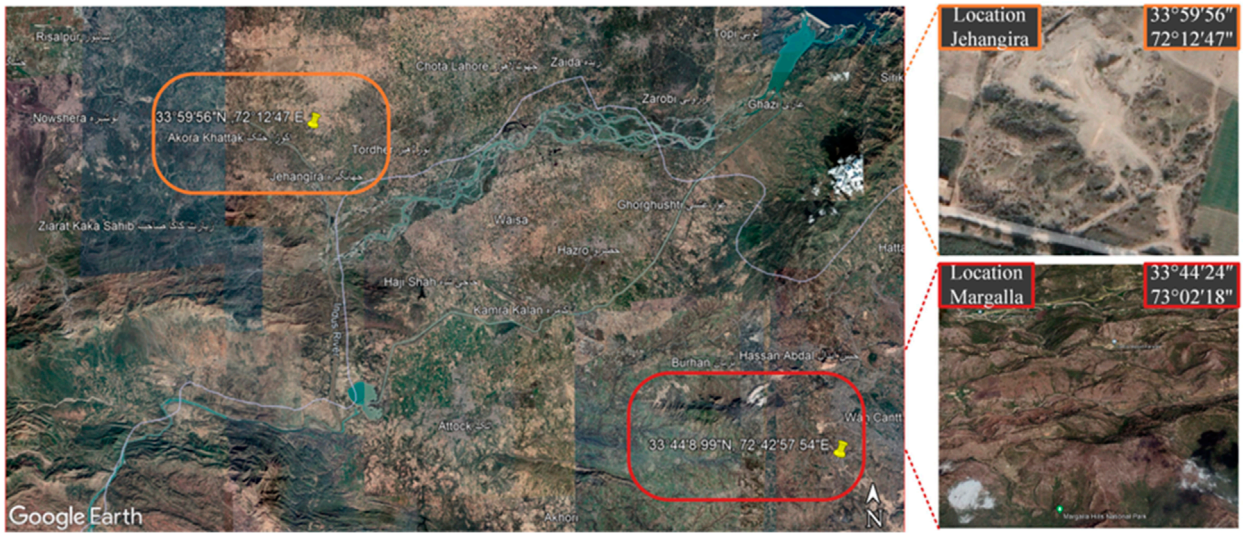

FIGURE 1
A map of the study area to identify the sampling location. Map data ©2024 Google (Google Earth, 2024).

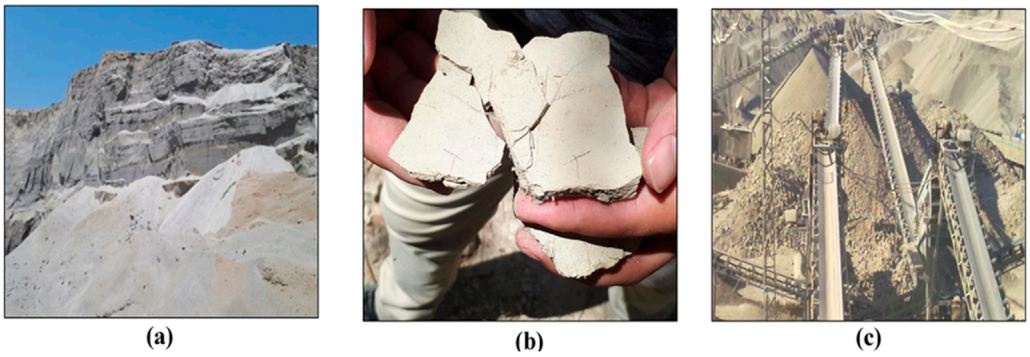

FIGURE 2
(A) Bentonite deposits **(B)** bentonite clay **(C)** Quarry dust deposits.

TABLE 2 Physical properties of material.

Material	Specific gravity	Water absorption%	Fineness (cm^2/gm)
Bentonite clay	2.61	1.07	2.93
Quarry dust	2.64	1.17	2.83
Fine aggregates	2.67	1.12	2.74
Coarse aggregates	2.80	3.40	—

A Panalytical Empyrean XRD instrument was employed, equipped with Cu Kα radiation (λ = 1.5406 Å). The analysis was performed under the following operating conditions: a voltage of 45 kV and a current of 40 mA. The diffraction data were collected over a scanning range of 5°–80° (2θ) with a step size of 0.02° and a scan speed of 2°/minute. For bentonite clay, the XRD pattern reveals a predominance of montmorillonite, which is characterized by its high cation exchange capacity and swelling properties that can impact the water retention and mechanical properties of concrete. Notable peaks of montmorillonite are visible in the diffraction pattern, confirming its significant presence. In addition to montmorillonite, the XRD spectrum of bentonite also shows the presence of other minerals such as illite and kaolinite. Illite, marked by specific peaks in the graph, contributes to the clay's overall plasticity and strength,

TABLE 3 Chemical composition of materials.

Chemical composition (%)	SiO_2	Al_2O_3	Fe_2O_3	CaO	MgO	SO_3	Na	K_2O	Moisture content	Loss on ignition
Cement	18.40	5.60	3.00	66.8	1.40	2.80	0.84	0.50	—	2.00
Bentonite	51.38	20.41	3.11	12.21	3.13	0.71	0.56	2.09	2.92	4.77
Quarry dust	58.32	9.60	1.44	5.13	2.50	0.04	2.40	5.91	—	0.48

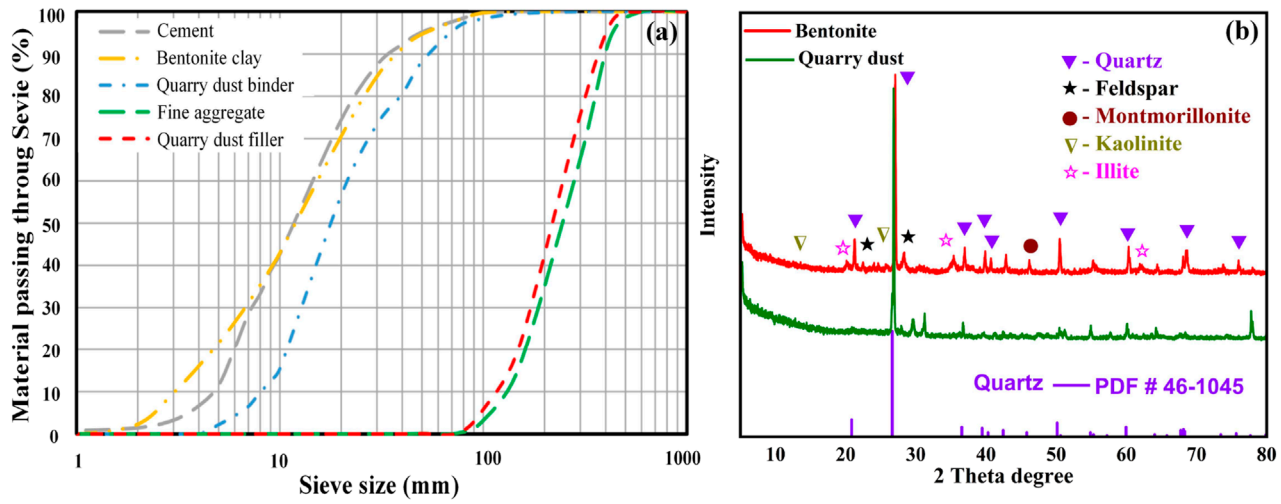

FIGURE 3
(A) Gradation curve of dry ingredients **(B)** XRD analysis of bentonite clay and quarry dust.

while kaolinite, indicated by its distinct peaks, is known for its less expansive nature compared to montmorillonite but adds to the durability when used in cementitious mixes.

Quarry dust, represented in the XRD analysis, primarily comprises quartz, as indicated by the strong peak aligned with the Quartz PDF #46-1045 standard, which is a common phase in many geological materials and significantly impacts the hardness and durability of the resulting concrete. The presence of feldspar and minor traces of kaolinite in quarry dust is also noted, which can influence the chemical durability and workability of the concrete mixes. The identification of these minerals in both bentonite clay and quarry dust is crucial for evaluating their suitability as partial replacements in concrete. The distinct peaks corresponding to quartz, feldspar, montmorillonite, illite, and kaolinite provide insights into the materials' crystallography and structural characteristics, essential for predicting their behavior in concrete applications. Understanding the composition and distribution of these minerals helps in tailoring the mix designs for enhanced performance and sustainability of the concrete products.

2.2 Casting and mixing proportion

Throughout this research, various percentages of SCM were utilized to achieve maximum strength, improved workability, and long-lasting characteristics; 96 specimens were created, each representing one of 13 possible mix proportions, before RSM was performed. For example, cement was substituted with bentonite clay in proportions of 5%, 10%, 15%, and 20%, denoted as 5BN, 10BN, 15BN, and 20BN, respectively. The coarse and fine aggregate proportions were kept constant across all the mixes mentioned above. Quarry dust was categorized into two types as filler, replacing fine aggregates and binder replacing cement. The differentiation between these two groups lies in particle size. The filler group passed through a sieve with a 4.75 mm opening and was retained on a sieve with a 0.3 mm opening. The 'as binder' group consisted of particles 0.05 mm or smaller. Mixes falling under the 'as filler' category were designated 5QDF, 10QDF, 15QDF, and 20QDF, corresponding to 5%, 10%, 15%, and 20% replacement of fine aggregate with quarry dust. Mixes using quarry dust from the 'as binder' group were labelled as 5QDB, 10QDB, 15QDB, and 20QDB, indicating 5%, 10%, 15%, and 20% replacement of cement with quarry dust. A control mix was also prepared without adding any SCM, and a consistent water-to-cement ratio of 0.5 was maintained for all the mixes. Table 4 outlines the concrete mix proportions required to produce one cubic meter of the final product. To validate the RSM results, nine samples were cast according to the specified ratios generated by the statistical analysis software.

Cylindrical specimens measuring 305 mm in length and 152 mm in diameter were employed to assess the material's

10.3389/fmats.2024.1458836

TABLE 4 Mix proportion of concrete mixes.

Specimen ID	Cement (Kg/m^3)	Coarse aggregate (Kg/m^3)	Fine aggregate (Kg/m^3)	Water (Kg/m^3)	Bentonite clay (Kg/m^3)	Quarry dust (Kg/m^3)
CM	367	1,120	798	183.5	0	0
5BN	348.6	1,120	798	183.5	18.3	0
10BN	330.3	1,120	798	183.5	36.7	0
15BN	311.9	1,120	798	183.5	55.0	0
20 BN	293.6	1,120	798	183.5	73.4	0
5QDF	367	1,120	758.1	183.5	0	39.9
10QDF	367	1,120	718.2	183.5	0	79.8
15QDF	367	1,120	678.3	183.5	0	119.7
20QD F	367	1,120	638.4	183.5	0	159.6
5QDB	348.6	1,120	798	183.5	0	18.3
10QDB	330.3	1,120	798	183.5	0	36.7
15QDB	311.9	1,120	798	183.5	0	55.0
20QDB	293.6	1,120	798	183.5	0	73.4

compressive and split tensile strengths, respectively. Compressive strength, following ASTM C39, was measured after curing for 7 and 28 days. Following ASTM C496, split tensile strength was determined after the same curing periods. Flexural strength tests confirming ASTM C78 were conducted on concrete specimens with widths of 101 mm, depths of 101 mm, and lengths of 305 mm after 7 and 28 days of curing. Fresh concrete properties were evaluated using ASTM C 143, incorporating quarry dust and bentonite clay. Additionally, 152 mm cubic concrete specimens were immersed in separate solutions of 5% sulfuric acid and 5% hydrochloric acid. Furthermore, it was observed that the specimens exhibited water observation characteristics. Lastly, the Response Surface Methodology (RSM) was employed for statistical analysis to optimize the percentage of partial cement replacement with SCM.

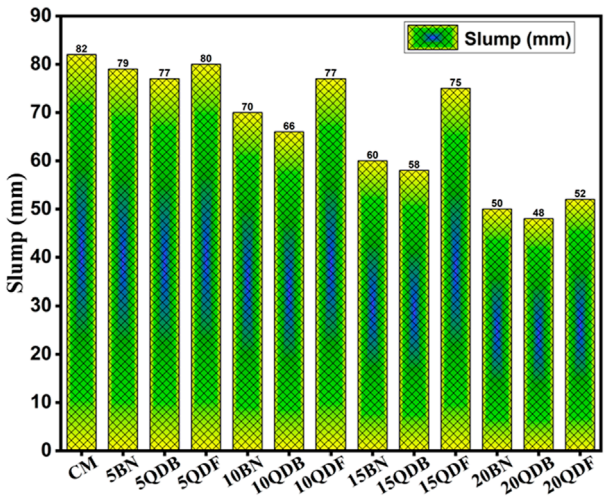

FIGURE 4
Slump variations.

3 Test results and discussion

3.1 Fresh properties

Increasing the quarry dust "as binder" group resulted in a notable decline in the workability of all the mixtures compared to the control mix while maintaining a constant water-cement ratio. The graphical representation in Figure 4 shows that mix 5QDB exhibited the most pronounced slump value among all the mixes categorized under the "as binder group," surpassing the performance of all other mixes. Conversely, mix 20QDB displayed substantially reduced workability compared to the preceding mixtures. This decrease in workability can likely be attributed to the elevated presence of fine particles within the mix, exceeding the levels found in other mixtures. The amplified surface area of these fine particles in quarry dust, acting as a binder, necessitated a higher demand for water to ensure thorough saturation of the mixtures (Passuello et al., 2015).

For compositions incorporating quarry dust in the capacity of a filler material, the highest observed slump was 72 mm, as recorded in mix 5QDF. Stone dust particles are characterized by

their coarse, rough, angular morphology, and the introduction of quarry dust into the concrete mix led to an increased proportion of fine particles, imparting a coarse texture and angular shape to the particles. This augmentation in inter-particle friction and the surface area likely contributed to the unfavorable flow characteristics observed. Furthermore, due to the higher water absorption rate of quarry dust particles, there was a reduction in the available water for lubricating cement particles.

The greater specific surface area of bentonite clay in the mix enhanced the demand for water to adequately wet the particles in the mixture. As the water added to the mix is absorbed by the bentonite clay particles, insufficient water remains available to lubricate the cement and bentonite particles. Consequently, the workability diminishes for a consistent water-cement ratio as the content of bentonite clay increases. In this context, it is important to note that the workability was lower than that of the control mix but higher than the mixes incorporated with quarry dust, as reported by (Xie et al., 2018) and (Nataraja and Nalanda, 2008). While this study focused on maintaining a constant water-cement ratio across all mixes, future research should explore the use of water-reducing admixtures or superplasticizers. These additives could counterbalance the negative impact of fine particles (quarry dust and bentonite clay) on workability without sacrificing the mechanical strength and durability properties of the concrete mix.

3.2 Compressive strength

The compressive strength, as measured after 7 days of curing, for the mixes containing different proportions of quarry dust filler, namely 5QDF, 10QDF, 15QDF, and 20QDF, are as follows: 17.38, 18.78, 16.60, and 15.43 MPa, respectively. The control mix (CM) exhibits a compressive strength of 16.77 MPa. As presented in Figure 5, it is evident that the optimal strength performance is achieved at the 10% quarry dust filler ratio (10QDF), resulting in an impressive 11.9% increase in strength when compared to the control mix. Upon extending the curing period to 28 days, the compressive strength values for the quarry dust filler mixes are as follows: 29.13 MPa for 5QDF, 30.11 MPa for 10QDF, 27.95 MPa for 15QDF, and 26.19 MPa for 20QDF. In contrast, the CM maintains a compressive strength of 28.04 MPa. Figure 5 reinforces the observation that the 10% quarry dust filler mix (10QDF) outperforms the CM with a notable 7.38% increase in strength (Ho et al., 2002; Khan, 2023).

The observed trend in the compressive strength of quarry dust mixes, whether used as a binder or filler, exhibited remarkable similarity, except for a slight enhancement in strength. After 7 days of curing, the compressive strengths for mix proportions of 5% QDB, 10% QDB, 15% QDB, and 20% QDB were measured at 16.77, 17.38, 18.78, 16.60, and 15.43 MPa, respectively. These strengths improved to 28.04, 29.13, 30.11, 27.95, and 26.19 MPa at the 28-day mark. A similar growth and reduction pattern emerged when comparing the "as binder" mixes to the "as filler" mixes. Notably, the 10% QDB mixes exhibited the highest strength at all ages compared to control mixes. This enhancement could be attributed to the early acceleration of the hydration reaction, facilitated by the finer particles of quarry dust filling gaps and creating a denser matrix, thus increasing load resistance. However, it is essential to note that

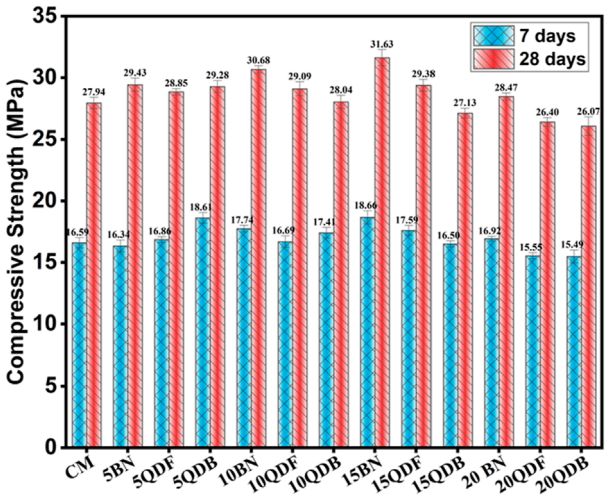

FIGURE 5
Compressive strength at 7 and 28 days of curing.

increasing the proportion of quarry dust led to reduced workability and poor compaction, resulting in decreased strength (Febin et al., 2019). This decline in strength became more pronounced beyond the 10% replacement threshold, possibly due to limited water availability for dust particles to engage in the hydration process and an increase in the surface area resulting from higher quarry dust concentration.

In contrast, the compressive strength values for mixes containing bentonite (5BD, 10BD, 15BD, and 20BD) showed different trends. After 7 days of curing, these mixtures displayed strengths of 16.59, 16.63, 15.84, and 14.55 MPa, respectively. The decrease in compressive strength in the early stages can be attributed to the slower hydration of bentonite. However, at 28 days, the measured strengths improved to 28.94, 29.42, 25.75, and 24.55 MPa, with 5BD and 10BD mixtures showing increases of 3.15% and 4.91%, respectively, compared to the control sample. The rise in strength is linked to the pozzolanic characteristic of bentonite, which exhibits gradual improvement between 3 and 28 days and further enhancement after 56 days. It is noteworthy that insufficient dust particles are present in specimens with 0% and 5% bentonite content to fill gaps and participate effectively in the hydration process, leading to decreased compressive strength. However, increasing the bentonite clay content beyond 10% tends to reduce the compressive strength of specimens due to the presence of small particles, which increases the total particle surface area (Masood et al., 2020).

3.3 Flexural strength

In flexural strength analysis, mixes containing quarry dust and bentonite clay demonstrate a consistent strength pattern similar to that reported for compressive strength when subjected to 7 and 28 days of curing. Specifically, at a 7-day mark, the mixture denoted as "10QD" exhibits a notable increase in strength, registering a rise of 19.7% compared to the control mix. Similarly, at the 28-day juncture, it demonstrates an incremental strength gain of 7.17%. This augmentation in strength can be attributed to the rapid

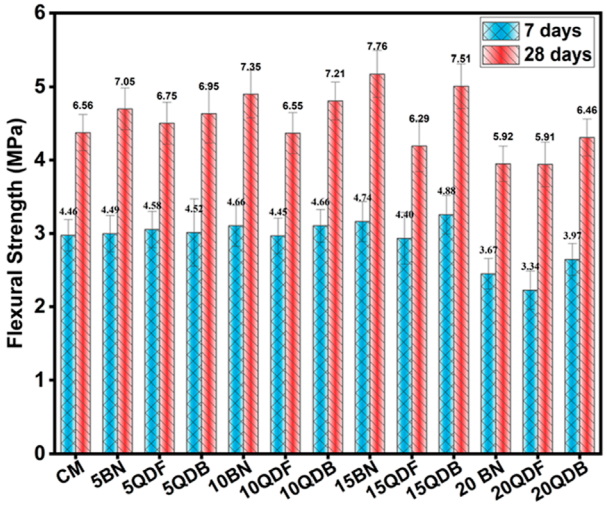

FIGURE 6
Flexural strength at 7 and 28 days.

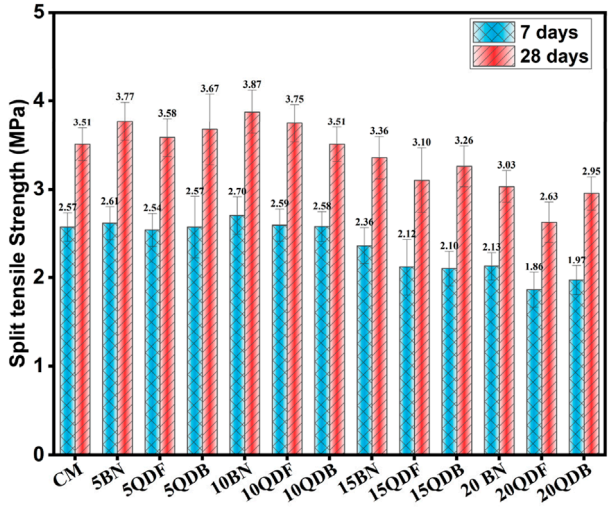

FIGURE 7
Split tensile strength at 7 and 28 days.

hydration process inherent in the quarry dust mixture, which also acts as a filler (Ramos et al., 2013).

In Figure 6 the 10BN mixtures containing bentonite clay exhibit different behavior, at 7 days of curing, there is a modest 4.2% increase in strength, whereas at 28 days, a more substantial boost of 11.8% is observed. This disparity can be ascribed to bentonite clay's relatively sluggish hydration reaction, resulting in lower flexural strength at the 7-day interval. This phenomenon aligns with the observations reported in reference. As mentioned earlier, similar dynamics regarding the increase and subsequent decrease in strength have been discussed in the context of compressive strength.

3.4 Split tensile strength

Tensile strength for quarry dust and bentonite clay mixes was observed at 7 days and 28 days of curing. For quarry dust mixes, an increase of 14.6% at 7 days and 9.9% at 28 days of curing was noted, respectively. Various researchers have established that the optimum replacement of cement with quarry dust is 10%–15% to increase split tensile strength. Beyond this replacement, split tensile strength tends to decrease (Abd Elmoaty, 2013; Qian et al., 2024). It is observed in Figure 7 that split tensile strength is affected similarly to compressive strength. The bentonite mix shows a decrease of 6.6% at 7 days and an increase of 3.8% at 28 days of curing compared to the control mix, as reported by. The reduction in early-age strength may be attributed to the slow hydration of bentonite clay at early ages (Mirgozar Langaroudi and Mohammadi, 2022).

3.5 Acid attack

The acid resistance of concrete specimens was evaluated using a constant pH method designed to maintain the pH consistently at 2.0 ± 0.2 throughout the testing period. This analysis was performed using both sulfuric acid (H_2SO_4) and hydrochloric acid (HCl), each diluted to a 5% concentration by volume. Concrete sections were immersed in a solution initially comprising 12 L of water. The necessary volume of each acid at 5% concentration was added to achieve and maintain the solution at a pH of 2.0, with adjustments based on the initial alkalinity of the concrete. An automatic titrator continuously controlled and adjusted the pH in the reservoir. A magnetic stirrer was employed to ensure the even distribution of the acid throughout the reservoir. The acid solution was replaced weekly for the first 28 days to ensure consistent exposure to the acidic environment. After the immersion period, each section was manually brushed in water to remove any loose or deteriorated material, and then dried with adsorbent paper. The degradation of the concrete was quantified by measuring the mass loss after the test period, expressed in kg/m^2, to facilitate comparative analysis across different samples.

Concrete is susceptible to acid attacks in various industrial facilities, water treatment plants, agricultural operations, transportation infrastructure, swimming pools, battery storage areas, food processing plants, garages, and auto repair shops. Aggressive chemicals like H_2SO_4 and HCL react highly with the cement paste matrix, consuming $Ca(OH)_2$ and C-S-H (Castillo Lara and Chagas Cordeiro, 2019). Consequently, the formation of $CaSO_4.2H_2HO$ (gypsum) and ettringite will increase the concrete volume by nearly 2.2 times, leading to internal crack propagation, strength loss, and quick deterioration. Eventually, the degradation of specimens due to acid leads to mass loss. The performance of acid attacks on concrete has been evaluated in terms of mass loss by various researchers (Khan M. et al., 2022). The weight loss absorbed by the quarry dust mix 20QD was found to be the lowest for hydrochloric acid and sulfuric acid, with the difference in weight loss for both specimens not being significant, i.e., 1.21% and 1.31%. The minimal weight loss may be attributed to the abundance of quarry dust particles, which form a compact mass, thus reducing the permeability of the specimens (Chintalapudi and Pannem, 2022). The mass loss due to acid attack is graphically displayed in Figure 8.

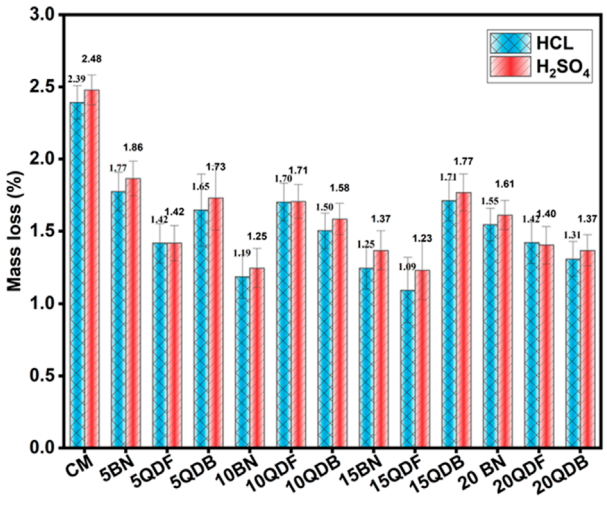

FIGURE 8
Mass loss due to acid attack.

For the bentonite clay mix 20BN, the weight loss in hydrochloric acid was 1.20%, and sulfuric acid was 1.25%. The resistance to acid attack in both mixes is due to the lower production of lime in the mix, resulting from the replacement of cement content, where calcium hydroxide reacts with silica to form silica. Overall, the mass loss decreases with an increase in the proportions of SCM, with minimal variations. The highest weight loss was observed in the control mix for both acid solutions. The presence of free lime in the mixes increases susceptibility to acid attacks, softening the mix, a phenomenon noted by other researchers as well. Additionally, the chemical reaction of cement with the salt solution leads to the disintegration of the specimens (de Siqueira and Cordeiro, 2022; Thomas and Harilal, 2016).

3.6 X-ray radiography analysis and porosity correlation

X-ray radiography, a non-destructive testing (NDT) method, was employed to assess the internal structure and detect defects such as air voids, pockets, and cracks within the concrete specimens. This technique was crucial in evaluating the homogeneity and bonding integrity of the control mix and mixes modified with supplementary cementitious materials (SCMs). Specimens were placed in a high-resolution X-ray cabinet, with the X-ray source adjusted to 150 kV and 5 mA to ensure optimal penetration and contrast. Each specimen was exposed for 10 s, maintaining uniform imaging conditions across all tests. Digital detectors captured the radiographs, facilitating a precise assessment of internal structures at room temperature, and adhering to standardized procedures to ensure consistency in the findings.

Figure 9A, presents an optical photograph of the concrete mix containing 10% bentonite clay after exposure to sulfuric acid. The surface condition shown here complements the X-ray analysis in Figure 9B which highlights areas of reduced porosity indicated by fewer lighter shades. This suggests effective mitigation of acid impact through enhanced matrix density and cohesion, indicative of bentonite clay's protective role. X-ray radiograph of the same mix further substantiates the visual observations from the optical photograph by showcasing limited acid penetration and damage. The radiograph reveals a denser structure with minimal voids, contrasting sharply with the control mix's results, pointing to a significant enhancement in acid resistance due to the incorporation of bentonite clay.

Figure 9C is an optical photograph of the control mix, illustrating pronounced surface damage such as cracks and voids from acid exposure. This damage is visually more severe compared to the bentonite clay mix, reflecting the susceptibility of the standard mix to chemical degradation. Figure 9D provides the X-ray radiograph for the control mix, showing extensive lighter areas that denote high porosity and structural weakening. The comparison of radiographic data between the mixes visually underscores the stark contrast in durability and integrity, highlighting the detrimental effects of acid exposure on the control mix, which exhibits increased material loss and degradation.

3.6.1 Porosity and mechanical strength relationship

The porosity data obtained from the X-ray radiography was cross-referenced with the mechanical strength results to establish a correlation. As expected, mixes with higher porosity, such as the control mix, exhibited a lower compressive strength after acid exposure. In contrast, the modified mix containing bentonite clay demonstrated a lower porosity, which translated to a higher residual strength after acid exposure. This observation aligns with findings from previous research, which have established that porosity is a critical factor influencing the durability and strength of cementitious composites (He et al., 2023; He et al., 2024).

4 Response surface methodology (RSM) analysis

The response surface approach is a statistical technique that maximizes an output or response affected by several input variables or factors. A contour plot or graphical representation of the response or output in three dimensions can be used (Ma et al., 2022; Kursuncu et al., 2022). The response surface provides the matrix for the ideal strength value in concrete at different percentages of SCM. The results of the ANOVA analysis for the measured parameters, including compressive strength (σ_c), flexural strength (σ_f), and split tensile strength (σ_{st}), are presented in Tables 5, 6, 7. The calculated F-values for the created model are 12.58, 8.92, and 10.26, indicating their significance. These values suggest that there is only a 0.08%,0.06%, and 0.02% chance that such large F-values could occur by random variation alone. Values of "Prob > F" less than 0.08 or greater than 0.10 signify the significance or insignificance of the model terms, respectively.

In this study, the optimization of compressive strength (σ_c), flexural strength (σ_f) and split tensile strength (σ_{st}) was achieved through response surface methodology (RSM) using design expert. The analysis utilized ANOVA to evaluate the significance of model terms, identifying the primary factors influencing the model outcomes. The factors considered in the analysis were A (Bentonite

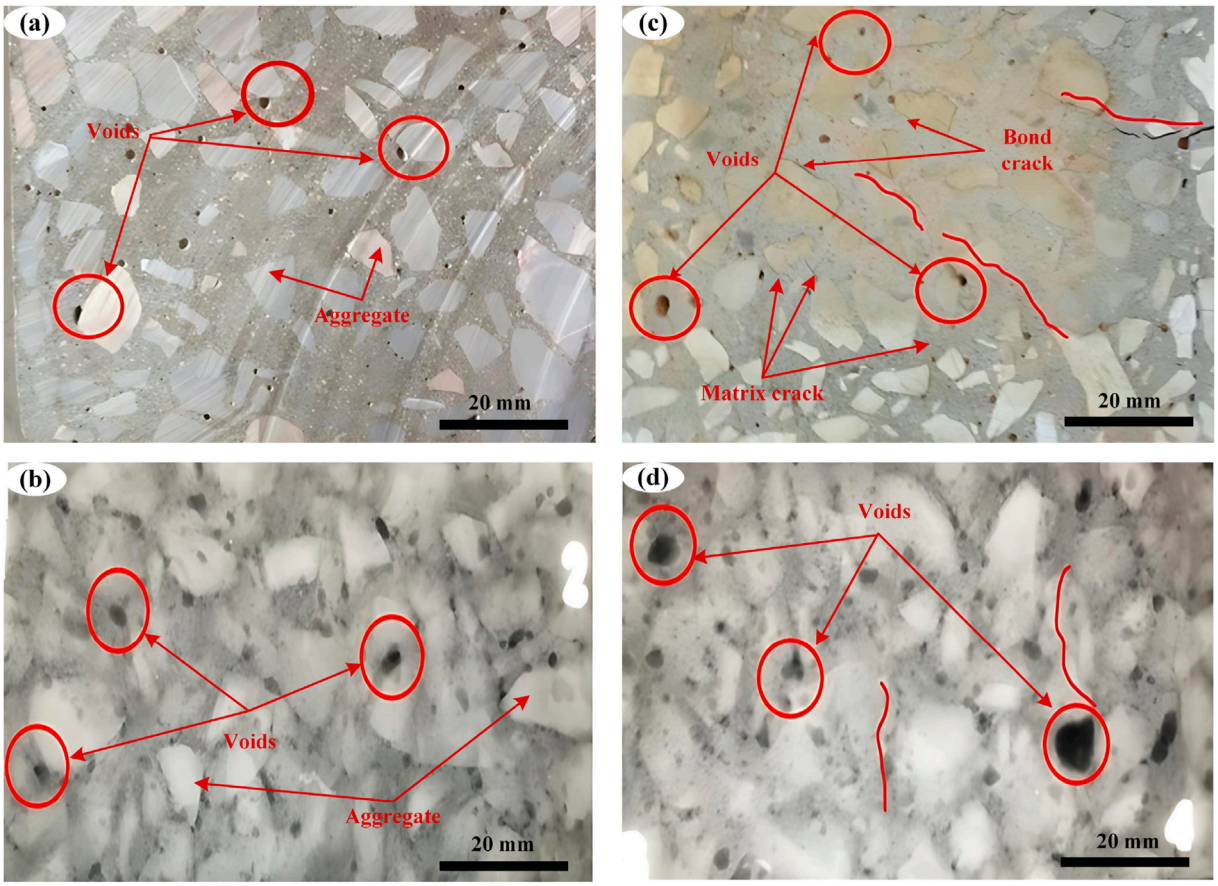

FIGURE 9
(A) Optical photo of 10BN mix **(B)** X-ray radiograph of 10BN mix **(C)** Optical photo of the CM mix **(D)** X-ray radiograph of CM.

TABLE 5 ANOVA: Quadratic model for compressive strength.

Source	Sum of squares	df	Mean square	F-value	p-value	Comments
Model	20.24	12	1.37	12.58	0.00231	R^2 = 0.942 Adj.R^2 = 0.874 Pre.R^2 = 0.689 C.V % 2.06
A (BN)	1.62	1	1.62	2.21	0.00188	
B (QDF)	0.049	1	0.049	0.067	0.00375	
C (QDB)	0.379	1	0.379	0.516	0.00499	
AB	0.088	1	0.088	3.21	0.00156	
AC	0.056	1	0.056	2.88	0.00345	
BC	0.045	1	0.045	2.76	0.00467	
A2	0.54	1	0.54	4.81	0.00707	
B2	0.81	1	0.81	6.54	0.00431	
C2	0.96	1	0.96	4.02	0.00916	
Residual	2.41	6	0.7358			
Total	24.65	12				

TABLE 6 ANOVA: quadratic model for flexural strength.

Source	Sum of squares	df	Mean square	F-value	p-value	Comments
Model	3.22	9	0.5358	8.92	0.00204	R^2 = 0.910 Adj.R^2 = 0.78 Pre.R^2 = 0.57 C.V % 4.06
A (BN)	0.1310	1	0.1310	0.9583	0.03654	
B (QDF)	0.0164	1	0.0164	0.1203	0.03405	
C (QDB)	0.3300	1	0.3300	2.41	0.01712	
AB	0.034	1	0.034	1.17	0.0092	
AC	0.076	1	0.076	0.76	0.0076	
BC	0.092	1	0.092	2.54	0.00667	
A^2	0.46	1	0.46	6.68	0.0171	
B^2	0.5862	1	0.5862	4.29	0.0838	
C^2	0.12	1	0.12	5.18	0.0288	
Residual	0.8200	6	0.1367			
Total	4.03	12				

TABLE 7 ANOVA: a quadratic model for split tensile strength.

Source	Sum of squares	df	Mean square	F-value	p-value	Comments
Model	1.51	10	0.2519	10.26	0.0031	R^2 = 0.961 Adj.R^2 = 0.89 Pre.R^2 = 0.75 C.V % 2.46
A (BN)	0.0798	1	0.0798	3.25	0.0121	
B (QDF)	0.2777	1	0.2777	5.31	0.0015	
C (QDB)	0.1058	1	0.1058	4.31	0.0083	
AB	0.020	1	0.020	3.43	0.0034	
AC	0.043	1	0.043	2.45	0.0011	
BC	0.056	1	0.056	4.34	0.0028	
A^2	0.1227	1	0.1227	5.00	0.0468	
B^2	0.1924	1	0.1924	7.84	0.0312	
C^2	0.0733	1	0.0733	2.98	0.0134	
Residual	0.1473	6	0.0245			
Total	1.66	12				

Clay - BN), B (Quarry Dust as a Binder - QDB), and C (Quarry Dust as a Filler - QDF). Additionally, interaction terms such as AC (interaction between bentonite clay and quarry dust filler) and quadratic terms (A^2, B^2, C^2) were included to refine the model. ANOVA evaluates each factor's contribution to the response variables, revealing how interactions between these variables affect strength characteristics. For example, the interaction term AC shows how the combined effect of BN and QDF impacts strength. The Variance Inflation Factor (VIF) was calculated, with all values equal to 1, indicating that there is no multicollinearity. This orthogonality ensures that each variable contributes independently to the model without redundancy. Based on ANOVA results, the final models

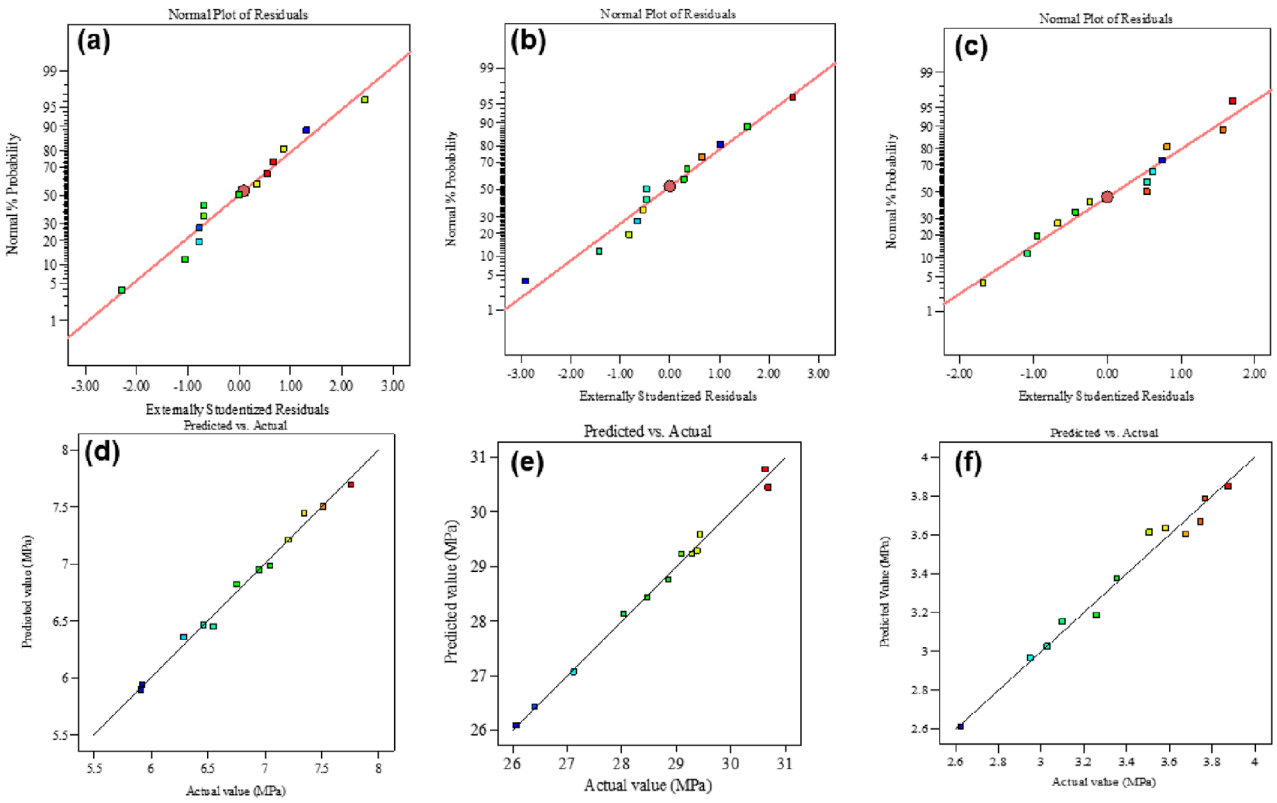

FIGURE 10
The normal plot of residual **(A)** compressive strength, **(B)** flexural strength, **(C)** tensile strength Predicted vs. actual plot **(D)** compressive strength **(E)** flexural strength **(F)** tensile strength.

for compressive, flexural, and split tensile strength were formulated, eliminating insignificant terms but maintaining hierarchy and necessary interactions.

Equations 1–3 represent the refined models.

$$\sigma_c = 33.19 + 0.49A - 0.47B - 0.92C + 0.088AB + 0.056AC + 0.045BC - 0.52A^2 - 0.26B^2 - 0.65C^2 \quad (1)$$

$$\sigma_f = 9.92 + 0.11A - 0.028B + 0.33C + 0.034AB + 0.076AC + 0.092BC - 0.62A^2 - 0.81B^2 - 0.18C^2 \quad (2)$$

$$\sigma_{st} = 3.76 - 0.303A - 0.49B - 0.32C + 0.020AB + 0.043AC + 0.056BC - 0.62A^2 - 0.81B^2 - 0.18C^2 \quad (3)$$

4.1 Contour plots and 3D surface response

The adequacy of the model was assessed through diagnostic plots, depicted in Figure 10, which are crucial for validating the model. In the normal residual plot Figures 10A–C the data points follow a normal distribution, with residuals parallel to an inclined straight line. The residuals vs. expected diagram reveals a random and consistent distribution of residuals above and below the reference line, indicating uniform data variation. Moreover, the plot comparing predicted and actual compressive, flexural, and split tensile strength Figures 10D–F demonstrates that the values closely align along the inclined straight line. The suggested optimized model accurately predicts these values.

Figures 11A–C display contour plots illustrating the compressive, flexural, and split tensile strength of concrete. These plots demonstrate that different combinations of input factors, such as Bentonite clay, quarry dust binder, and filler, result in a range of compressive, flexural, and split tensile strength values. Typically, contour plots in the literature emphasize the optimal response area and variable combinations. According to the figure, optimal 28-day compressive, flexural, and split tensile strengths within the range of 33, 9.5, and 3.5 MPa, respectively, can be attained by incorporating 10%–15% substitution of cement with bentonite clay and 8%–12% substitution of sand and quarry dust as a binder.

In Figures 11D, E, it can be observed that substituting cement by over 15% leads to a reduction in strength due to increased proportions of bentonite clay and quarry dust. Concrete with high levels of bentonite clay, especially at a 15% replacement level with cement, exhibits decreased strength. Figure 11F shows that replacing cement by over 10% with quarry dust binder reduces strength. This outcome is attributed to non-uniform distribution and unequal dispersion of additives, which weaken matrix bonds. Additionally, a higher fraction of supplementary cementitious material (SCM) leads to increased alkali-silicate reaction due to excess content not

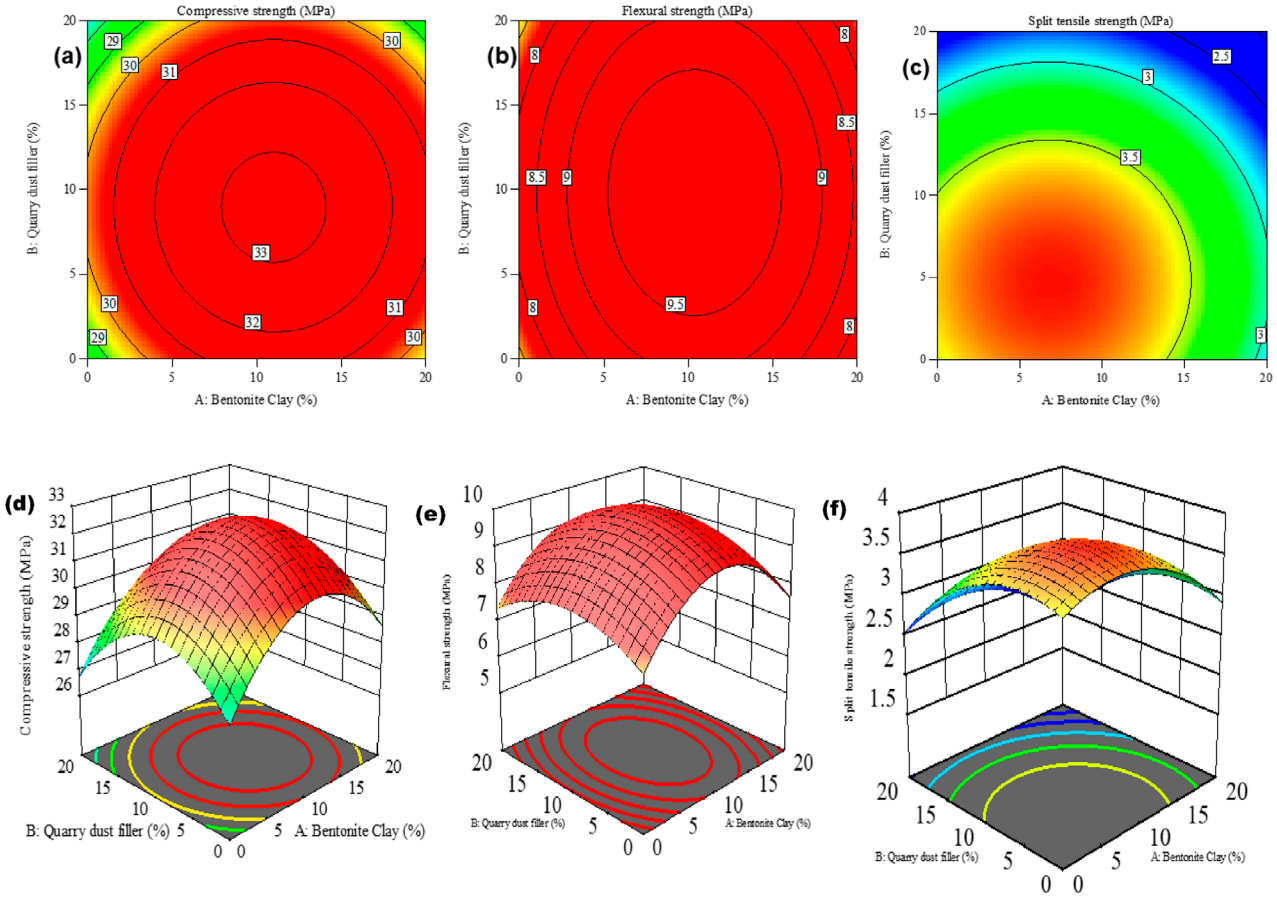

FIGURE 11
Response spectrum plot **(A)** contour compressive **(B)** contour flexural **(C)** contour tensile strength **(D)** 3D surface compressive **(E)** 3D surface flexural **(F)** 3D surface tensile strength.

undergoing pozzolanic reaction. This heightened reaction raises the risk of alkaline-silica response (ASR), detrimental to compressive, flexural, and split tensile strengths.

4.2 Optimization combination

Response Surface Methodology (RSM) was employed as a numerical optimization tool to identify the ideal mix design for maximizing the compressive strength of concrete after 28 days of curing. The optimal combination, predicted by the model and presented cubic Figure 12 representation of the optimized combinations of bentonite clay, quarry dust as a binder, and quarry dust as a filler, predicting their effects on compressive strength, flexural strength, and split tensile strength. The figure visualizes how different proportions of these materials influence the mechanical properties of the cementitious composite. It highlights the optimal mix designs that maximize the desired strengths, demonstrating the interaction between the three components and their combined effects on performance. The cubic figure shows that 13.92% of cement with bentonite clay, 10.418% with quarry dust, and 12.196% of fine aggregate with quarry dust. This optimized mix was predicted to achieve compressive, flexural, and split tensile strengths of 34.031, 10.232, and 3.458 MPa, respectively as shown in Table 8. It highlights the optimal mix designs that maximize the desired strengths, demonstrating the interaction between the three components and their combined effects on performance.

4.3 Validation of model

The optimal mix design was determined using response surface methodology, resulting in a composition of 10.29% bentonite clay and 7.20% quarry dust as cement replacements, along with 8.19% quarry dust replacing fine aggregate. This mix was experimentally validated over a 28-day curing period, with three samples tested per mix. The average compressive, flexural, and split tensile strengths achieved were 33.60, 9.49, and 3.95 MPa, respectively. The differences between the predicted and experimental values were consistently below 5%, highlighting the accuracy of the model. This validation confirms the optimal effectiveness of the mix in achieving maximum strength. Furthermore, the developed models reliably predicted strength values under experimental conditions. Compared to reference concrete, the optimized samples demonstrated notable strength improvements of 18.08%, 33.60%, and 11.15% in compressive, flexural, and split tensile strengths,

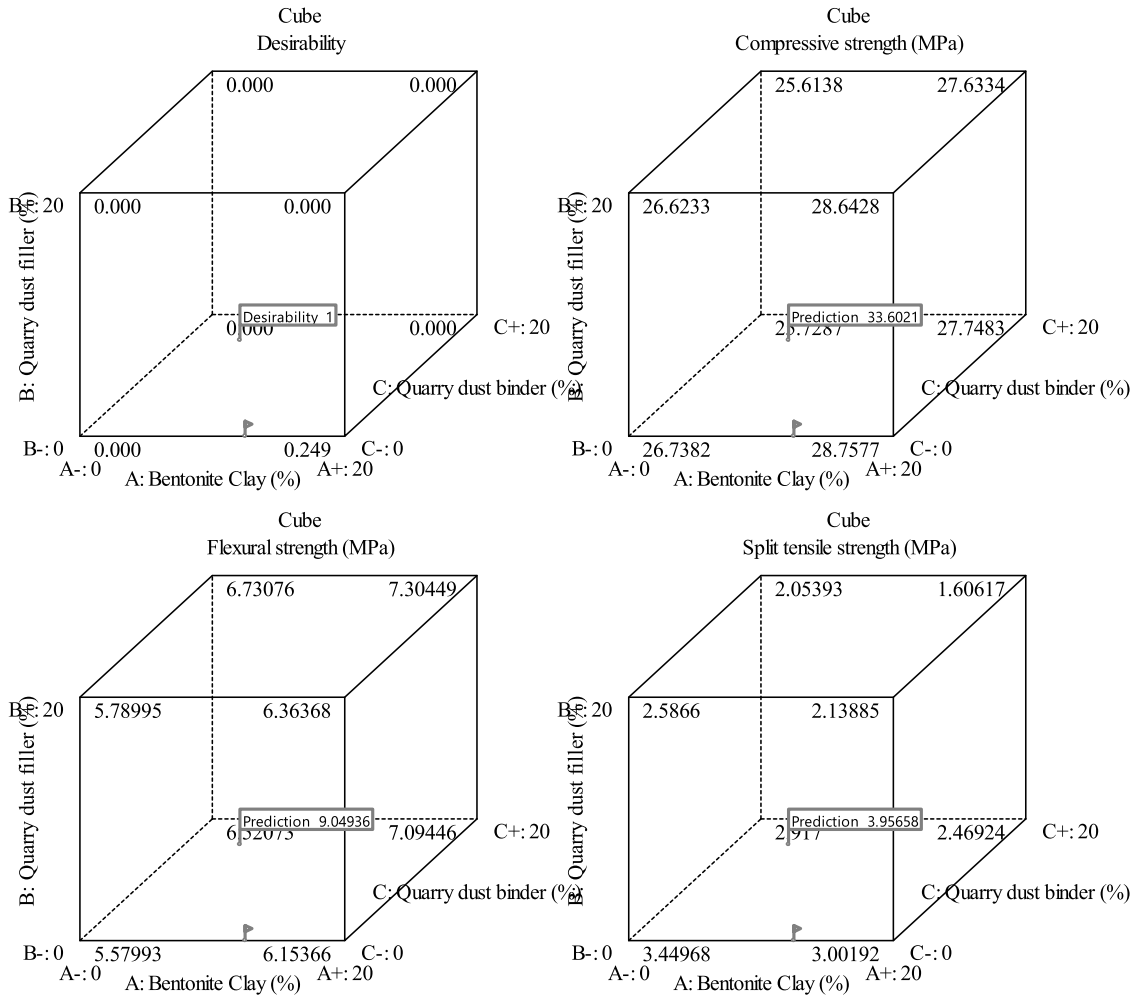

FIGURE 12
Optimization combination prediction of compressive, flexural, and split tensile strength.

TABLE 8 The optimum combination of SCM replacement.

Sr#	BN	QDF	QDB	Compressive strength (MPa)	Flexural strength (MPa)	Split tensile strength (MPa)
1	10.29	8.19	7.20	33.60	9.49	3.95
2	9.64	3.65	5.25	33.77	9.43	4.02
3	9.64	5.35	6.34	33.87	9.38	3.91

TABLE 9 Validation of results and error between actual and predicted values.

Mix	Compressive strength (Mpa)			Flexural strength (Mpa)			Split tensile strength (Mpa)		
	Actual	Prediction	Error (%)	Actual	Prediction	Error (%)	Actual	Prediction	Error (%)
1	34.11	33.60	1.50	9.88	9.49	3.95	3.79	3.95	−4.22
2	32.72	33.77	−3.21	9.65	9.43	2.28	3.87	4.02	−3.88
3	32.41	33.87	−4.50	9.10	9.38	−3.08	3.74	3.91	−4.57

TABLE 10 Unit costs of the raw materials used for concrete.

Raw material	Cement	Coarse aggregate	Fine aggregate	Bentonite clay	Quarry dust
Cost (PKR/kg)	29	8	5	4	3

TABLE 11 Cost analysis for various concrete mixtures.

Sr #	Specimen ID	Total cost (PKR/m^3)	Change in (%) cost	Sr #	Specimen ID	Total cost (PKR/m^3)	Change in (%) cost
1	CM	23593	1.000	8	15QDF	23353.6	−1.015
2	5BN	23132.6	−1.951	9	20QD F	23273.8	−1.353
3	10BN	22675.5	−3.889	10	5QDB	23114.3	−2.029
4	15BN	22215.1	−5.840	11	10QDB	22638.8	−4.044
5	20 BN	21758	−7.778	12	15QDB	22160.1	−6.073
6	5QDF	23513.2	−0.338	13	20QDB	21684.6	−8.089
7	10QDF	23433.4	−0.676				

respectively as shown in Table 9. The table also illustrates the minimal discrepancies below 5% between the model predictions and actual experimental results across all curing periods, further affirming the models' effectiveness in accurately predicting compressive strength with a 95% confidence level.

5 Cost-benefit analysis

It is well established that using supplementary cementitious materials (SCMs) like bentonite (BN) and quarry dust (QD) as substitutes for ordinary Portland cement (OPC) can effectively reduce pressure on natural resources and lower production costs. Additionally, such alternative concrete mixes can exhibit enhanced strength and durability. Consequently, it is essential to explore cost-reducing methods. In this study, bentonite and quarry dust were combined as OPC replacements to lower the overall expenses of the concrete mix. Table 10 summarizes the unit costs in Pakistani Rupees (PKR) for the raw materials used. The cost analysis for 1 m^3 of various concrete mixes with different percentages of BN, QDB, and QDF is presented in Table 11. The cost of the control mix with only OPC is PKR 23,593. However, as the bentonite content increases, the cost decreases; for example, mixes with 1.95% and 3.88% BN cost 5.84 and 7.77 times less than the control mix, respectively. When the bentonite content exceeds 20%, the cost is over 7% lower compared to the control mix, offering a cost-effective solution for the construction industry.

Similarly, increasing the quarry dust content also reduces costs. For instance, mixes with 2.02% and 4.0% QDB cost 6 and 8 times less than the control mix, respectively. When quarry dust content exceeds 20%, the mix cost is more than 8% lower than the control mix, making it a cost-efficient option for construction.

Moreover, a mix with a synergistic combination of 10% bentonite, 8% quarry dust as a filler, and 7% quarry dust as a binder costs approximately 8.4% less than the control mix. Given its enhanced strength and durability, this mix is well-suited for various structural applications. These benefits could be particularly significant for large-scale projects like dams and multi-story buildings, where concrete production constitutes a substantial portion of the costs (Ashraf et al., 2022; Memon et al., 2012).

6 Conclusion

This research investigated the effectiveness of locally available supplementary cementitious materials (bentonite clay and quarry dust) in enhancing concrete properties. The study investigated compressive strength, flexural strength, and acid resistance at 7 and 28 days of curing. Moreover, experimental results were compared using statistical analysis through the Response Surface Method. The summary of the key findings are:

1. Incorporating bentonite clay and quarry dust tends to lower the workability of mixes compared to reference mixes. Due to smaller and coarser particles, mixes contained with quarry dust exhibited the lowest workability. This observation is crucial for practical applications, as adjustments in water content or admixtures may be required to maintain workability in field applications.
2. Quarry dust (10%) significantly improved compressive strength, with increases of 11.9% and 7.38% at 7 and 28 days of curing, respectively, compared to reference concrete. Bentonite clay (10%) initially reduced strength by 1.3% at 7 days but compensated with a 4.91% increase by 28 days of curing. The later age strength improvement is attributed to the late

hydration reaction of bentonite clay that produces C2S, which creates extra C-S-H. This delayed strength gain suggests that bentonite clay can be effectively used in applications where long-term strength development is desired, making it suitable for structures with extended curing periods.

3. Incorporating 10% bentonite clay and 10% quarry dust increased flexural strength. Bentonite clay showed a 4.2% increase at 7 days but improved to 11.9% at 28 days of curing. Quarry dust initially showed higher strength, 19.7%, but it was reduced to a 7.17% improvement. However, the strength gain for quarry dust decreased over time, whereas bentonite clay showed a consistent improvement. This suggests that while quarry dust offers significant early-age strength benefits, bentonite clay contributes to longer-term strength development, which is valuable for designing concrete that performs well over its service life.
4. The same trend was observed for the split tensile strength test. The highest split strength for bentonite clay bentonite clay was noted at 28 days of curing, whereas the highest strength for quarry dust was noted for mixes containing 10% quarry dust at 7 days of curing.
5. Mixtures containing 20% bentonite clay and 20% quarry dust demonstrated superior resistance to chemical attack compared to the control mix. The quarry dust filled the voids and concrete gaps, making acid ingress difficult—similarly, the formation of calcium hydrate due to bentonite clay made it difficult for acid ingress. The SEM analysis confirmed the capillaries produced after exposure to acids. The acids react with cement, lowering the C-S-H composition leading to voids and capillary formation, which is ideal for the formation of etrringite. This makes the SCM-modified concrete highly suitable for aggressive environments, such as chemical plants and coastal areas.
6. Statistical analysis revealed that a combination of 10.29% bentonite clay, 7.20% quarry dust replacing cement, and 8.19% replacing fine aggregate produced concrete with excellent strength matching theoretical predictions. This optimal mix provides a sustainable approach to concrete production, balancing performance and resource utilization effectively.

6.1 Significance and implications

This study underscores the potential of using bentonite clay and quarry dust as sustainable SCMs, offering both environmental and performance benefits. The findings highlight the practical advantages of these materials in improving concrete properties while contributing to waste reduction and resource conservation. Future research should explore the rheological behavior of these SCMs under varying conditions, such as elevated temperatures, to further validate their applicability in diverse construction scenarios.

Data availability statement

The raw data supporting the conclusions of this article will be made available by the authors, without undue reservation.

Author contributions

MU: Writing–original draft, Writing–review and editing. HQ: Writing–review and editing, Supervision. MK: Writing–original draft. MS: Software, Writing–original draft. HA: Formal Analysis, Validation, Writing–review and editing. AA: Methodology, Software, Writing–original draft. MB: Conceptualization, Data curation, Writing–original draft, Writing–review and editing. NV: Funding acquisition, Writing–review and editing.

Funding

The author(s) declare that financial support was received for the research, authorship, and/or publication of this article. This research was funded by Taif University, Saudi Arabia, Project No. (TU-DSPP-2024-33). The research is also partially funded by the Ministry of Science and Higher Education of the Russian Federation as part of the World-class Research Center program Advanced Digital Technologies (contract No. 075-15-2022-311 dated 20.04.2022).

Acknowledgments

The authors extend their appreciation to Taif University, Saudi Arabia, for supporting this work through project number (TU-DSPP-2024-33).

Conflict of interest

The authors declare that the research was conducted in the absence of any commercial or financial relationships that could be construed as a potential conflict of interest.

Publisher's note

References

Abd Elmoaty, A. E. M. (2013). Mechanical properties and corrosion resistance of concrete modified with granite dust. *Constr. Build. Mater.* 47, 743–752. doi:10.1016/j.conbuildmat.2013.05.054

Ahmad, J., Kontoleon, K. J., Al-Mulali, M. Z., Shaik, S., El Ouni, M. H., and El-Shorbagy, M. A. (2022). Partial substitution of binding material by bentonite clay (BC) in concrete: a review. *A Rev. Build.* 12, 634. doi:10.3390/buildings12050634

Al-Bakri, A. Y., Ahmed, H. M., and Hefni, M. A. (2022). Cement kiln dust (CKD): potential beneficial applications and eco-sustainable solutions. *Sustain* 14, 7022. doi:10.3390/su14127022

Ali, S., Khan, S. M., Ahmad, Z., Abdullah, A., Kazi, N., Nawaz, I., et al. (2023). Relative humidity, soil phosphorus, and stand structure diversity determine aboveground biomass along the elevation gradient in various forest ecosystems of Pakistan. *Sustain* 15, 7523. doi:10.3390/su15097523

Althoey, F., Ansari, W. S., Sufian, M., and Deifalla, A. F. (2023). Advancements in low-carbon concrete as a construction material for the sustainable built environment. *Dev. Built Environ.* 16, 100284. doi:10.1016/j.dibe.2023.100284

Aprianti S, E. (2017). A huge number of artificial waste material can be supplementary cementitious material (SCM) for concrete production – a review part II. *J. Clean. Prod.* 142, 4178–4194. doi:10.1016/j.jclepro.2015.12.115

Arrigoni, A., Panesar, D. K., Duhamel, M., Opher, T., Saxe, S., Posen, I. D., et al. (2020). Life cycle greenhouse gas emissions of concrete containing supplementary cementitious materials: cut-off vs. substitution. *J. Clean. Prod.* 263, 121465. doi:10.1016/j.jclepro.2020.121465

Ashraf, M., Iqbal, M. F., Rauf, M., Ashraf, M. U., Ulhaq, A., Muhammad, H., et al. (2022). Developing a sustainable concrete incorporating bentonite clay and silica fume: mechanical and durability performance. *J. Clean. Prod.* 337, 130315. doi:10.1016/j.jclepro.2021.130315

Castillo Lara, R., and Chagas Cordeiro, G. (2019). Effect of rice husk ash as supplementary cementitious material on the performance of cement-based pastes continuously exposed to organic acid solution (vinasse). *J. Mater. Civ. Eng.* 31. doi:10.1061/(asce)mt.1943-5533.0002739

Chengfang, Y., Raza, A., Manan, A., Ahmad, S., Chao, W., and Umar, M. (2024). "Experimental and FEM analysis on the impact of yellow river sand replacement rate on engineered cementitious composite (ECC)," in *Proc. Inst. Civ. Eng. Sustain.* (England: Emerald Publishing Limited), 1–18.

Chintalapudi, K., and Pannem, R. M. R. (2022). Enhanced chemical resistance to sulphuric acid attack by reinforcing Graphene Oxide in Ordinary and Portland Pozzolana cement mortars. *Case Stud. Constr. Mater.* 17, e01452. doi:10.1016/j.cscm.2022.e01452

da Silva Rego, J. H., Sanjuán, M. Á., Mora, P., Zaragoza, A., and Visedo, G. (2023). Carbon dioxide uptake by Brazilian cement-based materials. *Appl. Sci.* 13, 10386. doi:10.3390/app131810386

de Siqueira, A.A., and Cordeiro, G. C. (2022). Sustainable cements containing sugarcane bagasse ash and limestone: effects on compressive strength and acid attack of mortar. *Sustain* 14, 5683. doi:10.3390/su14095683

Dobiszewska, M., Bagcal, O., Beycioğlu, A., Goulias, D., Köksal, F., Płomiński, B., et al. (2023). Utilization of rock dust as cement replacement in cement composites: an alternative approach to sustainable mortar and concrete productions. *J. Build. Eng.* 69, 106180. doi:10.1016/j.jobe.2023.106180

Duchesne, J. (2021). Alternative supplementary cementitious materials for sustainable concrete structures: a review on characterization and properties. *Waste Biomass Valorization* 12, 1219–1236. doi:10.1007/s12649-020-01068-4

Escavy, J. I., Herrero, M. J., Trigos, L., and Sanz-Pérez, E. (2020). Demographic vs economic variables in the modelling and forecasting of the demand of aggregates: the case of the Spanish market (1995–2016). *Resour. Policy.* 65, 101537. doi:10.1016/j.resourpol.2019.101537

Fadaie, M. A., Nekooei, M., and Javadi, P. (2019). Effect of dry and saturated bentonite on plastic concrete. *KSCE J. Civ. Eng.* 23, 3431–3442. doi:10.1007/s12205-019-0835-2

Febin, G. K., Abhirami, A., Vineetha, A. K., Manisha, V., Ramkrishnan, R., Sathyan, D., et al. (2019). Strength and durability properties of quarry dust powder incorporated concrete blocks. *Constr. Build. Mater.* 228, 116793. doi:10.1016/j.conbuildmat.2019.116793

Google Earth (2024). Google Earth. Available at: https://earth.google.com/web/search/33°44'24",+73°02'18"/@33.74,73.0383333,806.57842694a,860.84456841d,35y,257.91465127h,45t,0r/data=CiwiJgokCbO2O9GGAEFAES9Opevw_UBAGQzQfO_4DVJAIS3xTcB8DFJAQgIIAUoNCP_____wEQAA.

He, R., Nantung, T., and Lu, N. L. (2024). Unraveling microstructural evolution in air-entrained mortar and paste: insights from MIP and micro-CT tomography amid cyclic freezing-thawing damage. *J. Build. Eng.* 94, 109922. doi:10.1016/j.jobe.2024.109922

He, R., Nantung, T., Olek, J., and Lu, N. (2023). Field study of the dielectric constant of concrete: a parameter less sensitive to environmental variations than electrical resistivity. *J. Build. Eng.* 74, 106938. doi:10.1016/j.jobe.2023.106938

Hemalatha, T., and Sindu, B. S. (2020). Experimental studies to investigate efficacies of slag as fine aggregate substitute. *ACI Mater. J.* doi:10.14359/51725981

Ho, D. W. S., Sheinn, A. M. M., Ng, C. C., and Tam, C. T. (2002). The use of quarry dust for SCC applications. *Cem. Concr. Res.* 32, 505–511. doi:10.1016/S0008-8846(01)00726-8

Isaksson, R., Rosvall, M., Babaahmadi, A., Buregyeya, A., Hazarika, A., Marangu, J. M., et al. (2023). Supplementary cementitious materials in building blocks—diagnosing opportunities in sub-saharan Africa. *Sustain* 15, 5822. doi:10.3390/su15075822

Javed, U., Khushnood, R. A., Memon, S. A., Jalal, F. E., and Zafar, M. S. (2020). Sustainable incorporation of lime-bentonite clay composite for production of ecofriendly bricks. *J. Clean. Prod.* 263, 121469. doi:10.1016/j.jclepro.2020.121469

Kankam, C. K., Meisuh, B. K., Sossou, G., and Buabin, T. K. (2017). Stress-strain characteristics of concrete containing quarry rock dust as partial replacement of sand. *Case Stud. Constr. Mater.* 7, 66–72. doi:10.1016/j.cscm.2017.06.004

Karagüzel, C., Çetinel, T., Boylu, F., Çinku, K., and Çelik, M.S. (2010). Activation of (Na, Ca)-bentonites with soda and MgO and their utilization as drilling mud. *Appl. Clay Sci.* 48, 398–404. doi:10.1016/j.clay.2010.01.013

Khan, I. U. (2023). Utilizing bentonite clay as a pozzolanic material to reduce cement consumption and cost in construction industry. *Juniper Online J. Mater. Sci.* 7. doi:10.19080/jojms.2023.07.555722

Khan, M., Cao, M., Chu, S. H., and Ali, M. (2022b). Properties of hybrid steel-basalt fiber reinforced concrete exposed to different surrounding conditions. *Constr. Build. Mater.* 322, 126340. doi:10.1016/j.conbuildmat.2022.126340

Khan, M. I., Shah, M. U., and Usman, M. (2022a). Experimental investigation of concrete properties using locally available coarse aggregates in Punjab, Pakistan. *NUST J. Eng. Sci.* 15, 26–29. doi:10.24949/njes.v15i1.655

Khan, M. Y., Turab, S. A., Riaz, M. S., Atekwana, E. A., Muhammad, S., Butt, N. A., et al. (2021). Investigation of coseismic liquefaction-induced ground deformation associated with the 2019 Mw 5.8 Mirpur, Pakistan, earthquake using near-surface electrical resistivity tomography and geological data. *Near Surf. Geophys* 19, 169–182. doi:10.1002/nsg.12148

Khan, S. U., Qureshi, M. I., Rana, I. A., and Maqsoom, A. (2019). An empirical relationship between seismic risk perception and physical vulnerability: a case study of Malakand, Pakistan. *Int. J. Disaster Risk Reduct.* 41, 101317. doi:10.1016/j.ijdrr.2019.101317

Kolawole, J. T., Babafemi, A. J., Fanijo, E., Chandra Paul, S., and Combrinck, R. (2021). State-of-the-art review on the use of sugarcane bagasse ash in cementitious materials. *Cem. Concr. Compos.* 118, 103975. doi:10.1016/j.cemconcomp.2021.103975

Kursuncu, B., Gencel, O., Bayraktar, O. Y., Shi, J., Nematzadeh, M., and Kaplan, G. (2022). Optimization of foam concrete characteristics using response surface methodology and artificial neural networks. *Constr. Build. Mater.* 337, 127575. doi:10.1016/j.conbuildmat.2022.127575

Ma, H., Sun, Z., and Ma, G. (2022). Research on compressive strength of manufactured sand concrete based on response surface methodology (RSM). *Appl. Sci.* 12, 3506. doi:10.3390/app12073506

Manjunatha, M., Preethi, S., Malingaraya, Mounika, H. G., Niveditha, K. N., Ravi, (2021). Life cycle assessment (LCA) of concrete prepared with sustainable cement-based materials. *Mater. Today Proc.* 47, 3637–3644. doi:10.1016/j.matpr.2021.01.248

Masood, B., Elahi, A., Barbhuiya, S., and Ali, B. (2020). Mechanical and durability performance of recycled aggregate concrete incorporating low calcium bentonite. *Constr. Build. Mater.* 237, 117760. doi:10.1016/j.conbuildmat.2019.117760

Memon, S. A., Arsalan, R., Khan, S., and Lo, T. Y. (2012). Utilization of Pakistani bentonite as partial replacement of cement in concrete. *Constr. Build. Mater.* 30, 237–242. doi:10.1016/j.conbuildmat.2011.11.021

Mirgozar Langaroudi, M. A., and Mohammadi, Y. (2022). Effect of nano-clay on the freeze–thaw resistance of self-compacting concrete containing mineral admixtures. *Eur. J. Environ. Civ. Eng.* 26, 481–500. doi:10.1080/19648189.2019.1665107

Mirza, J., Riaz, M., Naseer, A., Rehman, F., Khan, A. N., and Ali, Q. (2009). Pakistani bentonite in mortars and concrete as low cost construction material. *Appl. Clay Sci.* 45, 220–226. doi:10.1016/j.clay.2009.06.011

Mugi, K. (2022). Comparative study on the effects of quarry dust and natural fines on performance of concrete blocks. *Afr. J. Sci. Technol. Soc. Sci.* 1. doi:10.58506/ajstss.v1i1.50

Nasier, S. (2021). Utilization of recycled form of concrete, E-wastes, glass, quarry rock dust and waste marble powder as reliable construction materials. *Mater. Today Proc.* 45, 3231–3234. doi:10.1016/j.matpr.2020.12.381

Nasiru, S., Jiang, L., Yu, L., Chu, H., Huang, Y., Pei, C., et al. (2021). Properties of cement mortar containing recycled glass and rice husk ash. *Constr. Build. Mater.* 299, 123900. doi:10.1016/j.conbuildmat.2021.123900

Nataraja, M. C., and Nalanda, Y. (2008). Performance of industrial by-products in controlled low-strength materials (CLSM). *Waste Manag.* 28, 1168–1181. doi:10.1016/j.wasman.2007.03.030

Ndahirwa, D., Zmamou, H., Lenormand, H., and Leblanc, N. (2022). The role of supplementary cementitious materials in hydration, durability and shrinkage of cement-based materials, their environmental and economic benefits: a review. *Clean. Mater.* 5, 100123. doi:10.1016/j.clema.2022.100123

Passuello, A., Rodríguez, E. D., Hirt, E., Longhi, M., Bernal, S. A., Provis, J. L., et al. (2015). Deflection analysis of flexible pavements-materials and test division report. *Constr. Build. Mater.*

Qian, H., Umar, M., Khan, M. N. A., Shi, Y., Manan, A., Raza, A., et al. (2024). A state-of-the-art review on shape memory alloys (SMA) in concrete: mechanical properties, self-healing capabilities, and hybrid composite fabrication. *Mater. Today Commun.* 40, 109738. doi:10.1016/j.mtcomm.2024.109738

Qureshi, L. A., Ali, B., and Ali, A. (2020). Combined effects of supplementary cementitious materials (silica fume, GGBS, fly ash and rice husk ash) and steel fiber on the hardened properties of recycled aggregate concrete. *Constr. Build. Mater.* 263, 120636. doi:10.1016/j.conbuildmat.2020.120636

Ramos, T., Matos, A. M., Schmidt, B., Rio, J., and Sousa-Coutinho, J. (2013). Granitic quarry sludge waste in mortar: effect on strength and durability. *Constr. Build. Mater.* 47, 1001–1009. doi:10.1016/j.conbuildmat.2013.05.098

Raza, A., Junjie, Z., Shiwen, X., Umar, M., and Chengfang, Y. (2024). Experimental analysis of frost resistance and failure models in engineered cementitious composites with the integration of Yellow River sand. *Sci. Eng. Compos. Mater.* 31, 20240017. doi:10.1515/secm-2024-0017

Rehman, S. U., Kiani, U. A., Yaqub, M., and Ali, T. (2020). Controlling natural resources depletion through Montmorillonite replacement for cement-low cost construction. *Constr. Build. Mater.* 232, 117188. doi:10.1016/j.conbuildmat.2019.117188

Shaheen, A. ul H., Ahmed, K. S., Sarfraz, Y., Riaz, M. T., and Shahzad, A. (2023). Physico-mechanical characterization of cement concrete using quarry waste as fine aggregate replacement of natural sand. *Arab. J. Sci. Eng.* 48, 13807–13821. doi:10.1007/s13369-023-07981-9

Snellings, R., Suraneni, P., and Skibsted, J. (2023). Future and emerging supplementary cementitious materials. *Cem. Concr. Res.* 171, 107199. doi:10.1016/j.cemconres.2023.107199

Soomro, M., Tam, V. W. Y., and Jorge Evangelista, A. C. (2022). Production of cement and its environmental impact. *Recycl. Concr. Technol. Perform.*, 11–46. doi:10.1016/B978-0-323-85210-4.00010-2

Sousa, V., Bogas, J. A., Real, S., and Meireles, I. (2023). Industrial production of recycled cement: energy consumption and carbon dioxide emission estimation. *Environ. Sci. Pollut. Res.* 30, 8778–8789. doi:10.1007/s11356-022-20887-7

Sun, Z., gui Chen, Y., and min Ye, W. (2022). A systematic review of bentonite/concrete interaction system in HLW disposal repositories: theoretical, experimental and geochemical modelling analysis. *Constr. Build. Mater.* 353, 129075. doi:10.1016/j.conbuildmat.2022.129075

Sundaralingam, K., Peiris, A., Anburuvel, A., and Sathiparan, N. (2022). Quarry dust as river sand replacement in cement masonry blocks: effect on mechanical and durability characteristics. *Materialia* 21, 101324. doi:10.1016/j.mtla.2022.101324

Thomas, J., and Harilal, B. (2016). Mechanical properties of cold bonded quarry dust aggregate concrete subjected to elevated temperature. *Constr. Build. Mater.* 125, 724–730. doi:10.1016/j.conbuildmat.2016.08.093

Umair, M., Mehmood, A., Rukh, S., Khan, A., Ahmad, Z., Rafique, M., et al. (2023). Controlling arsenic contamination through bentonite clays: a batch sorption study. *J. Soil Sci. Plant Nutr.* 23, 2381–2391. doi:10.1007/s42729-023-01191-w

Uratani, J. M., and Griffiths, S. (2023). A forward looking perspective on the cement and concrete industry: implications of growth and development in the Global South. *Energy Res. Soc. Sci.* 97, 102972. doi:10.1016/j.erss.2023.102972

Xie, Y., Li, J., Lu, Z., Jiang, J., and Niu, Y. (2018). Effects of bentonite slurry on air-void structure and properties of foamed concrete. *Constr. Build. Mater.* 179, 207–219. doi:10.1016/j.conbuildmat.2018.05.226

Zhang, Y., Raza, A., Umar, M., Chen, Y., and Yuan, C. (2023). Study on frost resistance and interface bonding performance through the integration of recycled brick powder in ultra-high-performance concrete for structural reinforcement. *Mater. (Basel)* 16, 6999. doi:10.3390/ma16216999

Zhao, Y., Goulias, D., Dobiszewska, M., and Modrzyński, P. (2022). Life-Cycle sustainability assessment of using rock dust as a partial replacement of fine aggregate and cement in concrete pavements. *Sustain* 14, 12449. doi:10.3390/su141912449

Frontiers in Materials

Investigates the discovery and design of materials for future application

A multidisciplinary journal that explores the breadth of materials science, engineering and mechanics - from carbon-based materials to smart materials.

Discover the latest Research Topics

See more →

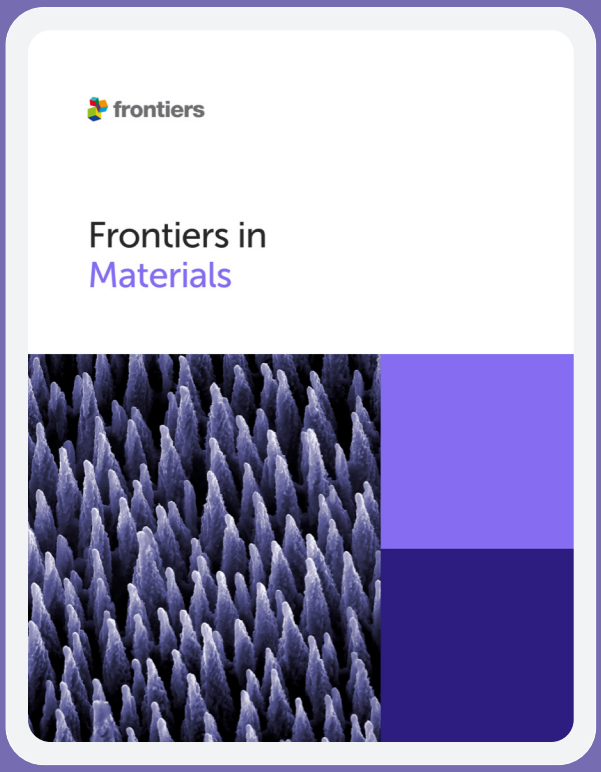

Frontiers

Avenue du Tribunal-Fédéral 34
1005 Lausanne, Switzerland
frontiersin.org

Contact us

+41 (0)21 510 17 00
frontiersin.org/about/contact